Investigation of the cycling mechanisms in silicon and germanium-based Lithium-ion batteries by ex-situ and operando X-ray scattering techniques

Diana Zapata Dominguez

THÈSE

Pour obtenir le grade de

DOCTEUR DE L'UNIVERSITE GRENOBLE ALPES

Spécialité : **Physique de la matière condensée et du rayonnement**

Arrêté ministériel : 25 mai 2016

Présentée par

Diana ZAPATA DOMINGUEZ

Thèse dirigée par **Sandrine LYONNARD** et
Codirigée par **Stéphanie POUGET**

préparée au sein des laboratoires **Modélisation et Exploration des Matériaux (MEM) et Systèmes Moléculaires et nanoMatériaux pour l'Énergie et la Santé (SyMMES)**
dans **l'École Doctorale Physique de Grenoble**

Etude par des techniques de diffusion des rayons X *ex-situ* et *operando* des mécanismes de (de)lithiation dans les batteries Lithium-ion à base de silicium et germanium

Investigation of the cycling mechanisms in silicon and germanium-based Lithium-ion batteries by *ex-situ* and *operando* X-ray scattering techniques

Thèse soutenue publiquement le **18 décembre 2020,**
devant le jury composé de :

Mme. Fannie ALLOIN
Directrice de recherche, LEPMI CNRS, Présidente du jury
Mme. Kristina EDSTRÖM
Professeur, Ångström Advanced Battery Centre (ÅABC), Examinatrice
Mme. Laure MONCONDUIT
Directrice de recherche, CNRS-Université de Montpellier, Rapportrice
Mme. Montserrat CASAS CABANAS
Coordinatrice scientifique, CIC energiGUNE, Rapportrice
Mme. Nathalie HERLIN-BOIME
Directrice de recherche, NIMBE, CEA Paris Saclay, Invitée

Acknowledgments

I would like to acknowledge all the people without this manuscript, I would not have been possible and made my Ph.D. a successful and exceptional work. I would like to start thanking my jury committee, who carefully read and evaluated this manuscript, and I greatly acknowledge the interesting discussion we had during my thesis defense.

These three years have been formidable, and there were thanks to my supervisors, Sandrine Lyonnard and Stephanie Pouget, who welcome me for the first time at the best place to do synchrotron x-ray and neutron experiments at the same time (as Sandrine usually says): the ESRF and ILL in Grenoble. Sandrine Lyonnard and Stephanie Pouget's unwavering enthusiasm, support, and encouragement have made it possible to finish this excellent research work and exciting experience. I sincerely thanked you to involved me in the Sintbat project, which enriches my experience with different materials and techniques.

I would not be able to produce great images of the thesis manuscript without Samuel Tardif, who introduce me to python and matplolib; neither fit all those scans obtained from the operando synchrotron measurements. To Natalie Herlin-Boime from CEA Saclay, who supplied us with the nanoparticles that make this research possible. I would like to express my deepest gratitude to our collaborators Pierre-Henri Jouneau and Praven Kumar, who made possible the complementary information obtained with the diverse microscopy techniques. To Michel Bardet and Anton Buzlukov, who measured our

samples using solid-state ^{7}Li-NMR. To Cedric Haon and Willy Porcher for the pouch cell preparation during the synchrotron experiments.

I would like to thank the beamline scientists at the BM02, ID 31, and ID20, especially Christoph Sahle and Chiara Cavallari, who introduced me to the XRS technique and helped me with the data analysis.

I would like to express my thanks to Christopher Berhaut, who was extraordinarily helpful in setting up challenging experiments at the synchrotron and whose company made easier this thesis and the different beamtime allocations at the ESRF, ILL, SOLEIL, and the FRM II. Besides, thanks for introduce me to climbing, la via ferrata, and Euromillion on Friday nights.

I want to thank my colleagues from the IRIG institute, the Ph.D. students, and post-docs who helped in this long journey every day. For instance, Jérôme Faure-Vincent, Antony Valero, Marc Dietrich, Adrien Mery, Manon Berthault, Caroline Keller, Guilhem Paradol, Nino Modesto, Sirine Layouni, Carolina Saavedra, Nicolas Martinez, and Claire Tougne, I would like to thank every coffee, meal, wine, or beer shared with you. I had a wonderful time in Grenoble, thanks to you. To Asma Medjahed, my co-bureau, I thanked you for the French grammar and speaking classes which improved my fluency, the cakes with tea every Friday (at least during the first year), the must-go places in Grenoble, and the P90X lessons. P.D. I know that you will read this one day 😊; it is your favorite part of the thesis.

Lastly, I would like to thank my family for all the support.

Résumé de la thèse

Les batteries Li-ion sont une solution de choix pour le stockage de l'énergie. Augmenter leurs performances requiert le développement de matériaux qui peuvent insérer de plus grandes quantités d'ions lithium (batteries de haute densité d'énergie). De ce point de vue, le silicium et le germanium sont des materiaux actifs prometteurs pour les anodes, grâce à leurs capacités théoriques (1623 et 3576 mAh/g, respectivelment) plus élevées que celles de l'état de l'art, c'est-à-dire le graphite (372 mAh/g). Toutefois, les réactions d'alliages au cours de la lithiation provoquent des variations volumiques très importantes dans le Si et le Ge, ce qui induit des déformations mécaniques préjudiciables au fonctionnement à long terme des anodes. Par conséquent, étudier en détail les mécanismes de lithiation pendant le cyclage est essentiel pour comprendre et limiter les processus de dégradation.

Un certain nombre de stratégies ont été proposées pour augmenter la cyclabilité et la durabilité de ces matériaux. L'une d'entre elle repose sur l'emploi de nanostructures, qui permettent de réduire la pulvérisation et la dégradation des phases actives. Cependant, l'utilisation de nanoparticules favorise la formation d'une couche interfaciale, appelée SEI (Solid Electrolyte Interphase), qui induit une diminution de la capacité réversible et, de fait, limite la cyclabilité. Une approche alternative consiste à utiliser des matériaux composites dans lesquels le silicium est mélangé avec d'autres composantes actives ou inactives. Toutefois, la quantité de silicium incorporé (moins que 20% dans l'anode) reste faible et les capacités obtenues limitées.

Le germanium a été beaucoup moins étudié que le silicium. Bien que moins abondant que le silicium, il possède des propriétés très intéressantes, en plus de sa capacité théorique élevée : une meilleure conductivité électronique et une meilleure diffusivité des ions lithium que le silicium. Mélanger le Ge au Si est ainsi une possibilité prometteuse, permettant d'augmenter la capacité par rapport au graphite et de bénéficier de la grande stabilité du Ge.

Cette thèse porte sur l'étude des mécanismes de (dé)lithiation dans des anodes pour batteries lithium-ion à base de silicium et germanium. Nous avons étudié d'une part des nanoparticules de Si, Ge et d'alliages Si-Ge, et d'autre part un matériau composite commercial. Nous avons utilisé des techniques de diffusion de rayonnement *operando* pour caractériser les mécanismes de lithiation et la formation des phases $Li_{15}(Si_{100-x}Ge_x)_4$, obtenant des résultats en accord avec les prédictions théoriques sur les propriétés de ces matériaux en cours de cyclage. Nous avons également exploré le potentiel de la spectroscopie Raman au synchrotron, pour étudier la composition de la couche d'interface électrode-électrolyte, permettant de quantifier sa composition en fonction de l'état de charge de l'anode.

Abstract

Lithium-ion batteries (LiBs) are one of the best solutions for energy storage. Increasing the performance of LiBs demands the use of materials that can host higher quantities of lithium ions (high energy density). Germanium and silicon are promising active anode materials due to their high theoretical capacities (1623 and 3576 mAh/g, respectively) compared to the commercial graphite (372 mAh/g). However, Si and Ge experience significant volume expansion upon the alloying-dealloying reactions with lithium-ions, provoking mechanical deformation. Understanding the mechanisms during cycling is essential to provide information about the degradation processes.

There are different strategies to improve the cyclability and durability of these materials. Using nanostructures is one of them, as it allows mitigating the pulverization and the active compound degradation. Nevertheless, the use of active nanoparticles favors the formation of a solid electrolyte interface layer (SEI), inducing a decrease of the reversible capacity and consequently limiting the cyclability. An alternative approach is to use composite materials in which silicon is mixed with other active or inactive components. However, to date, the silicon amount is limited (less than ~20% of the anode), decreasing the anode capacity.

Ge has received less attention than Si. Although it is less accessible than silicon, it has appealing characteristics besides its high theoretical capacity, such as better electronic conductivity and Li diffusivity than Si. Therefore,

mixing Ge with Si is interesting with respect to benchmark graphite to provide an increase in capacity while taking advantage of Ge stability.

This thesis aims at studying the (de)lithiation mechanisms in silicon and germanium-based negative electrodes, focusing on two types of systems: pure Ge, Si, SiGe-alloys nanoparticles, and a commercial-grade silicon-based composite. The structural evolution occurring upon (de)lithiation was probed mainly by *operando* X-ray scattering techniques, allowing to propose a detailed description of the lithiation mechanisms, as well as $Li_{15}(Si_{100-x}Ge_x)_4$ formation process, which support theoretical predictions on the physical properties of these materials during cycling. Besides, we explored the potentialities of synchrotron X-ray Raman scattering to gain insight into the Solid Electrolyte Interphase (SEI) composition, providing insights into the SEI evolution and its dependence on the state of charge. Our in-depth multi-techniques characterizations bring knowledge to design better Si-based anodes for high-density long-lasting batteries.

Contents

Introduction

Fifty-one years ago, human beings finally landed on the moon. However, today we must all look after our planet. Since 1880, the average global temperature on Earth has increased by a little more than 1° Celsius. More than two-thirds of the warming has occurred since 1969, at a rate of roughly 0.15-0.20°C per decade. This climate change is mainly due to human activities that release gases such as carbon dioxide (CO_2), methane (CH_4), and nitrous oxide (N_2O), responsible for the well-known greenhouse effect. In Europe, the sectors of activity that are the main emitters are electricity, heat, and transportation. One way to alleviate the energy sector emissions is to use low-carbon electricity based on renewable and nuclear energy. Renewable energy output depends on natural sources such as wind and sun, which are intermittent. Their integration into energy storage devices capable of responding reliably to electricity demands whenever needed is an essential yet challenging objective.

The incentive to decrease greenhouse emissions has motivated the increase in the budget for energy research. Among them, the 2019 estimated public energy research budget has increased (4%, USD 20.9 billion) in the International Energy Agency (IEA) country members, without counting the European Union funding under the Horizon 2020 program (USD 2.3 billion)[1]. Besides, the European Union spent a quarter of its budget on energy storage technologies, overtaking the other IEA country partners[2].

There are several energy storage systems available. For instance, Li-ion battery storage continues to be dominant in the market because of its high energy density (up to ~300 Wh kg^{-1}). As there is an enormous effort to improve the electric vehicle (EV) market batteries, this could likely boost the long-scale stationary storage for renewable energies. Nowadays, typical commercial Li-ion batteries use $LiFePO_4$ as a positive electrode, and graphite (Gr), as a negative electrode. However, this type of cell provides a limited energy density, an important parameter to accomplish a long driving range in EVs[3]. Increasing the energy density has become a goal for the next generation of commercial batteries. There are several ways to increase the capacity, such as 1) significant potential difference between the positive and negative electrode, 2) decreasing the mass and volume of the electrodes per electron exchange, and 3) developing high-capacity electrode materials that store more Li ions per mass and volume[4].

The possible candidates for achieving high specific capacity as the positive electrode are based on $LiMO_2$, where M can be nickel, cobalt, manganese (NMC) or Ni, Co, and Al (NCA) with capacities reaching 300 $mAhg^{-1}$. Positive electrodes are considered the bottleneck compared to the high capacities reached by the negative electrodes; however, this is generally obtained at the expense of stability, and there is still work to be done to develop stable negative electrodes[5].

Alloy-type electrodes composed of elements belonging to the groups III, IV, and V, of the periodic table, such as Si, Ge, Sn, Sb, metal oxides, sulfides, or phosphides, are promising negative electrodes because of their higher Li-ion

host stoichiometries, that exceed at least four times the capacity of graphite. Among these, Si is one of the most studied due to its high specific capacity (3570 $mAhg^{-1}$), and tentatively Ge that has a high capacity (1600 $mAhg^{-1}$) and improved transport properties, although its cost[6] remains an issue, explaining why it received less attention than Si to date.

Recently, mixing Si with Ge has shown to be a promising approach to increase the Ge capacity and improve the properties of Si as anode material. However, the negative alloy electrodes undertake high volume change upon cycling, electric connectivity loss from the current collector, and reduced cycling life.

One way to improve cycling problematics in negative alloy electrodes is to use nanostructures that show better cycling life and alleviate pulverization. Another possible method is to mix the alloy material, Ge or Si, with graphite, forming composites. This method improves not only the aging behavior but also the capacity retention[7]. Furthermore, to mitigate lithium loss, prelithiation can be an excellent strategy to have an additional source of lithium[8]. Likewise, while the negative electrodes are cycling, a solid electrolyte interphase layer (SEI) is formed. The capacity fading and the degradation mechanism depend on the properties of the SEI since this layer inhibits the direct electrode-electrolyte contact and continues to grow upon cycling.

Operando techniques for analyzing negative electrodes have become valuable tools to understand the cycling problematics of battery materials. X-ray and neutron-based techniques allow non-destructively probing while cycling the electrode. Nonetheless, it is essential to complement *operando* with *in-situ* and *post-mortem* studies, which can be more precise, to have a complete picture of

the cycling mechanism. Moreover, combining these techniques with electron microscopy and spectroscopy techniques is highly relevant to understand different scales and system parameters such as morphology and chemical environment.

Within this context, my thesis research work was conducted in two laboratories: the Modeling and Exploration of Materials (MEM) and the Molecular and nanoMaterials Systems for Energy and health (SyMMES), in the IRIG fundamental research institute at CEA Grenoble. We investigated the cycling mechanisms in Ge- and Si-based negative electrodes for Li-ion batteries, more precisely Si Nps, Ge Nps, $Si_{100-x}Ge_x$ alloys, and a composite compound made of a-Si, c-$FeSi_2$, and graphite.

In-lab and synchrotron *operando* and *post-mortem* X-ray scattering techniques were used to follow the structural and chemical environment changes during the electrochemical cycling. Our primary focus was to understand the (de)lithiation mechanisms and provide useful information to develop advanced and stable electrodes.

This thesis is divided into six chapters.

Chapter 1 gives a brief bibliography overview of the cycling mechanisms and problematics in negative electrodes. Chapter 2 presents the different types of materials we investigated and the various characterization techniques we used, including details on sample preparation and set-ups.

Chapter 3 discusses the lithiation and delithiation mechanisms of crystalline germanium nanoparticles (c-Ge Nps). We also explore the crystalline

deformation while cycling using X-ray diffraction (XRD), and we complete this analysis with ^{7}Li NMR. In Chapter 4, we study the lithiation of crystalline silicon-germanium alloys (c-$Si_{100-x}Ge_x$) by XRD and characterize the crystalline lithiated phases obtained.

Chapter V is devoted to the composite anode based on amorphous silicon, crystalline iron disilicide, and graphite (a-Si/c-$FeSi_2$/Gr) material, analyzed by *operando* synchrotron small and wide-angle X-ray scattering (SAXS/WAXS) in a full-cell.

The potential of synchrotron X-ray Raman Scattering (XRS) for battery studies is presented in Chapter VI, exemplified by the investigation of the solid electrolyte interphase (SEI) chemical environment of crystalline silicon nanoparticles (c-Si Nps) and the composite a-Si/c-$FeSi_2$/Gr.

Finally, in the last section of this manuscript, we summarize our conclusions and provide some perspectives for future studies.

Bibliography

1. IEA. Energy Technology RD&D Budgets. (2020).
2. Munuera, L. & Pavarini, C. Energy storage tracking report. (2020). Available at: https://www.iea.org/reports/energy-storage. (Accessed: 7th December 2020)
3. Duan, J. *et al.* Building Safe Lithium-Ion Batteries for Electric Vehicles: A Review. *Electrochem. Energy Rev.* **3**, 1–42 (2020).
4. Pender, J. P. *et al.* Electrode Degradation in Lithium-Ion Batteries. *ACS Nano* **14**, 1243–1295 (2020).
5. Schmuch, R., Wagner, R., Hörpel, G., Placke, T. & Winter, M. Performance and Cost of Materials for Lithium-Based Rechargeable Automotive Batteries. *Nat. Energy* **3**, 267–278 (2018).
6. Liu, X., Wu, X.-Y., Chang, B. & Wang, K.-X. Recent Progress on Germanium-Based Anodes for Lithium-Ion Batteries: Efficient Lithiation Strategies and

Mechanisms. *Energy Storage Mater.* **30**, 146–169 (2020).

7. Berhaut, C. L. *et al.* Multiscale Multiphase Lithiation and Delithiation Mechanisms in a Composite Electrode Unraveled by Simultaneous Operando Small-Angle and Wide-Angle X-Ray Scattering. *ACS Nano* **13**, 11538–11551 (2019).

8. Berhaut, C. L. *et al.* Prelithiation of silicon/graphite composite anodes: Benefits and mechanisms for long-lasting Li-Ion batteries. *Energy Storage Mater.* **29**, 190–197 (2020).

Chapter 1

Introductory concepts

Our main motivation is on negative electrodes for lithium-ion batteries (LiBs), principally electrodes based on the first three elements of the group IV: silicon, germanium, and composites using graphite with Si or Ge. This chapter briefly reviews the concepts needed to understand our study and present a literature review. In particular, we describe the working principle of a battery and *operando* studies on Li-ion batteries. We focus on negative electrodes for Li-ion batteries based on Si and Ge, specifically the (de)lithiation structural mechanism reported for silicon, germanium, SiGe alloys, and composites. Finally, we describe the solid electrolyte interphase formation, one of the main problems encountered when cycling negative electrodes.

1.1 Li-ion batteries

The components of a lithium-ion battery (LiB) consist of a positive electrode, a negative electrode, and a separator embedded with electrolyte (see Figure 1.1). While cycling a LiB, there are two processes: charging and discharging. Upon charging, the lithium-ions move from the positive electrode to the negative electrode, and external energy is chemically stored in the battery. As this process is reversible, the opposite happens during discharging, and the chemical energy stored is converted into electrical energy[1]. The positive electrode is made of intercalation compounds of lithium-ion metal oxides such as lithium iron phosphate ($LiFePO_4$, LFP with a specific capacity of 163 mAhg-

[1]), Li_xMO_2, where M= Ni, Co, and Mn. Also, non-stoichiometric versions contain all three metals, such as NMC positive electrodes or Al instead of Mn (NCA)[2].

The negative commercial electrode is commonly graphite (with a specific capacity of 372 $mAhg^{-1}$), and recently, significant efforts have been made to exploit the potential of Silicon, which has a much higher specific capacity (3576 mAh/g).

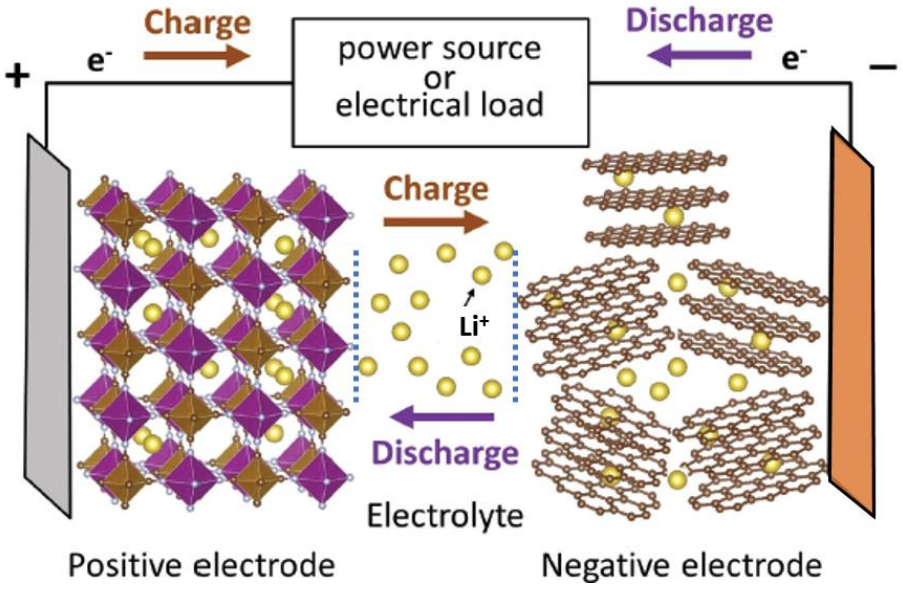

Figure 1.1 illustration of the working principle of LiB. Adapted from [3].

The battery performance characteristics are essential to understand the cycling process and are briefly summarized in the following paragraphs[4].

-Open-circuit voltage (OCV): this refers to the voltage difference between the electrodes when current is not applied to the battery. For instance, at the beginning of the cycle, the OCV of Si (vs. Li metal) is about to 2.9 V.

- Theoretical specific capacity: this refers to the number of electrons transferred during the lithiation process. It is usually expressed as a product of time and current, such as milliampere-hour/grams, as follows:

$$Q = (\Delta x\ F)/M$$

Equation 1

Where M is the molecular weight of the materials, F is the Faraday's constant equal to 26801 mAh/mole. For example, as carbon in graphite stores, one Li^+ for every six carbon atoms, the theoretical capacity for graphite is 372 $mAhg^{-1}$. The theoretical volumetric capacity is calculated by multiplying the density by the theoretical specific capacity; thus, the theoretical volumetric capacity for graphite is 837 $mAhcm^{-3}$ (graphite density: 2.26 g cm^{-3}).

- Energy density refers to the nominal battery energy storage per unit of volume or mass and is expressed in Wh kg^{-1} or Wh l^{-1}. The energy is the product of the discharge capacity by the voltage divided by the mass or volume of the system. Electric vehicles demand, i.e., high energy contents up to 260 Wh kg^{-1} or 700 Wh l^{-1} at the cell level, that is in the pouch, cylindrical or prismatic cell for assembling the battery pack[5].

- C-rate is a measure of the rate at which a battery is lithiated to a specific voltage. C/10 means that the lithiated current will lithiate the battery in 10 hours, and this C-rate is typically suitable for fundamental studies. However, for automotive batteries, the goal of car manufacturers is to achieve lithiation in 20 min, thus approximately 3C rate[5].

-Coulombic efficiency: this is a ratio (expressed as a percentage) between the discharge capacity and the charge capacity. For intercalation cathode materials such as $LiFePO_4$, the coulombic efficiencies are often high thanks to the robustness to successive lithium intercalation and deintercalation, resulting in high reversibility (>95%), whereas, for anode materials such as Si that undertakes some aging problematics (described in section 1.3), the coulombic efficiencies are lower than 95%[6].

1.2 *Operando* studies in Li-ion batteries

The main difference between *operando* and *in-situ* studies is that *operando* studies are undergone simultaneously as the battery is cycling. In contrast, in *in-situ* studies, battery cycling is stopped to measure the electrode. In an *ex-situ* characterization (also called *post-mortem*), the electrochemical cell is opened to extract and characterize the electrode. This sample preparation needs to be done using a glovebox to avoid contamination with atmospheric species. *In-situ* and *ex-situ* experiments are essential to complement *operando* analysis but have several disadvantages, as the electrode species can react or relax while the sample is prepared.

On the contrary, *operando* studies can capture the real state of the battery while cycling, avoiding sample contamination and relaxation. Several techniques have been used for studying Li-ion batteries by *operando* approaches such as NMR[7–10], Raman spectroscopy[11,12], TEM[13,14], atomic force microscopy[15,16], neutron reflectometry[17,18], X-ray scattering methods, which will be further detailed. *Operando* approaches have been employed to tackle

multiple length scales from the macroscopic to microscopic scales and different problematics in Li-ion batteries.

Operando X-ray scattering methods are remarkable tools because of the sensitivity to observe changes in the structure and composition of electrodes for LiBs while using synchrotron radiation to study battery cells improves time-space resolution and penetration into the matter since synchrotron sources have high power and flux. These characteristics allow the investigation of different C-rates and the aging of materials when cycling. Using lab X-rays allows the study of structural transformation at lower C-rates during lithiation/delithiation that lasts longer than 20 h, which may not be feasible in synchrotron sources due to beamtime assignments. X-ray scattering techniques such as X-ray radiography[19], tomography[20–22], or X-ray diffraction[23,24] have been used to perform operando studies while cycling electrodes.

A critical issue to consider while conducting *operando* studies is the interaction of the X-rays with materials that are part of the battery, such as electrolyte, current collector, and a window, which might affect the data quality. Thus, specially designed cells or set-ups are crucial elements to perform *operando* experiments[25].

1.3 Negative electrodes based on the first three elements of the group IV.

The group IV elements such as carbon, silicon, germanium, and tin constitute promising materials for negative electrodes. Graphite is the most widely used negative electrode material in commercial LiBs, even though graphite capacity (372 $mAhg^{-1}$) is one of the most limiting factors for commercial LiBs. Research has been undertaken to develop other negative electrodes that have a higher capacity. Negative electrodes can be divided into intercalation, conversion, and alloy-type electrodes. Here, we discuss alloy-type electrodes focusing on lithiation and degradation mechanisms.

Alloy-type negative electrodes based on Si and Ge react with Li-ions forming intermetallic phases. They are promising as anode materials that can host a higher number of Li-ions in the structure than graphite, namely 3.75 Li-ions per atom, which produces gravimetric capacities of 3570 $mAhg^{-1}$, and 1384 $mAhg^{-1}$, respectively[26,27].

However, alloy-type anodes, more particularly Si-based ones, have a low cycle life because while cycling, the volume of the particles changes during lithiation/delithiation, producing mechanical degradation and electrode pulverization. After many cycles, these cycling problems result in a loss of electrical contact and rapid capacity fading (see Figure 1.2, left).

Besides, the solid electrolyte interphase layer (SEI) is formed during lithiation; it can break when Si or Ge shrinks during delithiation, exposing fresh Si or Ge surface to the electrolyte. After aging, the SEI continues growing on the

newly exposed Si or Ge surfaces, producing a thick SEI layer. The SEI results from electrolyte decomposition and evolves while cycling, consuming Li-ions, resulting in an irreversible capacity loss (see Figure 1.2, left).

Some strategies have been used to mitigate alloy-type mechanical fractures such as 1) nanostructures of electrodes that alleviate the volume changes; thus, pulverization[28], 2) mixture of the alloy-type elements with a graphite matrix that supports the volume changes[29] (see Figure 1.2, right). Consequently, we will review the investigations that focused on the lithiation and mechanical mechanisms on these structural features of Si, Ge, and $Si_{x-1}Ge_x$ alloys that improve the cycling properties in the alloy-type negative electrodes, producing high efficiency and long cycle life.

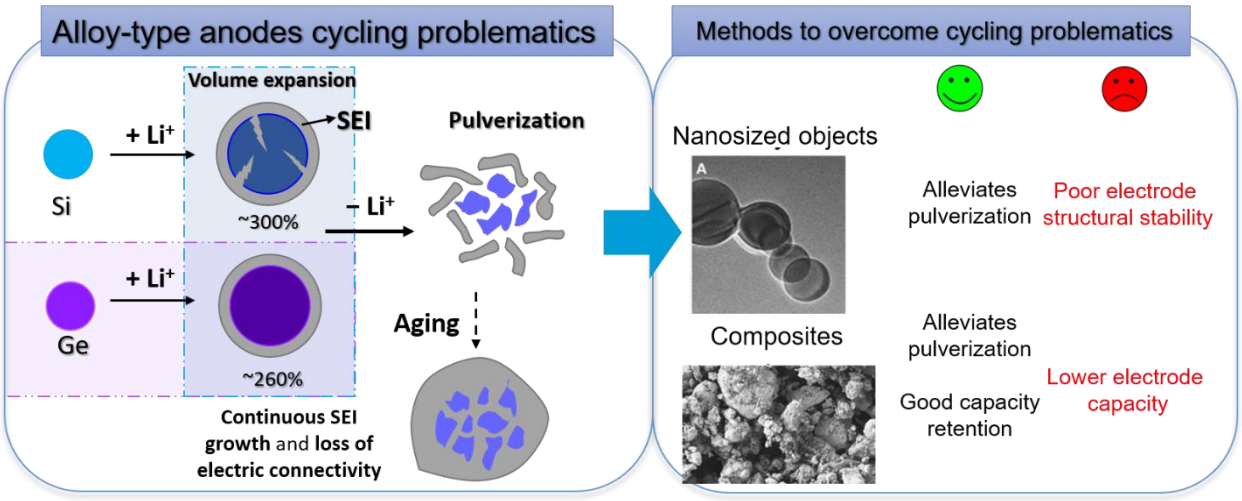

Figure 1.2 left: Schematic cycling problematics on alloy type anodes surfaces. Right: some of the methods used to resolve the mechanical issues encountered in the alloy-type electrodes.

1.4 Lithiation mechanism in Si and Ge based electrodes

This section reviews the fundamental studies on bulk and nano-structured Si and Ge to understand the structure, volume changes, and deformation evolution. We also outline other suggestions to overcome Si cycling problems

such as the preparation of solid solutions with Si and Ge and the incorporation of carbon materials in Si and Ge negative electrodes.

1.4.1 Silicon

Silicon is one of the most studied group-14 with almost 300 paper publish/year due to its low cost, natural abundance, and high capacity. Si as a material for Li batteries has been investigated for nearly three decades[30,31], although one of the major issues while cycling is the volume variations of ~300%[32]. Si has been synthesized as crystalline or amorphous solids in different morphologies and sizes such as thin-films, bulk, micro-structured, and nano-structured objects like nanoparticles (Nps), nanowires (Nws), nanopillars[28,33,34]. The lithiation mechanism in silicon highly depends on the atomic organization, amorphous, or crystalline. These different mechanisms will be discussed in more detail in the following sections.

1.4.1.1 The lithiation mechanism of crystalline silicon (c-Si)

Crystalline Si reacts with Li-ions by a so-called two-phase mechanism[35]. During the reaction with Li^+, the outer shell is transformed into amorphous Li_xSi, while the c-Si core remains unlithiated (see the upper part Figure 1.3). The diffusion of Li-ions into c-Si has been reported to depend on the crystallographic directions. SEM and TEM images on c-Si Nps showed that the lithiation is faster along the <110> direction, causing preferential volume increase in this direction[14,32]. This anisotropy has also been seen in c-Si nanowires (Nws)[36], and c-Si nanopillars[37], which swelled preferentially on the <110> orientation. The mechanical stability for c-Si strongly depends on the particle diameter. Liu *et al.* reported that the critical particle diameter was

~150 nm. Above this diameter, the volume changes experienced upon lithiation/delithiation induce fractures and cracks in the c-Si particles[32].

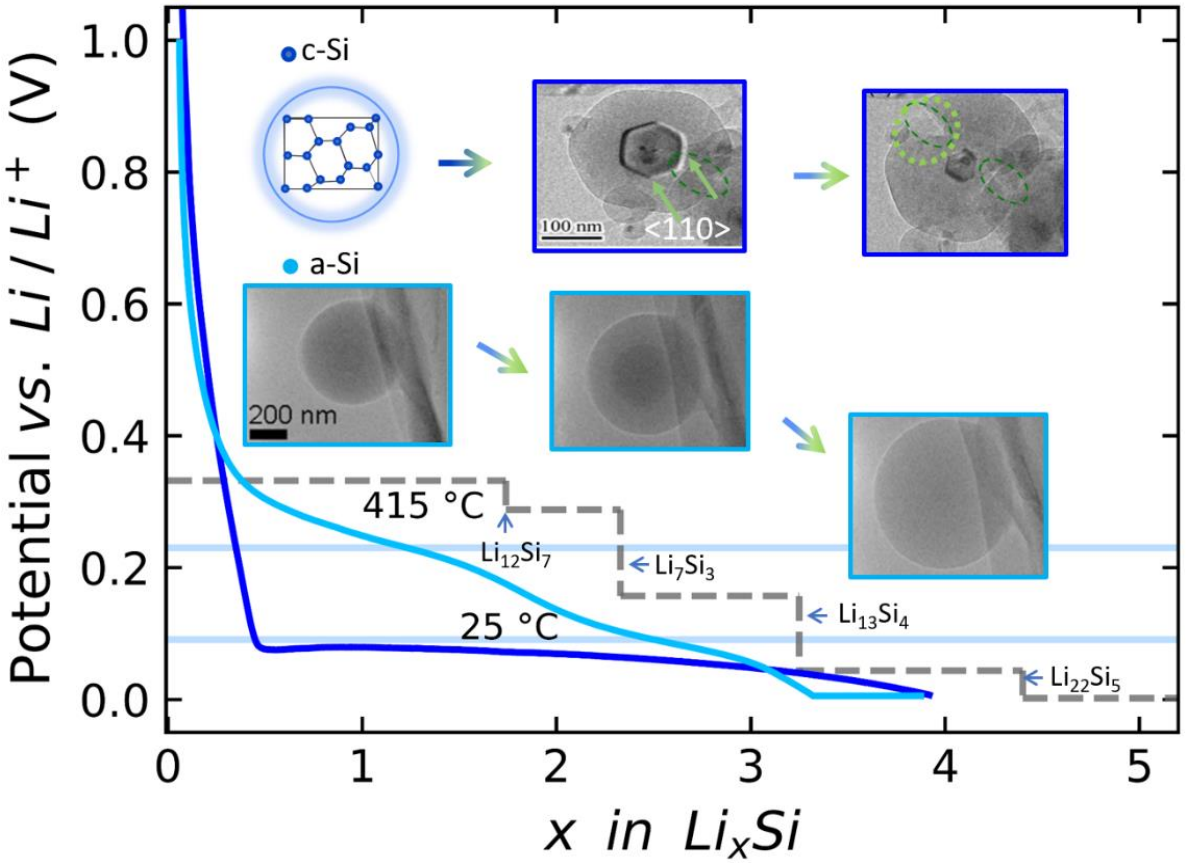

Figure 1.3 illustration of the core-shell lithiation mechanism for c-Si (upper part of the figure) and a-Si (lower part of the figure). TEM figures adapted from [13,14], respectively.

The electrochemical lithiation of c-Si at 415 °C showed four voltage plateaus associated with intermediate phases with nominal compositions $Li_{12}Si_7$, Li_7Si_3, $Li_{13}Si_4$, and $Li_{22}Si_5$, respectively[31] (see the gray line in Figure 1.3). The electrochemical profile of c-Si at room temperature shows a flat voltage zone at ~ 0.1 V, instead of the several plateaus formed at high temperature (see the blue line Figure 1.3).

Key *et al.* investigated the lithiation mechanism of bulk c-Si and c-Si Nws using ^{7}Li-NMR, which allows characterizing the different local Li environments

in the a-Li_xSi phases formed while cycling. They report that the lithiation starts once Li-ions enter into the interstitial sites at the lithiation front. Li-ions weaken the external Si-Si network, provoking the formation of Si clusters. Then, it is easier (kinetically) to break up these clusters to form structures with isolated Si atoms rather than continue with the main Si crystalline structure[7,38].

Figure 1.4 shows the ^{7}Li-NMR chemical shift for b) bulk c-Si and c) c-Si Nws. This figure shows 1) at lithiation cycling voltages below 100 mV, the observed resonances correspond to structures with small Si clusters, dumbbells, and isolated Si atoms (i.e., $Li_{12}Si_7$, Li_7Si_3, and $Li_{13}Si_4$ structures Figure 1.4a); 2) at 0 V, the obtained resonances at almost zero and negative frequencies correspond to structures with isolated atoms (i.e., $Li_{15}Si_4$). Nevertheless, the kinetics and volume expansion prevent the system from reaching equilibrium and forming most of these structures as crystals[38]. In other words, the lithiation of c-Si occurs locally, and it is inhomogeneous.

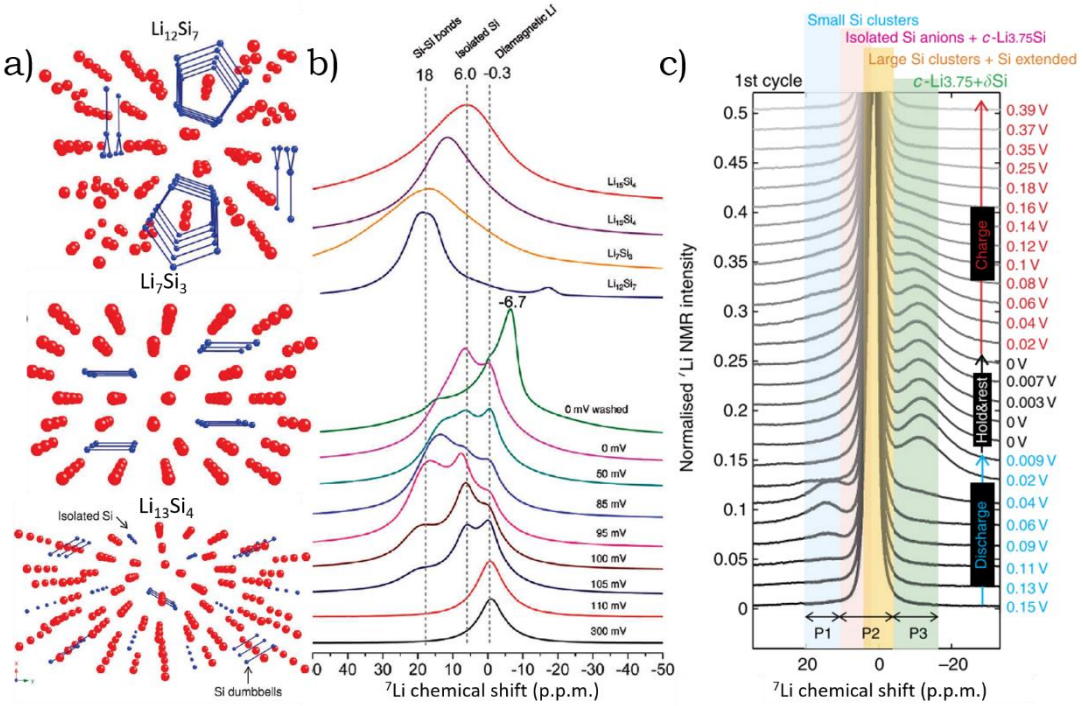

Figure 1.4 a) crystallographic structures of $Li_{12}Si_7$, Li_7Si_3, and $Li_{13}Si_4$. b) ex-situ ^{7}Li-NMR studies on bulk c-Si during lithiation compared to references chemically synthesized. c) in-situ ^{7}Li-NMR spectra for c-Si NWs. Adapted from [7,8].

1.4.1.2 The lithiation mechanism in amorphous Si (a-Si)

The lithiation mechanism in a-Si particles of almost 900 nm is isotropic; in other words, the structure does not fracture or swell in a preferential direction. The electrochemical cycling at room temperature for a-Si shows two slightly flat zones around ~ 230 mV and 100 mV that implies a one-phase mechanism (see light blue in Figure 1.3). On the other hand, McDowell, M. T. *et al.* reported using in-situ TEM that the lithiation mechanism proceeds by a two-phase mechanism[13] (see TEM images highlighted in light blue, Figure 1.3). These results imply that a-Si undertakes softer physical transformations than c-Si. Moreover, the kinetics of the reaction is different than in the crystalline case, suggesting different stress evolution.

The lithiation mechanism of a-Si is different from c-Si since Li-ions seem to penetrate the amorphous structure more easily. Using ^{7}Li-NMR, Key *et al.*

studied the second cycle of c-Si bulk, where they assumed that the c-Si structure was totally amorphous. They suggested that in the a-Si matrix, once Li-ions enter on the whole external shell (the a-Si core remains unlithiated), the lithiation occurs step by step, forming larger Si clusters, then smaller Si clusters, and later dumbbells. Thus, the lithiation of a-Si seems to happen more sequentially and homogeneous, that is, by increasing the quantity of xLi in a-Li_xSi. Finally, c-$Li_{15}Si_4$ was obtained [8,38].

First principle calculations reported that the different deformation while cycling between amorphous and crystalline materials likely happens because of the significant activation energy to break the crystalline Si lattice[39–41]. Thus, a high concentration of Li-ions in the phase boundary on the reaction front is needed to weaken Si-Si bonds in the crystalline network.

1.4.1.3 Formation of crystalline $Li_{15}Si_4$

The lithiation performed at high temperature reported a final plateau at ~44 mV, which is supposed to correspond to the formation of $Li_{22}Si_5$ with a specific theoretical capacity of 4200 $mAhg^{-1}$. At room temperature, XRD showed that c-$Li_{15}Si_4$ was the only phase formed below 50 mV after the lithiation of bulk c-Si[42,43] and a-Si[44]. As mentioned before, since the crystalline Si structure is difficult to break, and the lithiation happens at the reaction front, the Li_xSi phases formed are amorphous and metastable.

The complete lithiation of Si should lead to crystalline $Li_{15}Si_4$ (c-$Li_{15}Si_4$). However, this highly depends on the size and the morphology of the active material. For instance, the formation of c-$Li_{15}Si_4$ has been reported in amorphous and crystalline bulk Si[42–45], and Nws[46]. Unlike Nws and bulk Si,

Si Nps below 100 nm do not form c-$Li_{15}Si_4$ or other crystalline Li_xSi phases after full lithiation. It has been reported that Si Nps undergo parasitic reactions with the electrolyte, suppressing the crystallization of $Li_{15}Si_4$[47].

Additional studies on c-Si bulk and Nws using ^{7}Li-NMR on bulk c-Si and c-Si Nws showed a resonance in negative frequencies at the end of lithiation (see Figure 1.4b and c). Key *et al.* assigned this frequency for the first time to overlithiated $Li_{15+\delta}Si_4$, where *ex-situ* XRD demonstrated that the long-range ordering is the same as c-$Li_{15}Si_4$[7,38]. They suggested that probably $Li_{15}Si_4$ is an electron-deficient phase such as $Li_{15}Ge_4$ that can accommodate excess charge. Ogata *et al.* also indicated that it was easier to add Li to the c-$Li_{15}Si_4$ already formed than convert a-Li_xSi to c-$Li_{15}Si_4$[8].

In summary, crystalline $Li_{15}Si_4$ is formed depending on the size of the silicon used and the organization of the atoms, favored in bulk crystalline and amorphous Si, and nanowires. c-$Li_{15}Si_4$ is difficult to form in nanoparticle sizes less than 100 nm.

1.4.1.4 Mechanical properties while cycling c-Si electrodes

Li concentration gradients within c-Si cause stress while cycling. Therefore, it is essential to study the deformation during the (de) lithiation of c-Si, which is responsible for the slow down of the lithiation and produces fractures in the material, provoking continuous SEI growth, contact electrical loss, and lower energy efficiency.

The two-phase lithiation mechanism in c-Si produces a sharp reaction front. A tensile front hoop is created at the surface of the shell, while a hydrostatic

compression occurs on the crystalline core[48,49]. This hoop stress results from the volume expansion of the a-Li_xSi shell and seems to be responsible for the cracks in c-Si.

Different techniques can be used to measure mechanical deformation while the battery is cycling. For instance, McDowell *et al.* studied the lithiation of c-Si Nps in real-time using in-situ TEM; they found that the reaction front slowed as the crystalline core was consumed[50]. Furthermore, measurements on the mechanical deformation using *operando* Raman spectroscopy and XRD have been done in c-Si[11,12]. These studies have also confirmed the two-phase mechanism, where the crystalline core in c-Si Nps suffers compression during lithiation with stress values in the range between 0.3 GPa and 0.1 GPa[11,12].

Another technique that is broadly used for measuring mechanical deformation in various electrode materials is the substrate curvature method[51]. This method uses a laser beam that probes the sample, mostly films, reflected by the electrode. The changes in the position of the laser beam are used to measure the change in substrate curvature, hence the mechanical deformation in the active material. The information obtained with this technique describes the whole electrode; consequently, the strain/stress estimation is indirect, and the analysis of the results becomes tricky, especially when multiple phases are interacting at a specific state of charge in the battery. In general, the results reported by the substrate curvature method in amorphous or crystalline bulk Si films also found the two-phase mechanism during lithiation[51–53].

1.4.2 Germanium

Germanium also has potential as a negative electrode for Li-ion batteries. Additionally to its high theoretical capacity (1384 $mAhg^{-1}$), it has 400 times higher lithium-ion diffusivity[54], lower resistivity (47 ohm-cm vs. 63 600 ohm-cm for Si)[55] and lower volume expansion (260% vs. 300%) than Si[14].

1.4.2.1 Lithiation mechanism in c-Ge and phases formed

The discharge and charge electrochemical profiles of molten salt Ge-Li at 400 °C show five two-phase voltage zones that correspond from lower Li amount to higher Li content to LiGe, Li_9Ge_4, $Li_{16}Ge_5$, $Li_{15}Ge_4$, and $Li_{22}Ge_5$[56] (see Figure 1.5, gray line).

Compared to the electrochemical cycling at room temperature, the voltage vs. x in the Li_xGe curve presents two slightly flat zones between ~350–300 mV and around 200 mV, indicating a one-phase process mechanism. However, *in-situ* TEM has demonstrated that the lithiation process is a two-phase mechanism in c-Ge[14] as in Si, except that the reaction front between the c-Ge core and the Li_xGe phases shell is less sharped (see Figure 1.5).

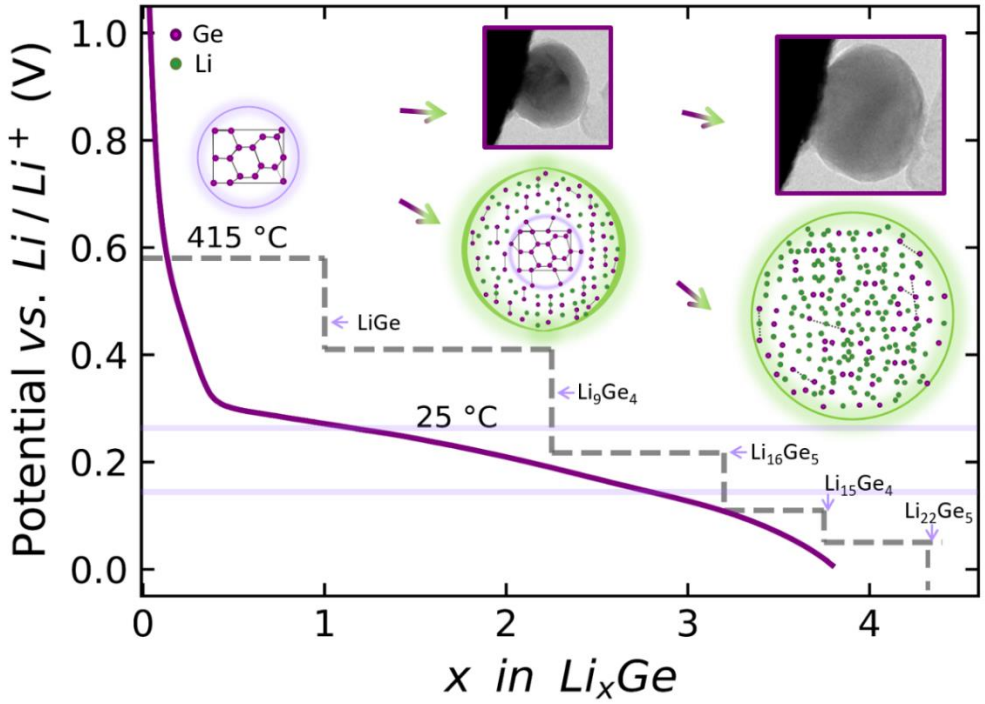

Figure 1.5 illustration of the two-phase lithiation mechanism for c-Ge. Upper TEM images are adapted from [14]. The low part of the figure illustrates the two-phase mechanism of c-Ge firstly proposed by [56].

The electrochemical cycling of Ge has been investigated by *in-situ* and *ex-situ* techniques to have insights into the phase transformation, lithium diffusion, and mechanical properties. Table 1.1 summarizes the phase formation and the methods used to study the lithiation mechanism of c-Ge electrodes.

Yoon *et al.* reported using *ex-situ* XRD that a micron-sized c-Ge carbon-coated electrode during lithiation was converted to c-Li_9Ge_4 and c-Li_7Ge_2, then to c-$Li_{15}Ge_4$ + $Li_{22}Ge_5$. During delithiation, c-$Li_{15}Ge_4$ and c-$Li_{22}Ge_5$ were converted to c-Li_7Ge_2 and c-Li_9Ge_4 until amorphous Ge[57].

Using *operando* XRD and X-ray absorption spectroscopy (XAS), Lim *et al.* proposed the lithiation mechanism for micron-sized c-Ge during lithiation at C/20, as indicated in Table 1.1. Using the structure factor to calculate the XRD diffracted intensity, Lim *et al.* calculated the amount of c-$Li_{15}Ge_4$

converted from c-Ge, and they found that at the end of lithiation, 56% of the c-Ge was transformed into c-$Li_{15}Ge_4$.

Table 1.1 State of the art of the lithiation mechanism for Ge electrodes.

Ref	Type of electrode	C-rate	Proposed Lithiation mechanism	Technique
Yoon *et al.*	micron sized c-Ge	100 mA/g	c-Ge → c-Li_9Ge_4 → c-Li_7Ge_2 → c-$Li_{15}Ge_4$ + c-$Li_{22}Ge_5$	*ex-situ* XRD
Lim *et al.*		C/20	c-Ge → a-Li_9Ge_4 + a-Ge → a-LixGe → c-$Li_{15}Ge_4$	*in-situ* XRD *in-situ* XAS
Jung *et al.*		C/50	c-Ge → c-Ge + c-Li_7Ge_3 → c-Li_7Ge_3 + a- Li_7Ge_2 → c-$Li_{15}Ge_4$ + c-$Li_{15+\delta}Ge_4$	*ex-situ* XRD *in/ex-situ* NMR analysis PDF
Loaiza *et al.*		20 h lithiation	c-Ge → a-LiGe → a-Li_7Ge_3 → c-$Li_{15}Ge_4$	*Operando* techniques -XRD -Raman Spectroscopy -XAS
		60 h lithiation	c-Ge → a-LixGe → c-$Li_{17}Ge_4$	
Tang *et al.*	c-Ge nanorods embedded in multiwall carbon nanotubes	C/5	c-Ge → a-$Li_{2.26}Ge$ → a-$Li_{3.5}Ge$ → c-$Li_{15}Ge_4$ + a-$Li_{3.5}Ge$ → c-$Li_{15+\delta}Ge_4$ + a-$Li_{3.5}Ge$	*in-situ* XRD *in-situ* NMR

In contrast, Jung *et al.*[9] reported that Li_9Ge_4 could not be formed during lithiation, as reported by Lim *et al.* using XAS. According to DFT calculations, this phase showed lower stability than Li_7Ge_3, which is a more stable phase[58] (see Figure 1.6b). Consequently, Jung *et al.* reported using *ex-situ* ^{7}Li-NMR and XRD that micron-sized c-Ge at C/50 is lithiated into c-Li_7Ge_3. Afterward, other stable phases with a high content of Ge-Ge dumbbells could also be formed, such as a-Li_5Ge_2, a-$Li_{13}Ge_5$, or a-Li_8Ge_3. Then, the breakage of Ge-Ge bonds and Ge-Ge dumbbells continued, and the quantity of Li and Ge isolated atoms increased, forming possibly a-Li_7Ge_2. Later with further lithiation, the

c-$Li_{15}Ge_4$ grows. Jung *et al.* also reported on the overlithiated phase, c-$Li_{15+\delta}Ge_4$for which, in analogy with the Si lithiation, the subsequent lithiation showed a different local environment at more negative frequencies in the ^{7}Li-NMR spectrum (see Figure 1.6a). Jung *et al.* supposed that like c-$Li_{15+\delta}Si_4$, c-$Li_{15+\delta}Ge_4$ has a more shielded environment because of the homogeneous distribution of Ge and Li in the matrix.

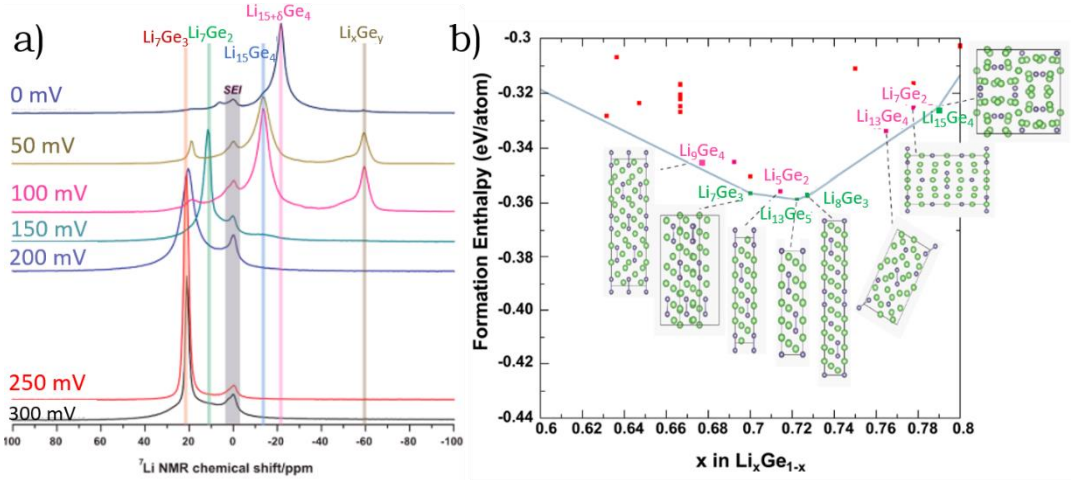

Figure 1.6 a) *ex-situ* ^{7}Li-NMR spectra of cycle Ge at different states of charge. b) Lithiation pathway showing the possible lithiated Ge phases predicted by DFT[58]. Green dots correspond to thermodynamic phases, and the red dots correspond to metastable phases. Adapted from [9].

Ex-situ XRD and pair distribution function analysis (PDF) demonstrates that the c-$Li_{15+\delta}Ge_4$ phase shows a similar long/short structure, except that the lattice parameter increased from 10.7232(3) Å to 10.7479(2) Å. In summary, Jung *et al.* reported the two-phase lithiation mechanism, as shown in Table 1.1[9].

In a more recent study on micron-sized c-Ge, Loaiza *et al.* have reported that the phases formed depend on the C-rates during the cycling using *operando* XRD, Raman spectroscopy, and XAS[59]. Through 20 h of lithiation, c-Ge turned into c-$Li_{15}Ge_4$. While, after 60 h of lithiation, c-$Li_{17}Ge_4$ was formed. The two different lithiation mechanisms are summarized in Table 1.1[59].

Tang *et al.* reported for the first time the (de) lithiation mechanism in nanostructures of c-Ge: Ge nanorods encapsulated in bamboo-type multiwall carbon nanotubes (Ge@CNT). They used ex-situ XRD and in-situ NMR to report the phase formation during the lithiation, as shown in Table 1.1[60].

To summarize, the nature of the phases formed during cycling depends on the type of study performed, such as *ex-situ*, *in-situ,* or *operando*, the lithiation rates, and the size of the particles. Overall, there is an agreement in the phase formed at the end of lithiation, c-$Li_{15}Ge_4$, for C-rates lower than C/50.

1.4.2.2 Mechanical properties of Ge while cycling

Since Ge has not been studied as much as Si, there is limited information on the mechanical deformation while cycling. As indicated, Ge also undergoes two-phase lithiation but with a less sharp reaction front. In-situ TEM showed that during cycling, c-Ge Nps maintained robust without cracks or fractures (see Figure 1.5), and there is no size-dependence from 100 nm to micrometers particles, in contrast with Si. It has been suggested that the resilient behavior in c-Ge comes from the weak anisotropy. In other words, Ge has nearly crystallographic orientation independence while cycling. Indeed, *in-situ* TEM studies on the lithiation of c-Ge Nps showed a diffused core in a lithiated shell (see Figure 1.5), which is opposed to the lithiation of c-Si Nps where the core exhibits a hexagonal shape with a sharp difference between the core-shell[14].

There is only one study dedicated to following the micro-strain in micron size c-Ge cycled at C/9 using *operando* XRD. This study revealed the c-Ge core amorphization, while compressive stress was building up after the electrode was lithiated at 300 mV vs. Li/Li+. At 200 mV, they calculated an average of

0.21% compressive stress along the [111] crystallographic direction and reported that the c-Ge core experienced hydrostatic stress of 0.49 GPa[61].

On the other hand, there are several strain studies on thin-film electrodes during cycling using the substrate curvature method (described in Section 1.4.1.4). Overall, they also reported compressive stress upon complete lithiation, and during delithiation, the stress turned tensile[62–66].

1.4.2.3 Comparison of the lithiation mechanism between Ge and Si

Few previous works have addressed the lithiation mechanism differences in Si and Ge. Mostly, these computational studies have compared the Li-ions incorporation on Si or Ge host lattices. These calculations showed that Si is more difficult to lithiate due to its short interstitial space and harder matrix (higher bulk modulus 98.0 GPa vs. 75 GPa for Ge). As well the incorporation of Li in the host lattice has a softer effect. Essentially, the weaker ionic Li–Li, Li–Ge, or Li–Si replace the Si-Si or Ge-Ge covalent and stronger bonds[67]. The bonding of Si or Ge with Li produces a more flexible lattice. Another reason for the significant difference in the lithiation mechanism between Si and Ge is that Si undergoes more complicated atomic rearrangements in Si lattices because of the suppressed Li-ions mobility (10^{-13} cm^2 s^{-1} for c-Si vs. 10^{-11} cm^2 s^{-1} for c-Ge). Besides, Li-ion diffusion (D_{Li}) in Si depends on Li concentration. For instance, D_{Li} in a-Li_xSi increases with increasing x, from 10^{-12} cm^2 s^{-1} for x = 0.14 to 10^{-7} cm^2 s^{-1} for x = 3.57[68]. On the contrary, Li-ion diffusion in Ge is less dependent on the Li concentration, and it presents facile atomic redisposition with the same orders (10^{-7} cm^2 s^{-1}) of magnitude for both x = 0.14 and x = 3.57[68,69].

Few experimental studies have compared the lithiation mechanism of crystalline Si and Ge, besides the mentioned study using *in-situ* TEM that showed the different core shapes upon cycling crystalline Si or Ge[14]. Pharr *et al.* reported measurements of the curvature on Si and Ge thin-films that highlighted the lower stress undertaken by Ge[64].

To summarize, germanium undertakes less mechanical instability than Si due to its improved Li-ion transport properties, an easy atomic rearrangement, and a softer matrix (lower bulk modulus). These attractive properties reinforce the idea that germanium could be an excellent material for Li-ion batteries.

1.4.3 SiGe alloys

Since Si and Ge are miscible independently of the composition range, mixing Si with Ge has proven to be a promising approach that combines the high capacity of Si with the stability of Ge. $Si_{100-x}Ge_x$ alloys have been synthesized as amorphous and crystalline in bulk[70,71], thin-films[72], Nws[73,74], Nps[75,76]. The lithiation mechanism depending on the structure and morphologies, is challenging to differentiate since these studies and the mechanical properties of $Si_{100-x}Ge_x$ alloys are scarce. This section is divided into the electrochemical advantages of cycling performance compared to pure Si and Ge, and secondly, the lithiation mechanism and mechanical properties leading to enhanced cycling.

Figure 1.7a shows the X-ray pattern of bulk $Si_{100-x}Ge_x$ vs. 2θ (Cu Kα) synthesized mechanically by Duveau et al[77]. The image on the right is an enlarged view of the (111) reflection, shifting to the right with increasing Si

quantity. The crystalline $Si_{100-x}Ge_x$ alloys follow Vegard's law, meaning that the calculated lattice parameter (see Figure 1.7b) shows a linear increase of lattice parameters with a growing amount of Ge.

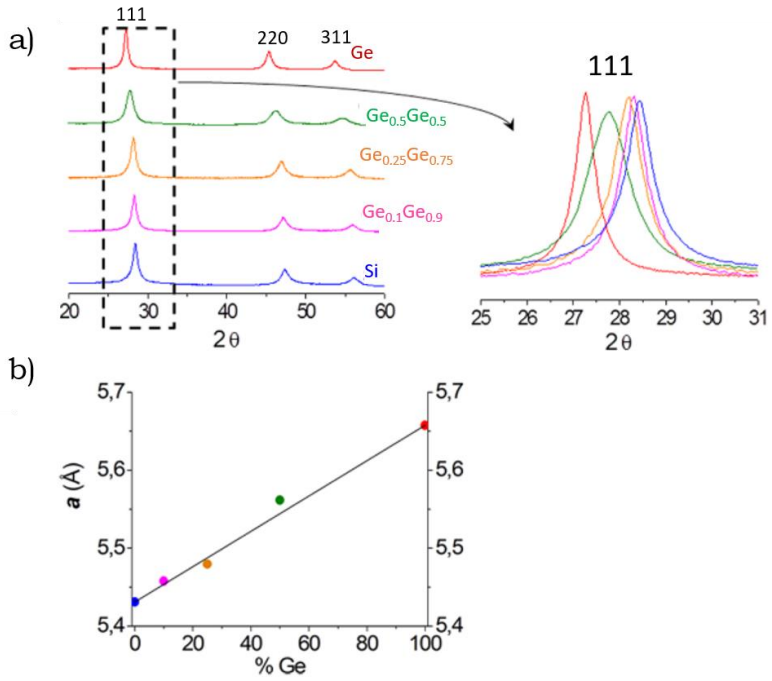

Figure 1.7 a) XRD of different $Si_{100-x}Ge_x$ alloys (x=0.1,0.25,0.5) compared to Si and Ge. The inset on the right is an enlarged view of the 111 peaks. b) lattice parameters vs. the amount of Ge[77].

1.4.3.1 Electrochemical advantages of $Si_{100-x}Ge_x$ alloys over Si and Ge

Figure 1.8a and b. present the electrochemical performances of $Si_{100-x}Ge_x$ nanoparticles. Electrochemical cycling curves show that when cycled at C/20 they have a lower initial specific capacity than Si but higher than Ge (see Figure 1.8a)[76]. The specific capacity value depends on the Si content $Si_{100-x}Ge_x$ alloys with more Si quantity have a higher specific capacity (see $Si_{80}Ge_{20}$, ~2500 $mAhg^{-1}$). In comparison, $Si_{100-x}Ge_x$ with higher Ge content shows lower capacity, i.e., $Si_{23}Ge_{77}$ has a capacity of ~1800 $mAhg^{-1}$ (see Figure 1.8a). While $Si_{100-x}Ge_x$ alloys with higher or middle Ge content may have a lower initial specific capacity, they undertake rapid charging rates with capacity retention

when increasing C-rates from C/5 to 5C (see Figure 1.8b). This superior cycling performance is related to improve Li-ion diffusivity in Ge[68].

The voltage vs. capacity curves give information on the different types of structural transformation in the active material. Distinguishing the voltages signatures can be more accessible using the derivative of the capacity. This analysis gives characteristic dQ/dV peaks that indicate the possible lithiation mechanism. Typical dQ/dV peaks depend on the quantity of Ge or Si. For instance, a-$Si_{75}Ge_{25}$ thin-films showed a similar electrochemical profile to the a-Si one. The a-$Si_{25}Ge_{75}$ showed dQ/dV peaks of germanium-like materials. In comparison, the thin-film with 50% percent of each component showed a combined voltage profile from the a-Si and Ge one[72]. These results indicate that the lithiation mechanism for the $Si_{100-x}Ge_x$ alloys with higher Ge content may be different from the $Si_{100-x}Ge_x$ alloys with lower Ge content.

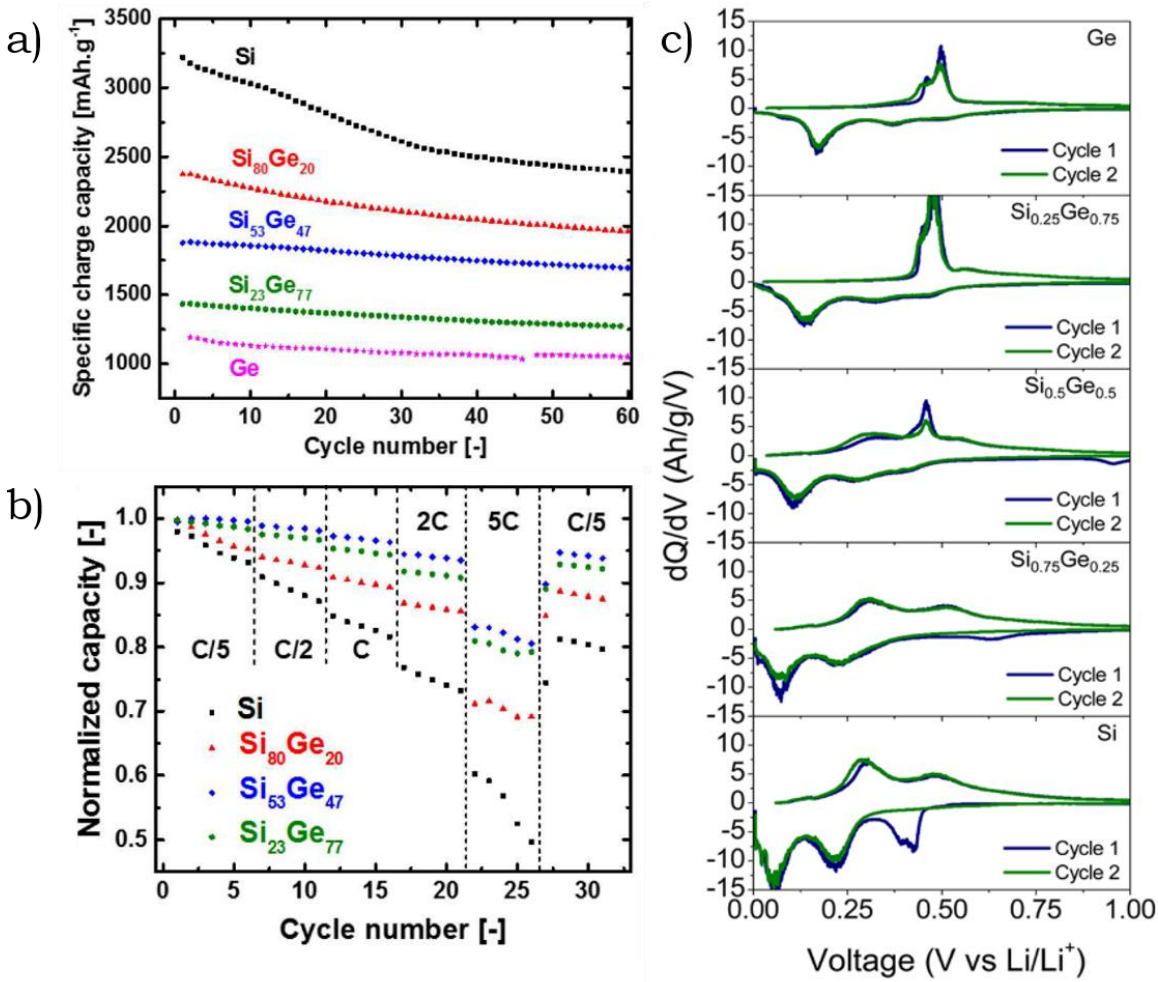

Figure 1.8 a) specific charge capacity vs. cycle number of the $Si_{100-x}Ge_x$ alloys Nps at C/20 compared to Si and Ge. b) normalized capacity vs. cycle number of the $Si_{100-x}Ge_x$ alloys Nps at increasing C-rates. c) Differential capacity plots for the first and second cycles of $Si_{100-x}Ge_x$ alloys thin-films at C/20. a) and b) are adapted from [76], and c) from [72].

1.4.3.2 Lithiation mechanism in $Si_{100-x}Ge_x$ alloys

Traditionally, most of the studies dedicated to $Si_{100-x}Ge_x$ alloys have been devoted to describing the synthesis of the $Si_{100-x}Ge_x$ alloys and the electrochemical performance. Fundamental knowledge to understand the lithiation mechanism and mechanical properties that lead to the improved cycling performance of the $Si_{100-x}Ge_x$ alloys is necessary. This section is divided into the approach used to study $Si_{100-x}Ge_x$ alloys, like computational studies, experimental studies to understand the $Li_x(Si_{100-x}Ge_x)$ alloys

formation, and fundamental studies supporting the increased cycling performance.

- *COMPUTATIONAL STUDIES ON THE MECHANICAL PROPERTIES*

These fundamental investigations have shown that the host lattices are more flexible than that of Si, and they undergo a more relaxed organization, improving the Li diffusivity, the strain accommodation, and the capacity retention[68]. However, it is not clear if $Si_{100-x}Ge_x$ alloys lithiate using the two-phase mechanism as Si and Ge, since there are no *in-situ* TEM studies on $Si_{100-x}Ge_x$ Nps. There are few studies on the mechanical properties of $Si_{100-x}Ge_x$ alloys while cycling. For instance, Bansal *et al.* used a chemo-mechanical model[78] to quantify the stress evolution in $Si_{50}Ge_{50}$ nanopillars. They compared this $Si_{50}Ge_{50}$ alloy with Si and Ge nanopillars, and they found a 17% reduction in the maximum stress compared to Si[79].

- *EXPERIMENTAL STUDIES TO UNDERSTAND THE* $Li_x(Si_{100-x}Ge_x)_y$ *PHASES*

Loaiza *et al.* used XRD to study the pristine bulk $Si_{50}Ge_{50}$ alloy, and they reported a lattice parameter value between c-Si and c-Ge (5.54 Å vs. 5.43 Å for Si, and 5.54 Å for Ge), following the Vegard's law. They also performed *operando* XRD while cycling c-$Si_{50}Ge_{50}$ in 60 h, and they found that the alloy was amorphized at ~100 mV. Below 100 mV, diffracted peaks coming from $Li_{15}(Si_{50}Ge_{50})_4$ appeared with a calculated lattice parameter of 10.745(2) Å (see Figure 1.9a)[70]. Additionally, Figure 1.9b shows the *in-situ* ^{7}Li-NMR results on c-$Si_{50}Ge_{50}$ cycled in 20 h. When the voltage reached 95 mV, a peak emerged at negative frequencies (-17 ppm), as already observed in Si and Ge studies using ^{7}Li-NMR. They assigned this peak to the overlithiated phase

$Li_{15+\delta}(Si_{50}Ge_{50})_4$ taking into account the previous ^{7}Li-NMR studies on Si[7,8,38] and Ge[9,60]. Upon delithiation, the $Li_{15+\delta}(Si_{50}Ge_{50})_4$ was transformed into a-Li_x(Si/Ge) intermediates, and at the end of delithiation, a-$Si_{100-x}Ge_x$ was recovered.

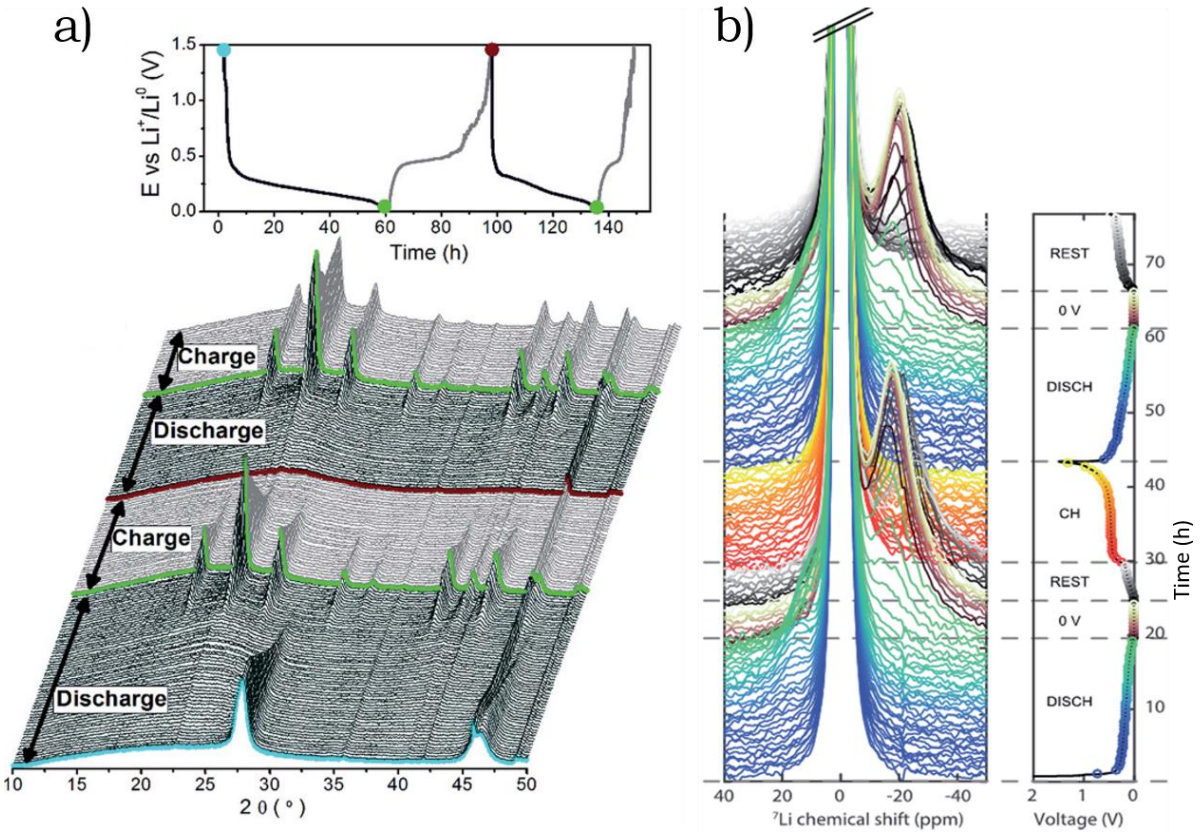

Figure 1.9 the electrochemical cycling of a c-$Si_{0.5}Ge_{0.5}$ self-supported film vs. Li metal by a) Operando XRD. b) *in-situ* ^{7}Li NMR. Adapted from [70].

- *FUNDAMENTAL STUDIES THAT SUPPORTED THE INCREASED CYCLING PERFORMANCE*

Kim et al. studied Nws of c-$Si_{100-x}Ge_x$ alloys with Si-rich shell alloys and Ge-rich core alloys annealed at 760 °C, which showed capacity retention 89% over 400 cycles. They presumed that c-$Si_{100-x}Ge_x$ alloys with higher Si content were lithiated while the inner c-$Si_{100-x}Ge_x$ alloys with richer Ge content reacted partially with Li, creating a supporting frame that tolerated pulverization[73].

Zhu *et al.* studied different c-$Si_{100-x}Ge_x$ alloys; they reported that during the first cycle, the c-$Si_{15}Ge$ alloy had the highest Coulombic efficiency in comparison with the other materials. They supported this result by using DFT calculations to look into the energy barrier of the Li diffusion path in Li-Si-Ge, Li-Ge, and Li-Si. DFT reported that the Li diffusion path in c-$Si_{15}Ge$ has the lowest energy barriers since the Ge atomic ratio in the crystal lattice has a local expansion effect, reducing Li trapping. They reinforced these calculations by demonstrating that c-$Si_{15}Ge$ has a decreased SEI and lower lithium trapped after the first cycle, using TEM, electrochemistry impedance spectroscopy, and atomic emission spectroscopy techniques[71].

In summary, the synthesis of $Si_{100-x}Ge_x$ alloys is possible in different morphologies, and their electrochemical performance is improved compared to pure Si. Little is known on the (de)lithiation mechanism of $Si_{100-x}Ge_x$ alloys that conferred enhanced performance. Theoretical studies predict a decrease in stress when cycling, and experimental studies show that $Li_{15}(Si_{50}Ge_{50})_4$ is formed, indicating changes in the physical properties compared to pure Si.

1.4.4 Composites

Several solutions have been proposed to relieve the pulverization in Si and Ge. One of them is incorporating carbon materials to produce a highly conductive matrix that contains the volume expansion of Si or Ge.

The composites can be classified into several groups, such as carbon-coated materials, mixture with carbon nanostructures, and mixture with graphite. For instance, carbon-coated Si Nps improved conductivity and avoided direct

contact with the electrolyte[80–82]. Even though the carbon-coated was enough to stand global volume expansion, it decreased by 18% of the volume expansion[83]. Adding carbon nanotubes or graphene can also provide electron transport pathways and reduced the volume[81,84].

Here, we are interested in the mixture of Si with graphite (Gr) and active/metal-silicide alloys.

A growing body of literature has investigated metal-silicide alloys blended in composites with Si that improve its cyclability[85–89]. This metal-silicide must have good mechanical properties for stress release, high electronic conductivity, and moderate reactivity with Li^+. The metal-silicides could be useful as a buffer matrix for Si during cycling. For instance, $FeSi_2$ seems to fulfill previous characteristics since it has a low reversible capacity of 10 $mAhg^{-1}$, lower resistivity than Si (2.6×10^1 Ω cm vs. 6.0×10^3 Ω cm), and low breaking strength (213 ± 44 MPa)[87]. Besides, it is widely used in the production of stainless steel, making it accessible. Chen et al. reported a c-$FeSi_2$/Si@C nanocomposite with high Li storage of ~1010 mAg^{-1} and 94% capacity retention after 200 cycles[86].

1.4.4.1 Mechanism of cycling and aging

The mechanism of cycling and aging of composite metal-silicide alloys is not yet well understood. There are few investigations in this type of composite; Si-graphite blended composites have been mostly studied. Müller *et al.* studied Si-graphite nanocomposites using X-ray tomographic microscopy to study the detachment when the capacity fades after ten cycles. They reported that the capacity loss was due to loss of electrical contact between the active materials

and the rest of the composite electrode (carbon black and binder), represented as a gap between Si particles and the rest of the electrode[20] (see Figure 1.10a). Another X-ray tomography study also reports the disconnection of the Si particles at the bottom of the electrode. The origin of this detachment came from large cracks from the expansion/contraction of the electrode[21]. Finegan *et al.* also studied c-Si/graphite electrodes, using X-ray tomography. Figure 1.10b shows an enlarged view of Si particles with sizes >5 µm that lithiate only in the exterior (dark blue). Simultaneously, in the Si particles, the inner structure was not lithiated (Si unlithiated in green)[22].

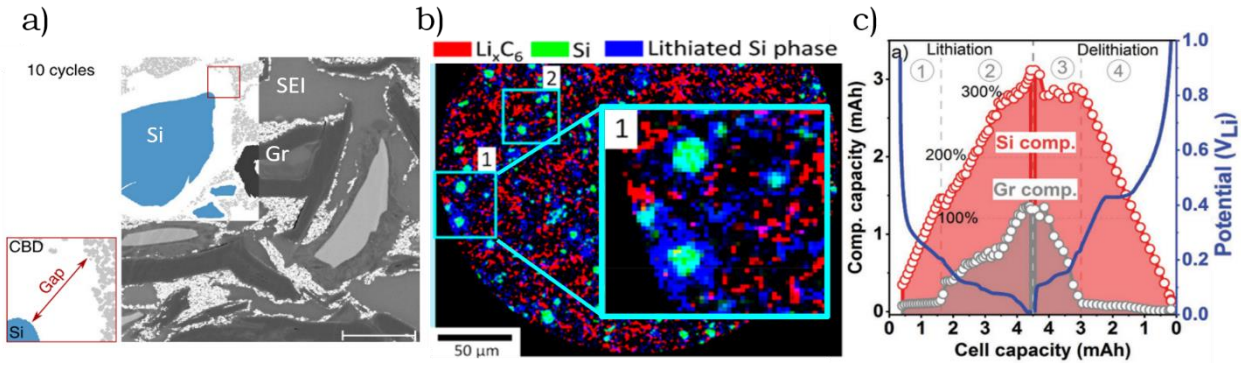

Figure 1.10 a) X-ray tomography raw data of a Si-Gr electrode after ten cycles. b) X-ray computed tomography of the Si-Gr electrode at the end of lithiation, showing a phase-distribution map of LiC_{12} (red), c-Si (green), and LixSi (blue). c) the specific capacity of the Gr and Si components in a Si-Gr electrode during lithiation and delithiation.

The evolution of blended a-Si and graphite has recently been investigated using *operando* X-ray diffraction following the diffracted peaks of the graphite and lithiated graphite peaks[24]. Yao *et al.* reported that the lithiation firstly began for Si since its calculated capacity composition increases while the graphite composition is constant (Figure 1.10c, red and gray line, respectively). The insertion of Li-ion in graphite occurs at lower voltages below 0.2 V. While on delithiation, Li extraction began for Li_xC before the Li_xSi particles[24].

In summary, composites have attracted attention as the next commercial negative electrode for Li-ion batteries due to the increased capacity and mitigation of cycling problems compared to pure graphite and silicon, respectively. A growing investigation at atomic and larger scales in silicon composite materials has been reported. At atomic scales, amorphous silicon cycled against lithium metal starts being lithiated while graphite is lithiated at lower voltages. At a microscopic scale, particles of a size larger than 5 μm are not internally lithiated, probably due to mechanical stress that retard reaction at the inner structure.

1.5 The solid electrolyte interphase

One of the main issues while cycling Li-ion batteries comes from the electrode/electrolyte interface. This interface is crucial to the appropriate conductivity of Li-ions, which will ensure high Coulombic efficiency, capacity retention, and voltage efficiency. The formation of a non-uniform interface can result in Li trapping and formation of lithium dendrites, affecting the battery lifetime and safety[90]. An ideal electrode/electrolyte interface should allow Li-ion diffusion between the positive and negative electrodes without further reducing electrolyte.

The solid electrolyte interface layer (SEI) formed on negative electrodes comes from reducing carbonate-based electrolytes. The typical electrolyte used on Li-ion batteries consists of lithium hexafluorophosphate ($LiPF_6$), an inorganic salt with high solubility in non-aqueous solvents. These solvents are carbonate-based formed of esters, such as ethylene carbonate (EC), propylene carbonate (PC), dimethyl carbonate (DMC), and ethyl methyl carbonate (EMC) (see Figure

1.11). One strategy to form a stable SEI consists of adding electrolyte-additives like fluoroethylene carbonate (FEC) and vinylene carbonate (VC).

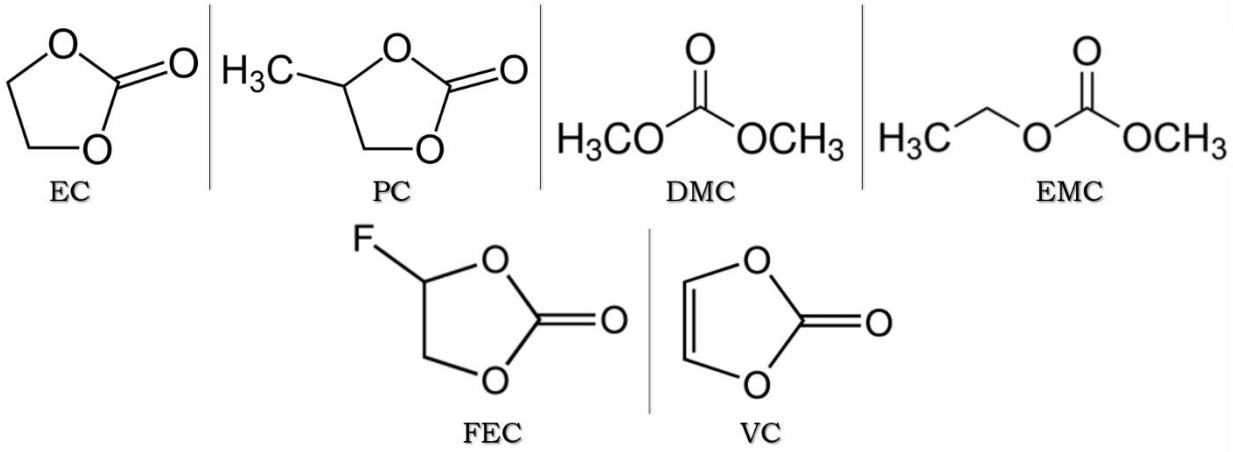

Figure 1.11 carbonated solvents and additives that are used in the electrolyte for LiB.

1.5.1 SEI model

Peled introduced the concept and the model of the SEI on alkali or alkaline earth metals after contact with electrolyte[91,92]. However, in his model, the compounds that formed the SEI were missing. The compounds were found later using XPS, FTIR, and XRD. These techniques showed that SEI in lithium and graphite is formed by Li_2CO_3[93,94], lithium alkyl carbonates (RCO_3Li)[95], LiF, and Li_2O[96,97]. With these findings, Peled *et al.* completed the SEI mosaic model that consisted of organic and inorganic products from the electrolyte decomposition[98,99] (see Figure 1.12a). The products formed at the surface nearby lithium or graphite are made of inorganic compounds such as Li_2O, Li_2CO_3, and LiF. Simultaneously, the surface closer to the electrolyte is made by oligomer species and semicarbonates (organic compounds)[90]. The influence of those (in)organic compounds in the properties and cycling performance is still under investigation.

Besides the reported compounds, Si reacts with the electrolyte to form siloxanes (See Figure 1.12b and c). Several studies on the SEI formed in Si Nps reported that Si binder-free electrodes had better cycling performance when adding FEC. The main SEI products were insoluble polymeric species such as Li_xSiO_y and an increased quantity of LiF compared to the study without FEC[100]. Indeed, calculations reported by Balbuena *et al.* confirmed that the reduction of FEC leads to LiF[101].

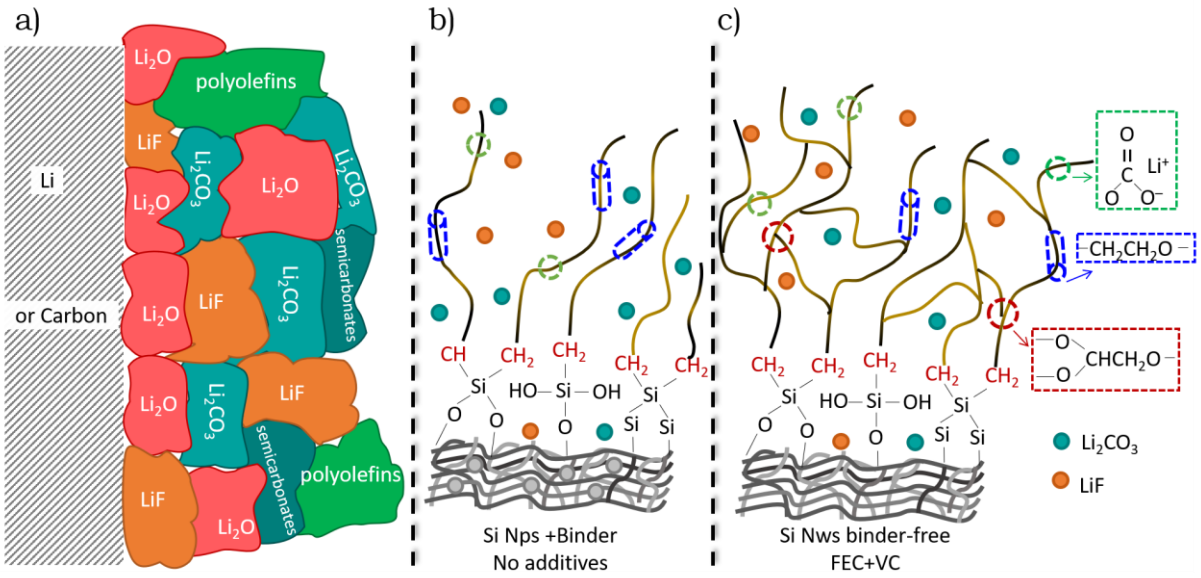

Figure 1.12 a) illustrative model of the SEI proposed by Peled[99]. B) SEI in Si Nps proposed by solid-state NMR without additives[102]. c) SEI in binder-free Si Nws using additives. Adapted from [103].

1.5.2 The role of LiF

The role of LiF may depend on several factors, such as the electrode system, binders, additives, and the interaction with the organic SEI. For lithium metal and graphite electrodes, the LiF strongly influences the resistivity of the SEI. Impedance measurements on lithium showed higher resistivity, which is attributed to a higher concentration of LiF[90,104]. In contrast, the influence of LiF on Si electrodes appeared to be beneficial. Since LiF has a lower solubility

in carbonate solvents[105], LiF formation next to the Si electrode may avoid the continuous evolution of the SEI[106].

1.5.3 The role of the electrolyte additives

Studies using solid-state NMR describe precisely the organic compounds formed in Si SEI when adding FEC and VC. Organic SEI decomposition products like poly(ethylene oxide) (PEO) such as (–OCH_2CH_2O–), and –OCH_2CH_2–, also the – CH_2CH_3–, and –OCH_2CH_3–, were found as R in $ROCO_2Li$[102].

The polymers compounds found in the SEI without additives were linear PEO. In comparison, the SEI polymers using additives were cross-linked PEO[103] (see Figure 1.12a, and b, respectively). The authors speculated that these cross-linked polymers slowed down the reaction of the solvents with Si and SiOx surface since they were bonded partially to the Si surface, creating a more stable SEI and avoiding the continuous solvent decomposition. Also, the cross-linked polymers had elastic properties in comparison with the linear ones. This study was performed in binder-free electrodes. In this way, the compounds found by NMR came from the electrode/electrolyte reaction[103]; however, this is not a real system used in nowadays LiBs.

1.5.4 The role of the binder

The binder is an important factor in the mechanical behavior of the active material. Thus, the degradation of the free-binder electrodes may not describe conventional Si electrodes. Nowadays, Si electrode formulation uses binders like carboxymethylcellulose sodium salt (Na-CMC) and lithium poly(acrylic

acid) (Li-PAA) (see structure in Figure 1.13). These binders have shown improvements in the electrochemical performance since the binder helps in the Si expansion/contraction. It has been proposed that the interaction of Si with the binder could be a direct covalent bond between the SiOx and the organic chains in the polymer or a strong hydrogen bond that conferred a spring-like conformation[107–110]. This same bond-type nature could be similar that the one found in the cross-linked PEO-typed polymers when using FEC and VC in a free-binder Si electrode.

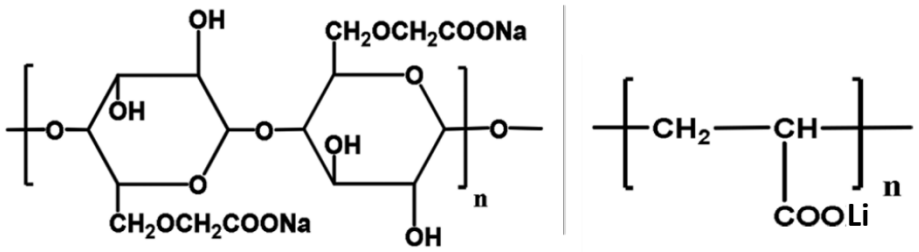

Figure 1.13 binders used in the formulation of Si electrodes.

1.5.5 Studying the SEI chemical environment

Studying the SEI is challenging because of the following reasons: 1) it is formed of several compounds that evolve while cycling, 2) it depends on experimental conditions such as cut-off potential, electrolytes, the type of anode material, and among others conditions, 3) the thickness of the SEI goes from few nanometers to hundreds of nanometers, and 4) the components are usually amorphous, making difficult the detection by X-ray diffraction.

Therefore, several techniques have been utilized to study the chemical composition of the SEI mostly by *post-mortem* characterization, such as NMR[102,111,112], X-ray photoelectron spectroscopy (XPS)[113,114–116], Raman

spectroscopy[117], Fourier transform infrared spectroscopy (FTIR)[118], and scanning transmission electron microscopy with energy-loss spectroscopy (STEM-EELS)[119]. Some of the mentioned techniques use soft photon energies to probe the sample (several tens of eVs to about two keVs), providing a chemical analysis at the surface or information on only a few particles. Indeed, the data obtained from using soft photons techniques may contain information based on superficial contamination. Hard X-rays photons are suitable for studying the SEI at the bulk since they can probe depths in the hundreds of nanometers to millimeters ranges.

In summary, investigating the SEI is essential, however highly challenging considering the sensitivity of the different components to the external conditions. While the SEI compounds are well known using different techniques, a quantitative study is more difficult due to the probes used to analyze the electrode materials, giving information at the surface and prompting contamination.

1.6 Summary and aim of the thesis

An extensive literature concerns Si, Ge, $Si_{100-x}Ge_x$ alloys, and composites, all of which show promising characteristics as negative electrodes for LiBs. As outlined, Si Nps (size<150 nm), Ge Nps, $Si_{100-x}Ge_x$ alloys, and composites can improve cycling problems such as pulverization and mechanical instability. However, this growing literature still shows a lack of understanding of the cycling mechanisms, such as the formed phases and the mechanical stress suffered by the material while cycling, principally when using nanoparticles of Ge and $Si_{100-x}Ge_x$ alloys. Therefore, it is necessary to use complementary

techniques to present a relevant and comprehensive description of the mechanisms at play. This thesis uses mainly XRD, complemented by ^{7}Li NMR and electron microscopy. With these powerful tools, we investigate model systems such as Ge and Si Nps and more complex systems such as $Si_{100-x}Ge_x$ alloys and Si-based composites. Finally, we present the opportunities of the synchrotron-based X-ray Raman scattering spectroscopy (XRS), that uses hard X-rays to study the chemical environment of Si Nps and the composite c-$FeSi_2$/a-Si/Gr electrodes by analyzing soft X-rays edges (i.e., Li K, C K, O K, and F K) of elements that are found in abundance in the SEI.

1.7 Bibliography

1. Jiang, J. & Zhang, C. Performance Modeling of Lithium-ion Batteries. in *Fundamentals and Applications of Lithium-ion Batteries in Electric Drive Vehicles* 9–42 (Wiley, 2015). doi:10.1002/9781118414798.ch2

2. Liu, C., Neale, Z. G. & Cao, G. Understanding Electrochemical Potentials of Cathode Materials in Rechargeable Batteries. *Mater. Today* **19**, 109–123 (2016).

3. Sottmann, J. Synchrotron Based Operando Methods for Characterization of Non-Aqueous Rechargeable Battery Electrode Materials. (University of Oslo, 2017).

4. Wu, Y., Yuan, X., Zhao, S. & Ree, T. V. Introduction. in *Lithium-Ion Batteries Fundamentals and Applications* (ed. Wu, Y.) 4–9 (CRC Press, 2015).

5. Schmuch, R., Wagner, R., Hörpel, G., Placke, T. & Winter, M. Performance and Cost of Materials for Lithium-Based Rechargeable Automotive Batteries. *Nat. Energy* **3**, 267–278 (2018).

6. Pender, J. P. *et al.* Electrode Degradation in Lithium-Ion Batteries. *ACS Nano* **14**, 1243–1295 (2020).

7. Key, B. *et al.* Real-Time NMR Investigations of Structural Changes in Silicon Electrodes for Lithium-Ion Batteries. *J. Am. Chem. Soc.* **131**, 9239–9249 (2009).

8. Ogata, K. *et al.* Revealing Lithium–Silicide Phase Transformations in Nano-Structured Silicon-Based Lithium-Ion Batteries Via In-Situ NMR Spectroscopy. *Nat. Commun.* **5**, 3217(1–11) (2014).

9. Jung, H. *et al.* Elucidation of the Local and Long-Range Structural Changes that Occur in Germanium Anodes in Lithium-Ion Batteries. *Chem. Mater.* **27**, 1031–1041 (2015).

10. Kitada, K. *et al.* Unraveling the Reaction Mechanisms of SiO Anodes for Li-Ion Batteries by Combining in Situ 7 Li and ex Situ 7 Li/ 29 Si Solid-State NMR Spectroscopy. *J. Am. Chem. Soc.* **141**, 7014–7027 (2019).

11. Zeng, Z. *et al.* In-Situ Measurement of Lithiation-Induced Stress in Silicon Nanoparticles Using Micro-Raman Spectroscopy. *Nano Energy* **22**, 105–110 (2016).

12. Tardif, S. *et al.* Operando Raman Spectroscopy and Synchrotron X-ray Diffraction of Lithiation/Delithiation in Silicon Nanoparticle Anodes. *ACS Nano* **11**, 11306–11316 (2017).

13. McDowell, M. T. *et al.* In-Situ TEM of Two-Phase Lithiation of Amorphous Silicon Nanospheres. *Nano Lett.* **13**, 758–764 (2013).

14. Liang, W. *et al.* Tough Germanium Nanoparticles under Electrochemical Cycling. *ACS Nano* **7**, 3427–3433 (2013).

15. Breitung, B., Baumann, P., Sommer, H., Janek, J. & Brezesinski, T. In-Situ and Operando Atomic Force Microscopy of High-Capacity Nano-Silicon Based Electrodes for Lithium-Ion Batteries. *Nanoscale* **8**, 14048–14056 (2016).

16. Kumar, R. *et al.* In Situ and Operando Investigations of Failure Mechanisms of the Solid Electrolyte Interphase on Silicon Electrodes. *ACS Energy Lett.* **1**, 689–697 (2016).

17. Seidlhofer, B. K. *et al.* Lithiation of Crystalline Silicon As Analyzed by Operando Neutron Reflectivity. *ACS Nano* (2016). doi:10.1021/acsnano.6b02032

18. Jerliu, B. *et al.* Neutron Reflectometry Studies on the Lithiation of Amorphous Silicon Electrodes in Lithium-Ion Batteries. *Phys. Chem. Chem. Phys.* **15**, 7777 (2013).

19. Sun, F. *et al.* Complementary X-ray and neutron radiography study of the initial lithiation process in lithium-ion batteries containing silicon electrodes. *Appl. Surf. Sci.* **399**, 359–366 (2017).

20. Müller, S. *et al.* Quantification and Modeling of Mechanical Degradation in Lithium-Ion Batteries Based on Nanoscale Imaging. *Nat. Commun.* **9**, 1–8 (2018).

21. Vanpeene, V., Etiemble, A., Bonnin, A., Maire, E. & Roué, L. In-Situ X-Ray Tomographic Study of the Morphological Changes of a Si/C Paper Anode for Li-Ion Batteries. *J. Power Sources* **350**, 18–27 (2017).

22. Finegan, D. P. *et al.* Spatially Resolving Lithiation in Silicon-Graphite Composite Electrodes via in Situ High-Energy X-ray Diffraction Computed Tomography. *Nano Lett.* **19**, 3811–3820 (2019).

23. Lim, L. Y., Liu, N., Cui, Y. & Toney, M. F. Understanding Phase Transformation in Crystalline Ge Anodes for Li-Ion Batteries. *Chem. Mater.* **26**, 3739–3746 (2014).

24. Yao, K. P. C., Okasinski, J. S., Kalaga, K., Almer, J. D. & Abraham, D. P. Operando Quantification of (De)Lithiation Behavior of Silicon–Graphite Blended

Electrodes for Lithium-Ion Batteries. *Adv. Energy Mater.* **9**, 1–7 (2019).

25. Tripathi, A. M., Su, W.-N. & Hwang, B. J. In-Situ Analytical Techniques for Battery Interface Analysis. *Chem. Soc. Rev.* **47**, 736–851 (2018).

26. Obrovac, M. N. & Chevrier, V. L. Alloy Negative Electrodes for Li-Ion Batteries. *Chem. Rev.* **114**, 11444–11502 (2014).

27. Liu, X., Wu, X.-Y., Chang, B. & Wang, K.-X. Recent Progress on Germanium-Based Anodes for Lithium-Ion Batteries: Efficient Lithiation Strategies and Mechanisms. *Energy Storage Mater.* **30**, 146–169 (2020).

28. Su, X. *et al.* Silicon-Based Nanomaterials for Lithium-Ion Batteries: A Review. *Adv. Energy Mater.* **4**, 1300882 (1–23) (2014).

29. Shen, X. *et al.* Research Progress on Silicon/Carbon Composite Anode Materials for Lithium-Ion Battery. *J. Energy Chem.* **27**, 1067–1090 (2018).

30. Lai, S.-C. Solid Lithium-Silicon Electrode. *J. Electrochem. Soc.* **123**, 1196 (1976).

31. Wen, C. J. & Huggins, R. A. Chemical Diffusion in Intermediate Phases in the Lithium-Silicon System. *J. Solid State Chem.* **37**, 271–278 (1981).

32. Liu, X. H. *et al.* Size-dependent fracture of silicon nanoparticles during lithiation. *ACS Nano* **6**, 1522–1531 (2012).

33. McDowell, M. T., Lee, S. W., Nix, W. D. & Cui, Y. 25th Anniversary Article: Understanding the Lithiation of Silicon and Other Alloying Anodes for Lithium-Ion Batteries. *Adv. Mater.* **25**, 4966–4985 (2013).

34. Zuo, X., Zhu, J., Müller-Buschbaum, P. & Cheng, Y. J. Silicon-Based Lithium-Ion Battery Anodes: a Chronicle Perspective Review. *Nano Energy* **31**, 113–143 (2017).

35. Limthongkul, P., Jang, Y.-I., Dudney, N. J. & Chiang, Y.-M. Electrochemically-Driven Solid-State Amorphization in Lithium-Silicon Alloys and Implications for Lithium Storage. *Acta Mater.* **51**, 1103–1113 (2003).

36. Liu, X. H. *et al.* Anisotropic Swelling and Fracture of Silicon Nanowires during Lithiation. *Nano Lett.* **11**, 3312–3318 (2011).

37. Lee, S. W., McDowell, M. T., Choi, J. W. & Cui, Y. Anomalous Shape Changes of Silicon Nanopillars by Electrochemical Lithiation. *Nano Lett.* **11**, 3034–3039 (2011).

38. Key, B., Morcrette, M., Tarascon, J. & Grey, C. P. Pair Distribution Function Analysis and Solid-State NMR Studies of Silicon Electrodes for Lithium-Ion Batteries: Understanding the (De)lithiation Mechanisms. *J. Am. Chem. Soc.* **133**, 503–512 (2011).

39. Shenoy, V. B., Johari, P. & Qi, Y. Elastic Softening of Amorphous and Crystalline Li-Si Phases with Increasing Li Concentration: a First-Principles Study. *J. Power Sources* **195**, 6825–6830 (2010).

40. Zhao, K. *et al.* Lithium-Assisted Plastic Deformation of Silicon Electrodes in Lithium-Ion Batteries: A First-Principles Theoretical Study. *Nano Lett.* **11**, 2962–2967 (2011).

41. Liu, X. H. *et al.* In-Situ Atomic-Scale Imaging of Electrochemical Lithiation in Silicon. *Nat. Nanotechnol.* **7**, 749–756 (2012).

42. Obrovac, M. N. & Christensen, L. Structural Changes in Silicon Anodes during Lithium Insertion\Extraction. *Electrochem. Solid-State Lett.* **7**, A93–A96 (2004).

43. Loaiza, L. C., Monconduit, L. & Seznec, V. Si and Ge-Based Anode Materials for Li-, Na-, and K-Ion Batteries: A Perspective from Structure to Electrochemical Mechanism. *Small* **16**, 1905260(1–29) (2020).

44. Hatchard, T. D. & Dahn, J. R. In-Situ XRD and Electrochemical Study of the Reaction of Lithium with Amorphous Silicon. *J. Electrochem. Soc.* **151**, A838–A842 (2004).

45. Wang, F. *et al.* Electrochemical Reaction of Lithium with Nanostructured Silicon Anodes: A Study by In-Situ Synchrotron X-Ray Diffraction and Electron Energy-Loss Spectroscopy. *Adv. Energy Mater.* **3**, 1324–1331 (2013).

46. Misra, S. *et al.* In Situ X-ray Diffraction Studies of (De)lithiation Mechanism in Silicon Nanowire Anodes. *ACS Nano* **6**, 5465–5473 (2012).

47. Gao, H. *et al.* Parasitic Reactions in Nanosized Silicon Anodes for Lithium-Ion Batteries. *Nano Lett.* **17**, 1512–1519 (2017).

48. Deshpande, R., Cheng, Y.-T., Verbrugge, M. W. & Timmons, A. Diffusion Induced Stresses and Strain Energy in a Phase-Transforming Spherical Electrode Particle. *J. Electrochem. Soc.* **158**, A718–A724 (2011).

49. Zhao, K. *et al.* Concurrent Reaction and Plasticity during Initial Lithiation of Crystalline Silicon in Lithium-Ion Batteries. *J. Electrochem. Soc.* **159**, A238–A243 (2012).

50. McDowell, M. T. *et al.* Studying the Kinetics of Crystalline Silicon Nanoparticle Lithiation with In-Situ Transmission Electron Microscopy. *Adv. Mater.* **24**, 6034–6041 (2012).

51. Jangid, M. K. & Mukhopadhyay, A. Real-Time Monitoring of Stress Development During Electrochemical Cycling of Electrode Materials for Li-Ion Batteries: Overview and Perspectives. *J. Mater. Chem. A* **7**, 23679–23726 (2019).

52. Sethuraman, V. A., Chon, M. J., Shimshak, M., Srinivasan, V. & Guduru, P. R. In-Situ Measurements of Stress Evolution in Silicon Thin-Films During Electrochemical Lithiation and Delithiation. *J. Power Sources* **195**, 5062–5066 (2010).

53. Kumar, R., Woo, J. H., Xiao, X. & Sheldon, B. W. Internal Microstructural Changes and Stress Evolution in Silicon Nanoparticle-Based Composite Electrodes. *J. Electrochem. Soc.* **164**, A3750–A3765 (2017).

54. Fuller, C. S. & Severiens, J. C. Mobility of Impurity Ions in Germanium and

Silicon. *Phys. Rev.* **96**, 21–24 (1954).

55. Conwell, E. Properties of Silicon and Germanium. *Proc. IRE 40* **40**, 1327–1337 (1952).

56. St. John, M. R. Thermodynamic Studies of Li-Ge Alloys: Application to Negative Electrodes for Molten Salt Batteries. *J. Electrochem. Soc.* **129**, 246 (1982).

57. Yoon, S., Park, C.-M. & Sohn, H.-J. Electrochemical Characterizations of Germanium and Carbon-Coated Germanium Composite Anode for Lithium-Ion Batteries. *Electrochem. Solid-State Lett.* **11**, A42–A45 (2008).

58. Morris, A. J., Grey, C. P. & Pickard, C. J. Thermodynamically Stable Lithium Silicides and Germanides from Density Functional Theory Calculations. *Phys. Rev. B* **90**, 054111(1–10) (2014).

59. Loaiza, L. C. *et al.* Electrochemical Lithiation of Ge: New Insights by Operando Spectroscopy and Diffraction. *J. Phys. Chem. C* **122**, 3709–3718 (2018).

60. Tang, W. *et al.* Probing Lithium Germanide Phase Evolution and Structural Change in a Germanium-in-Carbon Nanotube Energy Storage System. *J. Am. Chem. Soc.* **137**, 2600–2607 (2015).

61. Cortes, F. J. Q., Boebinger, M. G., Xu, M., Ulvestad, A. & McDowell, M. T. Operando Synchrotron Measurement of Strain Evolution in Individual Alloying Anode Particles within Lithium Batteries. *ACS Energy Lett.* **3**, 349–355 (2018).

62. Al-Obeidi, A., Kramer, D., Thompson, C. V & Mönig, R. Mechanical Stresses and Morphology Evolution in Germanium Thin-Film Electrodes during Lithiation and Delithiation. *J. Power Sources* **297**, 472–480 (2015).

63. Nadimpalli, S. P. V, Tripuraneni, R. & Sethuraman, V. A. Real-Time Stress Measurements in Germanium Thin-Film Electrodes during Electrochemical Lithiation/Delithiation Cycling. *J. Electrochem. Soc.* **162**, A2840–A2846 (2015).

64. Pharr, M., Choi, Y. S., Lee, D., Oh, K. H. & Vlassak, J. J. Measurements of Stress and Fracture in Germanium Electrodes of Lithium-Ion Batteries during Electrochemical Lithiation and Delithiation. *J. Power Sources* **304**, 164–169 (2016).

65. Wang, X., Yang, A. & Xia, S. Fracture Toughness Characterization of Lithiated Germanium as an Anode Material for Lithium-Ion Batteries. *J. Electrochem. Soc.* **163**, A90–A95 (2016).

66. Al-Obeidi, A., Kramer, D., Mönig, R. & Thompson, C. V. Mechanical Stresses and Crystallization of Lithium Phosphorous Oxynitride-Coated Germanium Electrodes during Lithiation and Delithiation. *J. Power Sources* **306**, 817–825 (2016).

67. Chou, C.-Y., Kim, H. & Hwang, G. S. A Comparative First-Principles Study of the Structure, Energetics, and Properties of Li–M (M = Si, Ge, Sn) Alloys. *J. Phys. Chem. C* **115**, 20018–20026 (2011).

68. Chou, C.-Y. & Hwang, G. S. On the Origin of the Significant Difference in Lithiation Behavior between Silicon and Germanium. *J. Power Sources* **263**,

252–258 (2014).

69. Chou, C.-Y. & Hwang, G. S. On the Origin of Anisotropic Lithiation in Crystalline Silicon over Germanium: a First-Principles Study. *Appl. Surf. Sci.* **323**, 78–81 (2014).

70. Loaiza, L. C. *et al.* Understanding the Lithiation/Delithiation Mechanism of Si1-xGex Alloys. *J. Mater. Chem. A* **5**, 12462–12473 (2017).

71. Zhu, B. *et al.* Minimized Lithium Trapping by Isovalent Isomorphism for High Initial Coulombic Efficiency of Silicon Anodes. *Sci. Adv.* **5**, eaax0651(1–8) (2019).

72. Abel, P. R. *et al.* Nanostructured Si(1- x)Gex for Tunable Thin Film Lithium-Ion Battery Anodes. *ACS Nano* **7**, 2249–2257 (2013).

73. Kim, H. *et al.* Germanium Silicon Alloy Anode Material Capable of Tunable Overpotential by Nanoscale Si Segregation. *Nano Lett.* **15**, 4135–4142 (2015).

74. Stokes, K. *et al.* Direct Synthesis of Alloyed Si1–xGex Nanowires for Performance-Tunable Lithium-Ion Battery Anodes. *ACS Nano* **11**, 10088–10096 (2017).

75. Ge, M. *et al.* Capacity Retention Behavior and Morphology Evolution of SixGe1–x Nanoparticles As Lithium-Ion Battery Anode. *Nanotechnology* **26**, 255702 (1–9) (2015).

76. Desrues, A. *et al.* Best Performing SiGe/Si Core-Shell Nanoparticles Synthesized in One Step for High Capacity Anodes. *Batter. Supercaps* **2**, 970–978 (2019).

77. Duveau, D., Fraisse, B., Cunin, F. & Monconduit, L. Synergistic Effects of Ge and Si on the Performances and Mechanism of the GexSi1– x Electrodes for Li-Ion Batteries. *Chem. Mater.* **27**, 3226–3233 (2015).

78. Yang, H. *et al.* A Chemo-Mechanical Model of Lithiation in Silicon. *J. Mech. Phys. Solids* **70**, 349–361 (2014).

79. Bansal, A., Bhandari, A., Chakraborty, P., Bhattacharya, J. & Pala, R. G. S. Alloying with Ge and Hollowing Reduces Lithiation-Induced Stresses in Si Nanopillar Anodes. *J. Electrochem. Soc.* **167**, 013542(1–7) (2020).

80. Hassan, F. M., Chabot, V., Elsayed, A. R., Xiao, X. & Chen, Z. Engineered Si Electrode Nanoarchitecture: A Scalable Postfabrication Treatment for the Production of Next-Generation Li-Ion Batteries. *Nano Lett.* **14**, 277–283 (2014).

81. Li, J. Y. *et al.* Research Progress Regarding Si-Based Anode Materials Towards Practical Application in High Energy Density Li-Ion Batteries. *Mater. Chem. Front.* **1**, 1691–1708 (2017).

82. Bernard, P., Alper, J. P., Haon, C., Herlin-Boime, N. & Chandesris, M. Electrochemical Analysis of Silicon Nanoparticle Lithiation – Effect of Crystallinity and Carbon Coating Quantity. *J. Power Sources* **435**, 226769(1–9) (2019).

83. Sourice, J. *et al.* Core-Shell Amorphous Silicon-Carbon Nanoparticles for High-Performance Anodes in Lithium-Ion Batteries. *J. Power Sources* **328**, 527–535 (2016).

84. Ashuri, M., He, Q. & Shaw, L. L. Silicon as a Potential Anode Material for Li-Ion Batteries: Where Size, Geometry and Structure Matter. *Nanoscale* **8**, 74–103 (2016).

85. Lee, H.-Y. & Lee, S.-M. Graphite–Fesi Alloy Composites as Anode Materials for Rechargeable Lithium-Batteries. *J. Power Sources* **112**, 649–654 (2002).

86. Chen, Y., Qian, J., Cao, Y., Yang, H. & Ai, X. Green Synthesis and Stable Li-Storage Performance of FeSi 2 /Si@C Nanocomposite for Lithium-Ion Batteries. *ACS Appl. Mater. Interfaces* **4**, 3753–3758 (2012).

87. Usui, H. *et al.* Influence of Mechanical Grinding on Lithium Insertion and Extraction Properties of Iron Silicide/Silicon Composites. *J. Power Sources* **268**, 848–852 (2014).

88. Kang, I., Jang, J., Yi, K.-W. & Cho, Y. W. Porous Nanocomposite Anodes of Silicon/Iron Silicide/3D Carbon Network for Lithium-Ion Batteries. *J. Alloys Compd.* **770**, 369–376 (2019).

89. Choi, W. J., Reddyprakash, M., Loka, C., Jo, Y. W. & Lee, K.-S. Carbon Coated Si-Metal Silicide Composite Anode Materials Prepared by High-Energy Milling and Carburization for Li-Ion Rechargeable Batteries. *J. Electrochem. Soc.* **166**, A5131–A5138 (2019).

90. Gauthier, M. *et al.* Electrode–Electrolyte Interface in Li-Ion Batteries: Current Understanding and New Insights. *J. Phys. Chem. Lett.* **6**, 4653–4672 (2015).

91. Peled, E. The Electrochemical Behavior of Alkali and Alkaline Earth Metals in Nonaqueous Battery Systems—The Solid Electrolyte Interphase Model. *J. Electrochem. Soc.* **126**, 2047–2051 (1979).

92. Peled, E. Film-Forming Reaction at the Lithium/Electrolyte Interface. *J. Power Sources* **9**, 253–266 (1983).

93. Nazri, G. & Muller, R. H. Composition of Surface Layers on Li Electrodes in PC, LiClO4 of Very Low Water Content. *J. Electrochem. Soc.* **132**, 2050–2054 (1985).

94. Nazri, G. & Muller, R. H. In-Situ X-Ray Diffraction of Surface Layers on Lithium in Nonaqueous Electrolyte. *J. Electrochem. Soc.* **132**, 1385–1387 (1985).

95. Aurbach, D., Daroux, M. L., Faguy, P. W. & Yeager, E. Identification of Surface Films Formed on Lithium in Propylene Carbonate Solutions. *J. Electrochem. Soc.* **134**, 1611–1620 (1987).

96. Kanamura, K., Tamura, H. & Takehara, Z. XPS Analysis of a Lithium Surface Immersed in Propylene Carbonate Solution Containing Various Salts. *J. Electroanal. Chem.* **333**, 127–142 (1992).

97. Kanamura, K., Tamura, H., Shiraishi, S. & Takehara, Z. XPS Analysis of Lithium Surfaces Following Immersion in Various Solvents Containing LiBF4. *J. Electrochem. Soc.* **142**, 340–347 (1995).

98. Peled, E. *et al.* The Role of SEI in Lithium and Lithium-Ion Batteries. *MRS Proc.* **393**, 209 (1995).

99. Peled, E., Golodnitsky, D. & Ardel, G. Advanced Model for Solid Electrolyte Interphase Electrodes in Liquid and Polymer Electrolytes. *J. Electrochem. Soc.* **144**, L208–L210 (1997).

100. Nie, M., Abraham, D. P., Chen, Y., Bose, A. & Lucht, B. L. Silicon Solid Electrolyte Interphase (SEI) of Lithium-Ion Battery Characterized by Microscopy and Spectroscopy. *J. Phys. Chem. C* **117**, 13403–13412 (2013).

101. Martínez de la Hoz, J. M. & Balbuena, P. B. Reduction Mechanisms of Additives on Si Anodes of Li-Ion Batteries. *Phys. Chem. Chem. Phys.* **16**, 17091–17098 (2014).

102. Michan, A. L. *et al.* Solid Electrolyte Interphase Growth and Capacity Loss in Silicon Electrodes. *J. Am. Chem. Soc.* **138**, 7918–7931 (2016).

103. Jin, Y. *et al.* Understanding Fluoroethylene Carbonate and Vinylene Carbonate Based Electrolytes for Si Anodes in Lithium-Ion Batteries with NMR Spectroscopy. *J. Am. Chem. Soc.* **140**, 9854–9867 (2018).

104. Zaban, A., Zinigrad, E. & Aurbach, D. Impedance Spectroscopy of Li Electrodes. 4. A General Simple Model of the Li−Solution Interphase in Polar Aprotic Systems. *J. Phys. Chem.* **100**, 3089–3101 (1996).

105. Tasaki, K. *et al.* Solubility of Lithium Salts Formed on the Lithium-Ion Battery Negative Electrode Surface in Organic Solvents. *J. Electrochem. Soc.* **156**, A1019–A1026 (2009).

106. Schroder, K. *et al.* The Effect of Fluoroethylene Carbonate as an Additive on the Solid Electrolyte Interphase on Silicon Lithium-Ion Electrodes. *Chem. Mater.* **27**, 5531–5542 (2015).

107. Hochgatterer, N. S. *et al.* Silicon/Graphite Composite Electrodes for High-Capacity Anodes: Influence of Binder Chemistry on Cycling Stability. *Electrochem. Solid-State Lett.* **11**, A76–A80 (2008).

108. Vogl, U. S. *et al.* Mechanism of Interactions between CMC Binder and Si Single Crystal Facets. *Langmuir* **30**, 10299–10307 (2014).

109. Li, J.-T. *et al.* Water Soluble Binder, an Electrochemical Performance Booster for Electrode Materials with High Energy Density. *Adv. Energy Mater.* **7**, 1701185(1–30) (2017).

110. Porcher, W. *et al.* Understanding Polyacrylic Acid and Lithium Polyacrylate Binder Behavior in Silicon-Based Electrodes for Li-Ion Batteries. *J. Electrochem. Soc.* **164**, A3633–A3640 (2017).

111. Hu, B. *et al.* Understanding of Pre-Lithiation Of Poly(Acrylic Acid) Binder: Striking the Balances Between the Cycling Performance and Slurry Stability for Silicon-Graphite Composite Electrodes in Li-Ion Batteries. *J. Power Sources* **416**, 125–131 (2019).

112. Michan, A. L. *et al.* Fluoroethylene Carbonate And Vinylene Carbonate

Reduction: Understanding Lithium-Ion Battery Electrolyte Additives and Solid Electrolyte Interphase Formation. *Chem. Mater.* **28**, 8149–8159 (2016).

113. Xu, C. *et al.* Improved Performance of the Silicon Anode for Li-Ion Batteries: Understanding the Surface Modification Mechanism of Fluoroethylene Carbonate as an Effective Electrolyte Additive. *Chem. Mater.* **27**, 2591–2599 (2015).

114. Philippe, B. *et al.* Nanosilicon Electrodes for Lithium-Ion Batteries: Interfacial Mechanisms Studied by Hard and Soft X-ray Photoelectron Spectroscopy. *Chem. Mater.* **24**, 1107–1115 (2012).

115. Philippe, B. *et al.* Role of the LiPF6 Salt for the Long-Term Stability of Silicon Electrodes in Li-Ion Batteries – A Photoelectron Spectroscopy Study. *Chem. Mater.* **25**, 394–404 (2013).

116. Xu, C. *et al.* Interface Layer Formation in Solid Polymer Electrolyte Lithium Batteries: an XPS Study. *J. Mater. Chem. A* **2**, 7256–7264 (2014).

117. Nanda, J. *et al.* Unraveling the Nanoscale Heterogeneity of Solid Electrolyte Interphase Using Tip-Enhanced Raman Spectroscopy. *Joule* **3**, 2001–2019 (2019).

118. Ruther, R. E. *et al.* Chemical Evolution in Silicon–Graphite Composite Anodes Investigated by Vibrational Spectroscopy. *ACS Appl. Mater. Interfaces* **10**, 18641–18649 (2018).

119. Boniface, M. *et al.* Nanoscale Chemical Evolution of Silicon Negative Electrodes Characterized by Low-Loss STEM-EELS. *Nano Lett.* **16**, 7381–7388 (2016).

Chapter 2

Materials and methods

In this chapter we present the materials used during this thesis, which consisted of active materials based on silicon and germanium. We worked with three types of materials: pure silicon or pure germanium nanoparticles (NPs), solid solutions of Si and Ge, and composites. We introduce next the basic concepts of the different experimental techniques we used. Besides the electrochemical characterization, I more particularly focused on X-ray scattering techniques.

2.1 Materials

2.1.1 Crystalline nanoparticles-based materials

Our collaborators in CEA Saclay/IRAMIS/NIMBE synthesized the nanoparticles of size between 60 and 100 nm by laser pyrolysis. We used silicon, germanium, and $Si_{100-x}Ge_x$ alloys nanoparticles. The synthesis has been thoroughly described by Desrues et al. in [1,2]. This method uses high-purity silane or germane depending on the material. For the $Si_{100-x}Ge_x$ alloys, different gas ratio silane vs. germane were used to synthesize nanoparticles with varying compositions of x (see Table 2.1.). In particular, for the Ge NPs, ethylene was used as a sensitizer to favors the absorption of the laser radiation by the germane.

This laser pyrolysis method consisted of placing a CO_2 laser beam (PRC SLS 2800) at a 10.6 μm wavelength with a 20 mm diameter and a power of 1050 W in a flow of silane or germane with He as a dilution gas. After the gas absorbs the radiation, the dissociation and collision of the atoms occur, producing nucleation and subsequently growing the active material particles. The powders were transferred by argon flow from the reaction zone to filters, where they are collected. The characterization of the pristine Ge Nps, Si Nps, and $Si_{1-x}Ge_x$ Nps powders will be presented in chapters 3 and 4, respectively.

Table 2.1. The gas ratio used for particle synthesis and the resulting Ge concentration in the powders.

Sample	GeH_4 in the gas mixture [%]	Ge in powder [%]
Si	0	0
SiGe	19	20
	49	47
	84	77
Ge	100	100

The electrodes were prepared at the Hybriden platform in CEA-Grenoble, and they were composed of 50 wt% Nps of the active material, 25 wt% of sodium carboxymethyl cellulose (Na-CMC, Merck), and 25 wt% carbon black (Super P). The powders were grinding manually using an agate mortar for 30 minutes, then they were dissolved in purified water (18.2 Ω at 25 °C) and stirred for 10 min. When a slightly thick ink was obtained, it was deposited on a Cu foil (20 μm, thickness) using a doctor blade (50 μm), and it was dried for 12 h at 80 °C. Finally, circular disks were cut to cycle electrochemically.

2.1.2 Composite materials

We used two types of composite materials. The model composite consisted of blending the nanoparticles synthesized by our collaborators with graphite. The electrode contained 25 wt% of c-Ge or c-Si Nps, 66 wt% Graphite (BTR918), 7% sodium carboxymethyl cellulose (Na-CMC, Merck), and 2 wt% carbon black (Super P). The same procedure to prepare the electrodes was performed, as described in section 2.1.1.

Besides, we used a composite made of a-Si/c-$FeSi_2$ and graphite. Known as L20772, it was provided by 3M in the frame of the H2020 European project SINTBAT and contains a mixture of amorphous silicon (a-Si) with crystalline iron disilicide (c-$FeSi_2$) inclusions, and graphite. The active material present in the L20772 powder is approximatively 20 % graphite, 25 % a-Si and 55 % c-$FeSi_2$ in weight. VARTA and CEA-Liten prepared the electrode with a mass loading of 2.4 $mAh.cm^{-2}$ composed of 50 wt% L20772, 41 wt% graphite (BTR918), 7 wt% lithium polyacrylic acid (LiPAA 450) as a binder, and 2 wt% carbon black (Super P). The active material present in the L20772 powder is approximatively 80 % graphite and 20 % Si. More information on the morphology of the electrode will be given in chapter 5.

2.2 Electrochemical characterizations

2.2.1 Galvanostatic cycling with potential limitation (GCPL)

In this thesis, we used galvanostatic cycling with potential limitation (GCPL). GCPL consists of applying a constant current while recording the evolution of the voltage for the time required to complete a cycle. When the lithiation voltage limit is reached, the current is reversed for the delithiation stage. Here, electrochemical measurements were performed on an MPG2 Biologic multichannel potentiostat.

The expected current is calculated from the theoretical capacity. Capacity refers to the number of electrons transferred during the cycling process, and it is expressed as follows:

$$Q = (\Delta x\ F)/M$$

Equation 2.1

Where M is the molecular weight of the material, F is the Faraday's constant equal to 26801 mAh/mole. The usual unit to express capacity is mAh/g.

The time needed for charging or discharging a battery is usually expressed as a C/rate ratio. This time is chosen depending on the type of experiment. For instance, C/10 means that the lithiation will happen in 10 hours, and the fixed current is determined as follows, knowing the capacity, the active material mass of the electrode, and the lithiation time:

$$I = \frac{Q\ \left[\frac{mAh}{g}\right] mass\ [g]}{[hours]}$$

Equation 2.2

The voltage profile under constant applied current is characteristic of changes in the active material structure or chemistry. The different types of structural transformations of the active material caused by the lithiation or delithiation have specific signatures in the voltage profile (that might vary significantly depending on the C/rate):

- One phase reaction, also called solid solution formation as in the case of Li_xSi_y phases. The voltage profile consists of a sloping shape (see Figure 2.1a).

- Two-phase reaction results from the continuous Li reaction with the active material forming two phases; the lithiation front is separating the Li-poor phase from the Li-rich one. This process is also known as core-shell, and the associated voltage curve is flat (plateau) (see Figure 2.1b).

- Multiphase-reaction: steps between several plateaus might be observed, associated with the formation of stable intermediate phases (see β and γ in Figure 2.1c).

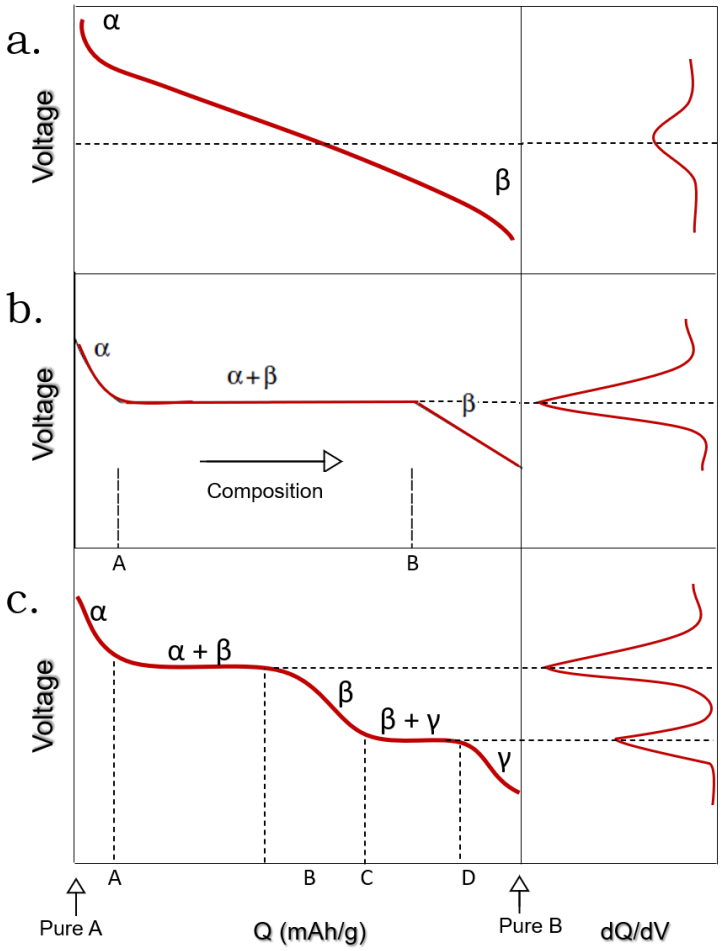

Figure 2.1 Illustration of the voltage and dQ/dV signature for a. one-phase, b. two-phase, c. multi-phase mechanisms. Adapted from [3].

Distinguishing these mechanisms is not straightforward. One useful tool is the derivative of the capacity. The differential capacity profile is obtained after differentiating the capacity vs. voltage curve. Plotting the dQ/dV vs. voltage highlights the voltage profiles obtained in the capacity vs. voltage, the plateaus appearing as peaks[4].

The characteristic dQ/dV peaks for a two-phase voltage profile are intense and narrow. In comparison, the peaks for the one-phase mechanism are broader and weaker.

In this thesis, an EC-Lab application for batteries called differential coulometry spectroscopy (DCS) was used to identify the characteristic peaks. This tool is a statistical method to investigate the electrochemistry behavior in electrodes, and it is similar to the differential capacity analysis, except that it leads to an accurate evaluation of the electrochemical changes without information loss due to the derivative[5]. The DCS analysis uses the number of measured points for every voltage step, resulting in the characteristic peaks highlighting the structural variations in the lithiation of a material[6].

2.3 X-ray diffraction characterization

X-rays are electromagnetic radiation with a high frequency and a short wavelength of ~0.5–2.5 Å. When X-rays were discovered in 1895 by Röntgen, they were used to study the internal structure of opaque objects by placing the object in between a source of X-rays and a photographic film. This experiment produced a shadow picture (radiograph) that could resolve sizes of about 10^{-3} mm. The particle-wave duality of the X-rays was discovered later by Max Von Laue (1912). He placed a zinc sulfide crystal between an X-rays beam and a photographic plate, showing a pattern of bright spots. Thus, he proved the wave-like nature of X-rays and thus their ability to generate diffraction patterns when interacting with a crystal, the interatomic distances of which are of the same order of magnitude as the X-Ray wavelength. This discovery inspired William and Lawrence Bragg to establish a relationship between the X-rays wavelength, the angle of incidence, and the space between the atom planes in a crystal. In a 1922 Nobel lecture, William and Lawrence Bragg clearly described this relationship, considering that the crystalline

lattice can be described as families of parallel and equidistant planes (Figure 2.2a)[7]. When X-rays interact with atoms in a crystal, they are scattered, and the different resulting spherical waves interfere and generate a diffracted plane wave characterized by the following equation, which is known as the Bragg law:

$$n\lambda = 2d_{hkl}\, sin\theta_{hkl}$$

Equation 2.3

Where n is a non zero integer, λ is the wavelength of the X-rays, d the interplanar distance for the {hkl} plane family, and θ_{hkl} is the angle between the incident beam and these planes.

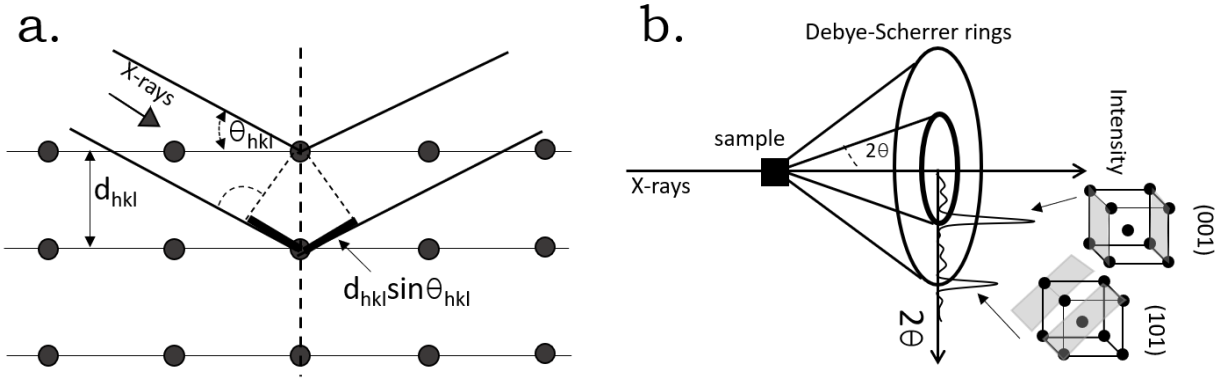

Figure 2.2. a. Illustration of the diffraction of X-rays by a crystal. b. Illustration of formation of a diffracted cone in the Debye-Scherrer geometry.

Polycrystalline materials (also often abusedly known as powders) are composed of many crystallites with random orientations. When a powder is placed in an X-ray beam, the incident beam is scattered in concentric cones (Figure 2.2b). The intersection of these cones with a perpendicular 2D area gives concentric rings called Debye-Scherrer rings. Each ring corresponds to the diffraction from a particular set of planes (hkl). Typical powder patterns

with Bragg peaks correspond to the interception of these rings by the scanning detector.

X-ray powder diffraction can give structural information on the investigated material[8].

- *The peak position* allows determining the value of the lattice parameters.

- *The peak profile,* i.e., peak shape and the full width at half maximum (FWHM), can give information on the sample microstructure: crystallite size, lattice distortion, and more generally, defects in the crystal lattice. The measured FWHM has to be corrected from the instrumental resolution, which is determined by measuring reference highly crystalline samples such as LaB_6.

Equation 2.4 relates the resolution corrected FWHM to the crystallite size and the lattice distortion (strain).

$$FWHM = \beta_e + \beta_L = C\varepsilon \cdot tan\theta + \frac{K\lambda}{L \cdot cos\theta}$$

Equation 2.4

Where λ is the incident radiation, L is the average crystallite size, and ε is the lattice distortion.

-*The peak intensity* depends, through the structure factor F, on the nature of the atoms and their position inside the unit cell. In reflection geometry, the diffracted intensity for an (hkl) Bragg peak is given by:

$$I_{hkl}(q) = I_0 \cdot \frac{\lambda^3 \cdot m_{hkl} \cdot |F_{hkl}(q)|^2}{2 \cdot \mu \cdot v_a^2} \cdot \frac{1 + cos^2 2\theta}{sin\theta \cdot \sin 2\theta}$$

Equation 2.5

Where I_{hkl} is the integrated intensity of the hkl reflection, I_0 is the intensity of the incident beam, m_{hkl} is the multiplicity, $|F_{hkl}(q)|^2$ is the structure factor, υ_a is the volume of the unit cell, μ the absorption, and $LP = 1 + cos^2 2\theta / sin\theta \cdot sin2\theta$ is the Lorentz-polarization factor.

The structure factor is calculated as follows:

$$F_{hkl}(q) = \sum_{1}^{N} f_n(q) \cdot e^{2\pi i(hx_n + ky_n + lz_n)} \cdot e^{-B\frac{sin^2\theta}{\lambda^2}} \cdot Occ$$

Equation 2.6

Where B is the thermal vibration parameter (Debye-Waller factor), *Occ* is the site occupancy, and $f_n(q)$ is the atomic scattering factor. The summation is made on all the atoms of the unit cell.

Different types of analysis can be performed with XRD data: 1) single peak procedures that reduce the diffraction data to a list of independent diffraction peaks and 2) the whole pattern fitting methods that refine a sample model. In the latter case, LeBail refinement allows determining the unit cell parameters and the microstructural information, the peak intensities being considered as free parameters. The peak intensities could be refined in Rietveld analysis, which allows determining atomic positions or site occupancies.

X-rays interact with matter leading to absorption, scattering, and other secondary emissions. These interactions are valuable to the analysis of materials. Here, we are interested in the material changes while Li-ions are introduced and removed during the battery cycling process. X-rays can be used for *ex-situ (post-mortem)*, *in-situ,* and *operando* studies while cycling a

battery. *Ex-situ* study consists of cycling the crystalline material to a particular SOC, and then the battery is opened in an argon-filled glove box. The material to be analyzed is placed in an air-tight sample holder. In this mode, the material may evolve once it is extracted from the cell. Also, it can be oxidized since it can be exposed to a few oxygen or water quantities. The other two types of experiments are discussed below.

2.3.1 *Operando* and *in-situ* XRD to study negative electrodes for LiB

The main difference between *operando* and *in-situ* studies is that *operando* measurements are performed simultaneously as the battery is cycling, while in the case of *in-situ* studies, the battery cycling is stopped to measure the sample. A critical issue to consider while performing *operando* and *in-situ* studies are the interaction of the X-rays with materials that are part of the battery, such as electrolyte, current collector window that affect the data quality.

We performed *operando* studies on Si and Ge based electrodes using a Bruker D8 diffractometer with Cu Kα (λ = 1.54 Å), which was installed in the lab at the beginning of my second thesis year. Figure 2.3 shows the electrochemical cell, which has been used. This Swagelok-type cell is used in reflection geometry. In this configuration, the material of interest is placed below a Be window (200 µm thick, 4 cm in diameter) that serves as both the current collector and window; it is mostly transparent to X-rays (more than 80% transmission at 8 KeV).

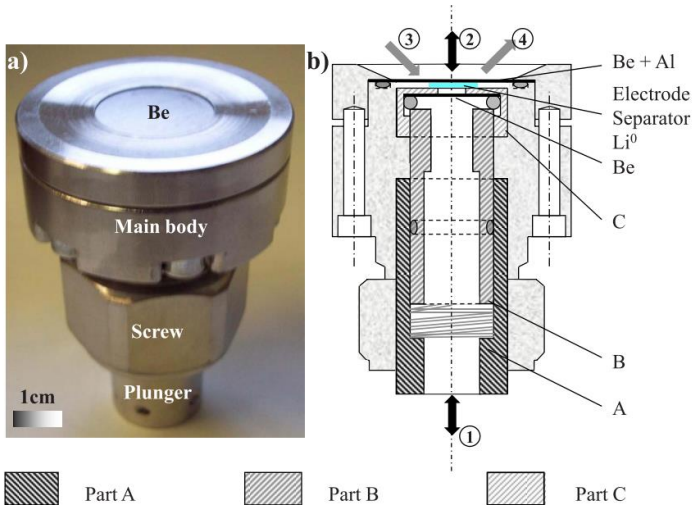

Figure 2.3. Electrochemical cell for *operando* experiments. a. Photo, and b. detailed view with incoming and outcoming beam paths in reflection geometry (3→4), and (1→2) transmission geometry [9].

Figure 2.4 shows the procedure for assembling the electrochemical cell for the *operando* experiments. The different parts of the cell are shown in Figure 2.4a. To begin the assembling, the active material to be analyzed is placed next to the Be window. Next to the negative electrode, a Whatman glass fiber separator soaked with electrolyte (1 M $LiPF_6$ in 3FEC/7EMC v/v with 2wt% VC) is placed (see Figure 2.4b and c). Subsequently, a Li metal spread in a stainless-steel separator is deposited (see Figure 2.4d). The main body of the cell is isolated from the plunger by using cellulose acetate film (see Figure 2.4e). Afterward, a spring and Teflon gasket are placed to assure good pressure of the plunger (see Figure 2.4f and g). Finally, the plunger is deposited, and the cell is closed by applying pressure with the finger while turning the screw (see Figure 2.4h and i). A good pressure helps to have effective electrochemical cycling. Figure 2.4j shows how to connect the cell to the potentiostat-galvanostat. The cell is connected to the negative and positive plunger before it is placed on the diffractometer holder (see Figure 2.4k).

Figure 2.4. a. Different parts of the cell. *Operando* cell assembly: after the active material is placed, the b. and c. the separator with electrolyte, d. the stainless-steel with spread Li metal. e. acetate film to isolate. f. and g. spring and Teflon gasket, respectively, and h. the plunger is placed. i. The screw is turned, applying pressure to close the cell. j. the cell is connected to a potentiostat-galvanostat, and k. the cell is placed on the diffractometer holder. Adapted from [10].

The active material to be analyzed was prepared as a self-supported electrode. This self-supported electrode was prepared using 50% active material, 25% carbon black, and 25% Na-CMC. The powders were ground in a mortar for 30 min, then dissolved in purified water (18.2 Ω at 25 °C) with 0.4% Triton X-100 and stirred for two days (see Figure 2.5b and c). The slurry was placed in Mylar foil with a doctor Blade (200 µm) (see Figure 2.5d). The solution 0.4% TritonX-100 is essential to reduce the surface tension allowing the deposition of the slurry in Mylar. The film was dried for one day at 80 °C. The plastic-like-film was detached while drying on its-own and cut into a circular disk of 16 mm

with an active mass of 4–5 mg (see Figure 2.5f). The preparation of the self-supported electrode is the crucial point in this type of experiment. In some non-ideal cases, the dried slurry resembled islands difficult to handle, preventing them from getting a robust plastic film (see Figure 2.5e). One possible way to fix this problem is to stir for a longer time.

In this cell configuration, electrochemistry is not as performant as in a coin-cell or a pouch-cell since the self-supported electrode undergoes several parasitic reactions due to its thickness (~200 µm). However, I was able to get satisfactory cycling conditions (which allowed us to correlate structural changes and electrochemical features from galvanostatic measurements performed independently with coin cells) and high-quality XRD data.

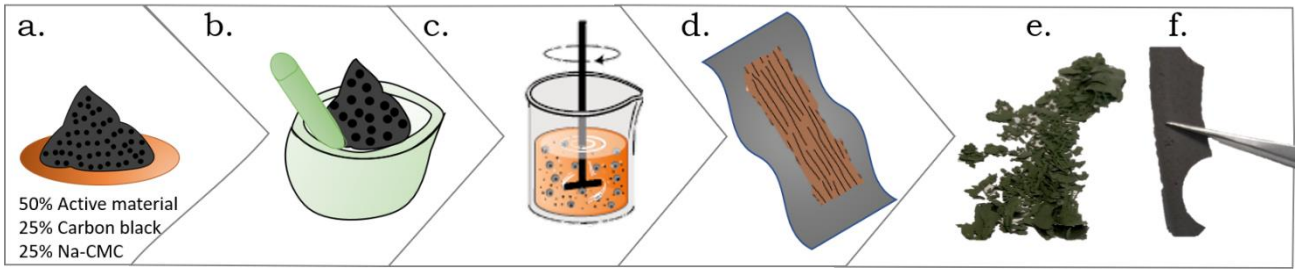

Figure 2.5. Self-supported electrode preparation a. weight, b. grinding, and c. mixing of the powders, d. deposition of the ink in a Mylar foil. Two examples of characteristic self-supported electrodes obtained: e. detached electrode and f. robust self-supported electrode.

2.3.2 Wide and small-angle X-ray scattering for LiBs (WAXS/SAXS)

The evolution of materials at two different scales (atomic scale and nanoscale) can be followed by simultaneous wide-angle and small-angle X-ray scattering. Depending on the sample-detector distance, it is possible to obtain information on the sample with scattered/diffracted X-rays at an angle of 2θ. The detector is placed closer to the sample in wide-angle X-ray scattering,

involving 2θ >1°. While for measuring small angles, the detector is placed farther from the sample to obtain information in 2θ < 0.3°, allowing the investigation in materials of long-range order from 10 to 1000 Å. For SAXS, the representation of intensity is usually reported in terms of the wave vector (q, $Å^{-1}$).

The SAXS intensity obtained is proportional to the contrast Δρ, defined by the difference in electronic density between an object and its medium (for instance, the difference of Si Nps in the matrix, i.e., $\rho_{Si} - \rho_{matrix}$), the volume *V*, the form factor *P(Q)* that depends on the shape and size of scattering objects, and the structure factor that depends on the position of scattering objects relative to one another S(Q):

$$I(Q) = I_0 \cdot (\Delta\rho)^2 \cdot V^2 \cdot P(Q) \cdot S(Q)$$

Equation 2.7

In simultaneous SAXS/WAXS measurements, the first detector needs to have a hole in the center to allow the scattered intensity at lower angles to be detected by a second detector at longer distances. As a result, the sample is measured in a transmission geometry (see Figure 2.6).

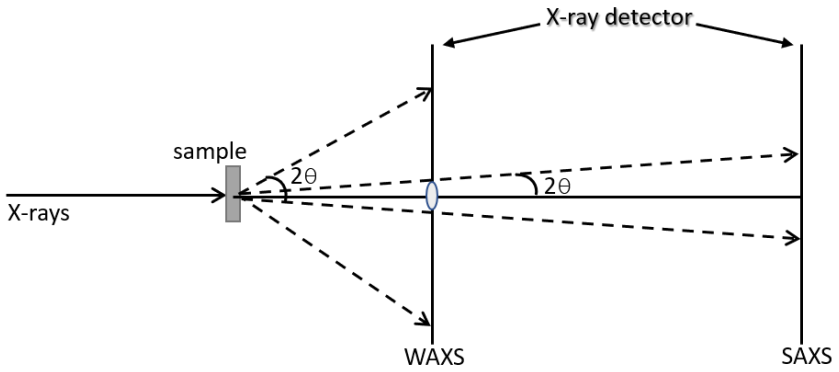

Figure 2.6. Illustration of the simultaneous WAXS/SAXS geometry.

The *operando* and simultaneous WAXS/SAXS experiment measurements were performed on the BM02 (D2AM) beamline at the European Synchrotron radiation Facility (ESRF, Grenoble, France). The energy of the incident X-ray beam was 17 keV (radiation wavelength $\lambda = 0.7293$ Å). The WAXS and SAXS detector were placed at 130 and 3170 mm, respectively, from the samples. The detector used for WAXS was an imXPAD WOS, and the SAXS detector was imXPAD S540. The standard sample-to-detector distance calibration was performed with silver behenate ($AgC_{22}H_{43}O_2$) for SAXS and lanthanum hexaboride (LaB_6), and chromium oxide (Cr_2O_3) for WAXS. The SAXS and WAXS intensity profiles collected as a function of the momentum transfer q were obtained by azimuthal integration of the 2D patterns using the PyFAI library.

In this experiment, several pouch-cells were mounted in transmission geometry on a homemade sample holder to assure the pressure between the electrodes and ensure correct electrochemical cycling. The cell holders were made with 3 mm holes to probe the pouch-cells with the X-rays without hampering the electrode analysis (see Figure 2.7b). The pouch cells were made by CEA-Liten using a positive electrode of nickel/manganese/cobalt oxide ($LiNi_{0.6}Mn_{0.2}Co_{0.2}$) with a loading mass of 2 mAh $\cdot cm^{-2}$ (see Figure 2.7a). The separator electrolyte was Celgard 2400 and 1 M $LiPF_6$ in 3FEC/7EMC, v/v with 2 wt% VC. As a negative electrode, it was used the composite a-Si/c-$FeSi_2$/graphite described in section 2.1.2.

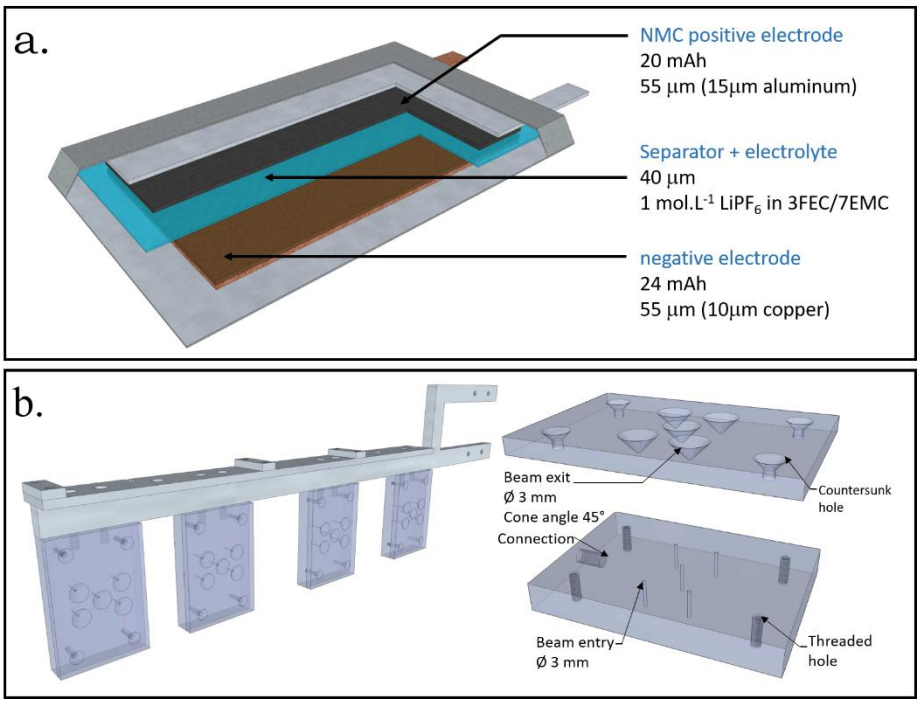

Figure 2.7. a. Components of the pouch-cell, and b. homemade pouch-cell holder.

2.4 X-ray Raman scattering (XRS) spectroscopy

X-ray Raman Scattering (XRS) spectroscopy, which is a non-resonant technique, provides information on the soft-X-ray region (light-elements Z < 10), albeit using hard X-rays that have more penetrating power and are less prone to surface contamination. Soft incident energy techniques require special measurement conditions such as high vacuum operation since soft X-rays photons below 1 keV are absorbed by the air. Besides, some of them require very thin samples that are challenging to prepare or have very limited probed depths[11]. However, the non-resonant character of the technique can lead to a less favorable signal to noise ratio. Considering the incident energy (i.e., 10 KeV > 285 eV for C K edge), different types of interactions such as Rayleigh and Compton scattering might contribute to the background signal.

Here, XRS spectroscopy measurements were performed on the ID20 beamline at ESRF. In this technique, a monochromatic incoming X-ray beam with initial energy Ei 9.8 keV ± energy of the edge is scattered by the sample to be analyzed. This scattered beam is reflected by twelve spherical bent Si (660) analyzer crystals, which select the final energy E_f = 9.8 keV, and then focused on the two-dimensional detector (see Figure 2.8a)[12]. The principle is to measure the scattered intensity as a function of E_f-E_i while varying E_i around a particular edge value.

The data were treated with the XRStools program package. Given that each of the twelve analyzer crystals gives a 2D image depending on the shape of the sample, the process consisted of selecting a region of interest (ROI) (red squares in the center of the spots). Then, the intensity is integrated over the ROI, giving a curve of the intensity vs. energy that shows the Rayleigh scattering (elastic peak with high intensity) and the low elements K edges on the top of the Compton scattering background[13] (see Figure 2.8b).

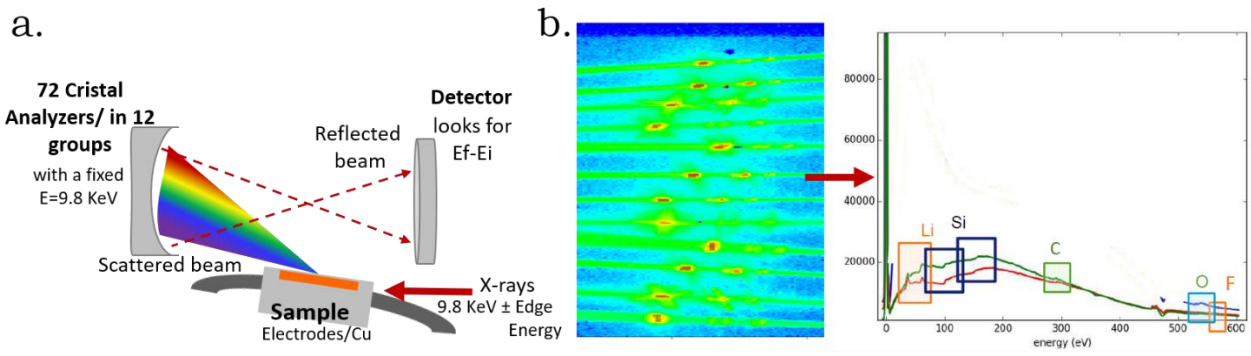

Figure 2.8. a) Schematic drawing of the experimental setup used in ID20 at the ESRF. b) left: two-dimensional image obtained by the detector with the region of interest (red rectangles in the center of the spots), right: ROI after being integrated results in intensity vs. energy curve.

Here the negative electrodes were measured *post-mortem*. Since the signal-to-noise ratio is quite unfavorable because of the high background level which is intrinsic to this non-resonant technique, the measuring time was about 10-14 h per sample. We studied two types of Si-based electrodes. The first system was an electrode composed of 50 wt% Si Nps, 25 wt% of Na-CMC, and 25 wt% carbon black (Super P). The second used the a-Si/c-$FeSi_2$/graphite electrode described in section 2.1.2. The selected separator and electrolyte were respectively celgard 2400 (monolayer polypropylene) and 1 mol.L-1 lithium hexafluorophosphate ($LiPF_6$) in a fluoromethyl carbonate and ethyl methyl carbonate (3FEC/7EMC, v/v) binary solvent mixture with 2 wt% vinyl carbonate (VC).

Pristine electrodes were prepared at different states of charge in a coin-cell (see Figure 2.9 a). The coin-cells were disassembled in a glovebox with Ar (with H_2O and O_2 levels <1 p.p.m.) and placed in an air-tight homemade sample holder (see Figure 2.9 b).

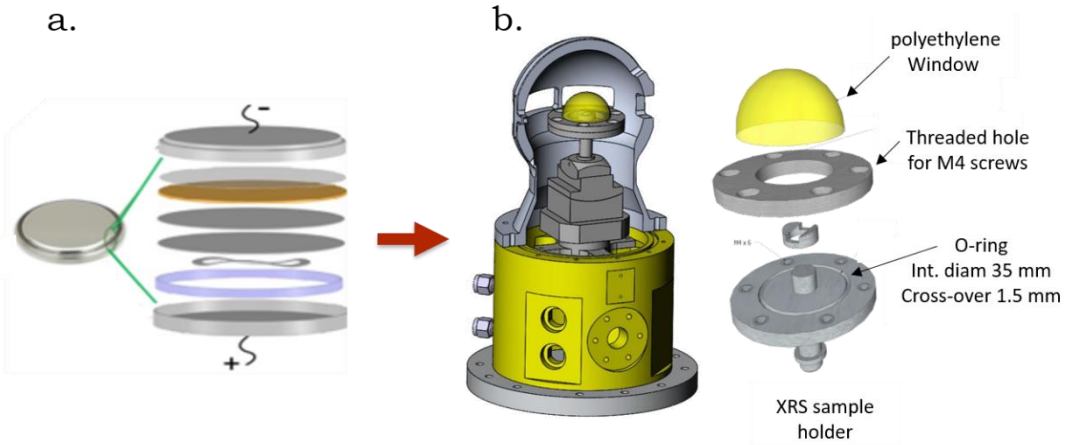

Figure 2.9. a. Characteristic half-cell coin-cell configuration for the *post-mortem* characterization. b. XRS homemade air-tight sample holder.

Li K, Si $L_{2,3}$, C K, O K, and F K spectra were measured to probe the chemical environment of the electrodes. Given that the study of the chemical environment in electrodes using XRS is relatively scarce, we measured references to compare with the electrode signals at a given SOC. Table 2.2 shows the references and the electrodes measured.

The XRS curves of the electrodes are analyzed using the reference spectra to identify the electrode components by comparison of the different peaks. In particular, those components that correspond to the formation of SEI, e.g., LiF and Li_2CO_3. When it is possible, the intensity of the electrode is compared with the sum of different reference intensities using the following formula:

$$I_{edge}(sample) = \sum x_i \, I_{edge} \, (ref_i)$$

Equation 2.8

Where I_{edge}(sample) is the intensity of the electrode at different SOC, x_i represents the weight of each reference spectrum intensity, I_{edge}(ref).

Table 2.2 References and electrodes measured in XRS.

	Samples	Edges Measured
References	Li metal	Li K
	Silicon powder 228 + CMC + Super P electrode	Si $L_{2,3}$, C K, O K
	Super P + CMC electrode	C K
	Li_2CO_3 in capillary	Li K, C K, O K
	CMC alone powder in capillary	C K, O K
	$LiPF_6$ salt in capillary	Li K, F K
	LiF salt in capillary	Li K, F K
ELECTRODES		
c-Si NPs /Cu	Pristine Lithiated Delithiated	Li K, Si $L_{2,3}$, C K, O K, F K
a-Si/c-$FeSi_2$/Graphite /Cu	Lithiated	Li K, Si $L_{2,3}$, C K, O K, F K
	Delithiated	Si $L_{2,3}$, C K
	Delithiated, 300 cycles	Li K, Si $L_{2,3}$, C K, O K, F K

2.5 Bibliography

1. Desrues, A. *et al.* Best Performing SiGe/Si Core-Shell Nanoparticles Synthesized in One Step for High Capacity Anodes. *Batter. Supercaps* **2**, 970–978 (2019).

2. Desrues, A. Matériaux composites Si@C nanostructurés pour anodes de batterie Li-ion à haute densité d'énergie. Relations entre structure/morphologie et mécanismes de dégradation. (Université Paris-Saclay, 2019).

3. Huggins, R. A. *Advanced Batteries*. *Advanced Batteries: Materials Science Aspects* (Springer US, 2009). doi:10.1007/978-0-387-76424-5

4. EC-Lab – Application Note #40 Differential (Incremental) Capacity Analysis. 1–3 (2019). Available at: https://www.biologic.net/documents/dcs-dca-battery-application-note-40/. (Accessed: 7th March 2020)

5. EC-Lab - Application Note # 57 Differential Coulometry Spectroscopy (DCS). 1–3 (2019). Available at: https://www.biologic.net/documents/dcs-dca-battery-application-note-57/. (Accessed: 2nd July 2020)

6. Huggins, R. A. Principles Determining the Voltages and Capacities of Electrochemical Cells. in *Advanced Batteries* 25–39 (Springer US, 2008). doi:10.1007/978-0-387-76424-5_2

7. Bragg, W. & Bragg, L. Nobel Lecture: The diffraction of X-rays by crystals. (1922). Available at: https://www.nobelprize.org/uploads/2018/06/wl-bragg-lecture.pdf. (Accessed: 31st July 2020)

8. Cullity, B. D. & Stock, S. R. *Elements of X-Ray Diffraction: Pearson New International Edition*. (Pearson Education Limited, 2014).

9. Leriche, J. B. *et al.* An Electrochemical Cell for Operando Study of Lithium Batteries Using Synchrotron Radiation. *J. Electrochem. Soc.* **157**, A606–A610 (2010).

10. Chotard, J.-N. How to mount the in-situ cell. Available at: https://extra.u-picardie.fr/nextcloud/index.php/s/y3r5eNPXHfPrMEC. (Accessed: 18th August 2020)

11. Bergmann, U., Glatzel, P. & Cramer, S. P. Bulk-sensitive XAS characterization of light elements: from X-ray Raman scattering to X-ray Raman spectroscopy. *Microchem. J.* **71**, 221–230 (2002).

12. Huotari, S. *et al.* A large-solid-angle X-ray Raman scattering spectrometer at ID20 of the European Synchrotron Radiation Facility. *J. Synchrotron Radiat.* **24**, 521–530 (2017).

13. Sahle, C. J. *et al.* Planning, performing and analyzing X-ray Raman scattering experiments. *J. Synchrotron Radiat.* **22**, 400–409 (2015).

Chapter 3

(De)Lithiation mechanism of crystalline germanium nanoparticles

3.1 Introduction

It is well known that in the course of electrochemical cycling Si and Ge, anode materials from the group 14 elements, undertake significant volume variations (280% vs. 260%, respectively[1]). This deformation is responsible for premature aging of the anode material, producing continuous solid electrolyte interphase growth, contact electrical loss, and lower reversible capacity. While Si has largely received attention over the last 20 years, germanium has been raising a growing interest because of its attractive properties for energy storage applications despite its lower capacity (1384 mAh/g) versus silicon (3579 mAh/g). For instance, the electronic and Li-ion conductivity of germanium exceeds by two orders of magnitude those of silicon because of its small bandgap (~0.6 eV vs. 1.12 eV for Si)[2].

Moreover, germanium presents mainly isotropic lithiation, facilitating lithium-ion diffusion.

This chapter investigates the (de)lithiation mechanisms in crystalline germanium nanoparticles synthesized by laser pyrolysis by Nathalie Herlin-Boime, and John Alper, our collaborators at CEA-Iramis. We mainly use *operando* XRD to gain access to the structural evolution of Ge lattice, mostly, its strain. These studies are complemented by *post-mortem* ^{7}Li NMR measurements performed by Michel Bardet and Anton Buzlokov from CEA-MEM-LRM to gain information on the different amorphous lithiated phases that formed during electrochemical cycling.

3.2 Structural and morphological characterization of crystalline germanium nanoparticles pristine powder

Ge was initially characterized in pristine powder using X-ray powder diffraction (Figure 3.1a). The diffracted pattern shows well-defined and sharp peaks, indicating highly crystalline structure[3]. Rietveld refinement of the powder data was performed using Fullprof software, assuming a diamond structure with space group *Fd-3m*. The obtained lattice parameter is a =5.657(1) Å, in agreement with the reported value for bulk Ge[4]. The (hkl) dependence of the diffraction peak widths could not be accounted for considering an isotropous shape of the Nps. The Rietveld refinement was performed using the spherical harmonics model[5], and the results showed that the particles have a cubic shape rounded on the vertices with a mean value edge of 58 ± 7 nm.

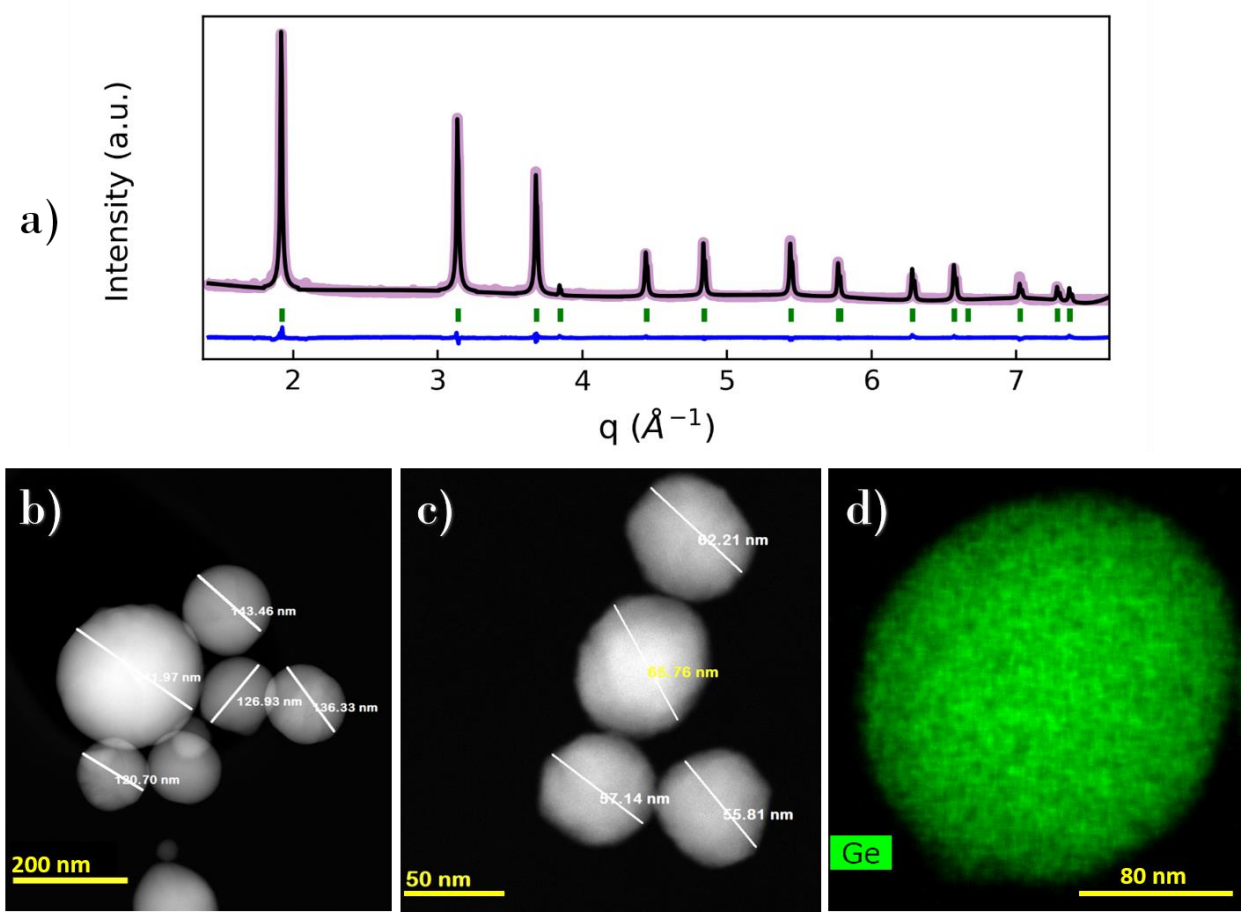

Figure 3.1 a) Rietveld refinement of X-ray powder diffraction data on Ge powder. Refined patterns (black) overlapped the observed patterns (purple). The difference between the calculated and the experimental is shown in blue. b) and c) STEM-HAADF images obtained in the Ge powder. d) corresponding EDX elemental mapping showing the distribution of Ge.

Electron microscopy measurements were performed on the powder to obtain further information on the morphology of these particles. Figure 3.1b–d shows high-resolution transmission electron microscopy (HRTEM) images of the Ge Nps, highlighting the significant spread in particle size from 55 to 300 nm. The Ge powder is made of both large Ge particles and smaller ones with faceted shape (Figure 3.1c). HRTEM observations suggest that the larger particles are made up of single-crystal particles of smaller size (~60 nm). This value is coherent with the values found by XRD. The STEM-EDX mapping highlights homogeneous Ge particles (Figure 3.1d).

3.2.1 Electrochemical characterization of c-Ge Nps

To examine the electrochemical performance, we cycled the c-Ge Nps in half cells at C/10. Figure 3.2a shows the evolution of the voltage vs. capacity, using a C-rate of C/10. The delithiation capacity is 700 mAh/g, with 8% capacity loss, in agreement with other Ge nanoparticles synthesized by laser pyrolysis[6]. The galvanostatic profile shows two zones with slightly flat regions around 280 and 150 mV (see horizontal lines in Figure 3.2a). These plateaus are characteristic of phase transformations in the germanium electrode[7]. They are highlighted by calculating the derivative of the voltage vs. capacity curve, as shown in Figure 3.2b. See section 2.2.1 for further details on the dQ/dV analysis.

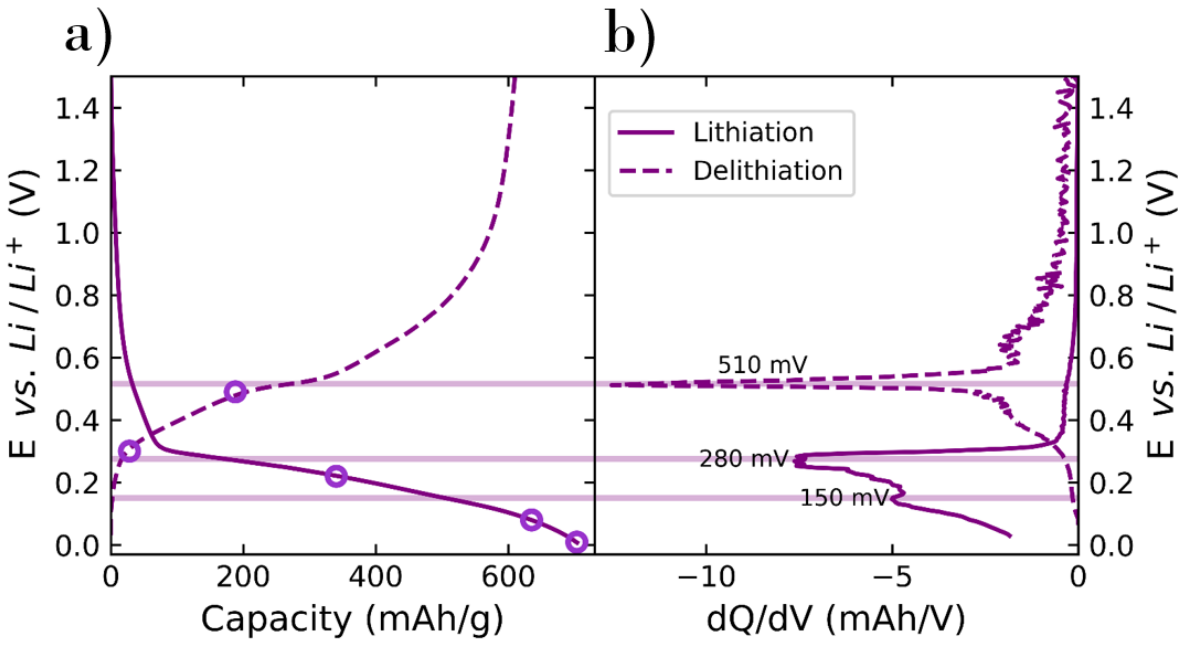

Figure 3.2 a) voltage vs. Li/Li^+ against the capacity of c-Ge Nps in a coin-cell. b) voltage vs. Li/Li^+ as a function of dQ/dV (the number of measured points for every voltage step) at C/10 during the first cycle. The points indicate the samples measure by *post-mortem* ^{7}Li-NMR.

The two broader peaks observed during lithiation and a sharp peak during delithiation emphasize the plateaus observed in Figure 3.2a.

Similar dQ/dV analysis has been done on crystalline Ge microparticles[4,8], and the dQ/dV lithiation peaks shift to higher voltages (350 and 200 mV, respectively). In our case, the high surface-area ratio in the Ge Nps could be responsible for the shift to lower voltage during lithiation[9].

Overall, the dQ/dV peaks highlight the features of the voltage vs. Li metal against capacity, emphasizing two broad peaks during lithiation and one strong peak during delithiation. In the following sections, we will focus on the correlations between electrochemical results and structural evolution.

3.3 *Post-mortem* ^{7}Li NMR on crystalline Ge nanoparticles

This technique provides insight into local lithium environments. Knowing that most of the lithiated phases that form upon lithiation are amorphous, NMR facilitates the comprehension of the (de)lithiation mechanism. We cycled Ge-based electrodes in coin-cells; the cycling was stopped at different states of charge of the (de)lithiation. The cells were then open in a glovebox, and the electrode ink was scratched from the current collector (Cu-foil) and placed into the rotor. The different selected states of charge are indicated by the markers in Figure 3.2a.

3.3.1 ^{7}Li NMR environments during lithiation

The obtained NMR spectra are shown in Figure 3.3. The two ^{7}Li resonances around 0 ppm are attributed respectively to the SEI (dark green) and surface lithium-ions (light green). Here, we are interested in the lines corresponding to Li-Ge phases.

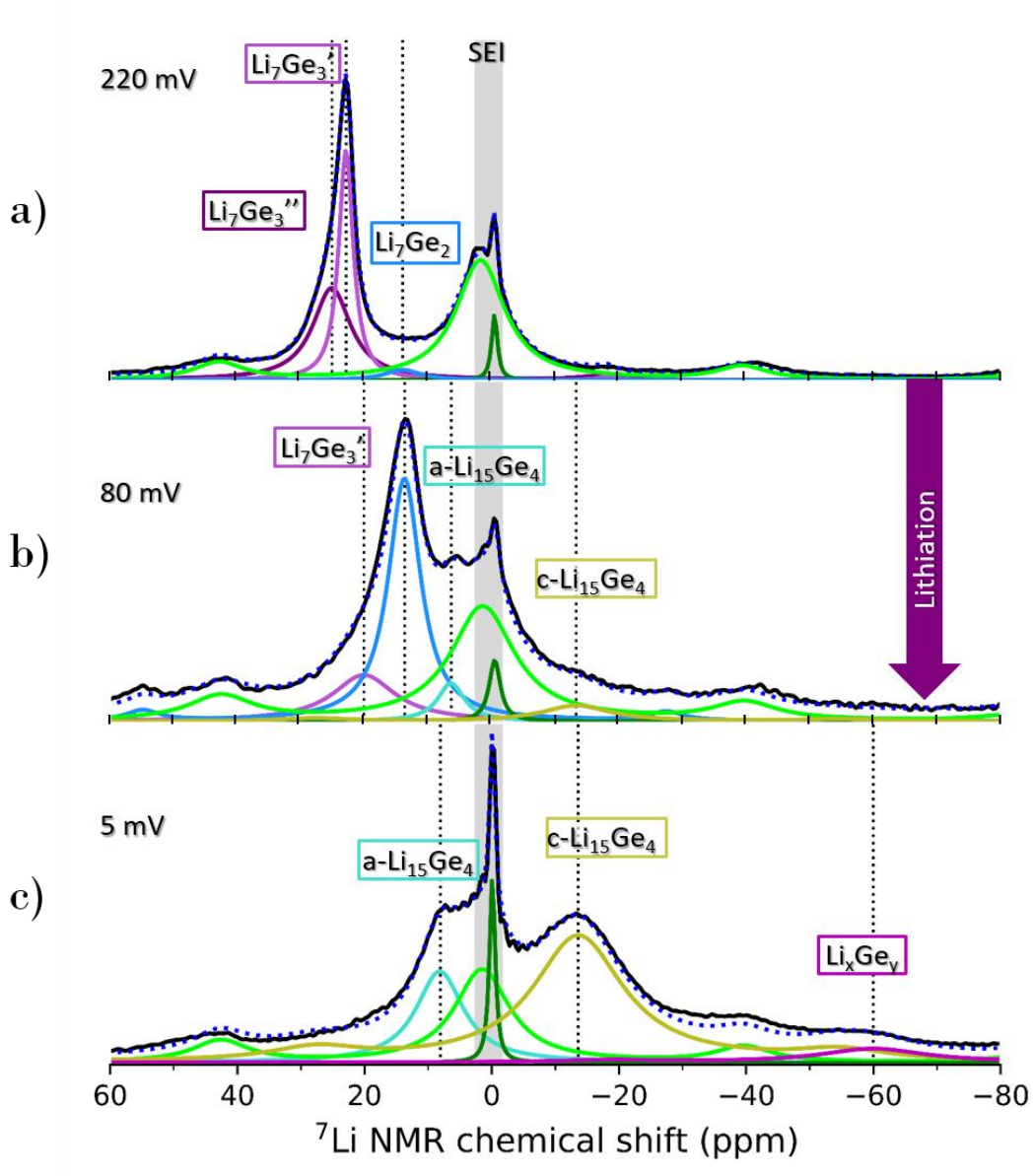

Figure 3.3 *post-mortem* ^{7}Li NMR spectra of cycled Ge electrodes during lithiation for different states of charge a) 220 mV, b) 80 mV c) 5 mV with voltages vs. Li/Li^{+}.

At 220 mV, the spectrum is dominated by two lines associated with the same stoichiometry (Li_7Ge_3' and Li_7Ge_3''). Tentatively, these pair lines could indicate

a slight disorder in the Li_7Ge_3, forming a phase with a composition closer to Li_7Ge_3, as observed in micron-size Ge[8]. Another possible explanation is that a phase with a structure similar to Li_7Ge_3, such as Li_9Ge_4, could be formed. However, according to a reported Li–Ge phase diagram[10], Li_7Ge_3 is more thermodynamically stable than Li_9Ge_4.

At 80 mV, the Li_7Ge_2 is the dominant phase. In comparison, the phase Li_7Ge_3' has decreased, broadened, and shifted significantly to lower chemical shift values, while the amorphous and crystalline $Li_{15}Ge_4$ phase begins to grow. The assignation of the sharp line in cyan to the a-$Li_{15}Ge_4$ phase is based on ^{7}Li NMR studies of Ge coated in carbon nanowires[11]. The authors have assigned a line observed at~ 8 ppm to an amorphous composition close to $Li_{15}Ge_4$. The line assignation will be clarified and supported by the XRD studies in the following sections.

The lithiation of crystalline nanoparticles at 5 mV results in two main ^{7}Li resonances at 8.1 and −13.6 ppm (cyan and olive) that we have assigned to amorphous and crystalline $Li_{15}Ge_4$. The line at −60 ppm could correspond to the decomposition of $Li_{15}Ge_4$, as already seen in micron-size Ge[8] by *ex-situ* ^{7}Li NMR studies. However, it could also be an artifact of *ex-situ* measurements.

The existence of a highly lithiated phase ($Li_{15+\delta}Ge_4$) has been reported in micron Ge, by both *ex-situ* and *in-situ* studies (characterized by the presence of NMR lines between −21 and −24 ppm)[8,11]. This phase is ascribed to extra lithium-ions that can be alloyed in the $Li_{15}Ge_4$ structure due to defects in the crystalline lattice at lower voltages (~0 mV). For silicon, the overlithiated phase has only been observed by *in-situ* measurements[12–14], and it has recently been

also reported for SiGe alloys[15]. In our case, the NMR data do not present this $Li_{15+\delta}Ge_4$ phase.

3.3.2 ^{7}Li NMR environments during delithiation

The electrode measured at the end of lithiation (5 mV) is used as a reference to follow the changes in ^{7}Li NMR environments during the delithiation process (see Figure 3.4a).

At 300 mV, while the a-$Li_{15}Ge_4$ phase has completely disappeared, the crystalline $Li_{15}Ge_4$ dominates the spectrum, together with the unidentified Li_xGe_y phase at −62 ppm.

Upon further delithiation (490 mV), the c-$Li_{15}Ge_4$ phase decreases in intensity, and the other less lithiated germanium phases such as Li_7Ge_2 and Li_7Ge_3' emerge, the latter dominating the spectrum at this voltage.

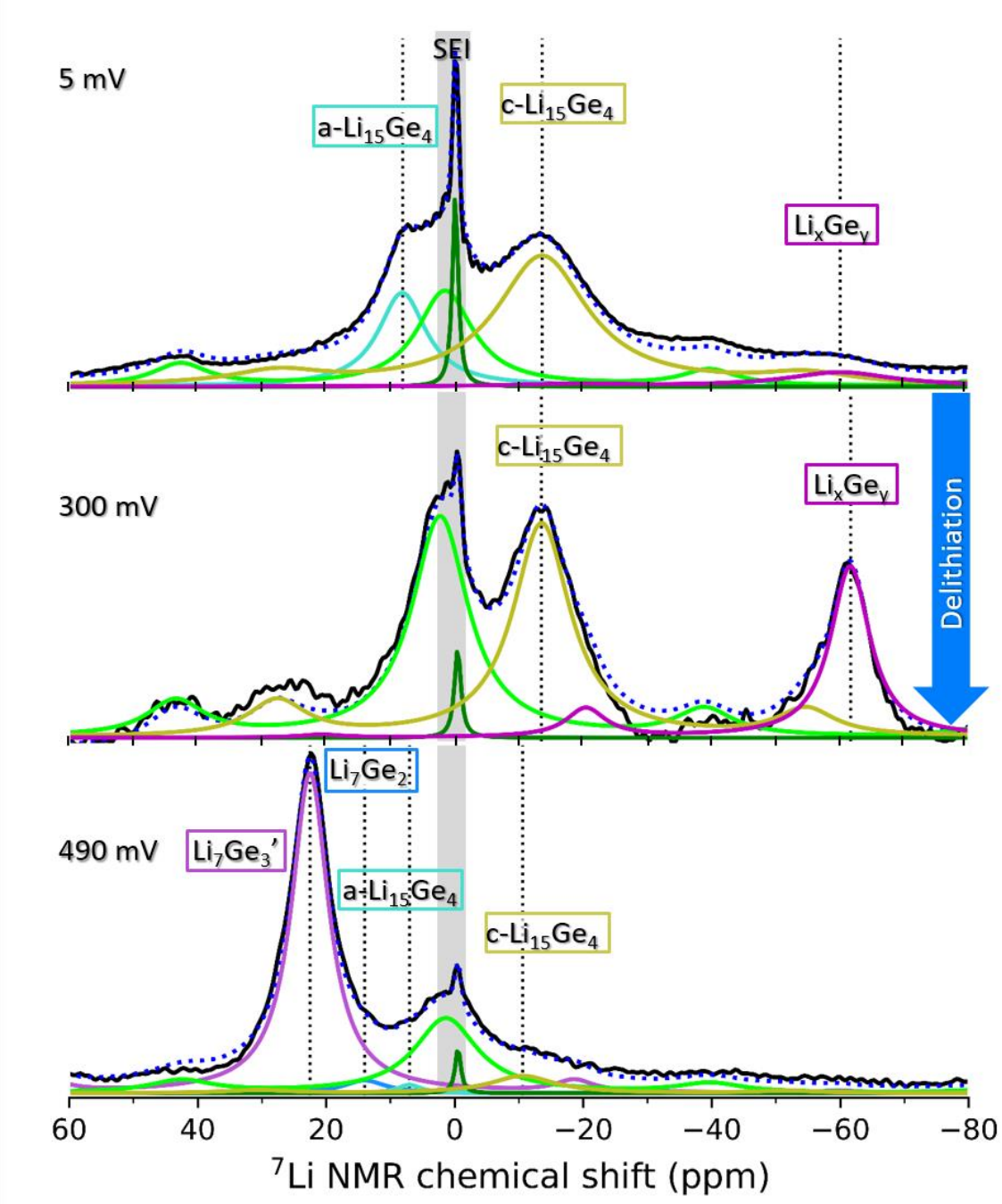

Figure 3.4 post-mortem ^{7}Li NMR spectra of cycled Ge electrodes during delithiation for different stages of charge at a) 5 mV, b) 300 mV c) 490 mV voltages vs. Li/Li+.

The different phases observed during lithiation and delithiation are summarized in Table 3.1.

Table 3.1 Parameters of NMR signals found in the Li-Ge phases

Phase	δ (ppm)	Δν (kHz)	Δδ (ppm)
Li_7Ge_3"	24 – 25	1.5	−30 – −35
Li_7Ge_3'	20 – 22	0.5 – 4.0	−20 – −30
Li_7Ge_2	14	1 – 1.5	−20 – −30
a-$Li_{15}Ge_4$	6 – 8	1 – 2	< −15
Surface Li	1.4 – 2.3	1.8 – 2.3	−55 – −70
SEI	−0.1 – −0.5	0.2 – 0.4	0
c-$Li_{15}Ge_4$	−11 – −13	2.5 – 3.5	−45 – −55
Li_xGe_y	−60	3 – 3.5	−55

To summarize, the ^{7}Li NMR measurements show the sequential formation of lithiated phases with higher Li content during the lithiation stage. This result is consistent with other studies on micron-Ge[8], and Ge coated with nanubes[11]. However, our system has unique features such as a double line, which could be attributed to two phases (Li_7Ge_3" and Li_7Ge_3') with slightly different compositions and the absence of $Li_{15+\delta}Ge_4$.

3.4 *Operando* XRD studies during lithiation/delithiation

In order to optimize the experimental conditions and minimize the background in the XRD data, I prepared self-supported electrodes from the pristine Ge powder. These electrodes were then placed in a Leriche electrochemical cell, as indicated in section 2.3.1.[16], using a beryllium window as a current collector. Our work aims to study the structural changes in c-Ge Nps while cycling. Therefore, we performed different operando studies, which are presented as follows:

1. Full lithiation of c-Ge Nps to get quantitative information on the crystal structure evolution and determine the voltage value at which the crystalline structure starts to be affected.

2. Partial lithiation. We cycled partially the crystalline Ge electrode three times to study the strain developed during lithiation and delithiation.

3. Finally, we performed full lithiation after the three partial cycles to follow the formation and then the disappearance of c-$Li_{15}Ge_4$, which is the most lithiated phase observed in this study.

3.4.1 Full lithiation: amorphization of crystalline Ge

Here, we follow the crystalline structural changes of the self-supported electrode upon complete lithiation by *operando* XRD. The investigated electrode was cycled down to 5 mV vs. Li metal and was lithiated at the C/10 rate in a half-cell configuration. The diffraction patterns were acquired every 20 min, approximately. Figure 3.5a and b show respectively the Bragg reflections of the battery components (current collector Be, Ge) upon lithiation as a function of the voltage (see color bar) and the enlarged view of the Ge(111) Bragg reflection. The Ge(111) peak broadens and shifts towards larger scattering angles below 0.6 V, and it has completely disappeared below 0.2 V, in agreement with previous XRD studies on crystalline, micron-size Ge[4,17,18].

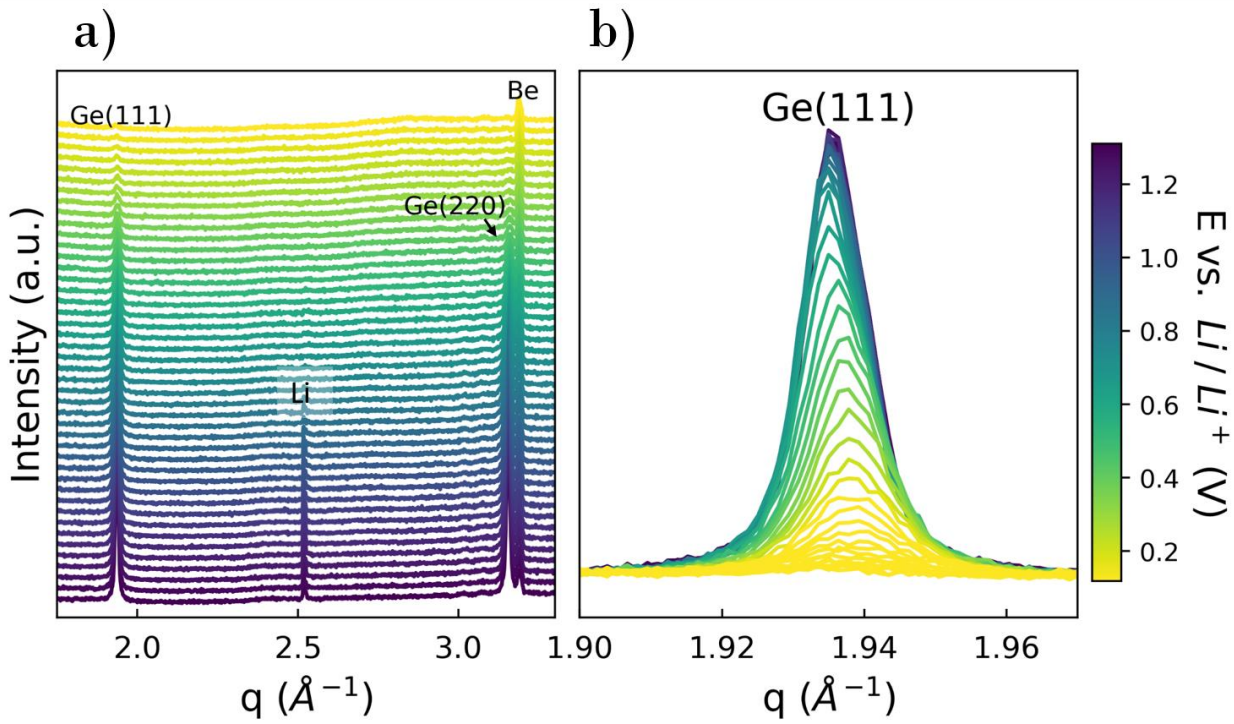

Figure 3.5 a) Evolution of Ge(111) and Ge(220) Bragg reflections during a full lithiation by *operando* XRD. b) Enlarged view of the Ge(111) Bragg reflection. The color bar shows the approximate voltage of each diffraction pattern.

To follow the c-Ge changes upon lithiation, we perform a single peak fitting analysis using the Ge(111), Ge(220), and Ge(311) Bragg reflections, considering Lorentzian functions. Figure 3.6 summarizes the results obtained from the data recorded from 0.600 V to 0.217 V vs. Li/Li^+.

Figure 3.6a and c respectively show the evolution of the intensity normalized to the value at SOC 0% and the full widths at half maximum (FWHM) for the three different peaks. Figure 3.6b shows the evolution upon lithiation of the lattice parameter calculated from the diffracted peak positions of the (111), (220), and (311) Bragg reflections. The obtained value is $a = 5.656 \pm 0.002$ Å at 0% charge, and it is consistent with the value resulting from the Rietveld refinement of the Ge powder data.

The main feature of Figure 3.6 is the decrease of both diffracted intensity and the lattice parameter at voltages lower than 0.3 V, and simultaneously, the increase of the FWHMs.

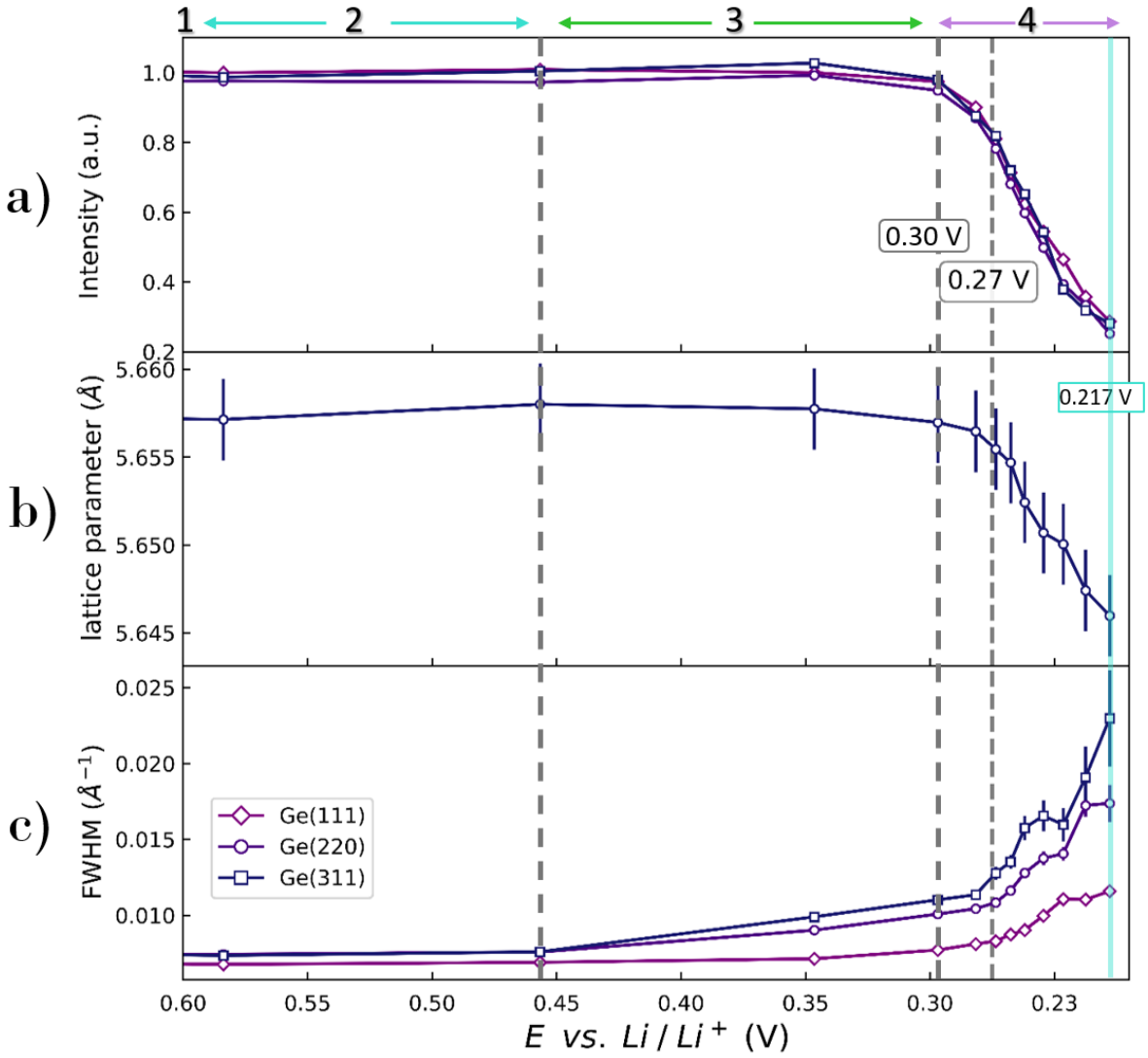

Figure 3.6 a) intensity, b) lattice parameter of Ge, and c) full widths at half maximum of the Ge(111), Ge(220), and Ge(311) reflections as a function of voltage vs. Li/Li^+ upon lithiation.

During the complete lithiation of c-Ge, four main changes stages can be distinguished: 1) before 0.6 V, the peak intensities, lattice parameter, and FWHM are constant. 2) Between 0.6 and 0.45 V, the lattice parameter is mainly constant. However, the increase in FWHM for the peaks at the larger diffraction angles reflects the increase in the degree of distortion in the Ge

lattice. 4) after 0.3 V, the diffracted intensities decrease, and the FWHMs strongly increase for all Bragg peaks indicating the decrease in crystallite size. Below 0.217 V, the intensities of the Ge Bragg peaks are too low to allow reliable data fitting. However, the Ge diffraction peaks completely disappear at 0.163 V.

It is worth mentioning that the voltage value (0.3 V) at which the intensity starts decreasing agrees with the dQ/dV peak at 0.280 V in Figure 3.2b. During the lithiation of crystalline Ge, Li-ions are alloyed in the Ge diamond structure leading to amorphous Ge and Li_xGe phases on which we will focus in the following sections.

In summary, this complete lithiation study allowed us to get an overview of the Ge structural evolution and, more importantly, determine the lithiation voltage value, close to 0.3 V, which is in good agreement with the dQ/dV peak during lithiation. This lithiation voltage value will be used to perform partial lithiation experiments presented in the next section.

3.4.2 Partial lithiation

3.4.2.1 A qualitative description of the evolution of Ge(111) Bragg reflection

This section examines the partial lithiation in crystalline Ge Nps to focus on the cycling mechanism and strain behavior. We performed three cycles at C/10 with successive cut-off voltage values of 230, 220, and 200 mV to avoid

a complete amorphization of the germanium phase (see Figure 3.7a, b, and c). The magenta curve corresponds to the last scan measured at the end of the lithiation.

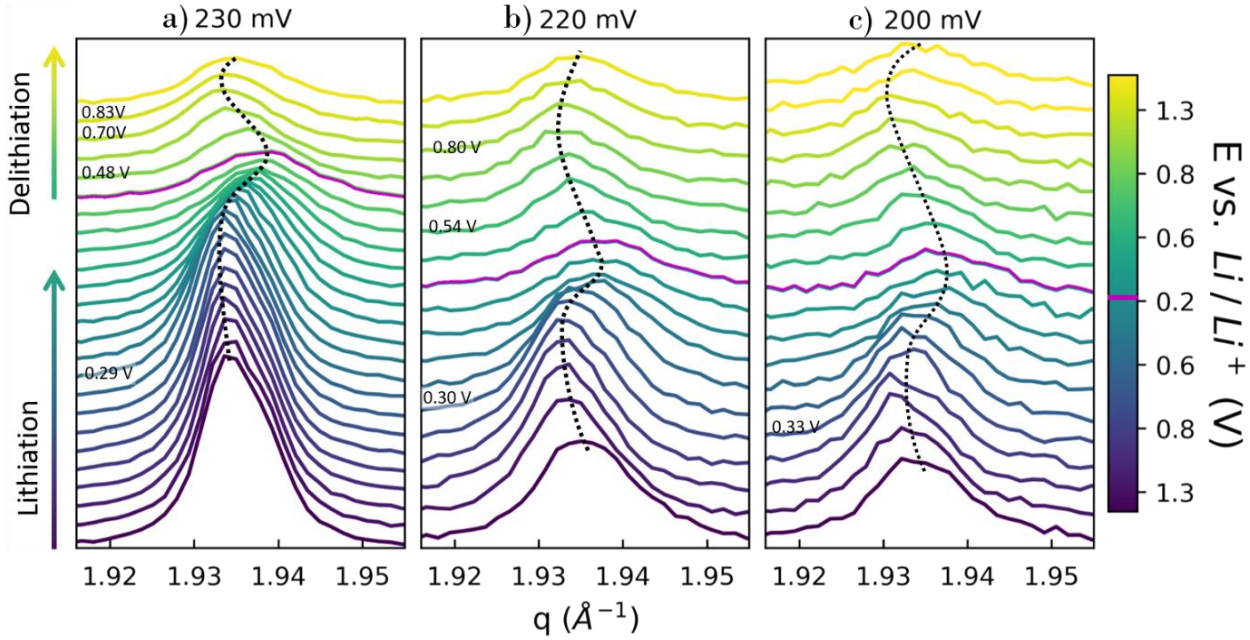

Figure 3.7 Evolution of the Ge(111) peak during the three partial lithiation down to a) 230, b) 220, and c) 200 mV.

During lithiation, two main stages can be distinguished 1) from the beginning until 0.29 V, the Ge(111) reflection shifts slightly to lower scattering angles, and 2) from 0.29 V until the cut-off voltage, the peak decreases in intensity and moves to larger scattering angles (purple to magenta). Note that the voltage value at which the peak starts shifting to larger scattering angles increases during the second and third cycles (0.30 and 0.33 V, respectively). Through delithiation, the intensity is maintained constant, and two main changes are observed, similar to those during lithiation. 1) Below 0.7 V, the Ge(111) shifts to the lower scattering angles (0.68 V for the second lithiation). Upon further delithiation, 2) the peak moves to larger scattering angles.

Analogous changes are observed during the second and third partial lithiation cycles.

To summarize, the diffracted peak shifts to lower scattering angles at the beginning of lithiation and roughly between 0.48 and 0.8 V during delithiation. Conversely, the peak moves to larger scattering angles after ~0.3 V and 0.8 V during lithiation and delithiation, respectively.

A core-shell lithiation mechanism has been reported based on an *in-situ* TEM study on c-Ge Nps[1], where the core corresponds to crystalline Ge and the shell to amorphous Li_xGe. The two-phase process is well known in crystalline Si[19]. However, a significant difference between Si and Ge concerns the boundary between the core and the shell, which is less sharp and isotropic in the case of Ge. We will come back to the Si / Ge comparison later in this chapter.

From the simultaneous changes in the intensity and the lattice parameter, we can access the lithiation and delithiation mechanism in the crystalline Ge core.

3.4.2.2 Quantitative analysis of the partial lithiation

To get quantitative information on the evolution of the crystalline Ge core during the three partial cycles, we performed Rietveld refinement of the scans recorded operando upon cycling, using the TOPAS software. A reduced q-range [q = 1.27–3.77 $Å^{-1}$] is probed to limit the measurement time for each scan. Concerning the Rietveld analysis, different heights have to be considered for the different contributing phases (Be, Ge, Li); this can be done in the programming mode of TOPAS. Moreover, different corrections have to be

applied to the measured intensities to consider the absorption by the Be window and the "finite" thickness of the electrode[20]. Figure 3.8 shows an example of refinement for data recorded before the onset of lithiation.

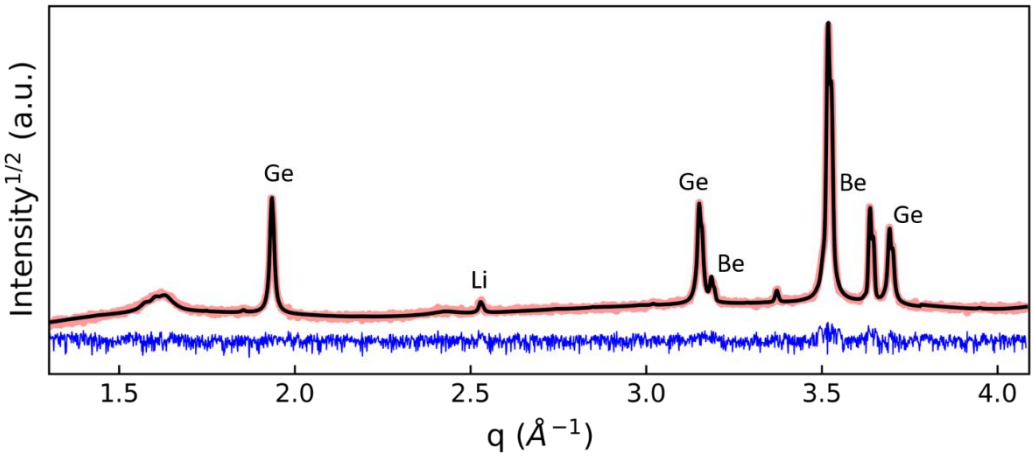

Figure 3.8 Example of Rietveld refinement for a scan recorded in the pristine electrode. The blue line is the difference curve. The intensity is presented in the root squared scale.

The results for the *operando* data are presented in Figure 3.9. Considerations on the coupling between the Ge lattice parameter and the Ge position are presented in the appendix Figure 8.1, to evaluate the reliability of the refined lattice parameter values. They conclude that the presented lattice parameter evolution is real, not an artifact of the refinement procedure.

Figure 3.9 shows the evolution upon time, for the three partial cycles of a) voltage vs. Li/Li^+, b) the intensity (scale factor) normalized to the pristine state, c) strain ε (= $\Delta a/a$) where a_0 is the lattice parameter relative to the pristine state (5.656 ± 0.002 Å). Finally, a simple scheme from successive (de)lithiation steps is presented in d).

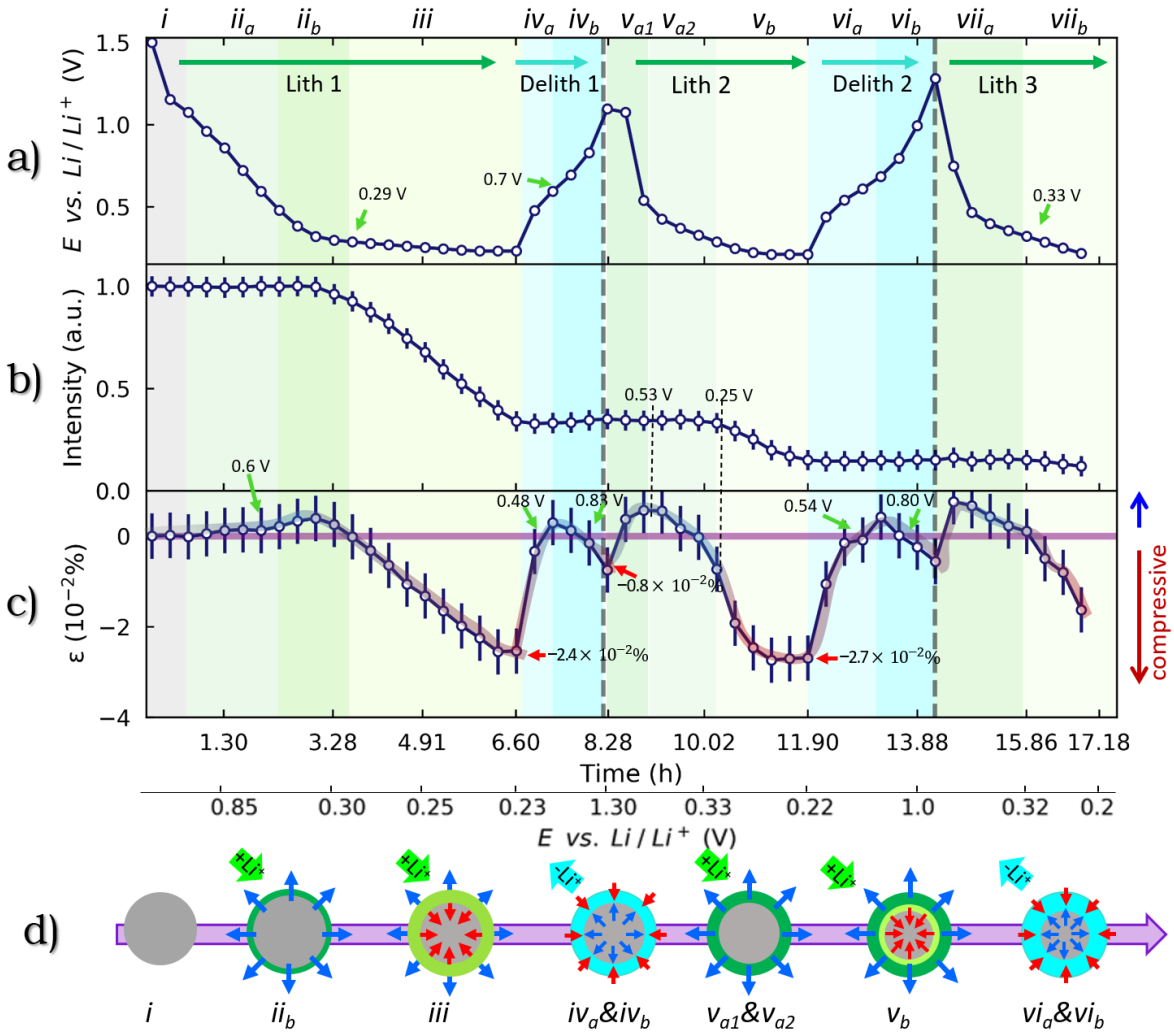

Figure 3.9 a) voltage vs. Li metal, b) Intensity of the Ge Bragg reflections, c) strain in c-Ge Np upon cycling. The figure is colored to highlight the different steps corresponding to compressive or tensile strain upon cycling. d) Scheme of the (de)lithiated changes in a crystalline Ge Np. In the scheme, the blue and red arrows indicate the tensile and compressive states, respectively.

The mechanism is highlighted by different steps (colored areas) from step *i* to *vii*. S*tep i* corresponds to the pristine state.

Step ii_a: the voltage decreases from 1.5 to 0.6 V. At this stage, the intensity and lattice parameter are constant. According to literature, the SEI is formed, impedance studies[21] demonstrate an increase of the SEI resistance, obstructing Ge lithiation. Further work needs to be done on the Ge SEI nature since little is known to date. Different behavior from the observed in Si can be

expected, as c-Ge Nps are less prompt to fracture during lithiation[1], therefore the evolution of the SEI may be reduced.

Step *ii*$_b$: from 0.6 V to 0.29 V, the voltage decreases slightly. The intensity remains mainly constant until 0.3 V. A small tensile strain appears. As the intensity is constant until 0.3 V, we may suppose that the germanium crystallites have not been amorphized. This tensile strain at the very beginning of lithiation is consistent with micro-Raman spectroscopy in Si Nps reported by Zeng *et al.*[22] Two propositions may explain this tensile strain at the very beginning of lithiation. The first one could be the elongation in the Ge–Ge bond distance (the lattice parameter increases) because of Li-ions diffusion in the very outer part of the Ge Nps[8,21,23]. The second possible explanation for the tensile strain, as proposed by Zeng *et al.*[22], could be the lithiation of native Ge oxide, corroborated by the change in the voltage regime (see Figure 3.9a).

Step *iii:* the voltage curve flattens, and the diffraction intensity strongly decreases down to about 30% of the pristine state value. The strain becomes compressive, reaching a magnitude of -2.4×10^{-2}%.

These observations are characteristic of a two-phase reaction mechanism, well known in silicon, the c-Ge core is submitted to compressive stress by the lithiation front. The outer crystalline Ge is transformed into a-Li$_x$Ge. The composition of this lithiated phase could be Li_7Ge_3, as indicated by ^{7}Li NMR (see Figure 3.3a). As mentioned before, the amorphous Li_7Ge_3 phase may show structural heterogeneities, as suggested by the pair lines we attributed to Li_7Ge_3' and Li_7Ge_3'. In the case of an ideal two-phase mechanism, the voltage is expected to remain constant. In our case, the slight slope observed could

indicate difficulty in breaking the crystalline, resulting in heterogeneity in the process and amorphous phases with a greater local disorder.

To summarize, our experiments corroborate a two-phase mechanism by the coexistence of crystalline Ge core and Li_7Ge_3 shell. The lithiation front is applying compressive strain on the c-Ge core. These results are consistent with previous studies[8].

Step iv_a and iv_b: Delithiation. The reversal of the current stops the progression of the lithiation front, and the diffraction intensities for the remaining c-Ge core are constant. Two steps are observed during delithiation: iv_a and iv_b. At the very beginning of delithiation up to 0.48 V (iv_a), strain relaxation is observed with an increase of the lattice parameter up to a value slightly above the reference one, thus associated with a slightly tensile state. Then iv_b, at 0.7 V, the voltage corresponding to the inflection point on the voltage curve, the lattice parameter decreases again down to a compression $-0.8 \times 10^{-2}\%$. The strain is compressive probably due to the remaining amorphous Ge shell that constrains the crystalline Ge core, as similarly reported in crystalline Si Nps coated with a polypyrrole thin layer [24].

The decreasing quantity of Li-ions in the a-Li_7Ge_3 shell may explain the crystalline Ge core decompression at the strain relaxation step (iv_a). This strain relaxation has been observed in Ge thin films[25,26] and core hollow Si Nps[27]. In the latter case, the authors explained the decompression during delithiation, referring to the wave-propagation-like motion, which is identical to a cause-effect trend. The continuous motion explains the tensile stress

applied to the core due to compression in the outermost part of the shell, resulted from the delithiation process.

Concerning the c-Ge lattice compression, which occurs at the end of delithiation, a similar behavior was observed by Tardif *et al.* with Si Nps[28]. However, both materials show differences; this will be further discussed in the following section.

Second partial lithiation. As current is reversed, the lattice parameter increases due to Li diffusion into the outer part of the Nps (υ_{a1}). The crystal lattice begins to contract with the lithiation of a-Ge (υ_{a2}), and then the c-Ge, accompanied by a decrease in the diffracted intensity (υ_b). The second lithiation of c-Ge occurs at a potential lower than for the first cycle (0.25 V vs. 0.29 V) due to the presence of the a-Ge shell, which begins to lithiate. At the end of the second lithiation, the intensity of the Ge diffraction peaks represents about 20% of the intensity in the pristine state. The compressive strain reached at the end of the second lithiation is similar to the one observed at the end of the first cycle. Another difference with the first cycle is the non-linear dependence of the strain vs. voltage, revealing a possible non-uniform deformation during the second lithiation.

Step vi-vii. These steps are remarkably similar to the one observed for the previous cycle. This result highlights the high reversibility of the mechanism involved in the lithiation of Ge due to its mechanical properties and conductivity.

From the detailed study of the various steps, we can draw several conclusions. Firstly, the crystalline Ge structural changes are characteristic and depend on (de)lithiation voltage. In fact, the variations of the strain are cyclic; that is, the same tendency is observed in consecutive cycles, reaching almost similar compressive stress values at the end of lithiation.

3.4.2.3 c-Ge vs. c-Si comparison of the (de)lithiation strain behaviors

As already mentioned, Tardif[28] investigated the (de)lithiation mechanism in crystalline Si Nps of about 100 nm in diameter, which is close to our Ge particle size. In the following, we will compare Si and Ge behaviors.

For both compounds, the maximum compressive strain is observed at the end of the lithiation (second lithiation for Si with $\varepsilon_{min} = -0.12\times 10^{-2}\%$) while for Ge, the different cycles are mainly equivalent ($\varepsilon_{min} = -2.6\times 10^{-2}\%$). The maximum tensile strain at the beginning of the second lithiation (and a subsequent one for Ge) is also much larger for Si ($\varepsilon_{max} = +7.0\times 10^{-2}\%$) than for Ge ($\varepsilon_{max} = +2.6\times 10^{-2}\%$). Considering the bulk modulus (B_{Ge} = 77.2 GPa[29], B_{Si} = 98 GPa[28]), the hydrostatic compressive stress on the core $\sigma = 3B\varepsilon$ is about 60 MPa and 350 Mpa for Ge and Si, respectively. The lower compression value for Ge is consistent with results obtained using the curvature method on Ge and Si thin films[25,26,30].

We compare the strain behavior of Ge (Figure 3.9) with Si (Figure 8.2, see appendix) adapted from Tardif *et al.*[28]. The most striking feature concerns the

Si limited strain relaxation in delithiation, while Ge strain relaxation is wholly released, varying from compressive to tensile (*step iv* and *step vi*).

Besides, the Ge strain dependence against potential is cyclic. In contrast, the changes of Si strain upon voltage are clearly distinct from the first to the second cycle. This difference is a clear indication of the improved Li-ion diffusion in Ge.

Considering reported computational studies that examine the differences in the lithiation mechanism for c-Si and c-Ge[31,32], we can consider that the origin of their different behavior lies in the stronger Li–Si interaction and the stiffer Si lattice, responsible for the reduced Li-ion mobility (D_{Li} = 10^{-13} cm^2s^{-1})[31,32]. Li-ions diffusion is reported to depend on the Li concentration in the amorphous lithiated phases (a-LixSi). In contrast, studies reported in Ge show a higher Li-ion diffusion and less Li concentration dependence (DLi = 10^{-11} cm^2s^{-1}) because of the facile rearrangements of host Ge atoms at the early stages of lithiation[31]. This is consistent with the difference in the values of the hydrostatic compressive stress generated by the lithiation front in the two compounds, and on the other hand, with the observed different lattice relaxations during the delithiation. Our results are in line with computational findings since the strain changes are an indirect demonstration of lithium-ion diffusion in both systems.

We speculate that the relaxation of strain during the delithiation of Ge is based on the Li*x*Ge shell properties. The weaker Li–Ge interactions and the independence of Li-ions diffusion with the Li concentration in the a-Li*x*Ge

phases contribute to higher Li-ion mobility, causing lower stress in Ge, contrary to Si.

To summarize, our results on the partial lithiation of Ge show a different (de)lithiation mechanism to that of Si. Three main differences are recognized. First, the changes of strain versus potential c-Ge Nps are recurrent over cycles, contrary to Si. Second, higher values of hydrostatic compressive stress are found at the lithiation for Si. Finally, during delithiation, the compressive strain for c-Ge Nps is released, turning to tensile, while for Si, it is released but is kept compressive.

3.4.3 Complete lithiation: formation of highly lithiated phases

After the third partial cycle, we performed a full lithiation until 0.005 V at C/10 to follow crystalline lithiated germanium phases and their structural modification during the cycle. Figure 3.10a shows the evolution of the diffraction pattern of the Ge-based electrode during the fourth electrochemical cycle. For clarity, in the electrochemical curve, time (y-axis) is replaced by voltage vs. Li/Li^+. Figure 3.10b is an enlarged view of the peaks attributed to the c-$Li_{15}Ge_4$ phase.

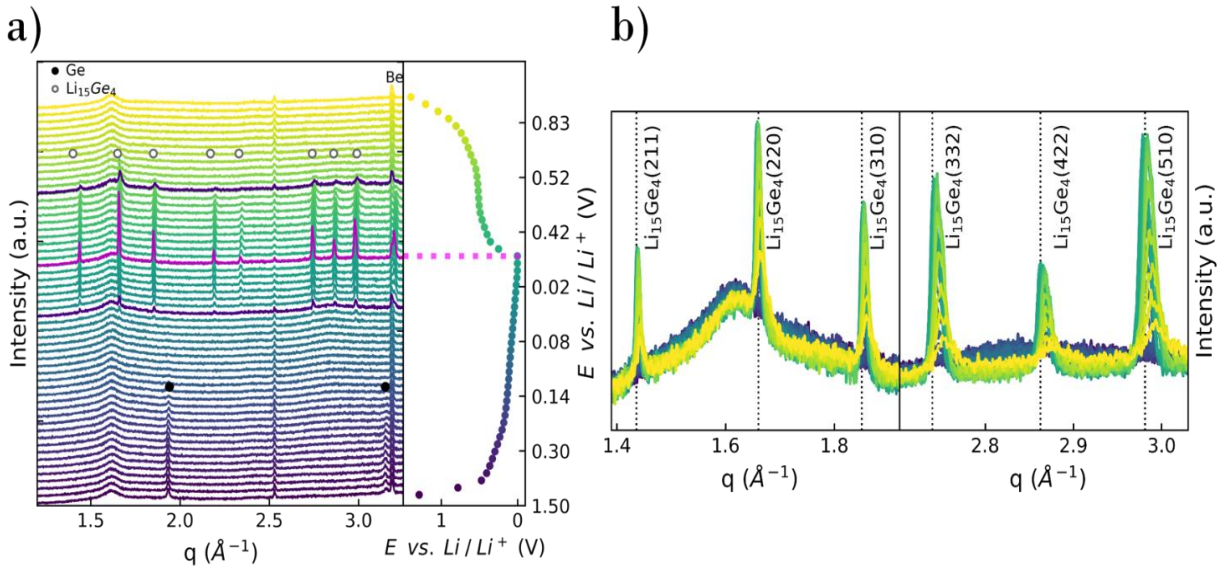

Figure 3.10 a) left: *operando* XRD patterns, right: electrochemical cycling during the complete lithiation at the fourth cycle for the c-Ge Nps. b) Enlarged view of the c-$Li_{15}Ge_4$ diffracted peaks.

3.4.3.1 A qualitative description of the changes in the fourth cycle

During the lithiation at the 4th cycle, the Ge peaks disappear at 0.143 V. Then, at ~0.042 V, only peaks corresponding to the c-$Li_{15}Ge_4$ phase emerges. The formation of this phase at the end of complete lithiation is consistent with other *operando* XRD studies[4,17].

In between the amorphization of c-Ge and the growth of c-$Li_{15}Ge_4$, two bumps at 1.62 and 2.82 Å emerge at ~0.125 V (see bumps in violet, Figure 3.10b). We fitted the large-q bump to get a quantitative indication of the bump evolution (see Figure 3.11a). Figure 3.11c presents the cycling time dependence of the bump integrated intensity, with the corresponding voltage values. The dashed cyan line is a guide for the eye. A green square in Figure 3.11b highlights the voltage zone in which the bumps appear during the fourth cycle. The maximum intensity is observed for voltages close to 0.08 V.

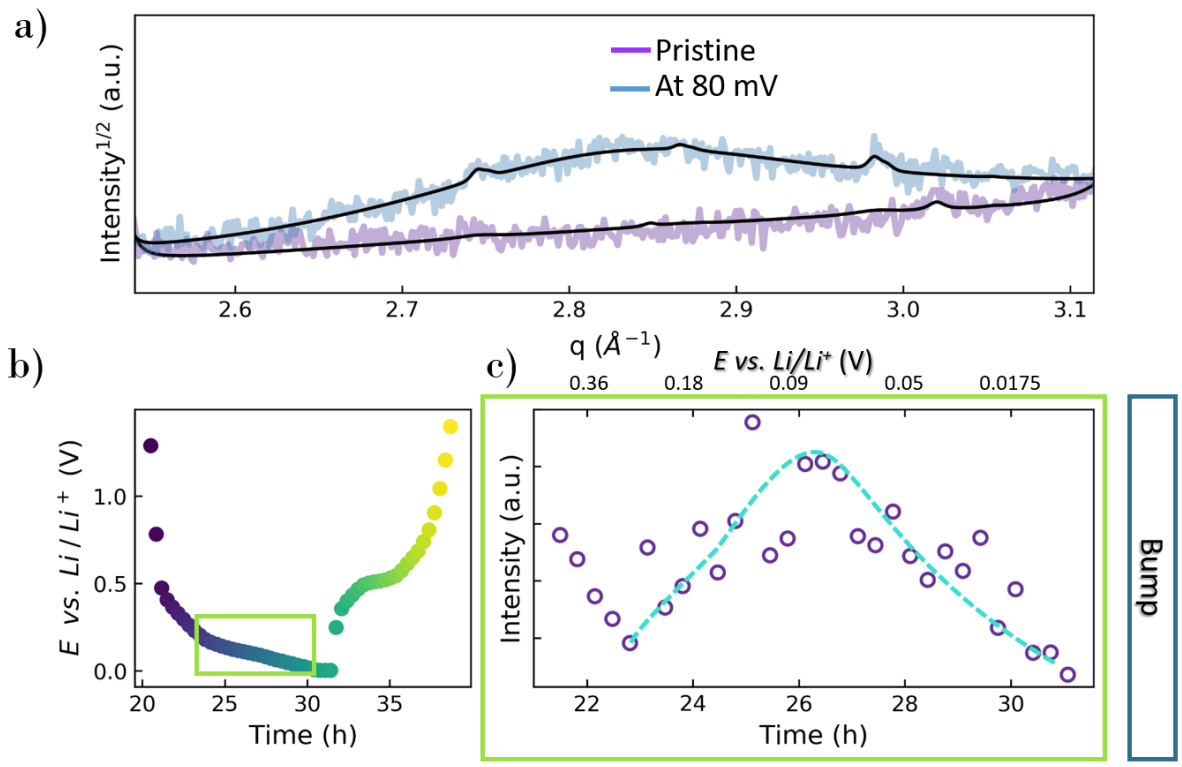

Figure 3.11 a) diffracted pattern of the bump at high q-values and the resulted fit (black). c) intensity vs. time resulted from the single peak fitting of the bump, highlighting the b) voltage vs. time zone where it varies in the corresponding forth complete cycle.

The nature of these bumps could be disentangled thanks to the ^{7}Li-NMR spectra measured at 80 mV during lithiation (see Figure 3.3b). The dominant phase at this voltage is the a-Li_7Ge_2. We can reasonably consider that the bumps present in the XRD data correspond to the phase Li_7Ge_2, before the appearance of c-$Li_{15}Ge_4$, which is presumably in a well-formed environment at short distances. Jung *et al.* [8] suggested that the 0.25–0.150 V potential region where the bumps are formed is highly sensitive to the electrochemical cycling settings due to several thermodynamically stable structures with similar energies that can be formed[10].

The diffraction peaks associated with the crystalline $Li_{15}Ge_4$ phase appear closed to 0.042 V. The second dQ/dV peak during lithiation suggests that $Li_{15}Ge_4$ may be formed at 0.15 V (Figure 3.2b). Nonetheless, the $Li_{15}Ge_4$ peaks

emerge later at 0.042 V. This fact suggests that the disorganization of the system at voltages between 0.25–0.15 V could delay the formation of the crystalline $Li_{15}Ge_4$ phase.

To get quantitative information on $Li_{15}Ge_4$ structural evolution, we performed Rietveld refinement of the data recorded *operando*. The results are shown in Figure 3.12. Examples of the diffracted patterns and Rietveld refinement profiles are shown in the appendix, Figure 8.3.

3.4.3.2 $Li_{15}Ge_4$ formation and evolution

Figure 3.12 shows the results from Rietveld refinement on the $Li_{15}Ge_4$ phases when they (dis)appear. Specifically, a) voltage vs. Li/Li^+ b) intensity, c) the lattice parameter and d) distortion. In Figure 3.12, the different background colors correspond to different stages in the evolution of c-$Li_{15}Ge_4$. The cyan horizontal line indicates the lattice parameter for c-$Li_{15}Ge_4$ reported in ICSD 43689.

Step i. Formation of c-$Li_{15}Ge_4$. From ~0.042 V during lithiation, the $Li_{15}Ge_4$ Bragg reflections increase gradually. The refined lattice parameter value of freshly formed c-$Li_{15}Ge_4$ is a = 10.777(2) Å. Indicatively, it can be compared to the reported value a = 10.783 Å (ICSD 43689). The evaluation of the crystallite size and lattice distortion evidences a rapid increase in size up to at least 100 nm. However, the size cannot be reliably determined as the peak broadening appears to be dominated by the distortion contribution, shown in Figure 3.12d.

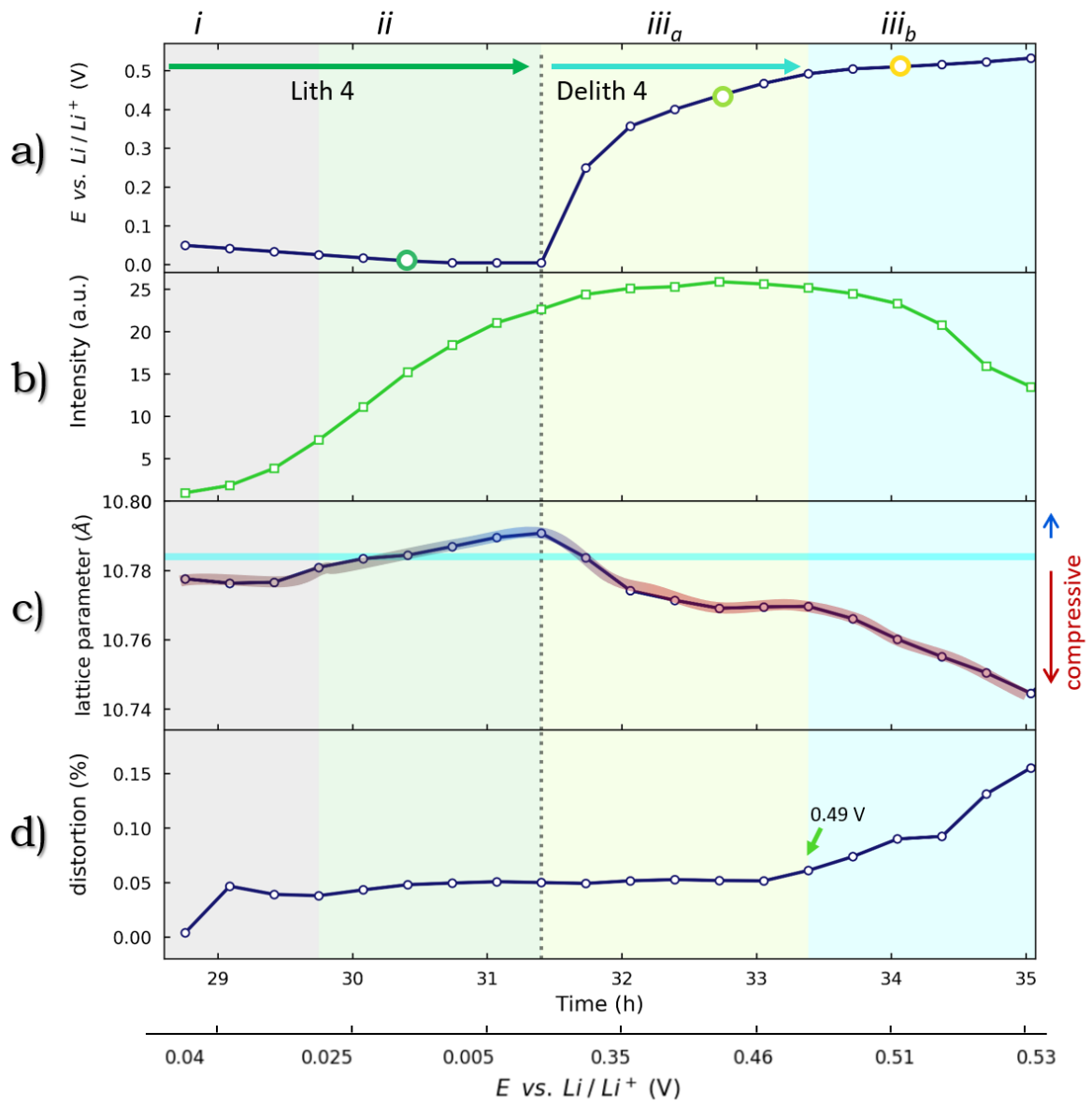

Figure 3.12 a) voltage vs. Li/Li+ during the (dis)appearance of $Li_{15}Ge_4$. b) Intensity (normalized), c) Lattice parameter, and d) distortion. The figure is colored depending on the different steps corresponding to lattice parameter changes upon cycling. The cyan line in d) corresponds to the lattice parameter (10.783(2) Å), reported in ICSD 43689. The big markers represent chosen diffracted patterns to illustrate the broadening of the $Li_{15}Ge_4$(510) while cycling.

Step ii. End of Lithiation, complete formation of c-$Li_{15}Ge_4$. A rapid growth of the diffraction intensity is observed between 0.025 V and the cut-off potential (0.005 V). The lattice parameter increases up to 10.791 (5) at the very end of lithiation. Similar behavior has been reported by Jung *et al.*, who observed an increase in the c-$Li_{15}Ge_4$ lattice parameter at the cut-off potential[8]. Similarly, the distortion slightly increases. Figure 3.13a shows an example of

$Li_{15}Ge_4$(510) Bragg reflection recorded at 0.025 V with an FWHM of 0.004 $Å^{-1}$. In contrast to our results, *ex-situ* XRD experiments reported a broad $Li_{15}Ge_4$(510) Bragg reflection at the very formation (0.023 $Å^{-1}$)[8].

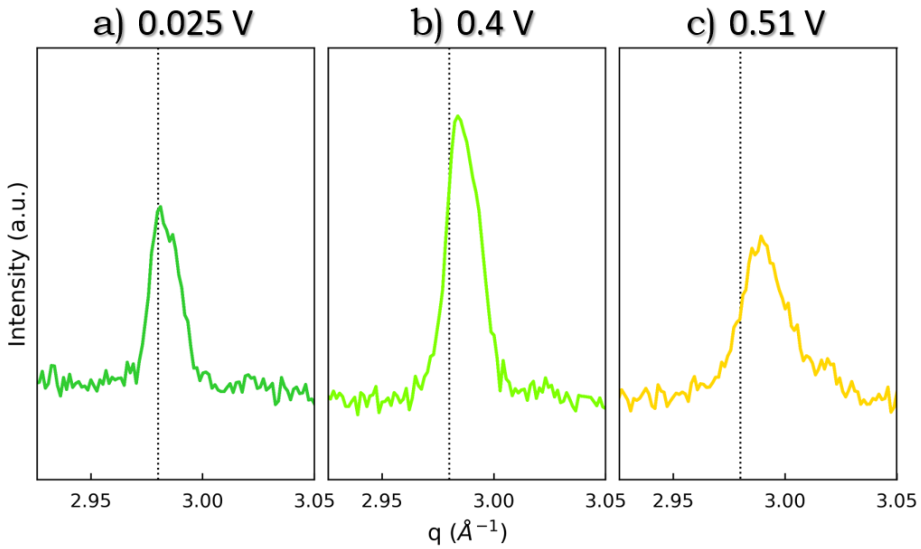

Figure 3.13 intensity vs. q for the $Li_{15}Ge_4$(510) at the selected state of charge, illustrating the evolution of the c-$Li_{15}Ge_4$.

Step iiia. During the beginning of delithiation until 0.49 V, the voltage increases rapidly. c-$Li_{15}Ge_4$ is still forming, as indicated by the slightly increasing intensity. After a decrease, the lattice parameter values stabilize to 10.77 Å. The distortion remains mainly constant, as shown by the stable FWHM (see Figure 3.13b).

The still increasing diffraction intensity indicates that this crystalline structure is thermodynamically stable during delithiation and the delithiation of this phase, e.g., conversion into less lithiated phases, happens later in potential during delithiation. The acquired ^{7}Li NMR spectra at 300 mV provide more information on the delithiation mechanism (see Figure 3.4b). Here, we observe that the amorphous $Li_{15}Ge_4$ phase has disappeared, and the crystalline $Li_{15}Ge_4$ has increased in intensity.

Step iiib From 0.49 V to 0.52 V, a voltage plateau is observed in the electrochemistry. The diffraction intensities decrease, indicating the progressive disappearance of c-$Li_{15}Ge_4$, the lattice experiences again compressive strain together with an increased distortion (see Figure 3.13c, the diffraction peak broadening at 0.51 V).

The plateau in voltage indicates that the disappearance of crystalline $Li_{15}Ge_4$ follows a two-phase mechanism, where it is supposed to transform into a less lithiated phase. However, in this study, we did not obtain a less crystalline lithiated phase. More information on the amorphous phase could be obtained from the acquired ^7Li NMR spectra at 490 mV (see Figure 3.4c). We observed in Figure 3.4c that the Li_7Ge_3 phase dominates at this voltage, indicating that probably, the c-$Li_{15}Ge_4$ is transforming into amorphous Li_7Ge_3 during delithiation.

Considering the diffraction intensity from the c-Ge phase at the pristine state and the intensity (scale factor) from c-$Li_{15}Ge_4$ at the end of lithiation and close to 0.42 V, we estimated the fraction of Ge atoms which transforms into $Li_{15}Ge_4$. This estimation can be calculated considering that the number of unit cells of a given diffracting crystalline phase is proportional to the product of the Rietveld refined scale factor multiplied by the unit cell volume. The fraction of Ge atoms in c-$Li_{15}Ge_4$ is then given by the following Equation 3.1:

$$f^{Ge}_{Li_{15}Ge_4} = \frac{S_{Li_{15}Ge_4} \times V_{Li_{15}Ge_4} \times N_{Li_{15}Ge_4}}{S_{Ge} \times V_{Ge} \times N_{Ge}}$$

Equation 3.1

Where $S_{Li_{15}Ge_4}$ and S_{Ge} correspond to the Rietveld refined scale factors. $V_{Li_{15}Ge_4}$ and V_{Ge} are the volume of the unit cell in Å^3. $N_{Li_{15}Ge_4}$ and N_{Ge} are the number of Ge atoms in the corresponded unit cell.

At the end of lithiation, we obtain $f^{Ge}_{Li_{15}Ge_4} = 52 \pm 15\%$, and at 0.42 V, $f^{Ge}_{Li_{15}Ge_4} = 59 \pm 15\%$. We have already mentioned that the data have to be corrected for the finite thickness of the electrode, knowing its density. These corrections have a non-negligible influence on the fitted value of the scale factor. However, for this experiment, the thickness and density are not precisely known (this is a point that needs to be improved in the future). Hence the large uncertainty on $f^{Ge}_{Li_{15}Ge_4}$.

To gain insights into the remaining percentage that was not converted into the crystalline phase, we consider the acquired ^{7}Li NMR spectra recorded at 5 mV during lithiation (see Figure 3.3c). The dominant lines at 8.1 and −13.6 ppm (cyan and olive) were attributed to the amorphous and crystalline $Li_{15}Ge_4$, respectively. Thus, one can assume that the remaining Ge atoms form a-$Li_{15}Ge_4$. These results indicate that the fully lithiated electrode is heterogeneous, mainly composed of crystalline and amorphous $Li_{15}Ge_4$. The relative proportions of those phases likely depend on the electrochemical cycling conditions, which we speculate is expected since it is probable that complete formation of the crystalline $Li_{15}Ge_4$ might require special conditions to equilibrate thermodynamically.

Interestingly the diffraction intensity from c-$Li_{15}Ge_4$ still increases at the beginning of the delithiation. This result is consistent with NMR results.

Indeed, the comparison of the spectra measured with the cycled samples stopped in the delithiation stage at 5 mV and 300 mV (see Figure 3.4b) evidences a higher proportion of c-$Li_{15}Ge_4$ at the higher potential, indicating a progressive crystallization. Unfortunately, more information is needed to understand the mechanism of this increase in crystallization and disentangle from which phase the extra c-$Li_{15}Ge_4$ amount is formed. Complemented information in this regard would be interesting.

Another remarkable aspect of the $Li_{15}Ge_4$ evolution is the non-linear evolution of the lattice parameter upon potential.

According to computational studies on the mechanical properties of Si[23,33], Ge[33], and $Li_{15}Si_4$[34–36], silicon suffers a transition from brittle to ductile with the increase of Li content alloyed in the crystal structure. It appears that the ductile properties of $Li_{15}Si_4$ occur from the increased quantity of Li–Li bonds[34,35], which can tolerate significant strain before breaking. The metallic Li–Li bond strength is weaker than the hard covalent Si–Si bonds, producing elastic softening of the structure.

Comparing the bulk modulus of Si and Ge, the reported studies show that Si is more difficult to lithiate[33]. Upon lithiation, Li-Ge tends to be more flexible than Li–Si [33,37]. However, for the high lithiated phases such as $Li_{15}Ge_4$ and $Li_{15}Si_4$, the amount of Ge–Ge or Si–Si bonds are so small that the mechanical differences become smaller because the Li–Li bonds are dominant. Consequently, both $Li_{15}Ge_4$ and $Li_{15}Si_4$ lattices are expected to be highly flexible and easily accommodate the compressive strain, presenting a non-

linear stress behavior upon electrochemical cycling and facilitating the Li-ion removal during delithiation. We observe a particular lattice parameter evolution that could be linked to strain exerted on the crystallite, which is non-linear upon (de)lithiation. The lattice parameter evolution in the $Li_{15}Ge_4$ crystallite could be for the phase to withstand deformation because of its high amount of Li–Li bonds that can tolerate significant strain before breaking.

Concerning our results, the existence of the $Li_{15}Ge_4$ phase has been identified at a specific voltage regime that goes from near the end of lithiation up to ~0.52 V at high voltages. At the beginning of the delithiation, the crystalline lattice is compressed and then stabilizes likely into the amorphous Li_7Ge_2 phase.

3.5 Conclusion

This chapter presents a detailed study of the (de)lithiation mechanisms at play in Ge Nps submitted to partial and complete lithiation, combining *operando* XRD and *post-mortem* ^{7}Li NMR to describe the structural changes of the system.

The investigation of a complete lithiation of Ge allowed us to correlate structural and electrochemical behaviors. Indeed, the voltage value of the first dQ/dV lithiation peak corresponds to the one at which the c-Ge starts to be amorphized (0.3 V).

Then, we performed partial lithiation cycles to study the c-Ge deformation and compare it with c-Si Nps. We evaluate that the hydrostatic compressive stress

exerted on the crystalline core at the end of lithiation is of the order of 60 MPa for Ge Nps while it reaches 350 MPa in the second cycle for Si Nps. The most striking difference concerns the very limited strain release in the first stage of the delithiation for silicon, while the Ge lattice relaxation is complete. Consequently, the Ge strain evolution is very similar from one cycle to another, while Si lattice strain strongly increases upon cycling. This result has a direct impact on the cyclability.

Finally, the complete lithiation performed after three partial cycles evidenced the formation of the c-$Li_{15}Ge_4$ phase, in contrast with Si, for which the corresponding $Li_{15}Si_4$ phase is metastable in the case of nanoparticles. We showed that this phase is thermodynamically stable and disappears during delithiation. The slight changes in the c-$Li_{15}Ge_4$ diffracted peaks related to strain and distortion led us to suppose that this phase is highly flexible.

According to both *operando* XRD and *post-mortem* ^{7}Li NMR, we can identify the following (de)lithiation mechanism in Equation 3.2.

$$c-Ge\ Nps \rightarrow c-Ge + a-Li_7Ge_3 \rightarrow a-Li_7Ge_3 + a-Li_7Ge_2$$
$$\rightarrow a-Li_7Ge_2 + a-Li_{15}Ge_4 \rightarrow a-Li_{15}Ge_4 + c-Li_{15}Ge_4$$
$$\rightarrow a-Li_7Ge_2 + a-Li_7Ge_3$$

Equation 3.2

Finally, our work presents essential findings on the electrochemical cycling of c-Ge Nps, highlighting major differences with Si Nps. We believe that our detailed results could support computational studies on the mechanical properties of Si and Ge-based electrodes. They highlight the major role of the mechanical properties, based on the clear correlation between the cyclability

performances and the degree of strain release achievable by the crystalline lattice. These uncovered structural and mechanical mechanisms will have an important implication in the designing of Si and Ge based negative electrodes to mitigate pulverization and improve structural stability.

3.6 Bibliography

1. Liang, W. *et al.* Tough Germanium Nanoparticles under Electrochemical Cycling. *ACS Nano* **7**, 3427–3433 (2013).

2. Fuller, C. S. & Severiens, J. C. Mobility of Impurity Ions in Germanium and Silicon. *Phys. Rev.* **96**, 21–24 (1954).

3. Holder, C. F. & Schaak, R. E. Tutorial on Powder X-ray Diffraction for Characterizing Nanoscale Materials. *ACS Nano* **13**, 7359–7365 (2019).

4. Loaiza, L. C. *et al.* Electrochemical Lithiation of Ge: New Insights by Operando Spectroscopy and Diffraction. *J. Phys. Chem. C* **122**, 3709–3718 (2018).

5. Rodríguez-Carvajal, J. Recent Developments of the Program FULLPROF. *Comm. Powder Diffr. Newsl.* 12–19 (2011).

6. Kim, T.-H., Song, H.-K. & Kim, S. Production of germanium nanoparticles via laser pyrolysis for anode materials of lithium-ion batteries and sodium-ion batteries. *Nanotechnology* **30**, 275603 (2019).

7. Huggins, R. A. Principles Determining the Voltages and Capacities of Electrochemical Cells. in *Advanced Batteries* 25–39 (Springer US, 2008). doi:10.1007/978-0-387-76424-5_2

8. Jung, H. *et al.* Elucidation of the Local and Long-Range Structural Changes that Occur in Germanium Anodes in Lithium-Ion Batteries. *Chem. Mater.* **27**, 1031–1041 (2015).

9. Balaya, P. *et al.* Nano-Ionics in the Context of Lithium Batteries. *J. Power Sources* **159**, 171–178 (2006).

10. Morris, A. J., Grey, C. P. & Pickard, C. J. Thermodynamically Stable Lithium Silicides and Germanides from Density Functional Theory Calculations. *Phys. Rev. B* **90**, 054111(1–10) (2014).

11. Tang, W. *et al.* Probing Lithium Germanide Phase Evolution and Structural Change in a Germanium-in-Carbon Nanotube Energy Storage System. *J. Am. Chem. Soc.* **137**, 2600–2607 (2015).

12. Key, B. *et al.* Real-Time NMR Investigations of Structural Changes in Silicon Electrodes for Lithium-Ion Batteries. *J. Am. Chem. Soc.* **131**, 9239–9249 (2009).

13. Key, B., Morcrette, M., Tarascon, J. & Grey, C. P. Pair Distribution Function

Analysis and Solid-State NMR Studies of Silicon Electrodes for Lithium-Ion Batteries: Understanding the (De)lithiation Mechanisms. *J. Am. Chem. Soc.* **133**, 503–512 (2011).

14. Ogata, K. *et al.* Revealing Lithium–Silicide Phase Transformations in Nano-Structured Silicon-Based Lithium-Ion Batteries Via In-Situ NMR Spectroscopy. *Nat. Commun.* **5**, 3217(1–11) (2014).

15. Loaiza, L. C. *et al.* Understanding the Lithiation/Delithiation Mechanism of Si1-xGex Alloys. *J. Mater. Chem. A* **5**, 12462–12473 (2017).

16. Leriche, J. B. *et al.* An Electrochemical Cell for Operando Study of Lithium Batteries Using Synchrotron Radiation. *J. Electrochem. Soc.* **157**, A606–A610 (2010).

17. Lim, L. Y., Liu, N., Cui, Y. & Toney, M. F. Understanding Phase Transformation in Crystalline Ge Anodes for Li-Ion Batteries. *Chem. Mater.* **26**, 3739–3746 (2014).

18. Cortes, F. J. Q., Boebinger, M. G., Xu, M., Ulvestad, A. & McDowell, M. T. Operando Synchrotron Measurement of Strain Evolution in Individual Alloying Anode Particles within Lithium Batteries. *ACS Energy Lett.* **3**, 349–355 (2018).

19. Liu, X. H. *et al.* Size-dependent fracture of silicon nanoparticles during lithiation. *ACS Nano* **6**, 1522–1531 (2012).

20. Rowles, M. R. & Buckley, C. E. Aberration corrections for non-Bragg–Brentano diffraction geometries. *J. Appl. Crystallogr.* **50**, 240–251 (2017).

21. Zhu, B. *et al.* Minimized Lithium Trapping by Isovalent Isomorphism for High Initial Coulombic Efficiency of Silicon Anodes. *Sci. Adv.* **5**, eaax0651(1–8) (2019).

22. Zeng, Z. *et al.* In-Situ Measurement of Lithiation-Induced Stress in Silicon Nanoparticles Using Micro-Raman Spectroscopy. *Nano Energy* **22**, 105–110 (2016).

23. Zhao, K. *et al.* Lithium-Assisted Plastic Deformation of Silicon Electrodes in Lithium-Ion Batteries: A First-Principles Theoretical Study. *Nano Lett.* **11**, 2962–2967 (2011).

24. Luo, L. *et al.* Surface Coating Constraint Induced Self-Discharging of Silicon Nanoparticles as Anodes for Lithium Ion Batteries. *Nano Lett.* **15**, 7016–7022 (2015).

25. Pharr, M., Choi, Y. S., Lee, D., Oh, K. H. & Vlassak, J. J. Measurements of Stress and Fracture in Germanium Electrodes of Lithium-Ion Batteries during Electrochemical Lithiation and Delithiation. *J. Power Sources* **304**, 164–169 (2016).

26. Wang, X., Yang, A. & Xia, S. Fracture Toughness Characterization of Lithiated Germanium as an Anode Material for Lithium-Ion Batteries. *J. Electrochem. Soc.* **163**, A90–A95 (2016).

27. Xiao, Q. *et al.* Inward Lithium-Ion Breathing of Hierarchically Porous Silicon

Anodes. *Nat. Commun.* **6**, 8844 (2015).

28. Tardif, S. *et al.* Operando Raman Spectroscopy and Synchrotron X-ray Diffraction of Lithiation/Delithiation in Silicon Nanoparticle Anodes. *ACS Nano* **11**, 11306–11316 (2017).

29. Wei, S., Allan, D. C. & Wilkins, J. W. Elastic constants of a Si/Ge superlattice and of bulk Si and Ge. *Phys. Rev. B* **46**, 12411–12420 (1992).

30. Al-Obeidi, A., Kramer, D., Mönig, R. & Thompson, C. V. Mechanical Stresses and Crystallization of Lithium Phosphorous Oxynitride-Coated Germanium Electrodes during Lithiation and Delithiation. *J. Power Sources* **306**, 817–825 (2016).

31. Chou, C.-Y. & Hwang, G. S. On the Origin of the Significant Difference in Lithiation Behavior between Silicon and Germanium. *J. Power Sources* **263**, 252–258 (2014).

32. Chou, C.-Y. & Hwang, G. S. On the Origin of Anisotropic Lithiation in Crystalline Silicon over Germanium: a First-Principles Study. *Appl. Surf. Sci.* **323**, 78–81 (2014).

33. Chou, C.-Y., Kim, H. & Hwang, G. S. A Comparative First-Principles Study of the Structure, Energetics, and Properties of Li–M (M = Si, Ge, Sn) Alloys. *J. Phys. Chem. C* **115**, 20018–20026 (2011).

34. Wang, H., Wang, X., Xia, S. & Chew, H. B. Brittle-to-ductile Transition of Lithiated Silicon Electrodes: Crazing to Stable Nanopore Growth. *J. Chem. Phys.* **143**, 104703 (1–7) (2015).

35. Shenoy, V. B., Johari, P. & Qi, Y. Elastic Softening of Amorphous and Crystalline Li-Si Phases with Increasing Li Concentration: a First-Principles Study. *J. Power Sources* **195**, 6825–6830 (2010).

36. Darbaniyan, F., Yan, X. & Sharma, P. An Atomistic Perspective on the Effect of Strain Rate and Lithium Fraction on the Mechanical Behavior of Silicon Electrodes. *J. Appl. Mech.* **87**, 031011(1–7) (2020).

37. Li, K. *et al.* From Chemistry to Mechanics: Bulk Modulus Evolution of Li–Si and Li–Sn Alloys via the Metallic Electronegativity Scale. *Phys. Chem. Chem. Phys.* **15**, 17658 (2013).

Chapter 4

De(lithiation) mechanism of $Si_{100-x}Ge_x$ alloys

4.1 Introduction

Even though germanium as an active material for Li-ion batteries has received less attention than silicon, it presents remarkable advantages, such a better conductivity and Li-ion diffusivity because of its small bandgap and less rigid lattice. Moreover, the lithiation of crystalline germanium is mainly isotropic, conferring better stability in the electrode. Combining Ge with Si at controllable compositions has shown to be an appealing approach to address cycling problematics in metalloid-based anodes since it improves the Li diffusivity and contributes to better strain accommodation.

Our collaborators in CEA-Iramis synthesized by laser pyrolysis three batches of $Si_{100-x}Ge_x$ alloy crystalline nanoparticles differing by the amount of germanium, as well as pure Si and Ge Nps. Details on the experimental conditions are provided in section 2.1.1. Alloys with different Ge contents were obtained by varying the gas ratio of silane vs. germane, resulting in three different powder batches, Si-rich, Ge-rich, and almost equal in composition (Si≈Ge) alloys.

Besides, our collaborators prepared electrodes and measured the cycling performance using the mentioned particles cycled between 1 and 0.01 V vs. Li metal at C/20. Figure 4.1 shows the specific charge capacity results for the three different SiGe alloys maintained during the 60 cycles (see red, blue, and green dots in Figure 4.1a). Moreover, the capacity is better retained when increasing C-rates from C/5 to 5C for the SiGe alloys than for pure-Si (Figure 4.1b). This improved retained capacity at high C-rates has also been reported for nanostructured $Si_{100-x}Ge_x$ thin-films[1] and Nws[2].

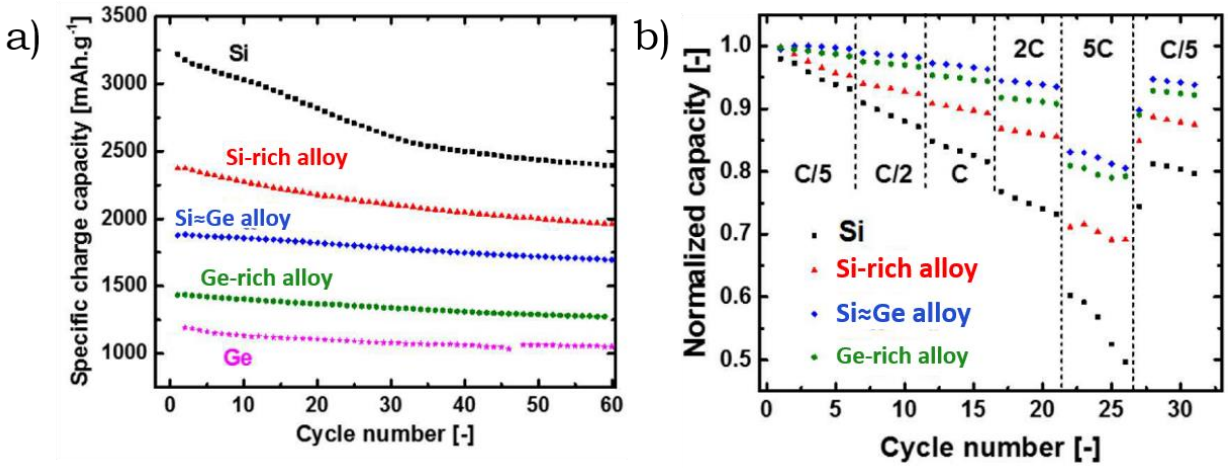

Figure 4.1 a) specific charge capacity vs. cycle number of the $Si_{100-x}Ge_x$ alloys Nps at C/20 compared to Si and Ge. b) normalized capacity vs. cycle number of the $Si_{100-x}Ge_x$ alloys Nps at increasing C-rates, adapted from [3].

Given the good electrochemical performance of the SiGe alloys, we decided to investigate the (de) lithiation mechanisms of these crystalline $Si_{100-x}Ge_x$ Nps and compare them to pure Si and pure Ge Nps.

We first characterized the morphology and structure of the pristine powders. As the SiGe alloy powders obtained by laser pyrolysis are heterogeneous in size and composition, we combined different techniques such as XRD, TEM EDX, and Raman spectroscopy. Then electrodes were prepared to investigate electrochemical cycling using in-lab and synchrotron *operando* X-ray

diffraction experiments. We followed the amorphization of the crystalline $Si_{100-x}Ge_x$ Nps and the formation and disappearance of $Li_{15}(Si_{100-x}Ge_x)_4$ and correlated these structural changes with electrochemical cycling studies.

Considering pure Si and Ge Nps as references, we investigated the influence of Ge content on the $Si_{100-x}Ge_x$ amorphization process and the formation of $Li_{15}(Si_{100-x}Ge_x)_4$.

For this study, I benefitted from the inputs of our collaborators who synthesized the nanoparticles and were in charge of Raman scattering and electron microscopy characterizations on the different pristine powders.

4.2 Characterization of $Si_{100-x}Ge_x$ and Si pristine powders

4.2.1 Morphological and structural characterization

As already mentioned, the $Si_{100-x}Ge_x$ powders are polydisperse in size, composition, and structure. Thus, it is necessary to analyze them using different techniques to obtain a detailed description of their complex nature, such as Raman spectroscopy, XRD, and advanced electron microscopy.

4.2.1.1 *Raman spectra for Ge, $Si_{100-x}Ge_x$ alloys, and Si Nps pristine powders*

Our collaborators in CEA-Iramis acquired Raman spectra on the pristine powders using a Horiba XploRA PLUS with a 532 nm Ar^+ laser and a power of 0.79 mW cm^{-2}. Figure 4.2 shows the Raman spectra evolution of the signatures for Si, Ge, and SiGe at 521, 298, and 385 cm^{-1}, respectively. These spectra show similarities with the reported micron size $Si_{100-x}Ge_x$ alloys by Duveau *et al.*[4] Raman spectroscopy also gives information on the organization

of the material. The Si Nps pristine powder presents a shoulder next to a sharp band (at 521 cm⁻1) at lower frequencies attributed to amorphous Si[5]. In comparison, the Ge Nps powder present at a sharp band at 385 cm^{-1} with no shoulder contribution. The Si-rich and Si≈Ge alloys present Si and Ge broad bands, which are shifted below 521 and 298 cm^{-1}, respectively. In contrast, the Ge-rich alloy powder presents a sharp Ge band at approximately the same position as the pure Ge Nps.

To summarize, the shifted Raman bands indicate that the Si Nps, Si-rich, and Si≈Ge alloys have a significant amorphous contribution.

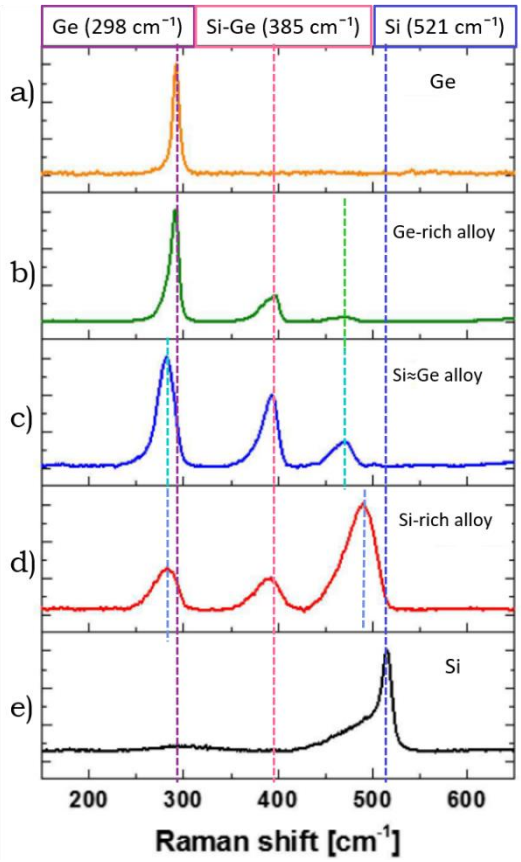

Figure 4.2 Raman spectra of the various $Si_{100-x}Ge_x$ alloys, pure Ge, and pure Si. Adapted from [3].

4.2.1.2 *The crystalline Ge-rich: $Si_{21}Ge_{79}$ Nps*

Figure 4.3a shows in red the diffracted pattern for the Ge-rich alloy. The peaks are strikingly broad, thus confirming the presence of composition heterogeneities in these powders. The following analysis methodology was applied:

Assuming the presence of different crystalline $Si_{100-x}Ge_x$ phases with different Ge contents, we first perform a LeBail fitting of the experimental data to determine the lattice parameter of the different phases. When mixing Ge and Si at different composition ratios that result in highly crystalline powders, the lattice parameters for the $Si_{100-x}Ge_x$ linearly increases with x composition, following Vegard's law[3,4,6]. Therefore, from the lattice parameter obtained values, and considering Vegard's law, we determine the composition of x of the different component phases.

Then, we perform a Rietveld refinement to determine the relative weight of the different phases. The mean Ge composition value x is calculated by weighting the Ge content of each crystalline phase by its relative amount in the powder.

In the Ge-rich alloy case, four different phases are needed to account for the peak shape. The obtained Ge compositions determined by the refined lattice parameters range from x = 100 (pure Ge) to x = 67. The average Ge content is $\langle x \rangle = 79 \pm 5$, considering the relative crystalline phase amounts. Therefore, the Ge-rich compound can be considered as the mixture of four different $Si_{100-x}Ge_x$ crystalline phases resulting in an average $Si_{21}Ge_{79}$ composition.

In addition, electron microscopy measurements were performed on $Si_{21}Ge_{79}$ powder to study its morphology and composition. Figure 4.3b–d shows the corresponding high-resolution transmission electron microscopy (HRTEM) images. Figure 4.3b shows the morphology of the Nps that consist of mostly spherical and faceted particles with sizes ranging between 100–180 nm. Besides, Figure 4.3c and d show the STEM-EDX mapping of two different particles. A typical inner-outer structure with different compositions is observable, where the outer structure presents strong signals of Si-rich (magenta), and the inner part has a mixture of Si and Ge (magenta and green).

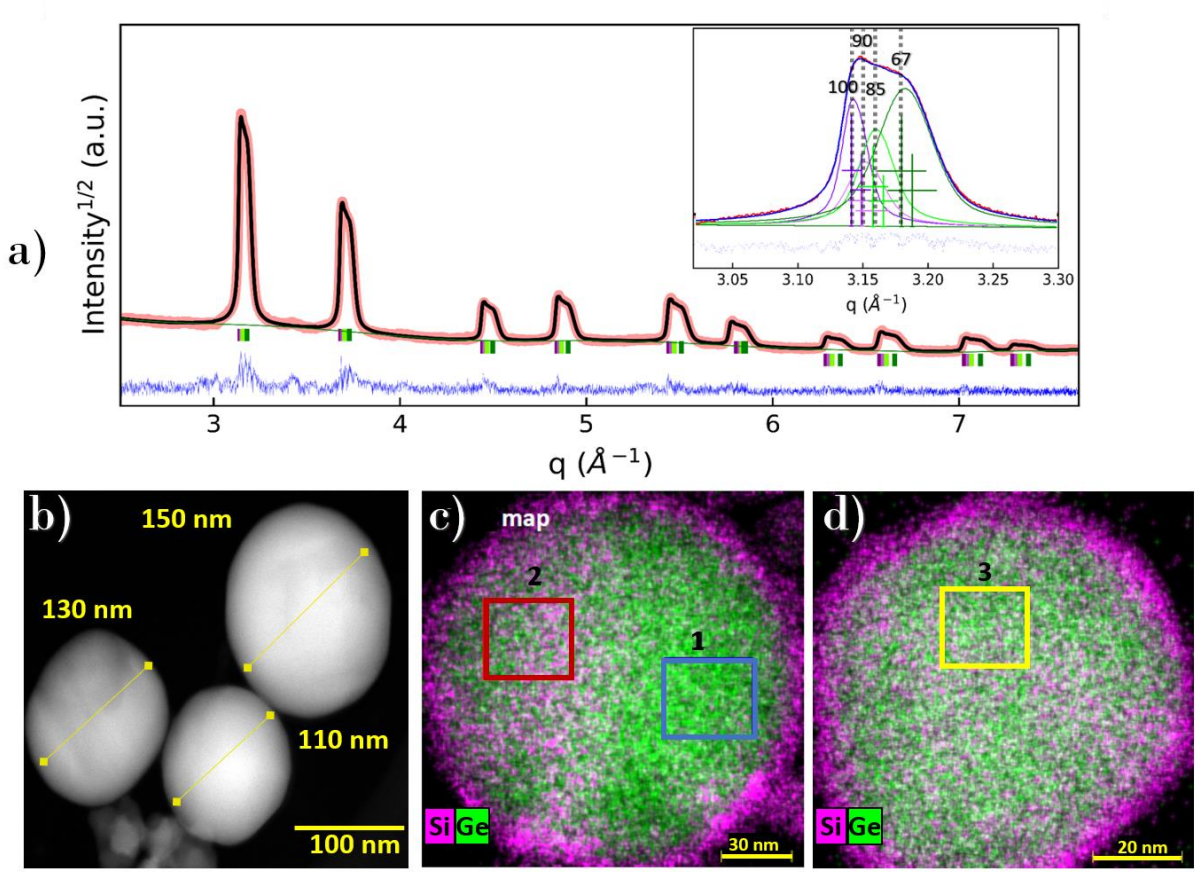

Figure 4.3 a) Rietveld refinement of the X-ray powder diffraction of the $Si_{21}Ge_{79}$ powder. Refined patterns (black) overlapped the observed patterns (red). The difference between the calculated and the experimental is shown in blue. The intensity is presented in the squared root scale. The inset figure shows the polydispersity for the $Si_{21}Ge_{79}$ powder with Ge composition from 67 to 100. b) STEM-HAADF image obtained in the $Si_{21}Ge_{79}$ powder. c) and d) EDX elemental mapping showing the distribution of Ge and Si on the powder.

A quantitative chemical mapping has been performed in the squared zones (see colored squares in Figure 4.3c and d). Table 4.1 shows the percentages of Ge, Si, and O in the Ge-rich alloy ($Si_{21}Ge_{79}$) in different zones. Area 1 (blue square) shows a composition with higher Ge content (x = 91), consistent with the fewer magenta spots in this zone, whereas area 2 and area 3 show a slightly lower Ge content (x = 76 and x = 74, respectively). We calculated the Ge average by considering the quantitative chemical mapping, giving an average $Si_{100-x}Ge_x$ alloy composition of $Si_{20}Ge_{80}$, in excellent agreement with the value determined by XRD (x = 79 ± 5).

Additional HAADF and EDX chemical mapping figures on this powder are presented in the Appendix, Figure 8.4, highlighting the polydispersity in morphology and composition in this powder.

Table 4.1. STEM-EDX quantitative analysis of the selected zones for Figure 4.3 and Figure 4.4.

$Si_{47}Ge_{53}$ (see Figure 4.4 c and d)					$Si_{21}Ge_{79}$ (see Figure 4.3c and d)				
Mapping zones	Ge [%]	Si [%]	O [%]	Composition	Mapping zones	Ge [%]	Si [%]	O [%]	Composition
Area 1	68.73	24.74	6.53	$Si_{27}Ge_{73}$	Area 1	88.04	8.52	3.44	Si_9Ge_{91}
Area 2	55.88	39.44	4.68	$Si_{42}Ge_{58}$	Area 2	74.61	22.85	2.54	$Si_{24}Ge_{76}$
Area 3	62.49	29.77	5.34	$Si_{32}Ge_{68}$	Area 3	71.94	24.29	3.47	$Si_{26}Ge_{74}$
Area 4	30.85	57.38	11.78	$Si_{62}Ge_{38}$				Mean	$Si_{20}Ge_{80}$
Area 5	31.91	54.76	13.13	$Si_{63}Ge_{37}$					
Area 6	75.52	17.12	7.36	$Si_{19}Ge_{81}$					
			Mean	$Si_{41}Ge_{59}$					

Globally, both XRD and STEM-EDX highlight the heterogeneity of the sample $Si_{21}Ge_{79}$ in size and composition.

4.2.1.3 *The crystalline Si≈Ge alloy: $Si_{47}Ge_{53}$ Nps*

Regarding the Si≈Ge alloy, Figure 4.4a shows in red the diffracted pattern, which, similarly to the Ge-rich alloy, exhibits broad peaks, corresponding to heterogeneities in the structural composition. Two different $Si_{100-x}Ge_x$ compositions have to be considered to account for the diffraction profile. Following the methodology described in section 4.2.1.2, the Ge contents determined for the two present crystalline phases are x = 65 and x = 50, with an average Ge content $\langle x \rangle$ = 53 ± 5.

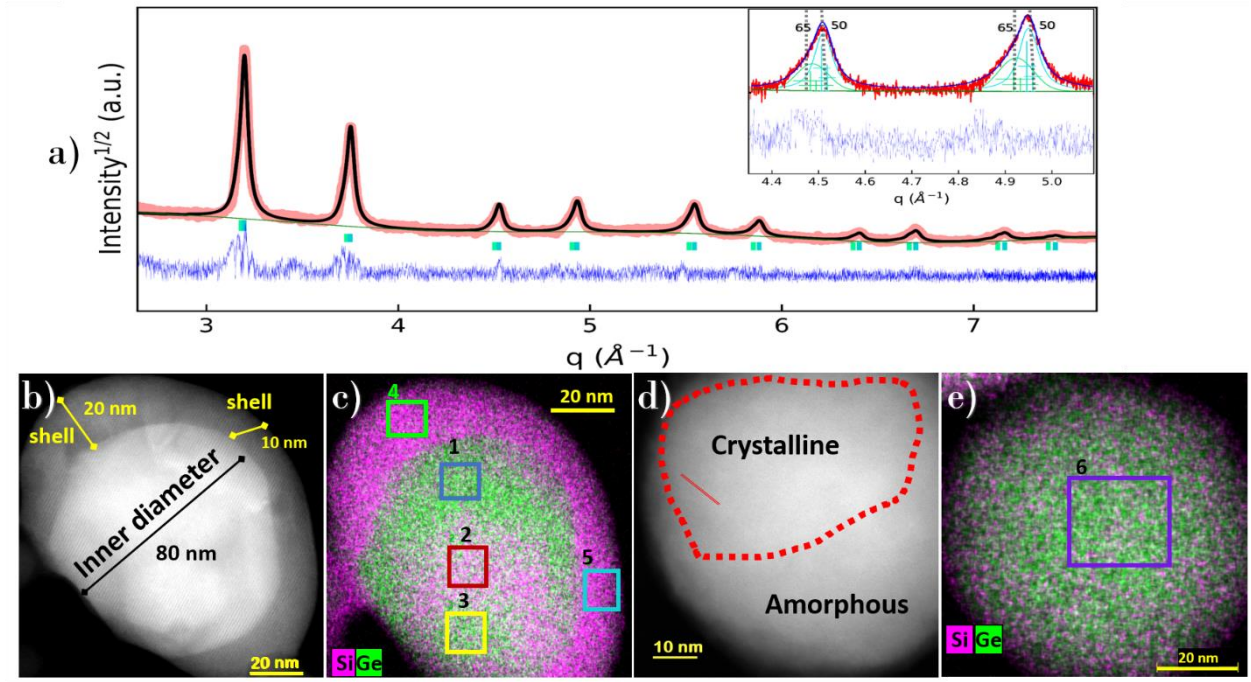

Figure 4.4 a) Rietveld refinement of the X-ray powder diffraction of the $Si_{47}Ge_{53}$ powder. Refined patterns (black) overlapped the observed patterns (red). The difference between the calculated and the experimental is shown in blue. The intensity is presented in the squared root scale. The inset figure shows the polydispersity for the $Si_{47}Ge_{53}$ powder with Ge composition from 50 to 65. b) and c) STEM-HAADF and EDX mapping example on a completely crystalline particle. d) and e) STEM-HAADF and EDX elemental mapping on a partially amorphous particle. The EDX elemental mapping shows a distribution of Ge and Si on the particles.

Figure 4.4b–c show the high-resolution transmission electron microscopy (HRTEM) for the alloy with average $Si_{47}Ge_{53}$ composition. In general, the pristine alloy powder contains a bimodal distribution of Np sizes, smaller as

50 nm, and larger particle of sizes between 70–150 nm (see additional HRTEM images in the Appendix, Figure 8.5). Bigger nanoparticles may be composed of several small particles, some being partially crystalline with an amorphous part. The amorphous contribution is confirmed by Raman scattering and evidenced on the shifted Si and Ge bands (see Figure 4.2c). Particles are very heterogeneous in terms of their chemical composition, size, and morphology.

Figure 4.4b–c show an example of a spherical particle for the $Si_{47}Ge_{53}$ alloy with a different composition in the inner/outer part (core-shell type structure). The inner diameter of the particle is about 80 nm, and the shell has a dimension of 10-20 nm. Figure 4.4c shows the chemical mapping of the particle for five different areas. Like the Ge-rich alloy, this alloy presents strong signals of Si-rich in the outer part, while the inner part is highly heterogeneous in composition. A quantitative analysis was performed in the colored areas (see Table 4.1). The interior of the particle presents three different zones with a different Ge composition: Area 1 shows a higher Ge composition x = 73, while area 2 and area 3 present a slightly lower Ge composition x = 58, and x = 68, respectively. Areas 4 and 5 placed in the exterior show the lowest Ge contents (x = 38 and x = 37, respectively) and higher oxygen content than the inner part of the particle (4–6% vs. 11–13%, respectively). To summarize, the inner structure of the particle is made of Ge-rich alloys, while the outer shell is made of Si-rich $Si_{100-x}Ge_x$ solutions.

We also obtained information on partially crystalline particles, such as the one in Figure 4.4d of about 75 nm in diameter. Figure 4.4e shows the STEM-EDX chemical mapping of this particle, revealing a Ge content of x = 81 (see area

6, Table 4.1) with higher Ge content than the fully crystalline in Figure 4.4a and b.

Considering both particles and their Ge compositions in different zones, the average Ge content for this alloy is 59, giving an alloy composition of $Si_{41}Ge_{59}$, close to XRD (Ge content = 53 ± 5).

Globally, the Si≈Ge powder contains at least two different $Si_{100-x}Ge_x$ crystalline phases. STEM-HAADF shows that the particles could also be partially amorphous in agreement with Raman spectroscopy.

4.2.1.4 *The crystalline Si-rich: $Si_{63}Ge_{37}$ Nps*

Figure 4.5a shows in red the diffracted pattern measured for the Si-rich alloy. The broad bump around 5 $Å^{-1}$ is characteristic of the presence of an amorphous contribution, in agreement with Raman spectroscopy results. This alloy appears to be less heterogeneous in composition than the two others. Assuming the presence of one single crystalline phase allows accounting for the peak profile. The corresponding composition is $\langle x \rangle = 37 \pm 5$. However, we have to underline that this composition determined by XRD concerns the crystalline component only. As Raman scattering suggests an amorphous organization, we must consider that the Ge content estimated from XRD is overestimated.

Figure 4.5b shows a transmission electron microscopy (TEM) for this alloy. In general, the pristine alloy powder contains a bimodal distribution of Np sizes, smaller than 10 nm, and larger particles ranging between 30–40 nm. The size distribution revealed an average diameter of 27 ± 9 nm.

Figure 4.5c shows EDX chemical mapping on the particles. Three different particles were mapped across. The EDX profile across line 1 is shown in Figure 4.5d. It is worth mentioning that the color scale is somehow misleading. While it could suggest a Ge-core/Si-shell structure, the core has more or less equivalent Si and Ge contents as demonstrated in the quantitative EDX mapping (see Figure 4.5d), while the outer part of the particles is made of Si-richer alloy.

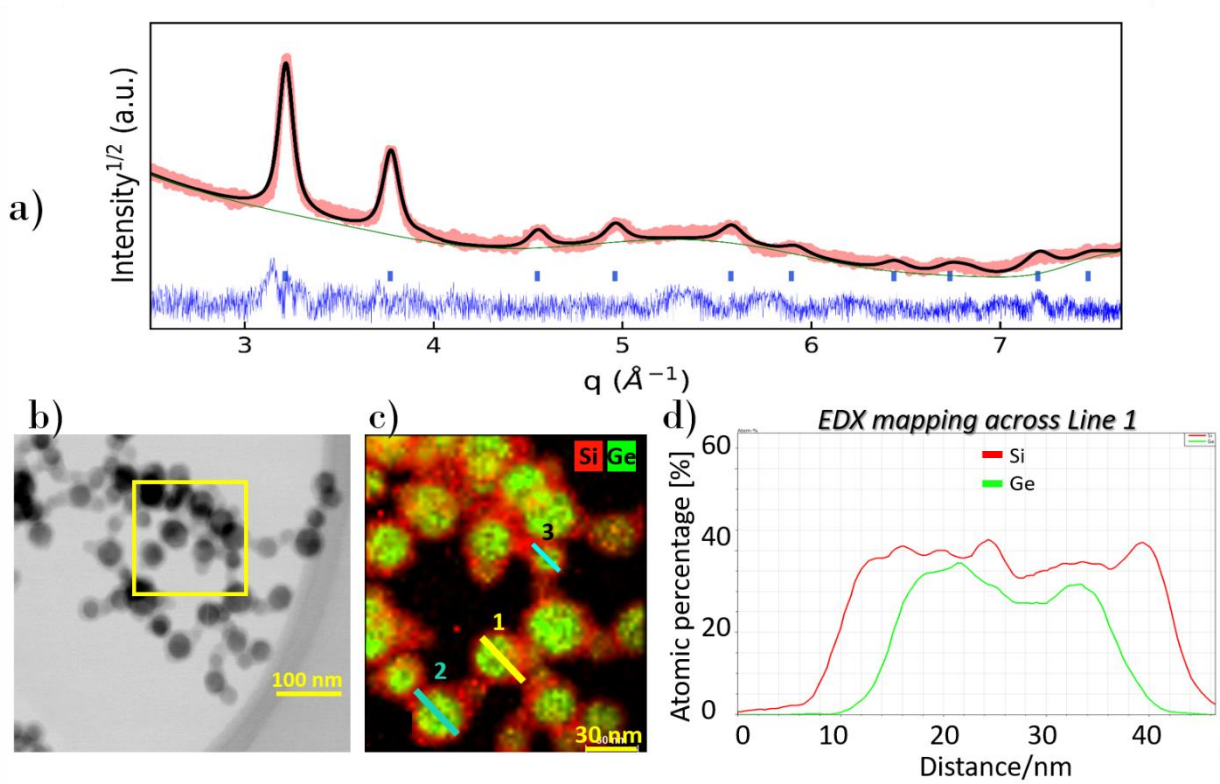

Figure 4.5 a) Le-Bail refinement of the X-ray powder diffraction of the $Si_{63}Ge_{37}$ powder. Refined patterns (black) overlapped the observed patterns (red). The difference between the calculated and the experimental is shown in blue. The intensity is presented in the squared root scale. b) and c) STEM-HAADF and EDX mapping example on different particles. d) quantitative chemical mapping on line 1 across one particle.

To summarize, for the Si-rich alloy, the XRD pattern allows accounting for a unique crystalline phase with an average composition $Si_{63}Ge_{37}$. This alloy also contains an important amorphous contribution, evidenced both by Raman spectroscopy and XRD.

4.2.1.5 *Main conclusions of the $Si_{100-x}Ge_x$ alloys*

Our interest in these compounds came from the galvanostatic studies performed by our collaborators, which showed very good cycling performances at first cycles and increasing current densities, demonstrating promising characteristics for Li-ion batteries.

Our investigation of the SiGe properties reveals strong heterogeneities in size, composition, and morphology.

- The Ge-rich alloy is mainly crystalline, and the broad diffracted peaks are accounted for considering four different crystalline phases, with an average composition $Si_{21}Ge_{79}$.

-The Si≈Ge alloy is mainly crystalline with two main compositions resulting in an average composition $Si_{47}Ge_{53}$. A minor amorphous contribution is revealed by Raman scattering.

-Concerning the Si-rich alloy, both XRD and Raman scattering evidence the presence of an important amorphous contribution. The crystalline component is less heterogeneous than the two other compounds with an average composition $Si_{63}Ge_{37}$.

4.2.1.6 *Structural characterization of crystalline Si nanoparticles (c-Si Nps)*

c-Si Nps were characterized in pristine powder using X-ray powder diffraction. Figure 4.6 shows in red the obtained diffracted pattern. Rietveld refinement on the diffracted pattern is performed, assuming a diamond structure a single phase with space group *Fd-3m*. The obtained lattice parameter was a = 5.428(1) $Å^{-1}$. The average size for the particles is 26 ± 2. However, BET measurements performed by our collaborators at IRAMIS have revealed a mean particle size of 71 nm[3]. The powder is probably formed by particles with an amorphous shell and a crystalline core of 26 nm. The important amorphous contribution is corroborated in the Raman spectrum on this sample (see Figure 4.2e), indicated by a shoulder next to the Si-Si band at 521 cm^{-1}.

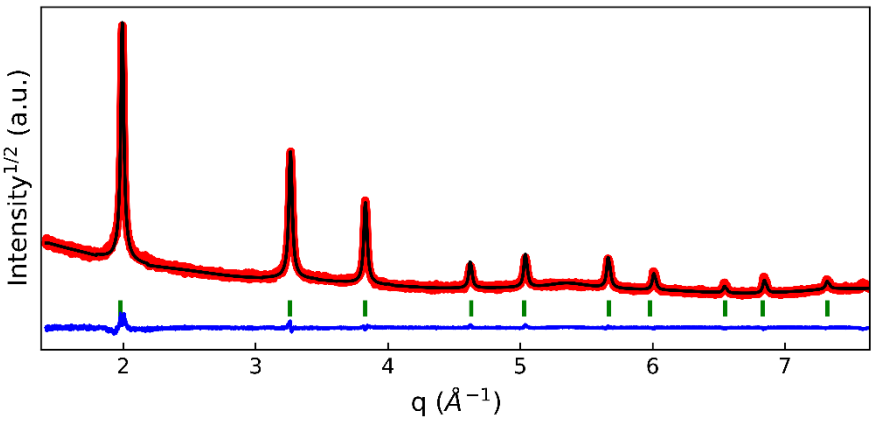

Figure 4.6 Rietveld refinement of the X-ray powder diffraction data of the Si powder. Refined patterns (black) overlapped the observed patterns (red). The difference between the calculated and the experimental is shown in blue. The intensity is presented in the squared root scale.

4.2.2 Electrochemical characterization of $Si_{100-x}Ge_x$ alloys Nps electrodes

Electrodes were prepared with the powders described in the previous section to perform galvanostatic lithiation and delithiation during the first cycle in coin-cells and investigate the effect of Ge content in the crystalline $Si_{100-x}Ge_x$ alloys Nps.

Figure 4.7a–e compare the de(lithiation) voltage vs. capacity profile measured at C/20 for the crystalline Ge, $Si_{21}Ge_{79}$, $Si_{41}Ge_{59}$, and $Si_{63}Ge_{37}$, and Si Nps. The theoretical capacities calculated considering 50% of active mass correspond to 692, 868, 1252, 2767, and 1789 mAh/g, respectively. Figure 4.7f–j show the differential profiles of the voltage for the first cycle lithiation and delithiation. These differential profiles are used to highlight the plateaus and semi plateaus in the voltage profile.

As expected, cell capacity increases when the amount of germanium decreases. Concerning the $Si_{100-x}Ge_{x,}$ when decreasing Ge content, the capacity increases from 763, 1043, and 1170 mAh/g for the alloys $Si_{21}Ge_{79}$, $Si_{47}Ge_{53}$, and $Si_{63}Ge_{37}$, respectively. The lower capacity loss corresponds to the $Si_{47}Ge_{53}$ with 8%, while the Ge-rich and Si-rich alloys present a capacity loss of 15% and 25%, respectively. These results agree with other reports, where the lowest capacity loss was obtained for Si≈Ge ($Si_{47}Ge_{53}$)[1,2,7]. In pure c-Si Nps, the delithiation capacity obtained is 1501 mAh/g, corresponding to 15% of capacity loss and agreeing with other reports on Si Nps[8,9].

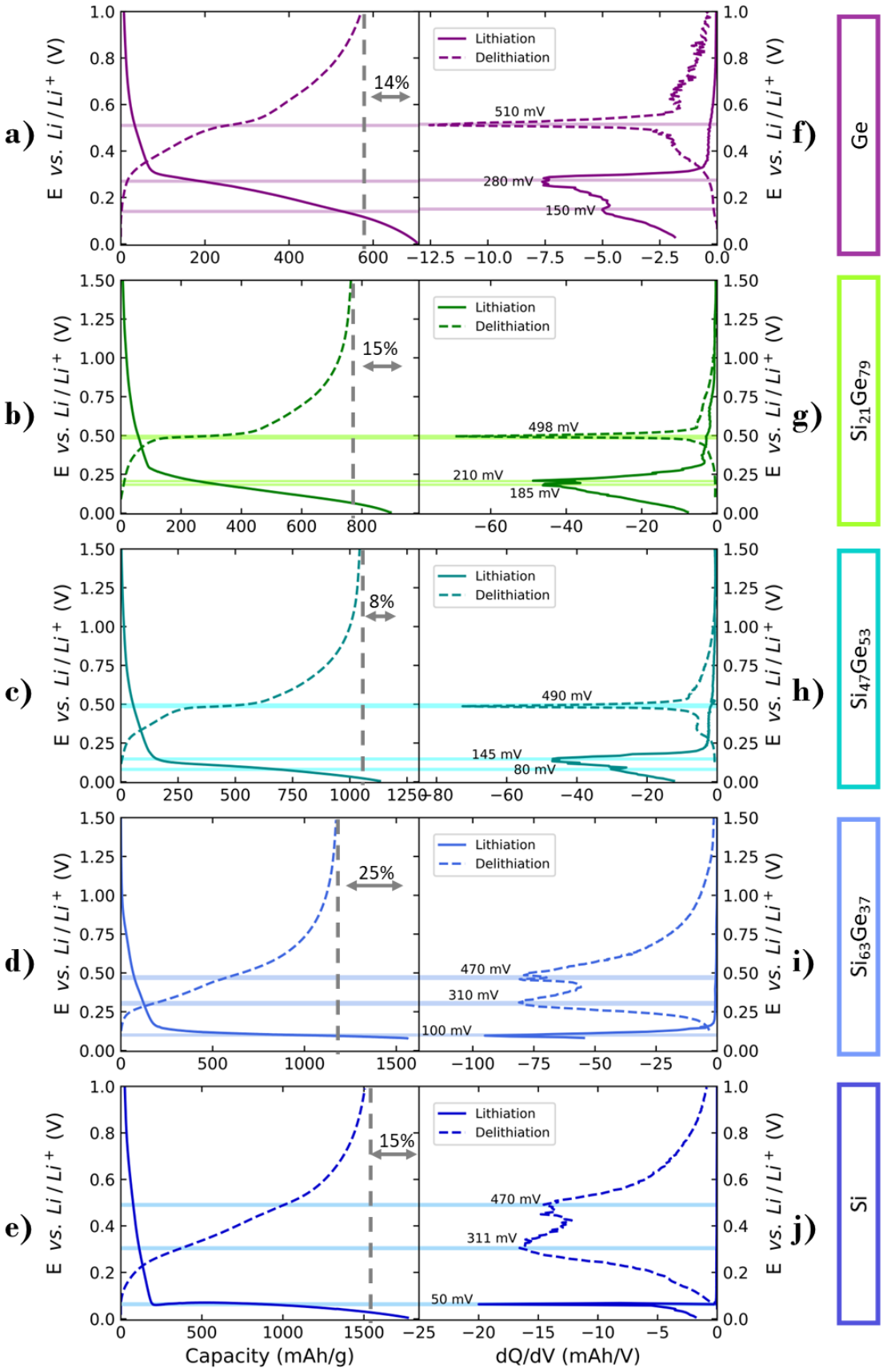

Figure 4.7 a–e) potential vs. Li/Li+ against capacity f–j) voltage vs. Li/Li⁺ as a function of dQ/dV for crystalline Ge, and the Ge-rich ($Si_{21}Ge_{79}$), Si≈Ge ($Si_{47}Ge_{53}$), Si-rich alloys ($Si_{63}Ge_{37}$), and Si Nps in a coin-cell at C/20 against Li metal.

While a sharp peak characterizes pure Si at 50 mV in the lithiation stage and two broad peaks during the delithiation around 311 and 470 mV, pure Ge presents two broad peaks during lithiation at 150 and 280 mV and a sharp peak at 510 mV in the delithiation stage. The Ge-rich and Si≈Ge alloys present dQ/dV signatures similar to Ge, while the Si-rich alloy behavior is closer to pure Si. The delithiation dQ/dV peaks for Si-rich and Si≈Ge alloys have sharp peaks, similar to Ge, resulting from a flat voltage at ~ 498 and 490 mV, respectively. In contrast, $Si_{63}Ge_{37}$ has two broad bumps at 470 and 310 mV during delithiation, similar to pure Si Nps. These results are consistent with previous works in submicron-sized $Si_{100-x}Ge_x$ particles[2,6].

Overall, the Ge-rich and Si≈Ge alloys behave like pure Ge (dQ/dV signatures), with the dQ/dV peaks shifting to lower voltages for lower Ge content. Likewise, the Si-rich alloy behavior is reminiscent of pure Si. Even though the SiGe alloys are heterogeneous in composition, there is no evidence of the heterogeneity impact in the electrochemical curves.

4.3 *Operando* XRD studies during lithiation of $Si_{100-x}Ge_x$ alloys

This section describes the *operando* study of the amorphization of the different $Si_{100-x}Ge_x$ alloys and the formation of new lithiated phases by in-house XRD and wide-angle X-ray scattering (WAXS) at the ESRF on the French beamline BM02-d2am. The Ge, Ge-rich ($Si_{21}Ge_{79}$), and Si Nps were measured in-house,

while the Si≈Ge ($Si_{47}Ge_{53}$) and Si-rich ($Si_{63}Ge_{37}$) were measured at the ESRF-BM02. All the experiments were performed at C/20 against Li metal.

For the in-house experiments, the measurements were performed in reflection geometry with the electrochemical cell described in chapter 2, section 2.3.1, together with the preparation of the used self-supported electrodes. Figure 4.8a shows an example of a diffracted pattern obtained in-lab for the $Si_{21}Ge_{79}$. Be diffraction peaks come from the upper window, which is used as a current collector.

Figure 4.8b shows an example of a diffracted pattern measured at BM02 in transmission geometry. In this case, a pouch cell was used; here, Cu and Al Bragg reflections in the diffracted pattern belong to the current collector and the pouch-cell case, respectively. As the X-ray beam passes through all the pouch-cell components and reaches the detector, the signal-to-ratio noise of the resulted diffracted pattern is lower than in the in-house experiment. Besides, to reduce beam absorption by the cell, the X-ray wavelength is shorter than for in-lab experiments, resulting in a lower resolution. Nevertheless, the electrochemistry is more favorable, and side-reactions coming from the method to prepare the electrode are less frequent.

4.3.1 Qualitative observations

Figure 4.8a–c shows in the inset the evolution of the (111) Bragg reflection for the $Si_{100-x}Ge_x$ alloys during lithiation down to 5 mV vs. Li metal at C/20.

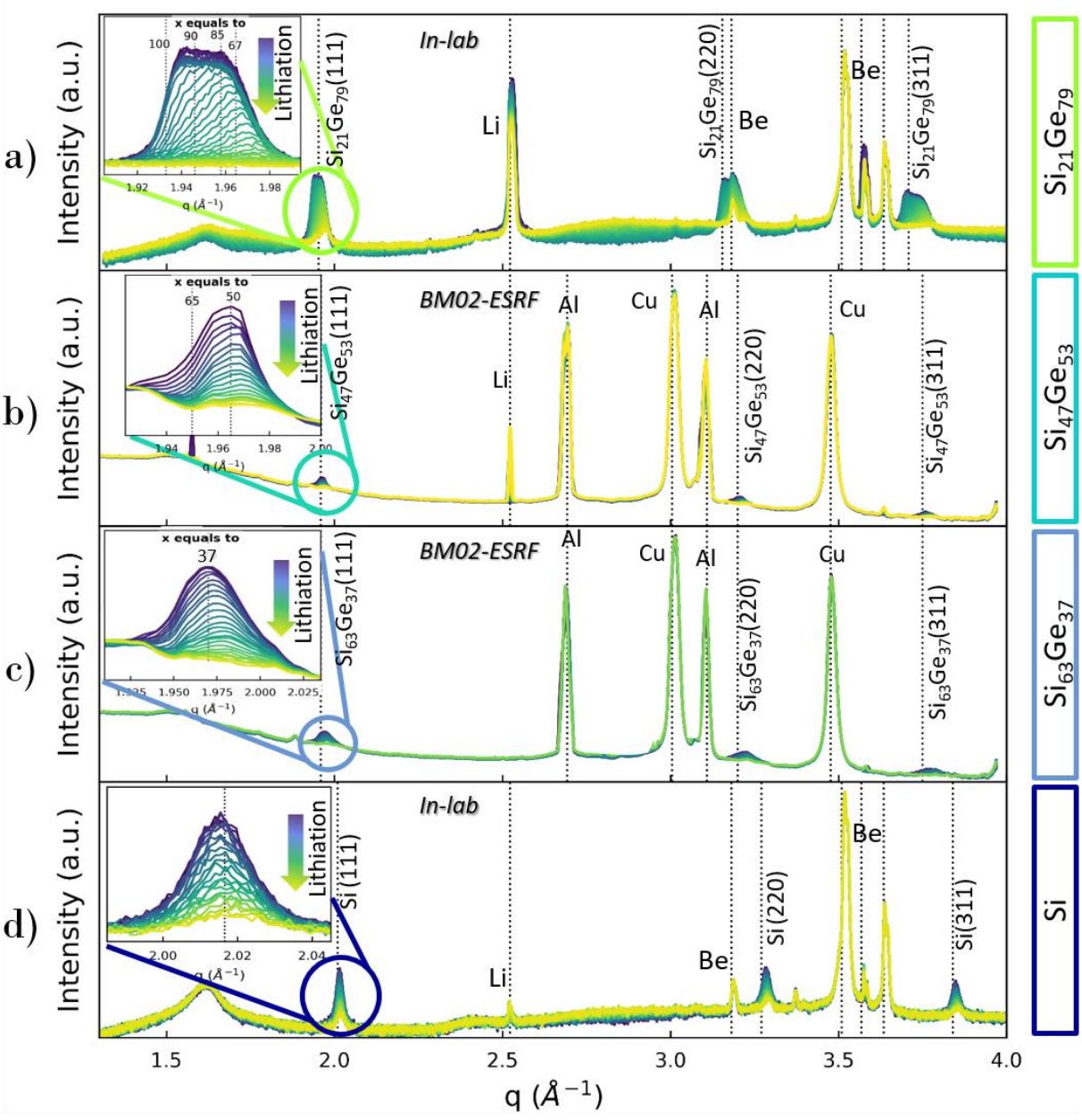

Figure 4.8 a) diffracted XRD pattern obtained in-house during lithiation for the Ge-rich ($Si_{21}Ge_{79}$) b) diffracted WAXS pattern obtained at BM02-ESRF in a pouch cell for the Si≈Ge ($Si_{47}Ge_{53}$), c) for the Si-rich ($Si_{63}Ge_{37}$), and d) diffracted XRD pattern obtained in-lab for Si Nps. The inset figures show an enlarged view of the reflection $Si_{100-x}Ge_x$(111) during lithiation. The dotted lines correspond to the distinct $Si_{100-x}Ge_x$111) phases found in the respective alloys in the inset figure.

At the beginning of the lithiation process, the peak profiles correspond to the ones observed in the pristine powders. Then, the peak shape evolves asymmetrically upon lithiation. The intensity of the small-angle part of the peak (left side) decreases before the right side. Knowing that the left side of the peak corresponds to the $Si_{100-x}Ge_x$ phases with higher Ge content, the distinct phases within the sample evolve differently depending on the Ge composition, which is correlated with the lithiation potential.

To obtain quantitative information on the lithiation processes in these complex compounds, we perform a single peak refinement of the reflection (111).

4.3.2 Quantitative analysis of the diffraction data

Figure 4.9a, b, and c show the Lorentzian functions used for the single peak refinement for Ge-rich ($Si_{21}Ge_{79}$), Si≈Ge ($Si_{43}Ge_{57}$), and Si-rich ($Si_{63}Ge_{37}$) alloys, respectively, as described in the characterization of the pristine materials in section 4.2.1.

Performing a full pattern LeBail type analysis would have been complicated in the synchrotron data considering the weak relative SiGe signal. For the lab data, it would have been necessary considering different heights for the different Be and SiGe contributions, as this has been done for pure Ge in chapter 3. However, given the complicated structure of the SiGe compounds and the weak electrode signal, compared to pristine powder, we use single peak fitting.

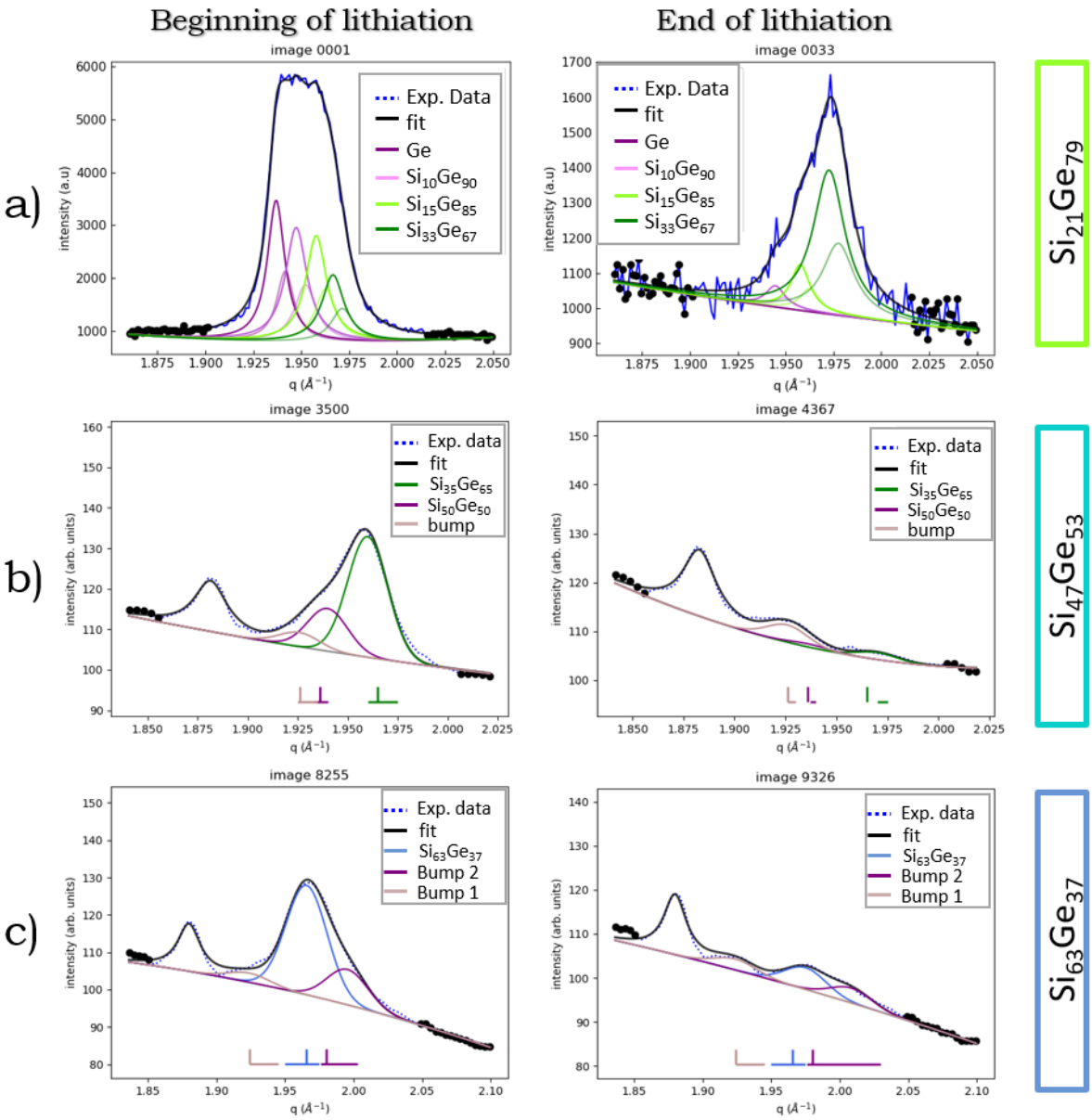

Figure 4.9 single profile fitting results for the (111) reflection in a) $Si_{21}Ge_{79}$, considering four phases, b) $Si_{47}Ge_{53}$ considering two phases, and c) $Si_{63}Ge_{37}$ considering one phase, at the beginning and ending of lithiation.

In the case of Si≈Ge ($Si_{43}Ge_{57}$) and Si-rich ($Si_{63}Ge_{37}$) alloys, we had to consider a bumpy background coming from the pouch-cell components. Specifically, the bump at 1.875 Å comes from the separator.

We consider only the normalized integrated intensity of the different phases upon lithiation from the single peak refinement results.

Figure 4.10a shows the voltage vs. Li metal for the first lithiation of the sample $Si_{21}Ge_{79}$ down to 0.005 V, with a current corresponding to C/20. Correspondingly, Figure 4.10b shows the evolution of the normalized integrated intensities obtained after the single peak results from the sample $Si_{21}Ge_{79}$ upon lithiation time. The different curves represent the four $Si_{100-x}Ge_x$ component phases. Note that for Figure 4.10b, a secondary x-axis was added to indicate the voltage at the corresponding time.

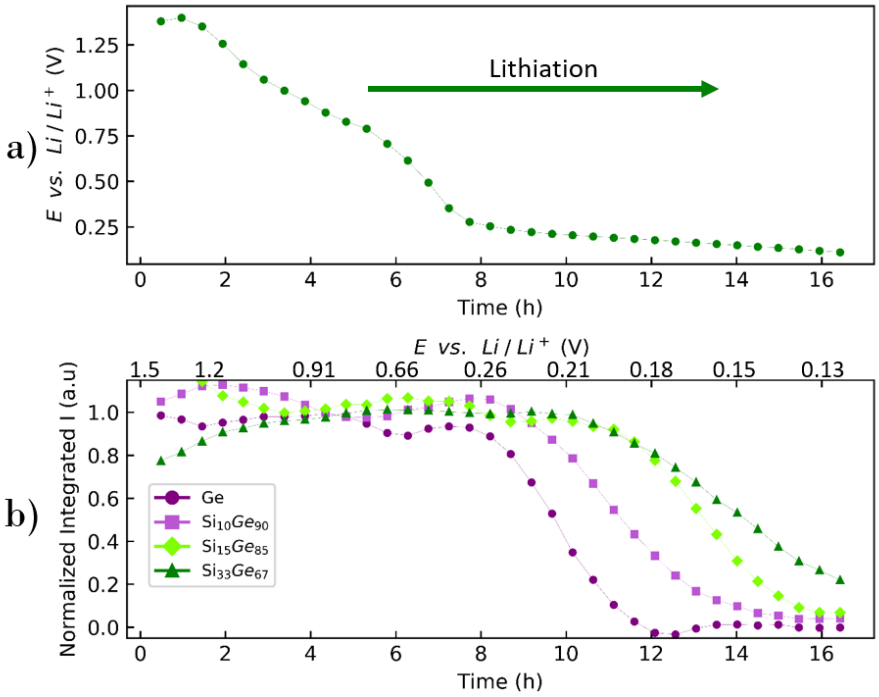

Figure 4.10 a) voltage vs. Li/Li⁺ against time for the complete lithiation of the alloy with an average composition $Si_{21}Ge_{79}$. b) Normalized integrated intensity obtained from the fit of the distinct phases in $Si_{21}Ge_{79}$ vs. time during a complete lithiation. Note that the secondary x-axis indicates the corresponding voltage.

The decrease of the integrated intensity is associated with the disappearance of the crystalline phase due to the lithiation. Figure 4.10b confirms that the lithiation potential increases with the Ge content, ranging from 0.26V for Ge down to about 0.18 V for $Si_{33}Ge_{67}$. These results evidence the sequential lithiation of the different $Si_{100-x}Ge_x$ component phases.

Despite the strong heterogeneity of the Ge-rich alloy ($Si_{21}Ge_{79}$), the four phases distinguished from the XRD give coherent electrochemical results with lithiation voltages depending on the Ge content.

The electrochemical results of the voltage against lithiation time and the evolution of the normalized integrated intensity for the Si≈Ge ($Si_{47}Ge_{53}$) and the Si-rich alloy ($Si_{63}Ge_{37}$) are in the Appendix, Figure 8.7 and 8.8, respectively.

The results obtained with the three different compounds are collected in Figure 4.11. To estimate a characteristic lithiation voltage value for the different $Si_{100-x}Ge_x$ phases, we calculated the minimum of the second derivative of the integrated intensity for the voltage (see Figure 4.12). The vertical lines indicate the obtained values.

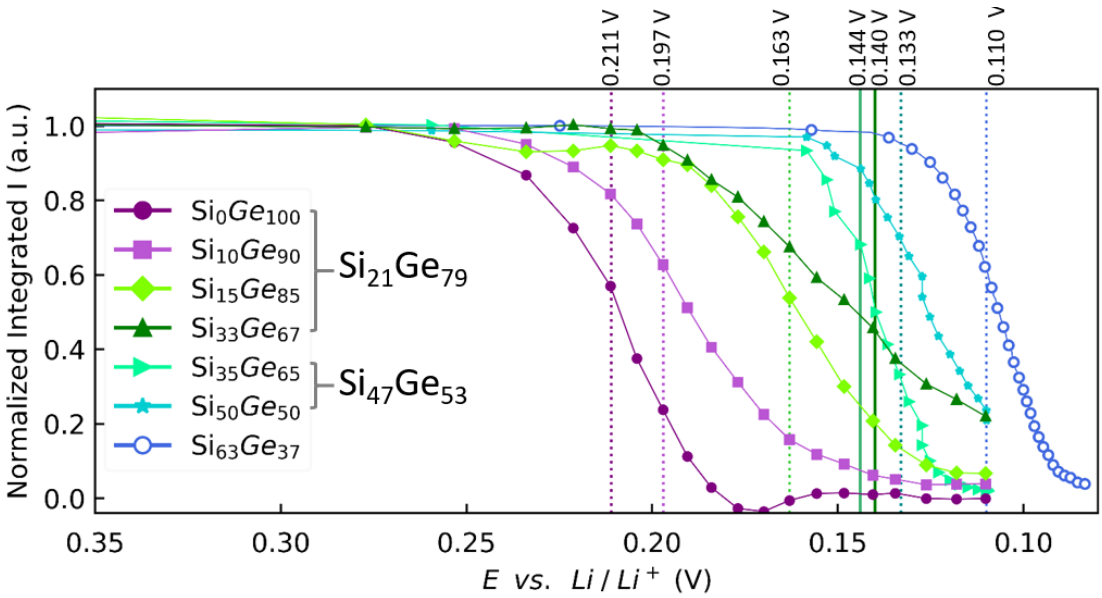

Figure 4.11 Normalized integrated intensity against voltage vs. Li/Li⁺ during a complete lithiation for the distinct phases found in the three synthesized alloys.

The normalized intensities of the distinct phases within the different $Si_{100-x}Ge_x$ samples decrease sequentially depending on the Ge content. Given that crystalline Ge and Si Nps have different lithiation voltages E vs. Li/Li⁺, close

to 0.3 V and 0.037 V, respectively, Ge-rich phases lithiate first (at higher voltages) in comparison with Si-rich phases, and the corresponding amorphization voltages vary between 0.250 V and 0.1 V.

To our knowledge, there is no clearly established method to identify the lithiation voltage of a crystalline phase. We tried different ways, and we selected the second derivative approach, which has the advantage of being unambiguously defined. However, the obtained voltage does not correspond to the value at which the lithiation starts but rather to where normalized integrated intensity has decreased by at least 40%.

The characteristic voltages for the different $Si_{100-x}Ge_x$ phases are plotted against the Ge content in Figure 4.13. The legend is indicated in Table 4.2.

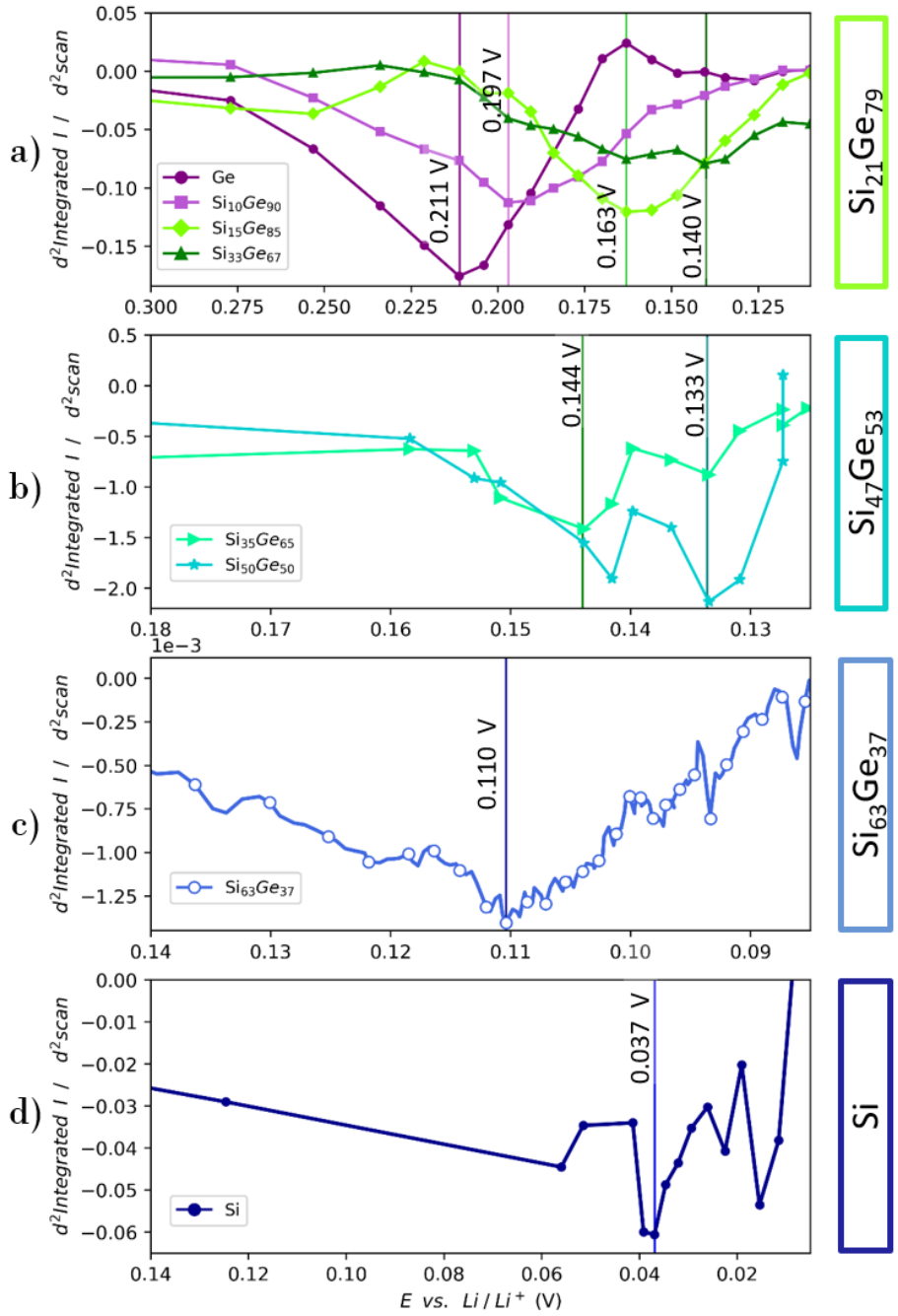

Figure 4.12 a–d) analysis of the second derivative on the normalized integrated intensity against voltages vs. Li metal for $Si_{21}Ge_{79}$, $Si_{47}Ge_{53}$, $Si_{63}Ge_{37}$, and Si Nps, respectively, to extract the value at which the phases start to amorphized. Note that a line indicates the lowest minimum of the second derivative.

Considering the lithiation average voltages, we obtained average values of 0.178, 139, and 110 mV for $Si_{23}Ge_{77}$, $Si_{47}Ge_{53}$, and $Si_{63}Ge_{37}$, respectively (see Table 4.2). Interestingly these values are close to the ones obtained in the

lithiation dQ/dV peaks by galvanostatic cycling (see Figure 4.7f–j) at 210, 145, and 100 mV for $Si_{23}Ge_{77}$, $Si_{47}Ge_{53}$, and $Si_{63}Ge_{37}$, respectively.

The lithiation dQ/dV peaks indicate the amorphization of the crystalline $Si_{100-x}Ge_x$ alloys phases and transformation into lithiated $Li_x(Si_{100-x}Ge_x)_y$ intermediates.

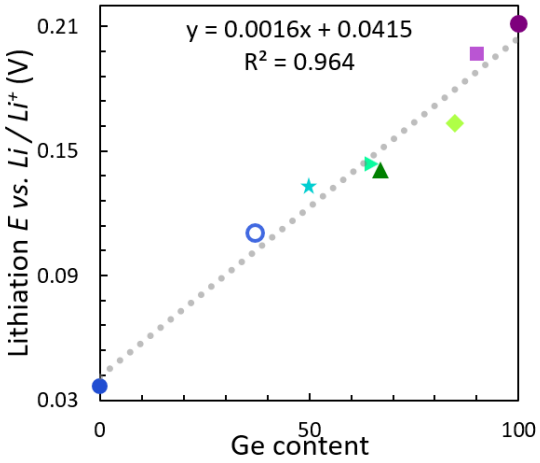

Table 4.2 Summary of the results

Sample	SiGe phases	Lithiation voltage (V)	Average voltage (V)
$Si_{21}Ge_{79}$	Si_0Ge_{100}	0.211	0.178
	$Si_{10}Ge_{90}$	0.197	
	$Si_{15}Ge_{85}$	0.163	
	$Si_{33}Ge_{67}$	0.140	
$Si_{47}Ge_{53}$	$Si_{35}Ge_{65}$	0.144	0.139
	$Si_{50}Ge_{50}$	0.133	
$Si_{63}Ge_{37}$	$Si_{63}Ge_{37}$	0.110	
Si	Si	0.037	

Figure 4.13 linear dependency of the amorphization voltage for the distinct phases vs. Ge content. The amorphization voltages were obtained from the second derivative of the curves in Figure 4.12.

Remarkably, despite the strong heterogeneous character of the SiGe samples, our results show that their electrochemical and structural properties can be accounted for considering mixtures of different $Si_{100-x}Ge_x$ phases, the characteristic lithiation voltage of which follow a linear increase with the Ge content.

4.3.3 Formation of the $Li_{15}(Si_{100-x}Ge_x)_4$ phases

During full lithiation of the SiGe compounds down to 0.005 V vs. Li/Li^+ and subsequent delithiation, we follow the formation of the crystalline $Li_{15}(Si_{100-x}Ge_x)_4$ phases. Figure 4.14a and b show the complete diffracted pattern for the Ge-rich ($Si_{21}Ge_{79}$) and Si≈Ge ($Si_{47}Ge_{53}$) performed in-lab and at the BM02-ESRF, respectively. The colored squares show an enlarged view of the $Li_{15}(Si_{100-x}Ge_x)_4$ Bragg reflections on the zones 1.35–1.9 $Å^{-1}$, indicating that the diffracted peaks evolve during cycling.

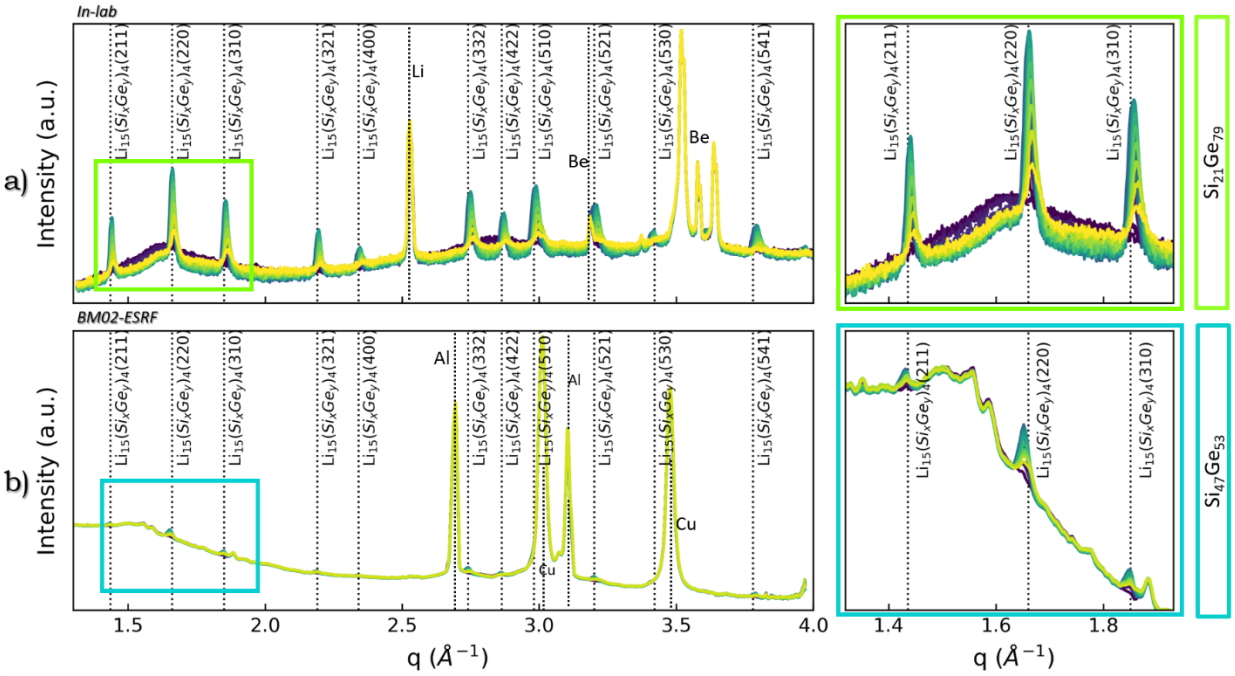

Figure 4.14 a) diffracted pattern of $Li_{15}(Si_{100-x}Ge_x)_4$ obtained from the complete lithiation of $Si_{21}Ge_{79}$. The *operando* diffracted patterns were obtained in a self-supported electrode. b) diffracted pattern of $Li_{15}(Si_{100-x}Ge_x)_4$ obtained from the complete lithiation of $Si_{47}Ge_{53}$ in BM02-ESRF. Note that this experiment was performed in a pouch-cell: thus, Cu and Al peaks are visible.

Loiza *et al.* used *operando* XRD to study bulk crystalline $Si_{50}Ge_{50}$ while cycling. They reported the amorphization of $Si_{50}Ge_{50}$, and the only crystalline phase found in this study was speculated to be $Li_{15}(Si_{50}Ge_{50})_4$ formed below 100 mV during lithiation[10]. However, the composition was not unambiguously

determined. Other studies on mechano-synthesized $Li_{4.4}Ge_{100-x}Si_x$ alloys over the whole composition range reported a linear increase in lattice constants vs. Ge content[11,12]. However, the determination of the $Li_{15}(Si_{100-x}Ge_x)_4$ composition formed by electrochemical means from pristine $Si_{100-x}Ge_x$ samples is still an open question.

Figure 4.14a shows an example of $Li_{15}(Si_{100-x}Ge_x)_4$ diffracted pattern by in-lab *operando* measurements. We underline the high signal to noise ratio of these data allowing precise quantitative analysis. Despite better electrochemical conditions, the measurements performed in transmission with pouch cells, as shown in Figure 4.14b, are characterized by a high background resulting from the pouch cell components in transmission geometry. Cu and Al contributions hamper a precise evaluation of the $Li_{15}(Si_{100-x}Ge_x)_4$ peaks.

For both $Si_{21}Ge_{79}$ and $Si_{47}Ge_{53}$, bumps (in purple) are forming just before the growth of $Li_{15}(Si_{100-x}Ge_x)_4$ peaks at approximately 70 mV. These bumps could be associated with the formation of $Li_7(Si_{100-x}Ge_x)_2$, as observed for c-Ge Nps (see Chapter 3). Loaiza *et al.* have also observed these bumps attributed to the formation of amorphous lithiated phases[10].

Unlike Ge-rich and Si≈Ge compounds, the Si-rich alloy does not form the crystalline $Li_{15}(Si_{100-x}Ge_x)_4$ phase at C/20 (see annexes, Figure 8.10). This result is not surprising as the dQ/dV curve in Figure 4.7i is qualitatively similar to the one obtained in pure Si Nps (Figure 4.7j), characterized by two broad dQ/dV bumps observed in the delithiation stage. In contrast, Ge shows a sharp dQ/dV peak associated with the formation of c-$Li_{15}Ge_4$. In the case of

high Si concentration for Si Nps, the formation of c-$Li_{15}Si_4$ by electrochemical means is metastable[13–15].

In order to get quantitative information on the $Li_{15}(Si_{100-x}Ge_x)_4$ formation, we performed a single peak refinement of different Bragg reflections. Figure 4.15 shows the evolution of the normalized integrated intensity and FWHM for the (211), (220), and (310) $Li_{15}(Si_{100-x}Ge_x)_4$ Bragg reflections after the full lithiation of $Si_{21}Ge_{79}$. The lattice parameter value was calculated considering the positions of six different Bragg peaks ((211), (220), (310), (332), (422), and (510)).

The results obtained with the Si≈Ge alloy ($Si_{47}Ge_{53}$) are presented in annexes, Figure 8.11.

Figure 4.15a–d shows the voltage vs. Li/Li^+, normalized integrated intensity, full widths at half maximum (FWHM), lattice parameter against time in hours, respectively. For clarity, the time (hours) was replaced by the corresponding voltage. The gray dotted vertical line represents the end of lithiation.

During lithiation beyond 0.03 V, the crystalline $Li_{15}(Si_{100-x}Ge_x)_4$ phase is formed. The amount of $Li_{15}(Si_{100-x}Ge_x)_4$, which is proportional to the diffraction peak integrated intensity, increases until the end of lithiation at 0.005 V vs. Li/Li^+. The full widths at half maximum (FWHM) for the $Li_{15}(Si_{100-x}Ge_x)_4$ reflections are constant, and the lattice parameter shows a slight increase during lithiation.

Through delithiation, there are two different processes: 1) the beginning of delithiation until 0.44 V, and 2) from 0.44 V until 0.51 V. In the first stage,

while the voltage is increasing considerably, the normalized integrated intensity and the FWHM stay constant. However, the lattice parameter first decreases rapidly (until ~ 10.75 $Å^{-1}$) and then stays constant. In the second process, the voltage is almost constant. In this plateau, the $Li_{15}(Si_{100-x}Ge_x)_4$ peak intensities decrease, and the FWHM increase, indicating a progressive disappearance of $Li_{15}(Si_{100-x}Ge_x)_4$. This lattice parameter behavior during the delithiation is similar to the $Li_{15}Ge_4$ phase in Chapter 3. The $Li_{15}(Si_{100-x}Ge_x)_4$ phase obtained with the $Si_{47}Ge_{53}$ compound also has similar behavior (see Appendix, Figure 8.11).

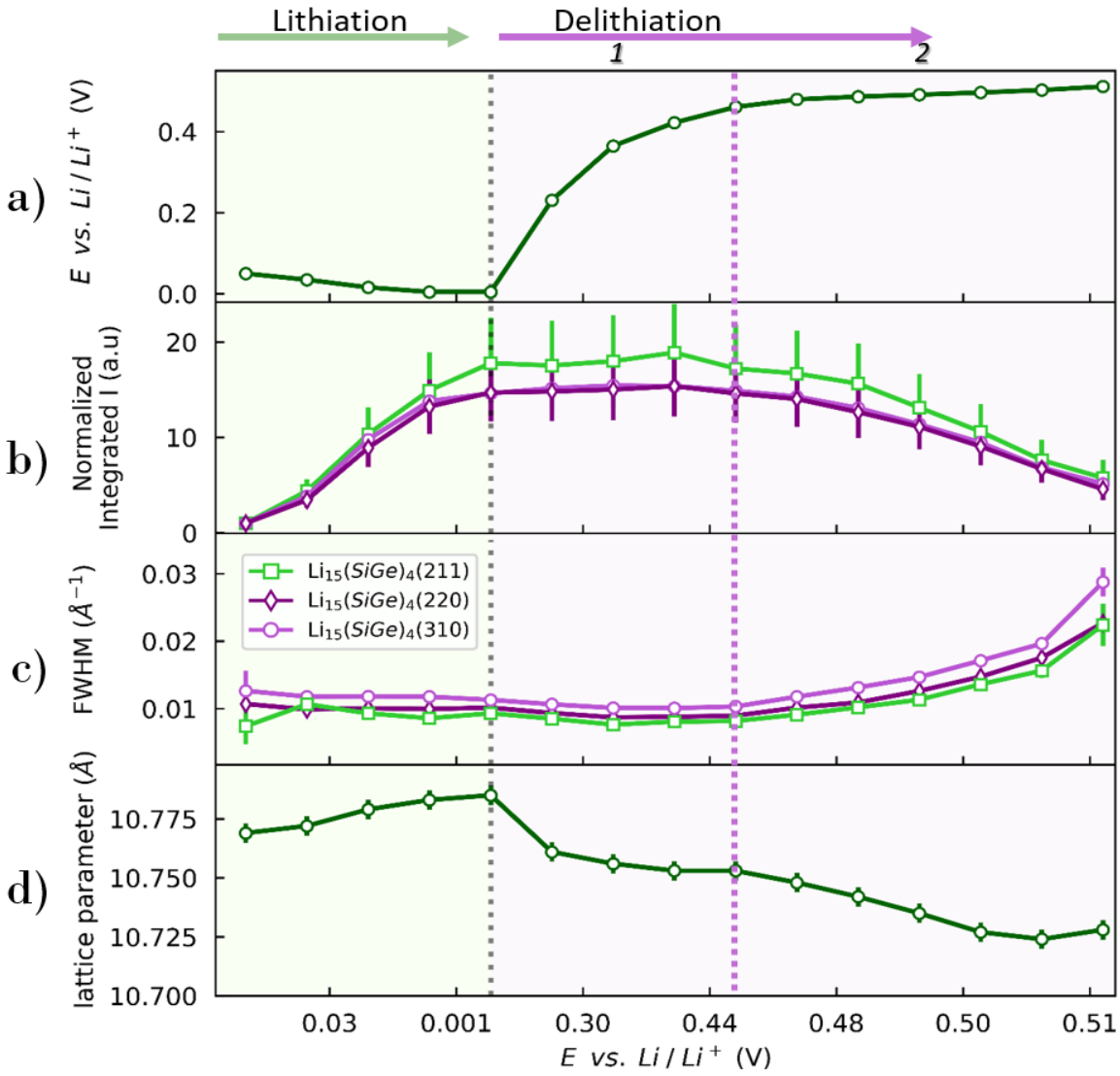

Figure 4.15 a) voltage vs. Li/Li⁺ b) Intensity c) FWHM for the mentioned reflections, and d) Lattice parameter for the obtained $Li_{15}(Si_{100-x}Ge_x)_4$ from the Ge-rich ($Si_{21}Ge_{79}$) self-supported electrode during lithiation/delithiation. Note that here, time was replaced by the corresponding voltage vs. Li/Li⁺.

Analogous lattice parameter behavior for $Li_{15}(Si_{50}Ge_{50})_4$ has been reported by Loaiza *et al*[10]. The behavior common to $Li_{15}(Si_{100-x}Ge_x)_4$ and $Li_{15}Ge_4$ phases could be related to the atomic restructuration to withstand deformation in $Li_{15}(Si_{100-x}Ge_x)_4$ or $Li_{15}Ge_4$ structure[16,17].

Figure 4.16 summarizes the evolution of the normalized integrated intensity of the $Li_{15}Ge_4(220)$ and $Li_{15}(Si_{100-x}Ge_x)_4(220)$ Bragg peaks obtained for Ge, $Si_{21}Ge_{79}$, and $Si_{47}Ge_{53}$, evidencing the voltages of formation and disappearance

of the crystalline lithiated phase. It clearly shows that the $Li_{15}(Si_{100-x}Ge_x)_4$ phase forms at the end of lithiation between 50 and 10 mV.

Then, it gradually disappears during delithiation at the potential plateau within 450 and 510 mV. The higher the Ge content, the higher voltage the $Li_{15}(Si_{100-x}Ge_x)_4$ phase disappears during delithiation. The corresponding values are approximately 0.46, 0.5, and 0.51 V, for $Si_{47}Ge_{53}$, $Si_{21}Ge_{79}$, and Ge, respectively.

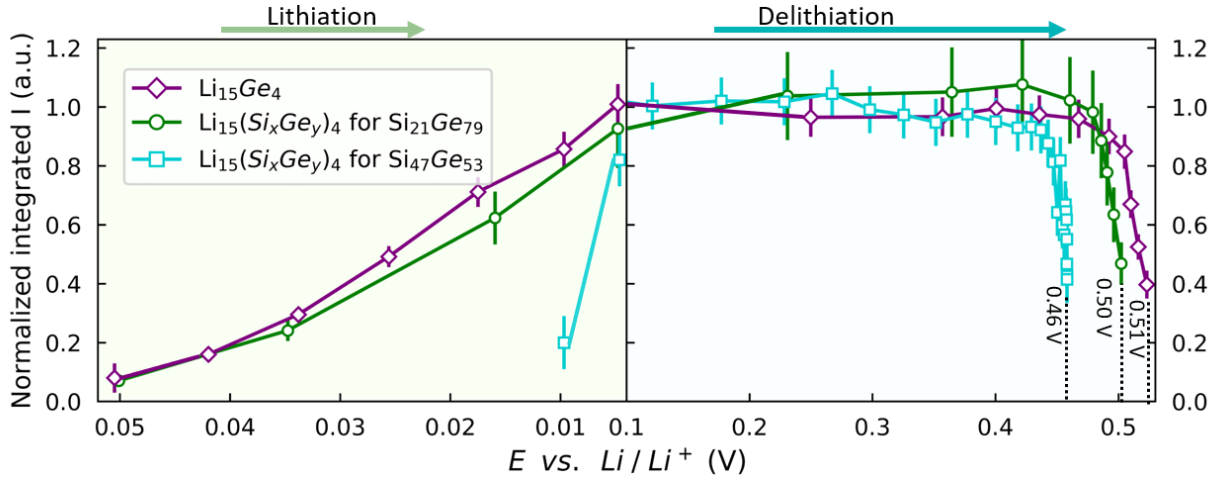

Figure 4.16 Normalized integrated intensity for the reflection $Li_{15}Ge_4(220)$ and $Li_{15}(Si_{100-x}Ge_x)_4(220)$, obtained for Ge, $Si_{21}Ge_{79}$, and $Si_{47}Ge_{53}$ against voltage vs. Li/Li^+ during lithiation and delithiation.

Figure 4.17 compares the dQ/dV lithiation peaks obtained from the galvanostatic cycling in coin-cells (Figure 4.7f–h) with the evolution of the $Li_{15}Ge_4(220)$ and $Li_{15}(Si_{100-x}Ge_x)_4(220)$ from $Si_{21}Ge_{79}$ and $Si_{47}Ge_{53}$ to correlate the effect of Ge content on these phases with the electrochemical curves.

Interestingly, for pure Ge, Ge-rich, and Si≈Ge alloys, the voltages at which the $Li_{15}Ge_4$ and $Li_{15}(Si_{100-x}Ge_x)_4$ phase disappears are in remarkable agreement with the voltage of the delithiation dQ/dV peak, and these values increase when increasing Ge content.

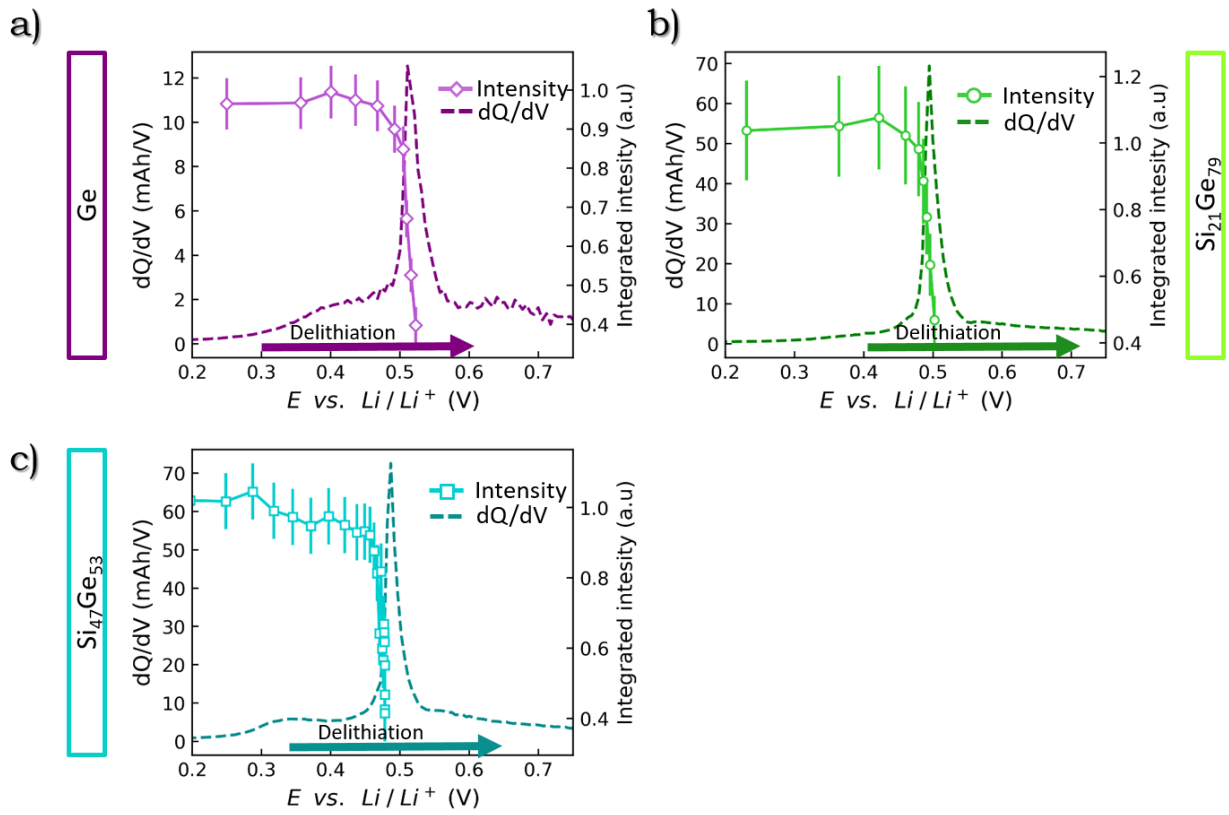

Figure 4.17 The dQ/dV graphs overlap the normalized integrated intensity for the (220) Bragg reflection of a) $Li_{15}Ge_4$ obtained from pure Ge b) $Li_{15}(Si_{100-x}Ge_x)_4$ obtained for $Si_{21}Ge_{79}$, and c) $Si_{47}Ge_{53}$.

4.3.3.1 *Considerations on the composition of the $Li_{15}(Si_{100-x}Ge_x)_4$ phase*

While the $Si_{100-x}Ge_x$ diffraction peaks are very broad due to the heterogeneities in composition, more particularly in the case of the Ge-rich alloy, it is not the case for the $Li_{15}(Si_{100-x}Ge_x)_4$ peaks. For instance, while the $Si_{100-x}Ge_x$(220) peaks are broader (FWHM ~ 0.6 $Å^{-1}$), the $Li_{15}(Si_{100-x}Ge_x)_4$ peaks are narrower (FWHM ~ 0.1 $Å^{-1}$). Moreover, the lattice parameter values for $Li_{15}(Si_{100-x}Ge_x)_4$ are very close to those determined for $Li_{15}Ge_4$, with values closer to 10.78 Å, for both pure Ge and the Ge-rich alloy. All this leads us to propose that under the lithiation conditions, which are those of our measurements, the lithiated

crystalline phase $Li_{15}(Si_{100-x}Ge_x)_4$ is formed only in a very restricted range of composition, namely for x close to 100.

4.3.3.2 *Correlating the structural changes with the electrochemical performance*

Some authors have reported a decrease in the specific capacity for micron size Ge when $Li_{15}Ge_4$ is partially formed at higher C-rates (such as C/10). In comparison, the specific capacity is constant over cycling when $Li_{15}Ge_4$ is entirely formed. They conclude that a cut-off potential could be applied to avoid the partial formation of $Li_{15}Ge_4$ at high C-rates, thus obtaining a constant specific capacity over cycling[18], as it is done for Si electrodes.

In our case, an excellent specific charge capacity is obtained when charging down to 10 mV over 60 cycles at C/20. At this voltage, the phase $Li_{15}(Si_{100-x}Ge_x)_4$ is totally formed for Ge, $Si_{21}Ge_{79}$ (formation at 50 mV), but only partially in $Si_{47}Ge_{53}$ (formation at 10 mV, see Figure 4.16). In any case, the SiGe alloys and pure Ge present a constant specific charge capacity over cycling. Thus, we believe that in our case, the formation of $Li_{15}(Si_{100-x}Ge_x)_4$ may not be an issue to obtain good cycling performance since the particle size, ranging from few to tens of nanometers, shortens the lithium diffusion length, improving the cycling stability together with the excellent diffusion properties of Ge. Therefore, $Li_{15}(Si_{100-x}Ge_x)_4$ may be formed even at high C-rates. We have obtained very recently data that prove the formation of $Li_{15}(Si_{100-x}Ge_x)_4$ at C/2.

4.4 Conclusion

After having demonstrated, in the previous chapter, the robust behavior of germanium during cycling compared to silicon, which can, to a large extent, be attributed to its mechanical properties, we have devoted this chapter to a detailed study of the (de)lithiation mechanisms at play in $Si_{100-x}Ge_x$ alloys. Silicon/germanium nanostructures that combine the high specific capacity of silicon with the mechanical resilience of germanium are promising anode materials for high stability, high capacity, and fast cycling Li-ion batteries. We investigated three compounds synthesized by laser pyrolysis and differing by their germanium content (Si-rich $\langle x \rangle$ = 37%, Si≈Ge $\langle x \rangle$ = 53%, and Ge-rich $\langle x \rangle$ = 79%) using *operando* X-ray scattering.

The characterization of the pristine powders evidenced strong heterogeneities in composition and size. The Ge-rich alloy was thus revealed to be mainly a mixture of four different $Si_{100-x}Ge_x$ phases with x ranging between 67% and 100%, while two component phases were identified for the Si≈Ge compound. A significant amorphous phase characterizes the Si-rich alloy. However, the crystalline part is more homogeneous with only one composition.

The different phases in a given sample start lithiating sequentially, depending on their Ge content upon cycling. Despite the heterogeneous character of these alloys, the different $Si_{100-x}Ge_x$ component phases behave remarkably coherent, their characteristic lithiation voltage following a linear increase with Ge content.

Galvanostatic cycling performed with coin-cells evidenced different voltage signatures for the three alloys, with a monotonous evolution of the characteristic voltage values with Ge content. Surprisingly the structural heterogeneities are not reflected in the electrochemistry curves. While the Si-rich alloy is reminiscent of pure Si, the two others behave qualitatively as pure Ge. In particular, they evidence a sharp peak in the delithiation stage, which we show to be directly correlated to the disappearance of the c-$Li_{15}(Si_{100-x}Ge_x)_4$ phase.

This crystalline $Li_{15}(Si_{100-x}Ge_x)_4$ phase forms with the Ge-rich and Si≈Ge alloys at the end of the lithiation and disappears in the delithiation stage at a voltage value that increases with the Ge content. The evolution of the integrated intensity, full width at half maximum, and the lattice parameter are very similar to $Li_{15}Ge_4$. The correlation between the electrochemistry and the structural evolution obtained from the *operando* XRD confirmed the specific behavior of the $Si_{100-x}Ge_x$ alloys, behaving differently from pure Si and Ge.

Moreover, the $Li_{15}(Si_{100-x}Ge_x)_4$ peak shape can be accounted for considering a single peak that does not support the existence of composition heterogeneities. This leads us to propose that under the lithiation conditions, which are those of our measurements, the lithiated crystalline phase $Li_{15}(Si_{100-x}Ge_x)_4$ is formed only in a very restricted range of composition, namely for x close to 1.

The studied $Si_{100-x}Ge_x$ *alloys*, characterized by a strong heterogeneity, consequently present an intrinsic variability of composition and, therefore, in the mechanical properties, which must reinforce their robustness. Indeed, they exhibit remarkable electrochemical properties and aging behavior.

Interestingly, the electrochemical behavior does not reflect the structural heterogeneity.

4.5 Bibliography

1. Abel, P. R. *et al.* Nanostructured Si(1- x)Gex for Tunable Thin Film Lithium-Ion Battery Anodes. *ACS Nano* **7**, 2249–2257 (2013).

2. Stokes, K. *et al.* Direct Synthesis of Alloyed Si1–xGex Nanowires for Performance-Tunable Lithium-Ion Battery Anodes. *ACS Nano* **11**, 10088–10096 (2017).

3. Desrues, A. *et al.* Best Performing SiGe/Si Core-Shell Nanoparticles Synthesized in One Step for High Capacity Anodes. *Batter. Supercaps* **2**, 970–978 (2019).

4. Duveau, D., Fraisse, B., Cunin, F. & Monconduit, L. Synergistic Effects of Ge and Si on the Performances and Mechanism of the GexSi1– x Electrodes for Li-Ion Batteries. *Chem. Mater.* **27**, 3226–3233 (2015).

5. Campbell, I. H. & Fauchet, P. M. The Effects of Microcrystal Size and Shape on the One Phonon Raman Spectra of Crystalline Semiconductors. *Solid State Commun.* **58**, 739–741 (1986).

6. Mishra, K. *et al.* Submicro-Sized Si–Ge Solid Solutions with High capacity and Long Cyclability for Lithium-Ion Batteries. *J. Mater. Res.* **33**, 1553–1564 (2018).

7. Ge, M. *et al.* Capacity Retention Behavior and Morphology Evolution of SixGe1– x Nanoparticles As Lithium-Ion Battery Anode. *Nanotechnology* **26**, 255702 (1–9) (2015).

8. Bridel, J.-S., Azaïs, T., Morcrette, M., Tarascon, J.-M. & Larcher, D. Key Parameters Governing the Reversibility of Si/Carbon/CMC Electrodes for Li-Ion Batteries. *Chem. Mater.* **22**, 1229–1241 (2010).

9. Philippe, B. *et al.* Nanosilicon Electrodes for Lithium-Ion Batteries: Interfacial Mechanisms Studied by Hard and Soft X-ray Photoelectron Spectroscopy. *Chem. Mater.* **24**, 1107–1115 (2012).

10. Loaiza, L. C. *et al.* Understanding the Lithiation/Delithiation Mechanism of Si1-xGex Alloys. *J. Mater. Chem. A* **5**, 12462–12473 (2017).

11. Hashimoto, Y., Machida, N. & Shigematsu, T. Preparation of Li4.4GexSi1-x Alloys by Mechanical Milling Process and Their Properties as Anode Materials in All-Solid-State Lithium Batteries. *Solid State Ionics* **175**, 177–180 (2004).

12. Zeilinger, M. & Fässler, T. F. Structural and Thermodynamic Similarities of Phases in the Li–Tt (Tt = Si, Ge) Systems: Redetermination of the Lithium-Rich Side of the Li–Ge Phase Diagram and Crystal Structures of Li17Si4.0−x Gex for x = 2.3, 3.1, 3.5, and 4 as well as Li 4.1 Ge. *Dalt. Trans.* **43**, 14959–14970 (2014).

13. Gu, M. *et al.* Electronic Origin for the Phase Transition from Amorphous LixSi to Crystalline Li15Si4. *ACS Nano* **7**, 6303–6309 (2013).

14. Wang, F. *et al.* Electrochemical Reaction of Lithium with Nanostructured Silicon Anodes: A Study by In-Situ Synchrotron X-Ray Diffraction and Electron Energy-Loss Spectroscopy. *Adv. Energy Mater.* **3**, 1324–1331 (2013).

15. Gao, H. *et al.* Parasitic Reactions in Nanosized Silicon Anodes for Lithium-Ion Batteries. *Nano Lett.* **17**, 1512–1519 (2017).

16. Wang, H., Wang, X., Xia, S. & Chew, H. B. Brittle-to-ductile Transition of Lithiated Silicon Electrodes: Crazing to Stable Nanopore Growth. *J. Chem. Phys.* **143**, 104703 (1–7) (2015).

17. Cho, Y.-H., Booh, S., Cho, E., Lee, H. & Shin, J. Theoretical Prediction of Fracture Conditions for Delithiation in Silicon Anode Of Lithium-Ion Battery. *APL Mater.* **5**, 106101(1–7) (2017).

18. Lim, L. Y., Fan, S., Hng, H. H. & Toney, M. F. Storage Capacity and Cycling Stability in Ge Anodes: Relationship of Anode Structure and Cycling Rate. *Adv. Energy Mater.* **5**, 1500599(1–8) (2015).

Chapter 5

Lithiation mechanism of a silicon-graphite industrial composite anode

5.1 Introduction

Mixing Si with graphite (so-called composites materials) has demonstrated improved cycling performance. In this direction, the design of complex hierarchical structures, including nanostructuration of the active silicon phase, specific coatings, and/or use of inactive components, was attempted in recent years to mitigate the structural degradation[1]. Besides, a growing body of literature has reported that the addition of metal silicide alloys to composites materials, especially metal transition silicides, could decrease the electrical resistance of Si and reduce the volume expansion while cycling[2–8]. These improvements come from metal silicide alloys properties such as low electrical resistance compared to silicon, moderate reactivity with Li-ions, and stress relief. For instance, $FeSi_2$ is a good candidate since it has low reactivity with lithium (capacity < 60 mAh/g), lower resistivity (2.6×10^1 Ω cm) compared to silicon (6.0×10^3 Ω cm), and low breaking strength (213 ± 44 MPa)[4]. Besides, it is highly accessible due to its use in the production of stainless steel. One

of the several works on the combined c-$FeSi_2$ and silicon with graphite composite has reported a high capacity of 1010 $mAhg^{-1}$ and 94% capacity retention over 200 cycles[3]. A commercially available powder consisting of amorphous silicon and iron disilicide particles combined with graphite showed good capacity retention and efficiency over 50 cycles with lower initial irreversible capacities[9]. Thus, demonstrating that metal silicides in Si plus graphite is a promising strategy to improve Si cycling problems.

We have been working on such a silicon-graphite composite material in the frame of the European project SINTBAT. The objectives of the project were to demonstrate high cyclability and durability of (relatively high, e.g.,> 10 wt%) Si-content anodes for potential use as industrial battery components. To complement the R & D activities in the project and bring fundamental knowledge on the anodes behavior during cycling, our team designed a dedicated synchrotron experiment to follow in real-time the structural evolution of the composite material at the relevant length scales.

The particularity of this study, concerning our previous investigations on nanoparticles-based electrodes, is that the material is composed of two active phases: 1) graphite and 2) a complex silicon-containing phase formed by $FeSi_2$ crystalline particles embedded in amorphous nanoscale Si-domains. The two active phases contribute to the total capacity of the anode during cycling by different mechanisms: intercalation of lithium in between graphite planes (therefore, the formation of the various Li_xC_6 phases) and alloying process in silicon (formation of Li_xSi phases). The former can be typically quantified using X-rays diffraction, while the latter may require a nanoscale technique to

investigate the volume changes. Thus, our idea was to apply the simultaneous SAXS/WAXS synchrotron technique, uniquely available at ESRF in Grenoble, to probe both graphite and silicon phases structural evolutions and determine the process of sequential lithiation in the material. The results were published in ACS Nano in 2019[10] and are summarized in this chapter. I contributed to the experiments, diffraction data analysis, and some interpretations as part of a team effort with C. Berhaut as principal investigator. The industrial partner fabricated the electrodes, the coin cells assembled by CEA-LITEN, the microscopy performed by P-H. Jouneau and P. Kumar at IRIG.

5.2 Morphological and chemical composition of the composite

The negative electrode of SINTBAT is referred to as a-Si/c-$FeSi_2$/graphite composite, as it is composed of:

- Graphite (41%wt)
- L20772 powder from the 3M company (50% wt), an active Si-metal alloy composed of amorphous silicon (a-Si), crystalline iron disilicide particles (c-FeSi2), and graphite.
- Carbon black as a conducting agent (2%, Super P).
- Lithium polyacrylate (Li-PAA, 7%) as a binder.

  The total amount of silicon in this material is of ~ 13%.

5.2.1 Characterization of the a-Si/c-$FeSi_2$ alloy in powder

The diffracted pattern obtained for the 3M L20772 powder (Figure 5.1) shows sharp reflections for graphite and broad diffracted peaks for the tetragonal iron disilicide (α-$FeSi_2$). The orthorhombic iron disilicide (β-$FeSi_2$) is also present but in small quantities.

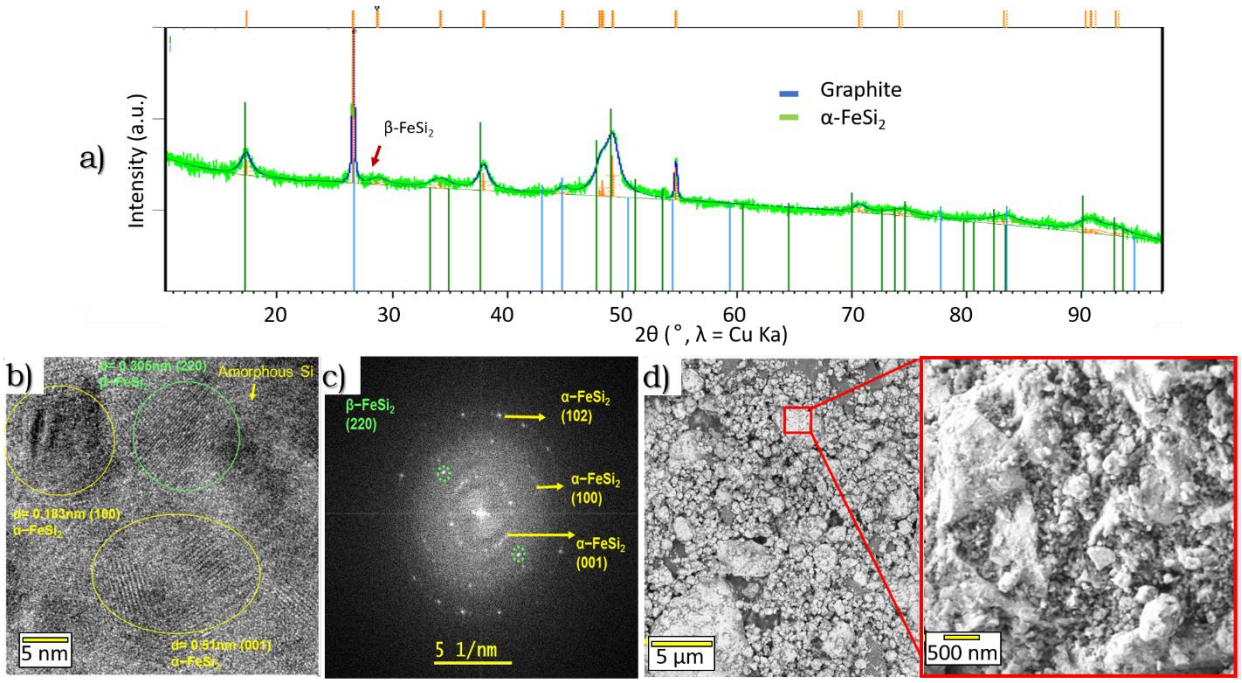

Figure 5.1 a) diffracted pattern of the alloy composed of a-Si/c-$FeSi_2$ and few graphite quantities. b) HRTEM images showing a-Si and c-FeSi2 regions of less than 20 nm in size. c) Fast Fourier transform (FFT) of the HRTEM image b) confirming the measured lattice spacings. d) SEM image of the alloy a-Si/c-$FeSi_2$ at two different lengths.

The high-resolution transmission electron microscopy (HRTEM) images of the 3M powder are shown in Figure 5.1 b–c, demonstrating distinct features: a continuous amorphous Si phase of diameter 15–20 nm, and the crystalline systems α and β $FeSi_2$ of about 5–15 nm. Figure 5.1b also displays the lattice fringes proving the crystallinity of the $FeSi_2$ that exists in two different crystal systems, mainly α-$FeSi_2$, and secondly, β-$FeSi_2$, confirming the XRD. Figure 5.1c shows the Fast Fourier Transform (FFT) of the corresponding image,

indicating that the nanodomains are crystalline, matching the α-$FeSi_2$ and β-$FeSi_2$ systems. Note that the background in the FFT pattern could come from the amorphous Si.

As seen on the SEM images on the active Si-metal alloy (Figure 5.1d), the powder morphology consists of disordered grains with two different length scales: large agglomerates up to 10 µm and smaller particles of 100–500 nm in diameter. A zoom into these (red square) reveals the existence of small embedded domains (from 5–20 nm).

These features confirm that the alloy is a complex mixture of active a-Si, graphite (in very few quantities), and c-$FeSi_2$ nanodomains with two crystalline phases: tetragonal iron disilicide (α-$FeSi_2$) and orthorhombic iron disilicide (β-$FeSi_2$).

5.2.2 Characterization of the pristine negative electrode

Varta Micro Innovation prepared the electrodes in the frame of the project. The diffracted pattern of a pristine negative electrode is shown in a. The α-$FeSi_2$ and β-$FeSi_2$ reflections are detected in powder, despite the high intensities from the copper (current collector) and the graphite reflections. The cross-sectional FIB-SEM image of the pristine electrode is reported in Figure 5.2, highlighting the main features of the morphology:

- Large graphite grains (size of ~10 µm).
- a-Si/c-$FeSi_2$ alloy domains of various sizes, ranging from few nanometers to few micrometers.
- Internal porosities in both graphite and alloy particles.

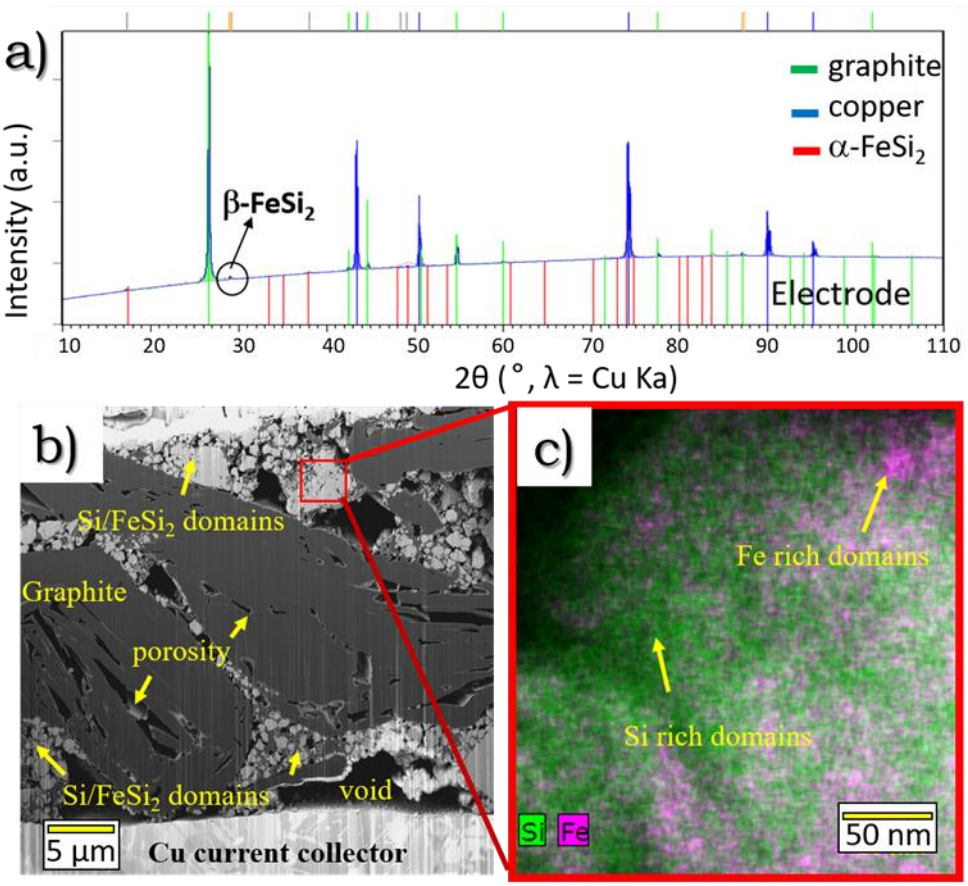

Figure 5.2 a) diffracted pattern of the negative electrode formulation in Cu. b) Cross-sectional FIB-SEM micrograph showing the hierarchical structure of different length scales for the negative electrode. c) High-resolution STEM-EDX chemical mapping of the a-Si/c-$FeSi_2$ alloy particle.

High-resolution elemental chemical mapping of the a-Si/c-$FeSi_2$ alloy was performed using STEM-EDX (Figure 5.2 c) to provide additional details on the nanoscale organization. It is observed that Si-rich (green) and Fe-rich (magenta) regions of less than 20 nm in size are dispersed through the alloy particle. Besides, Si-rich domains are connected across the particle, indicating an interlinked network of active a-Si material.

Globally, the electrode is a hierarchical material organized from nano-to micro-scales and composed of several distinct phases. Clearly, we can expect complex lithiation and aging mechanisms within such a multi-scale multiphase structure. In fact, excellent performances were obtained with this

anode in the full cell (e.g. After 300 charge/discharge cycles, the aged cell shows a 28.7% capacity loss at C/2), which must be related to their specific architecture.

5.3 Characterization of the composite anode by *Operando* small-angle and wide-angle X-ray scattering (SAXS and WAXS)

5.3.1 Principle of the measurement

The principle of the *operando* SAXS/WAXS synchrotron experiment is summarized in Figure 5.3.

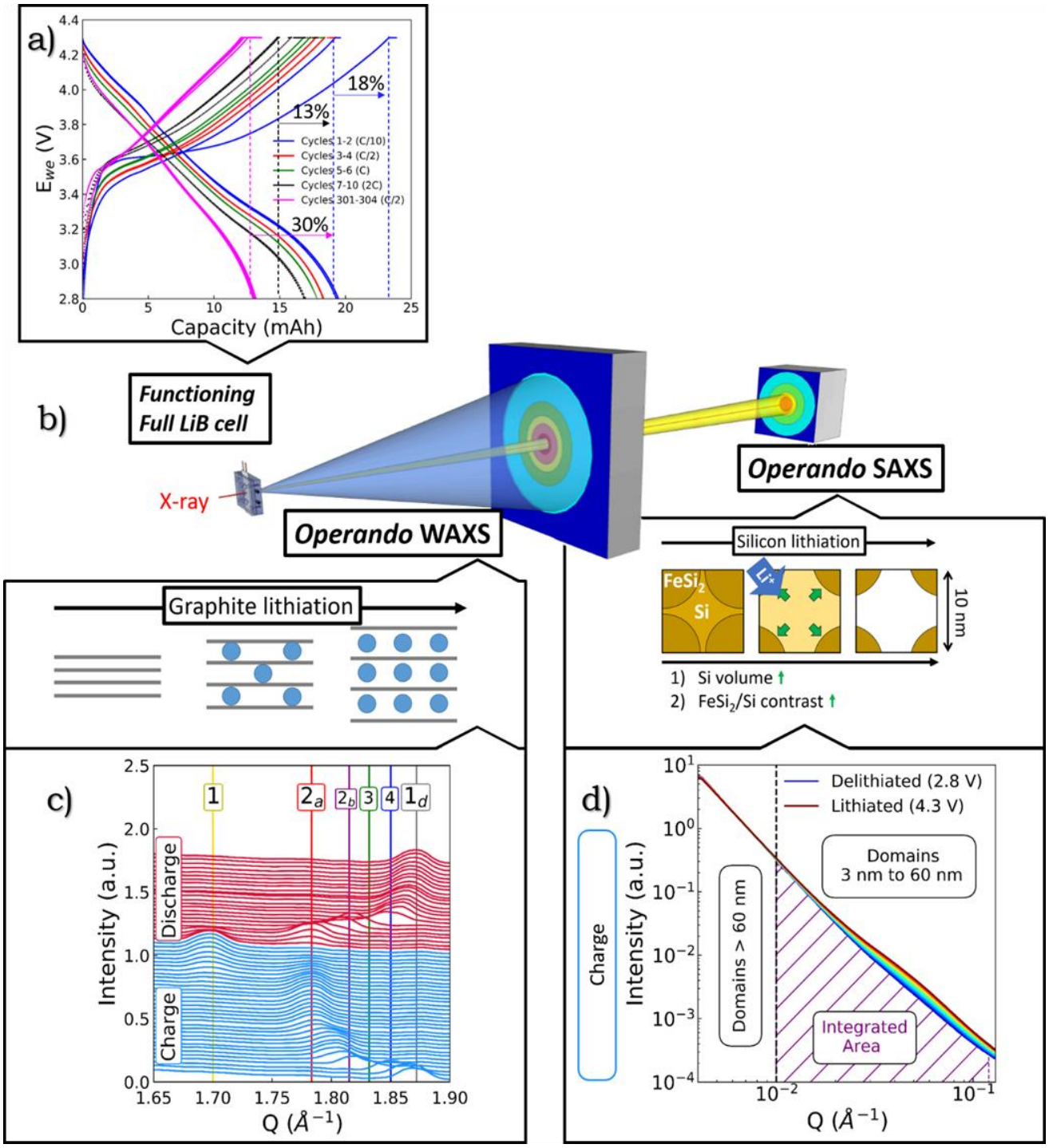

Figure 5.3 a) fresh and aged-cell charge/discharge profiles. The fresh full-cell was cycled at C/10, C/2, C, and 2C. The aged full-cell cycle 301 to 304 was cycled at C/2. Each cell charge ended with a constant voltage step. b) Scheme of the BM02 beamline set-up at ESRF. d) Variations of the WAXS intensities of the Bragg reflection for the graphite and graphite lithiated phases during full-cell charge and discharge. e) SAXS intensity variations over the full-cell charge from 2.8 to 4.3 V.

5.3.2 Cells and cycling conditions (Figure 5.3a)

Pouch cells assembled by our colleagues at CEA-LITEN (W. Porcher) were used. The investigated composite anode was cycled against $LiNi_{0.6}Mn_{0.2}Co_{0.2}$ (NMC) as a positive electrode in a full-cell configuration, using standard carbonate-based liquid electrolyte, hence fully representing the electrochemical cycle process that occurs within a real Li-ion battery. In this chapter, we describe the results obtained on a fresh cell cycled at C/10 and C/2. We also applied a sequence of charge/discharge with increasing rates up to 2C to evaluate the applied current impact on the (de)lithiation mechanism, and we also investigated the effect of aging after cycling by measuring a full-cell that was cycled 300 times before the synchrotron experiment (see the paper on ACS Nano for results on these aspects). On Figure 5.3a, the charge/discharge profiles of the $LiNi_{0.6}Mn_{0.2}Co_{0.2}$ (NMC)//a-Si/c-$FeSi_2$/graphite cells at different cycles are displayed. During the formation cycle (first cycle), the capacity loss is 18%, which could correspond to the formation of the SEI produced by the electrolyte decomposition at the surface of the negative electrode. The full-cell shows high capacity retention with a drop of 13% when increasing the C-rate from C/10 to 2C in the fresh cell, over the cycles number 2–10. After 300 charge/discharge cycles, the aged cell shows a 28.7% capacity loss at C/2, and the capacity loss does not vary much over cycles 301 to 304 at the same C-rate.

5.3.3 SAXS/WAXS set-up (Figure 5.3b)

The experiment was performed on the French beamline BM02 (D2AM) at the ESRF, which offers a unique set-up allowing the simultaneous, though independent, measurement of the small-angle and wide-angle scattering patterns. This is feasible thanks to the availability of two detectors, the first one being located close to the sample and having a hole in its center, allowing the beam scattered at very small angles to pass through it and to be collected on the second detector located 3 meters behind. Hence, WAXS data are recorded on the first detector while SAXS data are recorded on the second one, on the very same cell in the very same conditions. This is clearly very advantageous as it provides information on the local atomic structure and the nanoscale structures simultaneously in one single measurement.

5.3.4 Experimental data (Figure 5.3 c–d)

Typical 1D WAXS and 1D SAXS data obtained after radial averaging of the 2D patterns are shown in Figure 5.3c and d. The pouch-cell was measured in transmission geometry; thus, all the components contribute in principle to the scattering intensity. However, in the WAXS data, we can easily isolate the features of interest, e.g., graphite peaks and its lithiated phases. As seen in Figure 5.3 c, we can follow the evolution of the peaks during the charge (blue) and the discharge (red) and observe the different stages formed during cycling, starting from pure graphite (1d) up to the most lithiated LiC_{12} (2) and LiC_6 (1) phases. Quantitatively, the amount of each phase at a given potential is obtained by fitting the peaks with Gaussians and extracting their relative intensities. Regarding the SAXS data, we observe clear changes with time,

showing that we are sensitive to some structural evolutions in the range of typically few tens of nanometers. In general, SAXS measurements allow the observation of structural correlations at the nanoscale (1 to 100 nm, typically); thus, the technique is suited to investigating nanostructures like nano-object-assemblies or phase-separated composites. The SAXS profiles in Figure 5.3d are relatively smooth and decay in intensity as a function of momentum transfer Q, starting at low Q values of 10^{-2} $Å^{-1}$ by a so-called Porod's behavior (Q^{-4} power-law) typical of large objects (> 60 nm) that have well-ordered interfaces. Interestingly, the SAXS profiles show a continuous change during charge (blue to red) in the range of Q = [10^{-2}; 10^{-1}] $Å^{-1}$, corresponding to mean characteristic distances of 6 to 60 nm. These distances agree with the sizes of the active a-Si and c-$FeSi_2$ nanodomains as observed by microscopy (Figure 5.1b and Figure 5.2c), which supports the attribution of the additional SAXS intensity in the region [10^{-2}; 10^{-1}] $Å^{-1}$ to the nanostructural variations of the active amorphous silicon embedded in $FeSi_2$ crystallites. This amorphous silicon is expected to undergo significant volumetric variations due to the lithiation and delithiation (~300%). Of course, as said before, the data are recorded in transmission, therefore potentially containing contributions from all the battery components. However, no other phase than silicon is expected to vary on the length scales probed in the SAXS configuration (in particular, no evolution of the graphite or NMC particles nanoscale morphology; see post-mortem SANS results included in our publication to support this assumption). Finally, it is worth underlining that the SAXS profiles change both in intensity and shape during cycling. This is important because it indicates that both the mean composition and size/shape of the scattering objects is changing,

producing intricate effects in terms of contrast variation + form factor variations (as we will discuss later in more details, see also Methods, section 2.3.2 for the basics of SAXS theory).

To summarize, the realization of the SAXS/WAXS experiment on the cycling pouch cell provides two sets of data:

- *Operando* diffraction data allows quantifying the state of (de)lithiation of the graphite phase.
- *Operando* SAXS data allows probing the nanoscale swelling of the silicon phase (related to its lithiation state).

Consequently, *operando* and simultaneous small-angle and wide-angle X-ray scattering (SAXS and WAXS) present a crucial combination of experimental conditions to fully elucidate the (de)lithiation mechanism of the a-Si/c-$FeSi_2$/graphite anode. This method allows following the anode structure at two different scales, *i.e.*, atomic scale and nanoscale while cycling the full-cell.

5.4 Analysis of data: lithiation and delithiation mechanism

During the four days of the experiment we had on the BM02 beamline, we could apply a sequence of several charges/discharges on the fresh cell to continuously evaluate the behavior along with the first cycles. The evolution of the potential as a function of time is shown in Figure 5.4. The first cycle is different from the others because of the initial SEI formation. Hence, we

concentrate on the second cycle at C/10 to extract the main qualitative and quantitative information from these measurements.

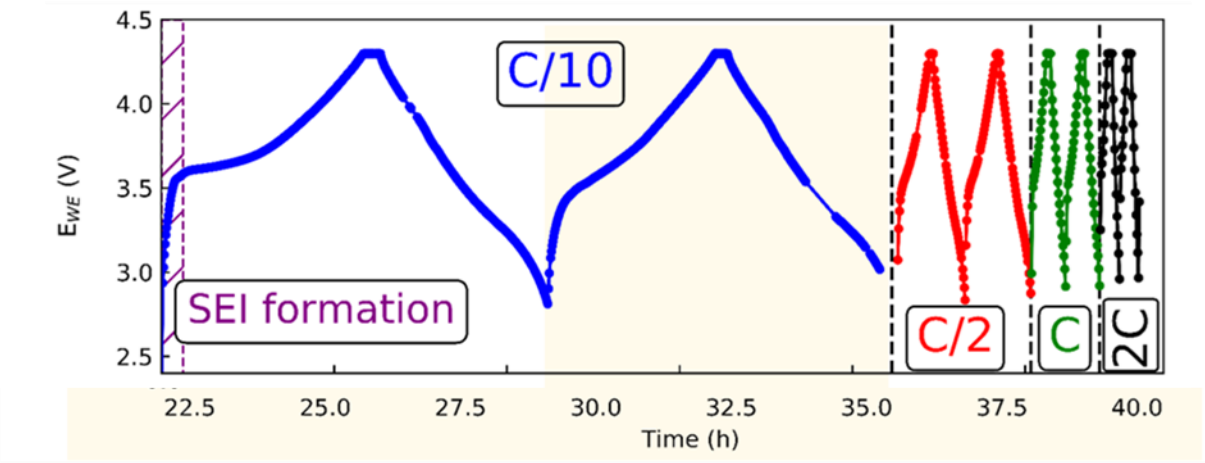

Figure 5.4 Electrochemical sequence applied to the fresh pouch cell at BM02. Evolution of the potential vs. time. The cell was cycled at several C-rates: C/10 (blue), C/2 (red), C (green), and 2C (black).

5.4.1 Analysis of the WAXS data

The analysis of the WAXS data (exemplarily during the second cycle, the shadowed region in Figure 5.4a) is performed using a three-step method (Figure 5.5):

1 - The diffraction peaks are fitted using Gaussian functions centered on the nominal Q values of each lithiated graphite phase and graphite, as shown in Figure 5.5a. The Bragg reflections considered to describe graphite (de)lithiation were graphite (002)[11,12], LiC_{30}(006)[11], LiC_{24}(001)[11], LiC_{18}(004)[11], LiC_{12}(002)[12], and LiC_6(001)[12] corresponding to phases 1d, 4, 3, 2b, 2a, and 1, respectively.

2 - The integrated intensity of the various Bragg peaks corresponding to graphite and the lithiated phases were extracted and normalized to pure graphite peak at 0% SOC (Figure 5.5b). Visually, we can represent the appearance/disappearance and amount of each phase as a function of time

(Figure 5.5b), potential (Figure 5.5c), allowing then to define regions of (co)existence of Li_xC_6 phases (from I to IV during lithiation, V to IX during delithiation, Figure 5.5c for data at second cycle at C/10).

3 – To obtain graphite contribution to the total capacity, we normalized the integrated intensities of graphite and lithiated graphite phases by the F^2/V^2 (structure factor and volume of the unit cell, respectively) and the maximum graphite intensity. The percentages obtained represent the volume and weight distribution of each phase. After obtaining these weight distributions, we used Faraday law (see Equation 1, chapter 1) to calculate the graphite contribution to the cell capacity. Silicon contribution was obtained after subtracting the capacity stored in the graphite from the full-cell reversible capacity. We also estimated that the capacity for carbon black (~150 mAh g^{-1})[13] at 2 wt% in the electrode coating formulation and the c-$FeSi_2$ (close to 60 mAh/g)[4] were negligible. Figure 5.5 shows the results for the second at C/10.

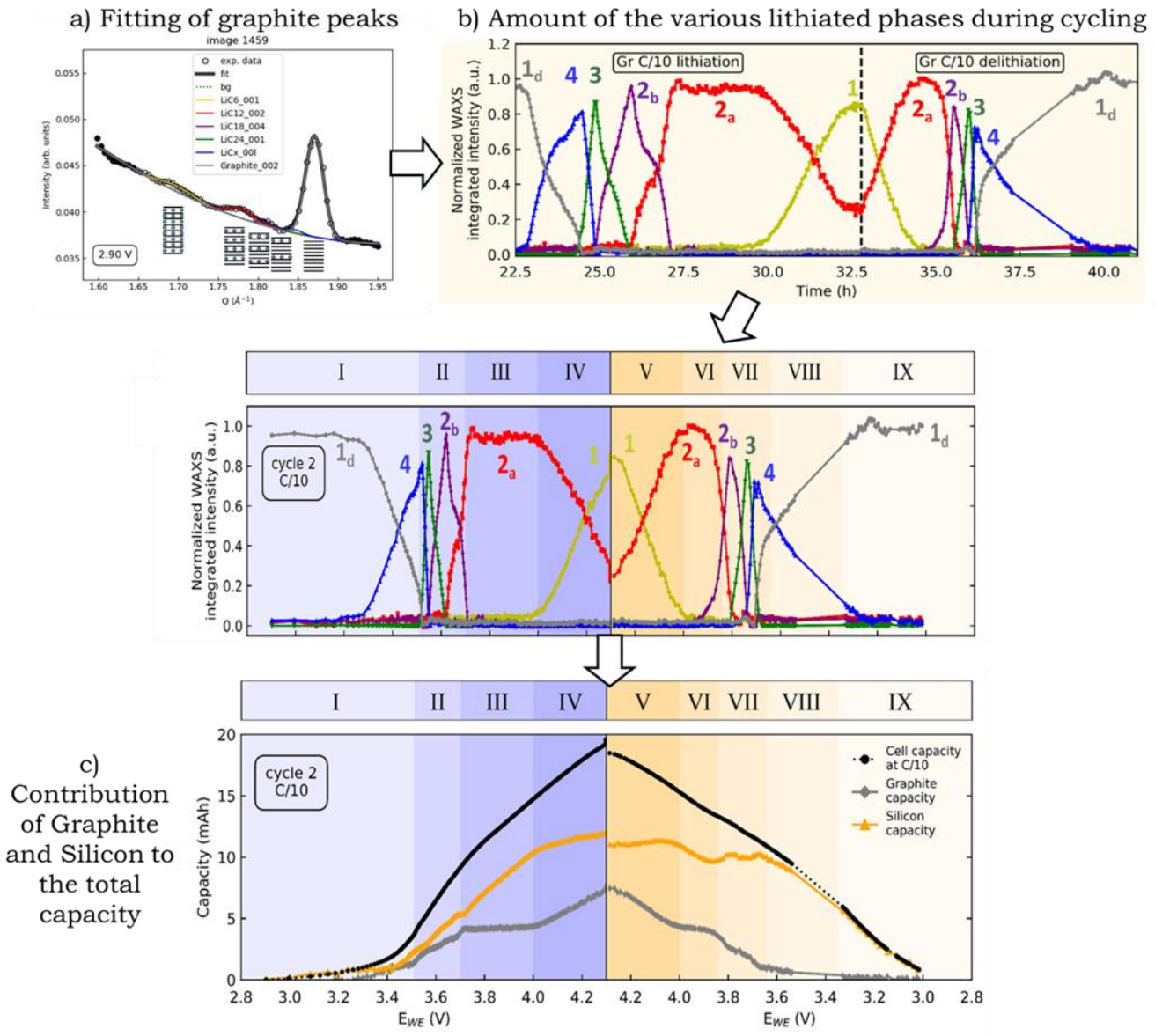

Figure 5.5 results for 2nd cycle at C/10. a) Example of WAXS data at a given potential/time during operando measurements (back dots) and fitting of the various peaks. b) Normalized peak areas of the lithiated graphite phases of the 1d (graphite), 4 (LiC_{30}), 3 (LiC_{24}), 2b(LiC_{18}), 2a (LiC_{12}), and 1 (LiC_6), as a function of time. Same data expressed in the function of potential. Shadowed area indicates lithiation (regions I to IV) and delithiation (regions V to IX). c) Amount of capacity provided by graphite (grey) and silicon (orange) to the total cell capacity (black) during lithiation (purple shadowed regions I-IV) and delithiation (orange shadowed regions V-IX) in the function of the potential.

The dilute lithiated graphite stage 1d (light gray) is present until 3.5 V. At this voltage, the phases 4 (blue), 3 (green), and 2b (purple) appear successively and coexist between 3.60 and 3.65 V, with maximum intensity at 3.55, 3.60 and 3.67 V, respectively. Phase 2a (red, LiC_{12}) appears at 3.66 V in the middle of stage II and reaches the maximum in integrated intensity at 4.0 V. At this

voltage; the full-cell capacity is above half of the total reversible capacity (20 mAh). At stage III, from 3.82 to 4.00 V, the only phase observed is 2a (LiC_{12}), and the change of the normalized intensity against capacity is almost flat. The presence of this plateau suggests that the graphite lithiation has paused. From 4.0 to 4.3 V, both phases 2a (LiC_{12}) and 1 (LiC_6) coexist, while phase 2a is slightly decreasing, phase 1 increases. After 4.3 V, a constant voltage was added to maximize the charge capacity.

Graphite delithiation occurs after the current is reversed, and the delithiation mechanism process is not similar to that one during lithiation. Once the full-cell is discharged to half of the capacity (10 mAh), most of the lithiated graphite has been delithiated. At 3.3 V, all the lithium has been deintercalated from graphite when the cell is 37.5% charged. Remarkably, the SAXS integrated intensity is almost flat without changes during the half of graphite delithiation, and it starts to decrease after ~10 mAh. The data obtained on the graphite using WAXS and SAXS can be further exploited after evaluating the contribution of the two active phases: graphite and silicon, to the respective mechanism of lithiation and delithiation.

5.4.2 Analysis of SAXS data: information and evolution of silicon phase

In the analysis of SAXS data, there is no standard method available for treating this type of anode material. Usually, the SAXS intensities can be modeled in two-phase systems by assuming: 1) a scattering length density for each (typically, phase 1 is the particle, phase 2 is the medium), 2) a defined

shape and size of the nano-objects (typically, spheres, cylinders, rods, ribbons, and others) and 3) a type of interaction potential between them (most commonly, hard spheres). Here, we face several difficulties to develop a quantitative model:

- There are not only two well-defined phases, but potentially more than four for describing the electrodes consisting of pure silicon (transformed into lithiated silicon), $FeSi_2$ (supposed to be inactive), carbon/graphite (at the interface with silicon particles), binder (equally distributed), pores + electrolytes (in contact with silicon, in some places necessarily), SEI (formed at the silicon surface).
- The geometrical features are not regular, highly polydisperse by nature, such that introducing a particle-like distribution of silicon may be far from reality.

Given these considerations, we proceed to a qualitative inspection of the data. Keeping in mind that a variation in intensity without shape change must correspond to a $(\Delta\rho)^2$ change, while a change in shape is associated with a characteristic dimensional variation, we adopt a two-fold treatment:

- First, we integrate the SAXS intensity in the Q region of interest. In our system, we expect the variations in contrast and the integrated intensity to be dominant and reflect the mean composition of the silicon, e.g., primarily, therefore, to be proportional to the amount of alloyed lithium in it.

- Second, we analyze the changes in profile shapes to relate it to nanoscale dimensions variations.

5.4.2.1 *SAXS integrated intensities*

Figure 5.6a shows the SAXS intensity integrated in the Q-region where changes are continuously detected (Q-region 10^{-2} to 10^{-1} $Å^{-1}$; see a dashed region in Figure 5.3d) , during the whole sequence of cycling. Clearly, there is a direct correlation between the increase (decrease) of SAXS intensity during lithiation (delithiation), which correlates well with the expected volume expansion (contraction) of silicon. Focusing on the second cycle at C/10 (Figure 5.6b), we can observe that the profiles of integrated SAXS exhibit a very specific shape:

- During lithiation, the increase in SAXS intensity is not linear, but there are two break-in-slopes (indicated by red arrows).
- Delithiation starts with a SAXS plateau (indicated by a red arrow), and then the SAXS linearly decreases with time.

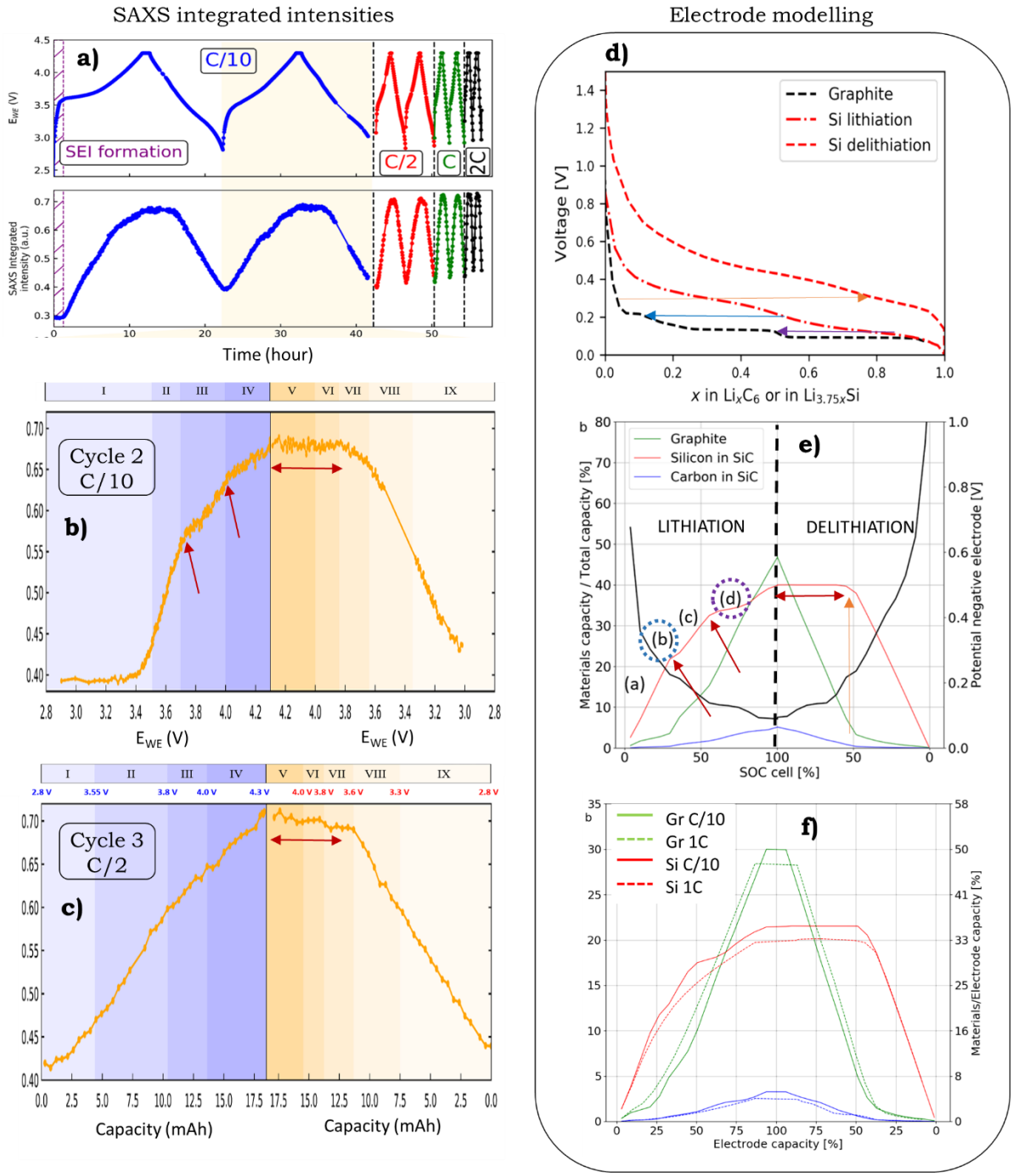

Figure 5.6 a) potential and SAXS integrated intensities as a function of time. Zoom on cycle 2. b) and cycle 3. c) data, expressed in function of potential and capacity, respectively. The arrows indicate changes in slopes during lithiation (purple shadowed regions) and delithiation (orange shadowed regions). d-f) Results from Newman-type modeling of composite electrodes containing 6.5 %wt silicon (courtesy of Marion Chandesris, LITEN). Voltage against lithiation degree (d). Simulated contributions of graphite (green) and silicon (orange) to the total capacity at C/10 (e) and higher C-rate (f).

On the third cycle at C/2 (Figure 5.6c), we observe that the lithiation profile is smoothed, showing a kinetics effect, while the delithation plateau is maintained.

To understand the origin of these features, we can compare our data to modeling data produced by our colleagues at CEA-LITEN (M. Chandesris and co-workers)[14], who developed a Newman-type approach on composites at the level of the porous electrodes (lower silicon content than ours, e.g., 6.5 wt%) (Figure 5.6d–f). By considering the equilibrium potentials of both graphite and silicon phases (Figure 5.6d), they were able to extract the amount of capacity provided to the cell by each phase (graphite in green, silicon in orange) during lithiation/delithiation at C/10 (Figure 5.6e) and higher C-rate (Figure 5.6f), as a function of the SOC of the cell. A striking resemblance is noticed regarding the silicon behavior concerning our data, pointing to 4 regions (labeled as a, b, c and d) with two characteristic boundaries indicated by red arrows, as well as the extended plateau in delithiation. In fact, regions b and c correspond to the plateau in the graphite voltage, while the delithiation is due to silicon hysteresis. Notably, the effect of increasing C-rate (Figure 5.6f) results in lithiation steps smoothed by kinetics effects and heterogeneity through the electrode, exactly as we have observed experimentally (Figure 5.6c).

The comparison with modeling allows us to:

- Ensure the consistency of our SAXS analysis and confirm that integrated intensities probably correlate directly to the state of lithiation of the silicon phase.

- The main features of the lithiation competition between graphite and silicon seem to be well captured by the electrode-level model.

- The main driving forces in the composite materials are the differences in potentials between the two active phases and the silicon hysteresis.

Although quite preliminary, these findings are a good indication of the benefits of using operando SAXS/WAXS to observe the behavior of silicon in complex multi-scale materials and use the data as validation inputs for further modeling and exploring a variety of designs and conditions numerically.

5.4.2.2 *SAXS profiles shapes and characteristic distances*

Besides the analysis using the integrated intensity, details on the nanoscale morphology can be accessed by considering the shapes of the SAXS scattering profiles and their evolution during charge/discharge.

As seen in Figure 5.7a, where selected spectra have been shifted vertically for visualization, a shoulder-type shape appears on lithiation (blue curves) and disappears on delithiation (red curves). Moreover, the position of the shoulder seems to vary in Q. Subtracting the initial SAXS intensity profile to the potential-dependent ones allows highlighting these Q-shifts of the local maximum (Figure 5.7b). Using this normalization of the SAXS operando data to the pristine SAXS profile, we can then treat these profiles more quantitatively. As seen in Figure 5.7c, the high Q intensity ($> 7 \times 10^{-2}$ Å^{-1}) scales as a power law of $Q^{-\alpha}$ (α closer to 4, independent of cycling state) because of well-defined interfaces between Si and $FeSi_2$ domains. Indeed, the closer is α to 4, the better defined are the interfaces between different domains. The asymptotic limit case ($\alpha = 4$, known as Porod's law) corresponds to sharp interfaces. The low-Q intensity ($< 3 \times 10^{-2}$ Å^{-1}) scales as a power law $Q^{-\beta}$ (β in the range 1 to 2), indicative of the dimensionality and rougher surfaces of the

scattering objects probed at this scale[15,16]. In the low-Q and intermediate Q region, the shape of the SAXS profiles is evolving, revealing local morphology changes.

The P(Q) and S(Q) variations (Equation 2.7, Chapter 2) are difficult to access by quantitative modeling due to the absence of any defined correlation peak, indicative of mean separation distances or oscillatory features that are usually ascribed to shaped objects of defined size and polydispersity. This lack of correlation peaks is due to the complexity and irregularity of the composite electrode nanostructure. However, a typical Q* value can be obtained by intercepting the power laws (Figure 5.7c).

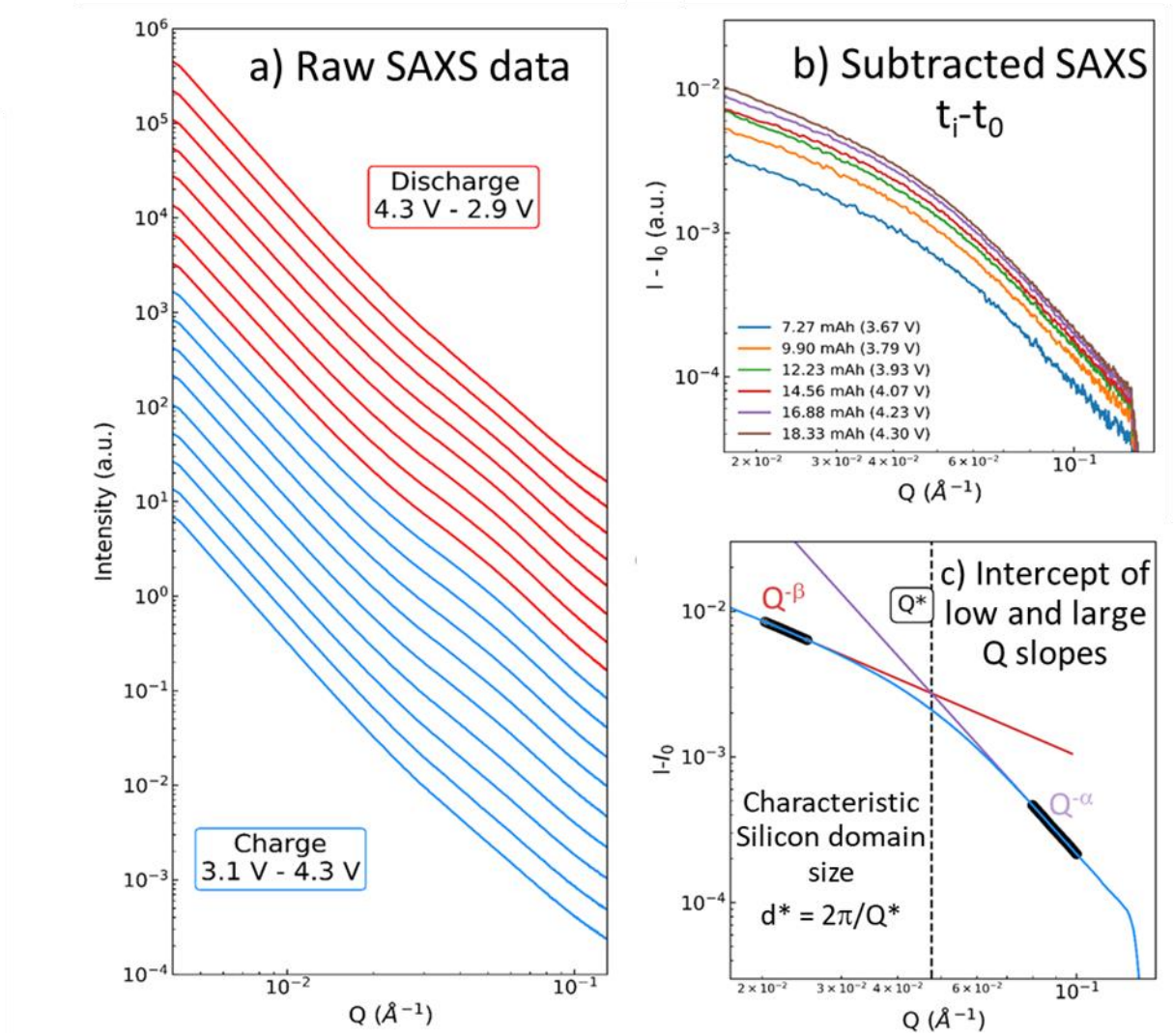

Figure 5.7 a) Selected SAXS profiles shifted vertically for clarity during lithiation (blue) and delithiation (red). b) Pristine-subtracted real-time data. c) Method to obtain the characteristic Q* value corresponding to the change in shape, i.e., intercepting the low-Q and high-Q asymptotic behaviors where the intensities scale as $Q^{-\beta}$ and $Q^{-\alpha}$ respectively.

The corresponding mean distance d* = 2π/Q* can be employed as a model-free, characteristic structural fingerprint of the material organization. The variations of d* as a function of the capacity are reported in Figure 5.8 for the fresh cell during charge/discharge at C/2 (a). Until the capacity reaches 6 mAh, the d* values increase from 9 to 12 nm, indicating a significantly expanded structure.

These d* values can be interpreted by considering a simplified model of the a-Si/c-$FeSi_2$ composite composed of isolated $FeSi_2$ of size d_{FeSi2} embedded in

amorphous active silicon with a characteristic extension of d*. Considering that the mass composition of a-Si and c-$FeSi_2$ closes to 30% and 70%, respectively, and assuming that d* = 9 nm, d_{FeSi2} can be calculated and is found to be close to 7 nm. Considering that d_{FeSi2} is constant, one can determine the value of d* in the fully lithiated state, which ends up around 12 nm. From the d* variations, it is thus believed that the active silicon does not behave like pure nanosized silicon. Pure nanosized silicon expands linearly with the silicon capacity during the whole lithiation phase as shown by Beaulieu *et al.*[17] We also notice that on the aged cell, where basically we could observe the same nature of mechanisms (although regions III–IV–V–VI are not attained), we measured d* varying from 11 to 12 nm, which could be a sign of irreversible aging of the silicon material that is not able to recover the initial size.

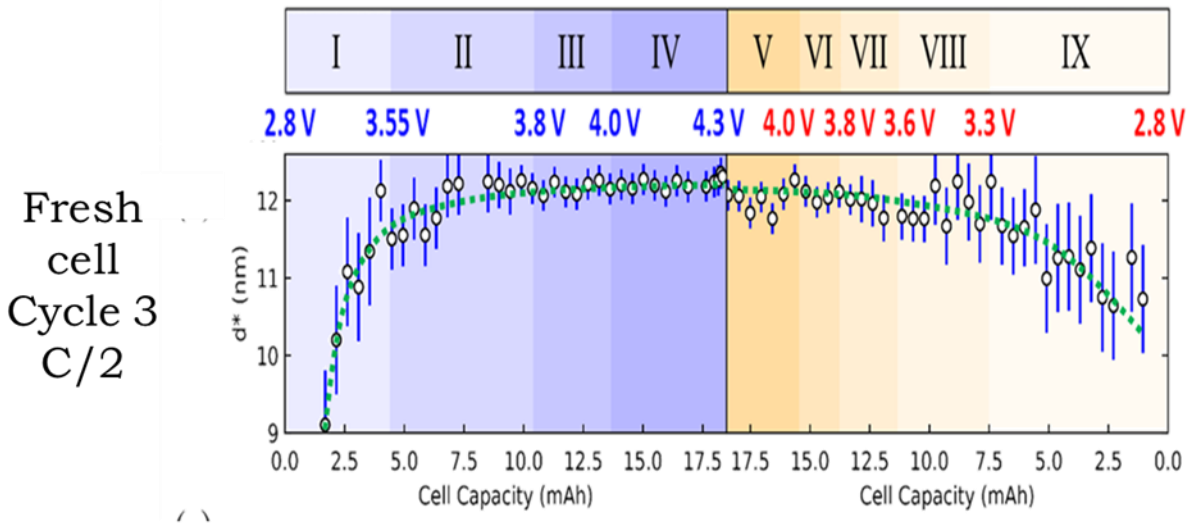

Figure 5.8 Variations of d* in the fresh cell.

5.5 Conclusions

We investigated the (de)lithiation mechanism of a-Si/c-$FeSi_2$/graphite composite and the role of the active components within a fresh full-cell at different current rates from C/10 up to 2C and after 300 cycles aged by using simultaneous *operando* small-angle and wide-angle X-ray scattering. Using WAXS, we investigated the graphite and lithiated graphite phases during cycling, making it possible to quantify graphite contribution to the capacity and deducing silicon contribution, in line with the previous works of Yao *et al*, for instance. Utilizing SAXS at the same time allow obtaining unique information on the nanoscale morphological changes of the silicon phase. Putting together SAXS and WAXS results, e.g., the impact of each phase into the capacity and the nanoscale changes, we could propose a mechanism of the a-Si/c-$FeSi_2$/graphite composite, as depicted in Figure 5.9.

Through the analysis of the results in Figure 5.4 and Figure 5.5, we could identify nine regions. In region I, the silicon and graphite start being lithiated while the active silicon phase is undergoing a significant volume increase. In region II, both silicon and graphite proceed with lithiation. The SAXS intensity becomes mostly dominated by contrast, and d* reaches its maximum; therefore, the silicon alloying process evolves to a continuous lithiation with a moderate nanoscale reorganization, a process more developed in phases III and IV. In region III, starting at 3.8 V, the graphite has been lithiated solely of LiC_{12}, and its lithiation pauses until the full-cell voltage reaches 4.0 V, while silicon capacity increases strongly. This process is consistent with the specific and different lithiation voltages for graphite and silicon. Once the LiC_{12} phase

is consumed, the voltage at which the graphite continues being lithiated becomes lower (voltage for producing LiC_6) than the needed for alloying silicon, favoring the lithiation of the later. Finally, the graphite lithiation continues in region IV, with the formation of LiC_6, while silicon lithiation slows down. The lithiation of graphite in this region suggests that the voltage is more favorable to the formation of LiC_6.

The delithiation process is also sequential; first, most lithium is extracted from the graphite lithiated phases, then from the silicon-alloy phases. The full-cell discharges in region V with the delithiation of LiC_6 into LiC_{12} between 4.3 and 4.0 V. Region VI is characteristic of samples lithiated at higher C-rates (> C/2), where the silicon phase delithiates 20% with no variation of SAXS integrated intensity profile. At the same time, the graphite capacity decreases weakly because of the coexistence of LiC_{12} and LiC_{18} phases. In region VII, most of the graphite is delithiated while the silicon capacity stays constant and higher than 40%. In region VIII, lithium-ions in the graphite are totally extracted, and silicon delithiation resumes. Interestingly, silicon shrinks (diminution of d*) in region IX once the graphite has been delithiated. The delithiation sequence also agrees with the one reported by Yao *et al.*[1818] and the modeling results. The morphology of the composite material consisted of dispersed c-$FeSi_2$ and amorphous silicon. Thus, the different volume variations compared to pure silicon could be the main reason for high cycling stability.

5.6 Perspectives

The SAXS data analysis using considerations based on chemical composition and typical sizes is insightful to follow the in-situ silicon (de)alloying mechanism by accessing both nanostructure and composition variations along with the battery cycling. Importantly, it provides direct observation of the silicon phase behavior, unlike the WAXS analysis, which is based on determining graphite phases and deducing silicon from it, which may have a range of error causes. In Figure 5.9, we summarize the advantages and drawbacks of our method with respect to the literature, main findings, and potential ways of improvements.

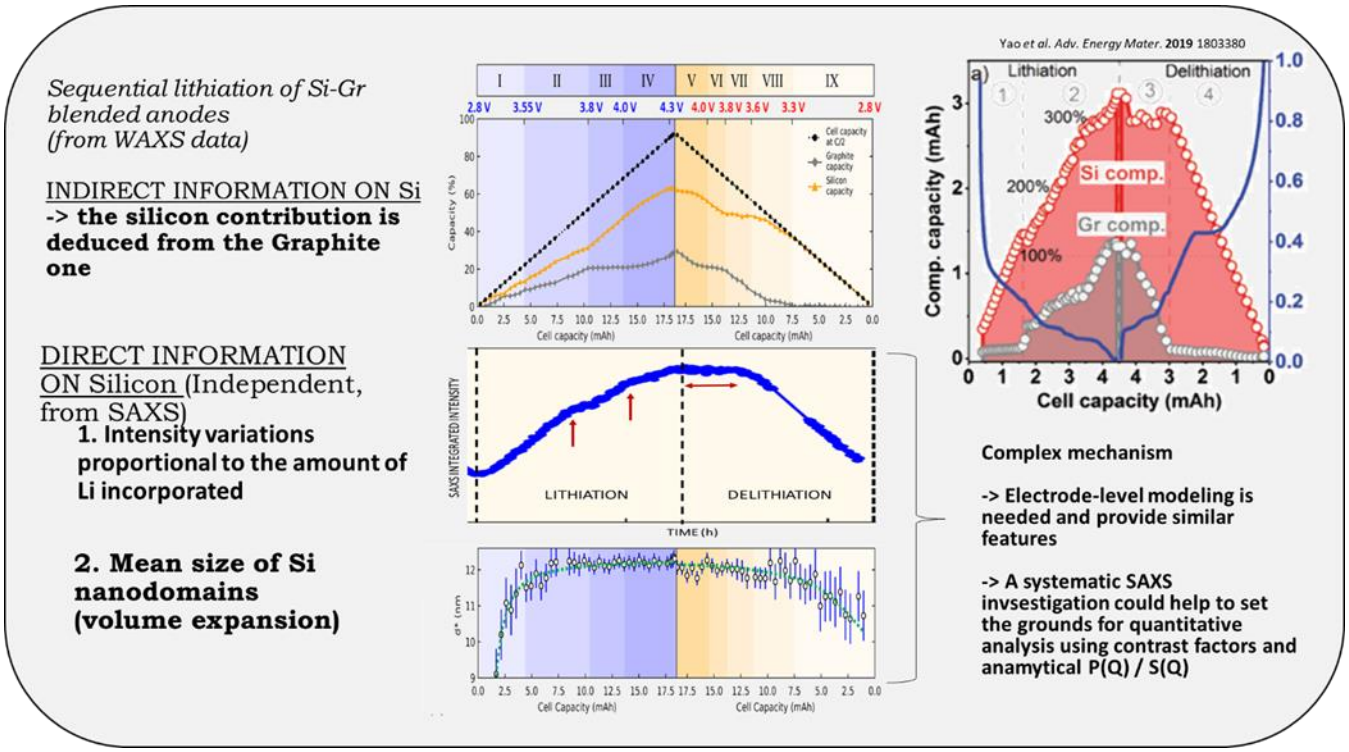

Figure 5.9 Summary of our approach, main findings, comparison to the literature.

5.7 Bibliography

1. Yang, Y. *et al.* Silicon-Nanoparticle-Based Composites for Advanced Lithium-Ion Battery Anodes. *Nanoscale* **12,** 7461–7484 (2020).
2. Lee, H.-Y. & Lee, S.-M. Graphite–FeSi Alloy Composites as Anode Materials for Rechargeable Lithium-Batteries. *J. Power Sources* **112,** 649–654 (2002).
3. Chen, Y., Qian, J., Cao, Y., Yang, H. & Ai, X. Green Synthesis and Stable Li-Storage Performance of FeSi 2 /Si@C Nanocomposite for Lithium-Ion Batteries. *ACS Appl. Mater. Interfaces* **4,** 3753–3758 (2012).
4. Usui, H. *et al.* Influence of mechanical grinding on lithium insertion and extraction properties of iron silicide/silicon composites. *J. Power Sources* **268,** 848–852 (2014).
5. Kang, I., Jang, J., Yi, K.-W. & Cho, Y. W. Porous Nanocomposite Anodes of Silicon/Iron Silicide/3D Carbon Network for Lithium-Ion Batteries. *J. Alloys Compd.* **770,** 369–376 (2019).
6. Choi, W. J., Reddyprakash, M., Loka, C., Jo, Y. W. & Lee, K.-S. Carbon Coated Si-Metal Silicide Composite Anode Materials Prepared by High-Energy Milling and Carburization for Li-Ion Rechargeable Batteries. *J. Electrochem. Soc.* **166,** A5131–A5138 (2019).
7. Kwon, H.-T. *et al.* Nanostructured Si-FeSi 2 -Graphite-C Composite: An Optimized and Practical Solution for Si-Based Anodes for Superior Li-Ion Batteries. *J. Electrochem. Soc.* **166,** A2221–A2229 (2019).
8. Jo, C. *et al.* Continuous-Flow Synthesis of Carbon-Coated Silicon/Iron Silicide Secondary Particles for Li-Ion Batteries. *ACS Nano* **14,** 698–707 (2020).
9. Chevrier, V. L. *et al.* Evaluating Si-Based Materials for Li-Ion Batteries in Commercially Relevant Negative Electrodes. *J. Electrochem. Soc.* **161,** A783–A791 (2014).
10. Berhaut, C. L. *et al.* Multiscale Multiphase Lithiation and Delithiation

Mechanisms in a Composite Electrode Unraveled by Simultaneous Operando Small-Angle and Wide-Angle X-Ray Scattering. *ACS Nano* **13,** 11538–11551 (2019).

11. Missyul, A., Bolshakov, I. & Shpanchenko, R. XRD Study of Phase Transformations in Lithiated Graphite Anodes by Rietveld Method. *Powder Diffr.* **32,** S56–S62 (2017).
12. Nazer, N. S. *et al.* In Operando Neutron Diffraction Study of a Commercial Graphite/(Ni, Mn, Co) Oxide-Based Multi-Component Lithium-Ion Battery. *J. Power Sources* **326,** 93–103 (2016).
13. Fransson, L., Eriksson, T., Edström, K., Gustafsson, T. & Thomas, J. O. Influence of Carbon Black and Binder on Li-Ion Batteries. *J. Power Sources* **101,** 1–9 (2001).
14. Lory, P.-F. *et al.* Probing Silicon Lithiation in Silicon-Carbon Blended Anodes with a Multi-Scale Porous Electrode Model. *J. Electrochem. Soc.* **167,** 120506(1-16) (2020).
15. Ciccariello, S., Goodisman, J. & Brumberger, H. On the Porod law. *J. Appl. Crystallogr.* **21,** 117–128 (1988).
16. Glatter, O. & Kratky, O. *Small angle x-ray scattering*. (Academic Press, 1982).
17. Beaulieu, L. Y., Hatchard, T. D., Bonakdarpour, A., Fleischauer, M. D. & Dahn, J. R. Reaction of Li with Alloy Thin Films Studied by In Situ AFM. *J. Electrochem. Soc.* **150,** A1457–A1464 (2003).
18. Yao, K. P. C., Okasinski, J. S., Kalaga, K., Almer, J. D. & Abraham, D. P. Operando Quantification of (De)Lithiation Behavior of Silicon-Graphite Blended Electrodes for Lithium-Ion Batteries. *Adv. Energy Mater.* **9,** 1803380 (2019).

Chapter 6

Capabilities of X-ray Raman scattering (XRS) for investigating the chemical environment in Si-based electrodes

6.1 Introduction

It is known that a stable solid electrolyte interface (SEI) is a key factor in maintaining a good cycling performance. The formation of the SEI comes usually from the decomposition of the carbonate-based liquid electrolytes and the inorganic fluorinated salt, e.g., most commonly, $LiPF_6$. One widely used strategy to form a stable SEI consists of using additives in the electrolyte, as fluoroethylene carbonate (FEC) and vinylene carbonate (VC)[1,2]. Besides organic polymers[3], the main decomposition products found in the SEI are Li_2O, Li_2CO_3, and LiF. Mainly, it has been reported that the reduction of FEC produces an additional quantity of LiF[4,5].

The SEI is formed on various active materials (including graphite; or cathodes, so-called CEI). The case of silicon in particular because Si-based materials

drastically change their volume during (de)lithiation, hence producing an unstable (often called “dynamic”) SEI that continuously forms and evolves during swelling/shrinking sequences.

The SEI in Silicon-based anodes SEI is characterized by:

- The main specific SEI products are insoluble organic polymers containing Li_xSiO_y.

- Some compounds of the SEI act as protective agents towards aging. For instance, the influence of LiF appeared to be beneficial since its formation next to the Si particles could avoid the continuous evolution of the SEI[6,7]. The distinctive products of decomposition of the FEC and VC additives in Si-based electrodes consist of interlinked polymers containing polyethylene oxides, called PEO with organic groups such as $–OCH_2CH_2O–$, $–OCH_2CH_2–$, and $–OCH_2CH_3–$ found as R in $ROCO_2Li$[8,9], which can also play a positive role. Jin *et al.* speculated that the effect of these interlinked polymers, which are directly linked with Si and SiO_x, consisted of slowing down the reactions of the solvents with the SEI[9]. Likewise, the interlinked polymers present elastic properties, helping to sustain the Si volume expansion[8,9].

In general, investigating the SEI is a true challenge because several compounds may be formed that can evolve during cycling. The internal structure of the layer (organic *vs.* inorganic regions, inhomogeneities, reactivity) and its thickness (from a few nanometers to hundreds of nanometers) make its observation and quantification extremely complicated.

Several techniques have addressed the chemical composition of the SEI in silicon anodes from different points of view by mostly *post-mortem* characterization, such as NMR[8,10,11], X-ray photoelectron spectroscopy (XPS)[1,12–15], Raman spectroscopy[16], Fourier transform infrared spectroscopy (FTIR)[17], and scanning transmission electron microscopy with energy-loss spectroscopy (STEM-EELS)[18].

Various of the mentioned techniques probe the sample with soft-photons (photon energy = several tens of eVs to few keVs), analyzing few nanometers of the sample. The main drawback of soft-photon spectroscopy techniques is that the information is restricted to the surface of the material, therefore not representative of the bulk characteristics, and potentially sensitive to surface contamination or intrusive sample preparation (for instance, washing may be necessary to remove electrolyte traces which may affect the integrity of the SEI and remove some compounds).

Alternatively, synchrotron X-ray Raman Scattering (XRS) is appealing as it can provide information on the electronic structures and chemical environment in the bulk of the material. Indeed, unlike well-known absorption techniques (XAS), where the incoming energy must be set to the value of the absorption edge of the probed element (typically, more than 1 keV – routinely used for Fe, Mn, Co, and other types of battery-containing heavy atoms), XRS is a non-resonant technique. Highly penetrating hard X-rays (10 keV) are used and inelastically scattered by the material with energy transfers ranging typically from few tens to few hundreds of eV. These characteristics provide access to soft X-ray edges (<1 keV, such as Li K, C K, O K, and F K edges) in the bulk of

the materials. Consequently, information on the light elements that form the main components of SEI, such as Li, C, O, and F, can be obtained. Of course, as the incoming energy is very far from the energy of the edge, other types of phenomena (for instance, Compton diffusion) contribute to the inelastic background in such measurements. It is important to optimize the signal-to-noise ratio, hence to count for typically few hours per edge (few days per sample), which makes *operando* studies unfeasible at present.

To date, XRS has been mainly used in battery research to study the chemical environment in cathode materials and graphite. For instance, Braun *et al.* demonstrated different oxidation states of Mn at the surface and the bulk in $LiMn_2O_4$ using XAS and XRS, respectively. They reported that the oxidation state changes within the electrode are due to progressive lithiation and delithiation in the material[19]. This effect has also been seen for $LiFePO_4$ electrodes using soft XAS and XRS, where the bulk had a higher lithiated level than the surface[20]. Changes in the spectra of C and Li K edge, while graphite is lithiated, have also been identified using XRS[21–24]. These pioneering studies indicated the potential interest of the technique, although quantitative analysis of the data is still in its infancy with respect to more established XAS or XPS.

In this work, we further explored the capabilities of X-ray Raman Scattering to study the SEI chemical environment at the bulk of silicon-based electrodes. To our knowledge, this is the first study that uses XRS on these anodes. XRS spectra data were obtained at the ID20 beamline at the ESRF with an X-ray beam of 9.8 keV. A general introduction to the concepts of XRS, our

experimental set-up, and data acquisition and processing methodologies were given in the methods chapter (section 2.4).

A quantitative description of the SEI is not straightforward, given that it is a multi-component layer with variable thicknesses, whose composition and characteristics depend on the nature of the active materials, the electrolyte, aging, cycling, and the state-of-charge conditions. Hence, our work was divided into three main tasks: define a methodology to exploit the XRS measurements, perform a qualitative inspection of the obtained data, and set the basis for a more quantitative type of analysis.

6.2 Aim and approach to investigate the SEI in electrodes by XRS

As said, XRS is a technique that can access chemical information from light elements using hard X-rays that can penetrate the bulk. To apply the technique to Si-based anodes, we adopted the following method:

1) Two types of negative electrodes were considered: crystalline silicon nanoparticles and the industrial composite made of amorphous silicon (a-Si), crystalline iron disilicide (c-$FeSi_2$), and graphite. The aim was to gather two sets of electrode data to perform XRS data interpretation and possibly identify the impact of the electrode architecture on the SEI.

1) All XRS measurements were performed *post-mortem*. The electrodes were cycled in coin cells *vs.* Li metal. The coin-cells were stopped in two states-of-charge, e.g., at the end of the first lithiation (lithiated state) and end of first

delithiation (delithiated state). One electrode was also stopped and dismounted after 300 cycles to evaluate the impact of long-term aging. Cells were dissembled in argon. Then, silicon-based electrodes were placed in a specially-designed air-tight XRS-compatible sample holder, as described in section 2.4.

3) We also measured XRS spectra on selected reference compounds to have a set of reference data. Since XRS has not been widely used to elucidate the organic and inorganic compounds in the SEI, there is almost no literature available to serve as a database. By reference compound, we mean:

- SEI-composing products of organic or inorganic type (expectedly formed in our systems). The main decomposition products from the SEI, as reported by NMR[8,9] and XPS[1,14,25] are Li_2CO_3 and LiF.
- Anode-making or containing components such as conductive additive (carbon black), binder (Na-CMC), and the salt used in the electrolyte, $LiPF_6$. The Na-CMC + Super P reference was prepared in a slurry that was deposited in Cu foil.
- The pristine anode composed of nanoparticles was also considered as a reference material representative of the typical environment of C, O, and Si in the absence of SEI.

By reference data, we mean XRS spectra that are, in principle, much simpler than the ones from the multi-component electrodes, where the signals arising from a given element present in distinct phases and/or

distinct environments. All measured references and anode samples are listed in Table 6.1.

Table 6.1 Reference compounds and Si-based electrodes measured by XRS.

Edges	References	Samples	
		c-Si	a-Si/c-$FeSi_2$/gr
Li K	• **Li**PF_6 • **Li**F • **Li**$_2CO_3$	• Lithiated • Delithiated	• Lithiated • 300 cycles delithiated *Delithiated: only C K edge
C K O K	• CMC (-**C**H_2-**C**O**O**H) • Li_2**C**O$_3$ • CMC+ Super P (Carbon black) • c-Si pristine electrode		
F K	• LiP**F**$_6$ • Li**F**		
Si $L_{2,3}$	• c-Si pristine electrode		

4) A qualitative study was performed by visually comparing the spectra of the lithiated and delithiated electrodes, on the one hand, and, next, by comparing them to the reference spectra to identify similar/different characteristic features allowing to hypothesize on the presence or not, of a given reference compound within one given anode sample. All edges were inspected in a systematic way. We usually considered the information from C and O edges together, as these relate to the same category of organic compounds, e.g., binder, polymers, carbonates. Similarly, we considered Li and F edge together, as they provide information on the $LiPF_6$ salt and the degradation compound LiF. Finally, we observed the Si edges as informative on the alloying process concerning the Li environment.

5) After the qualitative inspection of data, we used a semi-quantitative analysis by adjusting each electrode spectrum, at a given edge, with the best linear combination of reference spectra, according to Equation 6.1.

$$I_{edge}(sample) = \sum x_i \, I_{edge}\,(ref_i)$$

Equation 6.1

Where $I_{edge}(sample)$ is the XRS intensity of one electrode measured in the energy range of a given edge (for instance, Li was measured from 52 to 76 eV, F from 670 to 730 eV). $I_{edge}(ref_i)$ is the XRS intensity of the reference i compound measured at the same edge. x_i represents the corresponding weight of reference i spectra. This is a very simple way of decomposing the electrode signal onto a basis of elementary spectra, as for any function using its eigenvectors. However, this is correct only if the suite of reference spectra is orthonormal and dimension-complete. We will comment on these considerations later on in the results section.

6.3 XRS spectra of reference compounds

Figure 6.1 a–d shows the XRS spectra (intensity *vs.* energy loss, corrected from Compton effect) for the set of reference compounds that were measured to identify the chemical environment of the electrodes.

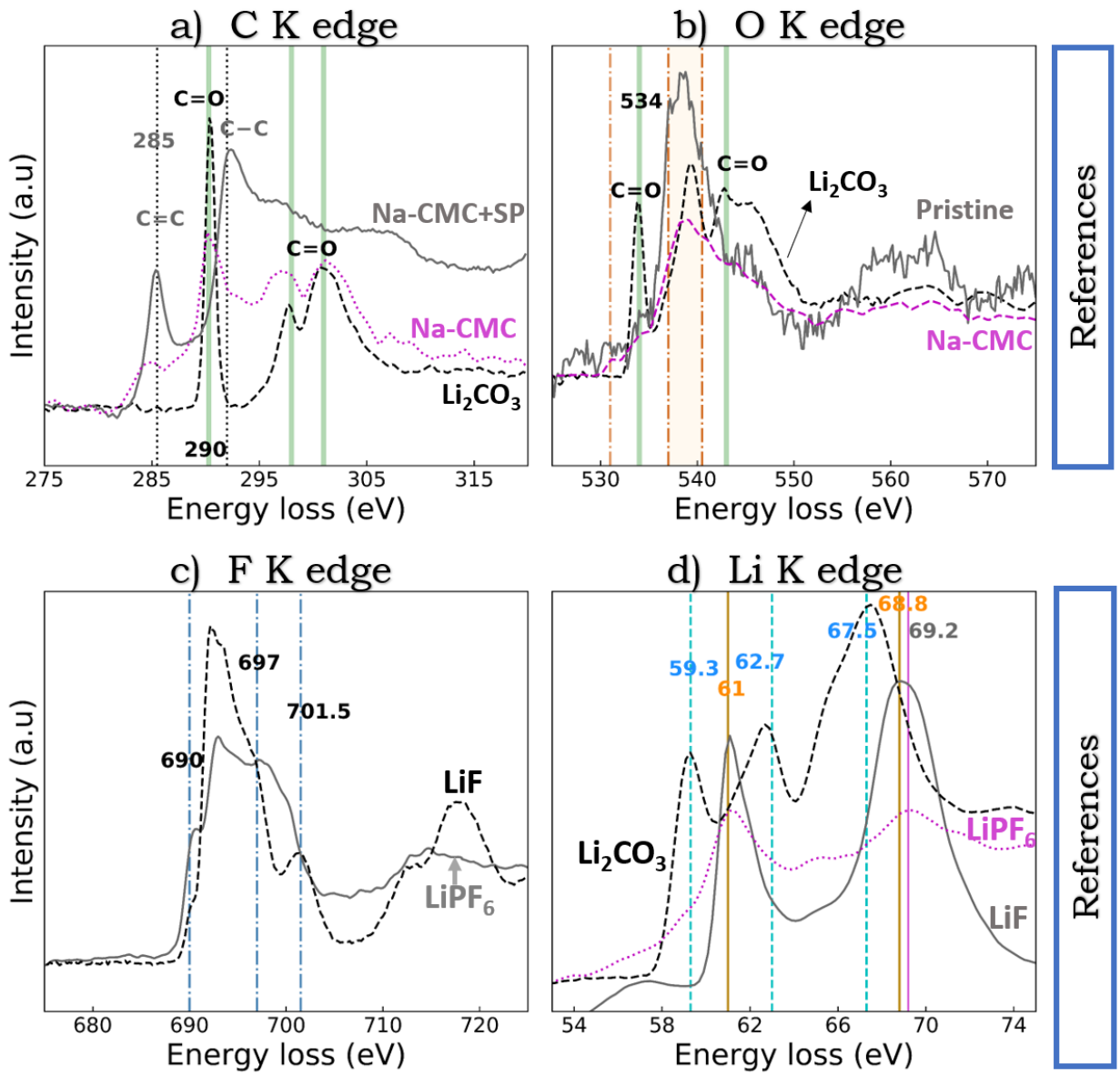

Figure 6.1 a) C K, b) O K, c) F K, and d) Li K edge spectra of the reference compounds measured as a comparison to the electrodes. Dashed lines highlight the position in the energy of the main features observed in the various systems, also indicated by the numbers with corresponding colors.

6.3.1 C K and O K edge

XRS spectra for the C K edge of the references Li_2CO_3, Na-CMC, and Na-CMC + super P are shown in Figure 6.1. The peaks of Li_2CO_3 at 290.4, 297.5, and 301 eV (indicated by green vertical lines) are attributed to **C**=O in CO_3^{2-} (1s–π*), **C**=O in carbonyl contained groups (1s–π*), and **C**=O 1s–σ*, respectively. Likewise, the XRS spectrum of the Na-CMC reference shows almost similar

peaks as Li_2CO_3 but with lower intensity and broader. We assigned these peaks to the carboxymethyl groups (CH_2**CO**Na) in the Na-CMC structure (see Na-CMC structure in Figure 1.13, chapter 1).

The Na-CMC + Super P reference has peaks at 285.4 and 292.4 eV corresponding to the transition C=C 1s–π* and C–C 1s–σ*, respectively. Comparing the two references Na-CMC + Super P with the Na-CMC alone, the Na-CMC + Super P has no longer the peaks corresponding to the carbonyl groups (290.4, 297.5, and 301 eV). The disappearance of these peaks could be explained by the formation of a chemical bond between the carboxymethyl (CH_2COONa) groups from the Na-CMC binder and Super P, forming ester like bonds (CH_2-COO-R) as reported by Hochgatterer et al. and Vogl et al.[26,27]

Figure 6.1 b shows the XRS spectra for the O K edge of the references Li_2CO_3, Na-CMC, and the pristine c-Si Nps electrode. The reference Li_2CO_3 shows one strong peak at 534 eV that corresponds to π* antibonding state from the C=**O** of the CO_3^{2-}. The second part of the spectrum corresponds to the σ* antibonding state[28].

The pristine c-Si Nps electrode measured as a reference has 50% of c-Si Nps blended with 25% Na-CMC and 25% Super P deposited in Cu foil. The c-Si Nps electrode was chosen because it shows the typical interactions resulted from the active materials (silicon and graphite) with the binder. The pristine c-Si Nps spectrum has a broad and bumpy peak from 535 and 545 eV, with a weak bump at 534 eV. This broad and bumpy peak from 530 and 545 eV resembles the typical feature of polymers with organic groups like R-COO-R (ester) or R-CO-R (ketone) that has been reported by NEXAFS[29]. Thus, the

interaction of the Na-CMC, Super P, and c-Si Nps could be similar to a ketone or ester-like-bond between the SiO_x natural surface in Si and the binder.

Both Na-CMC and the pristine c-Si Nps electrode also have a small bump at 534 eV, suggesting the presence of carbonyl (C=O) in a chemically inhomogeneous environment, which may indicate that C=O is probably in a polymerized chain.

6.3.2 F K and Li K edge

The two references measured at the F K edge are LiF[30] and $LiPF_6$, which are the inorganic components of the SEI (Figure 6.1c). Both XRS spectra are quite similar, with a broad multi-component feature between 690 and 705 eV, more peaked in the $LiPF_6$ than in LiF[30].

Regarding the Li K edge, the reference compounds we measured are LiF, $LiPF_6$, and Li_2CO_3, as shown in Figure 6.1d. The LiF and $LiPF_6$ spectra have bumps, mainly at 61 and 69 eV, while the reference Li_2CO_3 presents three peaks at 59.3, 62.7, and 67.5 eV, respectively.

6.3.3 Conclusions on reference spectra

The chemical environments for the references show specific signatures at determinate energy values, demonstrating not only different elemental composition but also the type of chemical bonds and if they combine chemically with other elements. This chemical specificity will allow us to use the reference spectra in order to evaluate the nature of the bonds present in the electrodes by comparison.

6.4 c-Si Nps electrodes: observation of the SEI evolution

Once we have acquired our reference spectra, we can analyze the data from real electrodes. This Section focuses first on the c-Si Nps electrodes, prepared in two states: end of lithiation and delithiation. The sample preparation after the electrochemical cycling and technical details of the experiment were described in section 2.4.

6.4.1 Electrochemical lithiation of c-Si Nps

Figure 6.2 shows the first electrochemical cycle during lithiation until 0.005 V vs. Li metal in a coin cell. The electrolyte used was 1 M $LiPF_6$ (3FEC/7EMC, v/v) with 2 wt% vinyl carbonate (VC). The electrochemical curve has a plateau at 0.08 V, similar to reported c-Si Nps[31–33]. The discharge capacity obtained is 1830 $mAhg^{-1}$ of the 50% of active mass used to prepare the electrode. During delithiation, the obtained capacity reaches 1530 $mAhg^{-1}$ with a Coulombic efficiency of ~84% and irreversible capacity loss of ~16%, in agreement with previous results on c-Si Nps[13,34]. The green points indicate the electrodes analyzed by XRS.

Overall, the irreversible loss in our obtained capacity is a reasonable value for a c-Si Nps system (16%). The capacity loss during the first cycle, which is different from any other, is usually related to the initial SEI formation observed for Si-based electrodes[13,35,36]. One of the reasons for probing by XRS the c-Si Nps samples after one cycle (in lithiated and delithiated states), and compare them to the pristine electrode, is to gain insights into the SEI.

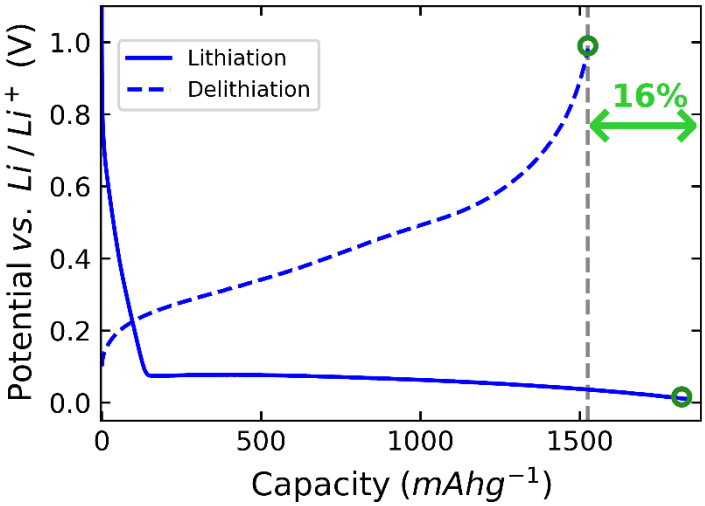

Figure 6.2 potential vs. Li/Li+ against the capacity during the first electrochemical cycle in a coin cell at C/20 for the crystalline silicon nanoparticles-based anodes. The electrodes analyzed *post-mortem* by XRS are indicated by green points.

6.4.2 Qualitative analysis of the XRS spectra for the c-Si Nps electrode

Figure 6.3e–h shows the XRS spectra for the lithiated (red lines) and delithiated (blue lines) c-Si Nps electrodes at the C, O, F, and Li K edges (bottom panels e-f) and the comparison with the references (top panels a–d). Dashed lines are used to highlight the main peaks and mark their energy position, allowing the visual comparison between each set of reference data and the corresponding electrode spectra. In the following, we describe in more detail the results edge by edge.

6.4.2.1 *C K and O K edge*

The C and O K spectra of the two c-Si Nps electrodes in lithiated and delithiated states (red and blue lines, respectively) are shown in Figure 6.3e and f. We qualitatively observe some striking features:

1) The C K spectra are incredibly similar in shape, except that the lithiated electrode has a more intense peak at 290.4 eV. This sharp peak is the typical signature of Li_2CO_3. Both electrodes, therefore, contain carbonates in a higher amount in the lithiated state.

2) The O K spectra present more differences between the lithiated and delithiated states, but the most notable feature is the sharp peak at 534 eV, more intense for the lithiated sample.

These two observations indicate that the electrodes contain C=O in CO_3^{2-} similarly to the Li_2CO_3, confirming the electrolyte decomposition.

Notably, we observe in the C K edge sharped and milder peaks at 285, and 294 eV, similar to the reference Na-CMC + Super P. These peaks correspond to C=C and C–C, resulting from the carbon black and the binder used to prepare the electrode.

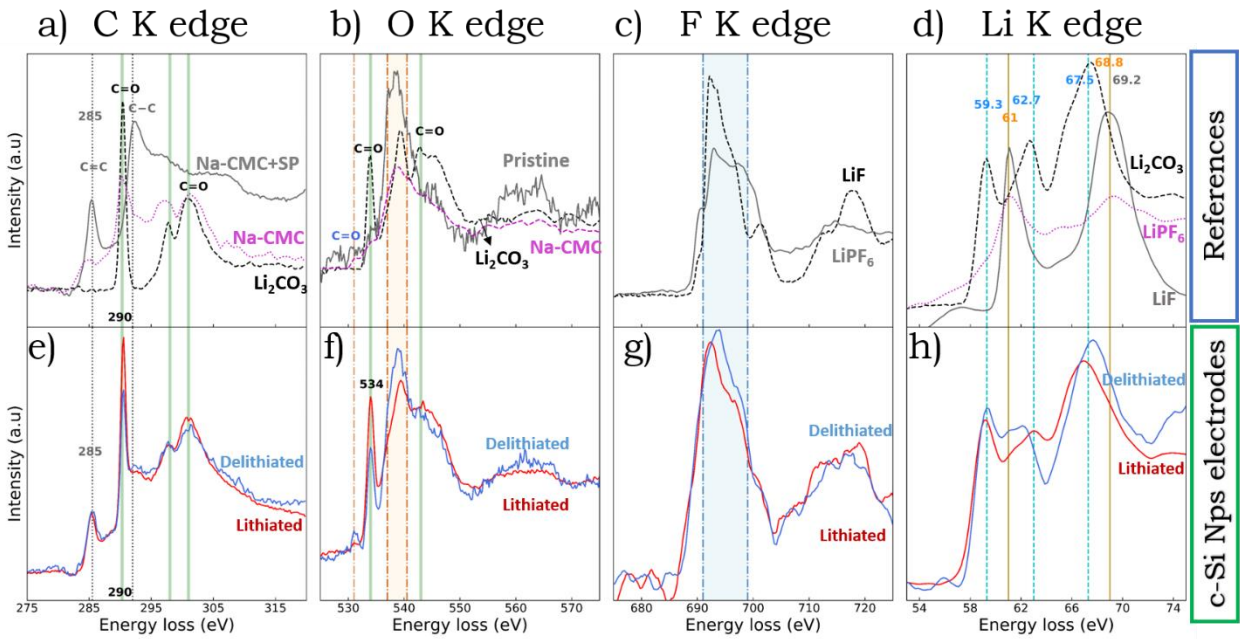

Figure 6.3 C K, O K, F K, and Li K edge spectra of **a–d)** the reference compounds Li_2CO_3, Na-CMC, Na-CMC+SP, LiF, $LiPF_6$ and pristine c-Si Nps electrode, and the **e–h)** c-Si Nps electrodes after the first cycle in the lithiated (red) and delithiated (blue) states.

There are additional subtle signatures in the O K spectra, such as a broad bump in the range from 535 and 540 eV, which seems to decrease in intensity and broadens in the delithiated state (see Figure 6.3f, highlighted in orange). Also, the delithiated sample has a small peak at 531 eV.

As observed, the intensity of the carbonates (CO_3^{2-}) decreases during delithiation, and at the same time, the broad and noisy bump increases (highlighted in orange). We speculate the possible evolution of the carbonates from the lithiation to delithiation. The broad noisy bump suggests the formation of oligomers or polymers with organic groups like R-COO-R (ester) or R-CO-R (ketone), similar to the interaction of the active materials with the binder (as explained in 6.3.1 for the c-Si Nps reference), and as it was proposed by several authors to explain the efficiency of the binder Na-CMC[26,27].

The main conclusions we can draw from the qualitative comparison of C and O K edge spectra is that CO_3^{2-} is formed in both (de)lithiated states, in a similar environment as the compound Li_2CO_3, that results from the decomposition of organic solvents or the solvent additives. Moreover, as the lithiated sample presents more intense peaks at 290 eV and 534 eV than the delithiated one, we can conclude that the number of carbonates present in the SEI depends on the state-of-charge and reduces after complete delithiation of the electrode.

6.4.2.2 *F K and Li K edge*

The F K spectra for the c-Si Nps electrodes is shown in Figure 6.3g. Both the delithiated and lithiated samples have a broad peak ranging from 690 and 705 eV (highlighted blue zone) as in the references. The main difference between the lithiated and delithiated electrodes is a small energy shift of the local maximum at 692–695 eV by a few eV to the right and a small increase in the spectrum intensity for the delithiated electrode.

Globally, the qualitative comparison of the electrode spectra to the references reveals their similarity with both LiF and $LiPF_6$, probably indicating the presence of both in the silicon anodes.

Following, we consider the Li K spectra of the lithiated and delithiated samples (Figure 6.3h). Note that one of the advantages of XRS is that the Li K edge can be obtained with a high signal-to-noise ratio. Discernable signatures are visible that could identify the principal SEI component when using reference

compounds. In contrast, XPS or Auger electron spectroscopy that shows imprecise signatures-like bumps.

Both electrodes have clear peaked signals at 59.3, 62.7, and 67.5 eV, similar to the reference Li_2CO_3, only that the delithiated sample presents the peaks shifted. Also, both samples present a peak at 61 eV that could correspond to LiF or $LiPF_6$.

Owing to the Li K edge, we can precisely identify the chemical compound Li_2CO_3 that probably has slightly polymerized to form carboxylates R-COOLi during delithiation, as shown by the broad bump in the range 535–540 eV, particular to organic groups like R-COO-R (ester) or R-CO-R (ketone).

In this scenario, the Li K edge spectra confirm the presence of Li_2CO_3 and LiF or $LiPF_6$.

6.4.2.3 *Si $L_{2,3}$ edge*

Figure 6.4 shows the Si $L_{2,3}$ spectra for the pristine, lithiated, and delithiated c-Si Nps electrodes. We can immediately see that the electrode after one cycle has changed significantly with respect to the pristine material, and also that the lithiated and delithiated states exhibit different silicon environments. The pristine c-Si Nps spectrum shows the peaks related to crystalline Si at 101.1 eV, and the naturally occurred SiO_2 at 108.7 eV. After lithiation, the intensities of both c-Si and SiO_2 peaks decrease. Regarding the delithiated sample, the peak at 108.7 eV increases in intensity, compared to the pristine electrode, which could correspond with the formation of Li_xSiO_y. The formation of Li_xSi

phases could also be detected in the excess signal observed in the low energy loss region, < 100 eV.

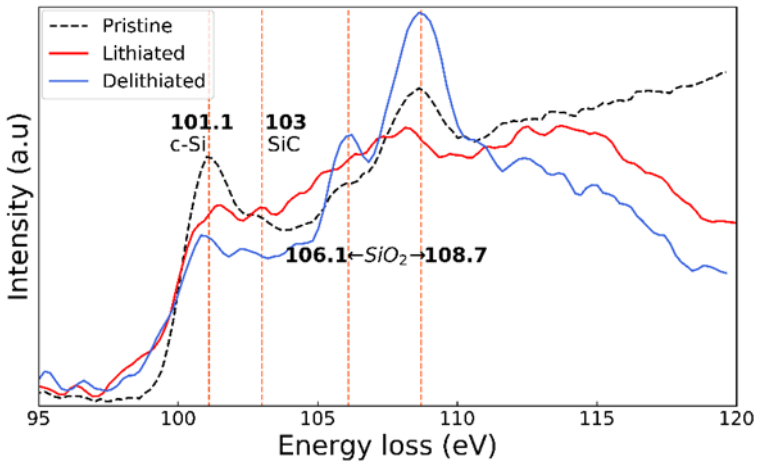

Figure 6.4 Si $L_{2,3}$ spectra for the c-Si Nps pristine (dashed line) and cycled electrode in lithiated (red line) and delithiated (blue line) states. Typical peaks of crystalline silicon, carbon-silicon, and silicon oxide are indicated by vertical dashed lines, with nominal energy positions noted.

While c-Si Nps are lithiated, the crystalline structure is amorphized, and the volume of the outer shell with Li_xSi phases increases, following the so-called two-phase mechanism[8,37]. The Si $L_{2,3}$ edge spectra corroborate that c-Si has been amorphized because of the disappearance of both Si and SiO_2 peaks. Thus, XRS can access the amorphization of Si when it is lithiated.

6.4.2.4 *Summary of qualitative analysis in c-Si Nps*

We observed the evolution of chemical environment signatures, depending on the state of charge of the electrode, specifically, SEI compounds such as Li_2CO_3, $LiPF_6$ (or LiF) by considering the C K, O K, F K, and Li K edges. The lithiated XRS spectra are different from the delithiated, with a more intense Li_2CO_3 signal. The appearance of the SEI compounds may be related to the irreversible capacity obtained (16%, loss of 300 $mAh.g^{-1}$).

6.4.3 A quantitative study of the XRS spectra or the c-Si Nps electrode

At this stage, we perform the semi-quantitative analysis using the reference compounds to simulate the sample spectra for each edge, as indicated in section 6.2. The results for the lithiated and delithiated c-Si Nps electrodes are reported in Figure 6.5a–h, where the top panels show the lithiated data (red) and the bottom panel the delithiated data (blue), for C K, O K, F K, and Li K edges. The linear combination of reference spectra best adjusting the electrode spectra is represented as the green line. The weighted reference spectra used for this decomposition are shown using greyish colored and black dashed lines.

6.4.3.1 *C K edge spectra*

The quantitative analysis results for the lithiated and delithiated samples are shown in Figure 6.5a and b, respectively.

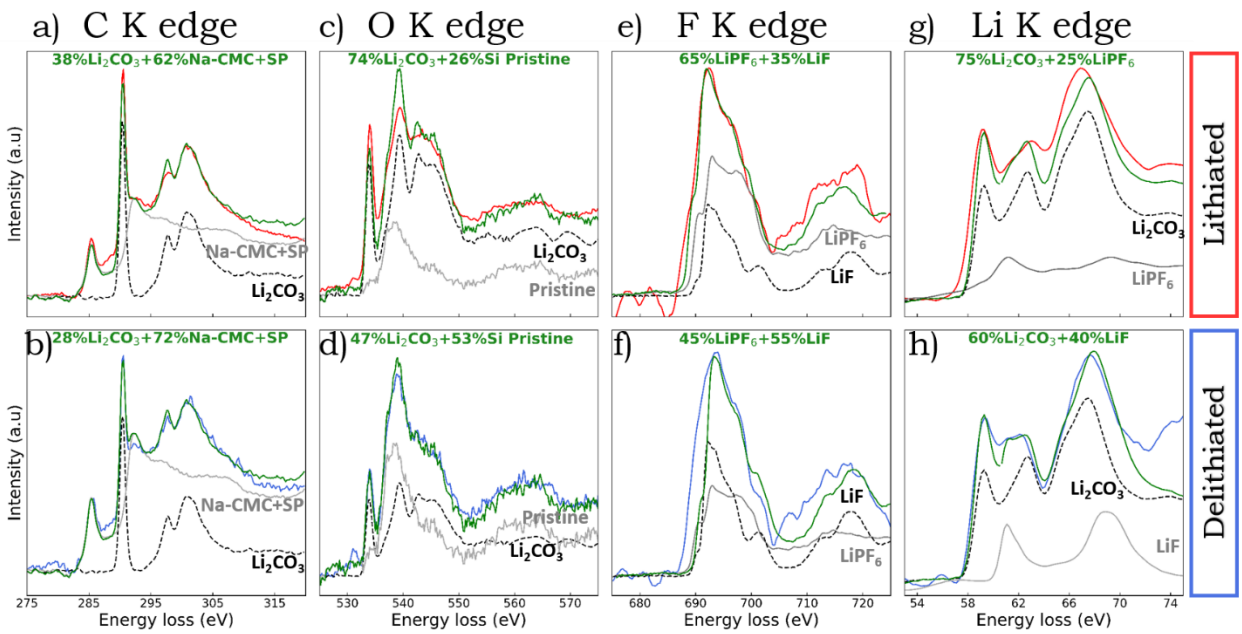

Figure 6.5 quantitative analysis of the c-Si Nps electrodes spectra (the lithiated state in red, top panels; delithiated state in blue, bottom panels), using the reference basis linear decomposition. A green line shows the best fit to the data, with the corresponding weighted reference components spectra indicated by black dashed or grey lines. a–b) C K edge, c–d) O K edge, e–f) F K edge, and g–h) Li K edge.

The references used for the linear combination and percentages obtained from the weights are summarized in Table 6.2.

Table 6.2 weight factors obtained from the quantitative analysis of the C K and O K edges

Edges	References	Weight factors	
		Lithiated	Delithiated
C K	Li_2CO_3+Na-CMC+Super P	38% $Li_2\mathbf{C}O_3$	28% $Li_2\mathbf{C}O_3$
O K	Li_2CO_3+c-SiNps electrode	74% $Li_2C\mathbf{O}_3$	47% $Li_2C\mathbf{O}_3$

For the C K edge, the linear combination adjusts fairly well the lithiated and delithiated spectra of the c-Si Nps electrodes. The Li_2CO_3 contents correspond to 38% and 28% for lithiated and delithiated, respectively, confirming the formation of more carbonates (CO_3^{2-}) during lithiation, in agreement with our qualitative observations earlier in the chapter.

6.4.3.2 *O K edge spectra*

Figure 6.5c and d show the quantitative analysis for the O K edge spectra for the lithiated and delithiated samples, respectively. The references used for the linear combination and the percentages calculated from the weights are summarized in Table 6.2.

The linear combination for the O K spectrum in the lithiated sample was not as ideal as for the C K edge (see Figure 6.5a and b), especially in the range 538–542 eV, where the linear combination (green line) is higher in intensity than the lithiated O K spectrum.

However, the Li_2CO_3 percentage for the O K edge confirms the higher carbonate compounds during lithiation; besides, they corroborate our qualitative observations.

6.4.3.3 *F K edge spectra*

Figure 6.5 e and f show the F K spectra and the quantitative analysis for the lithiated and lithiated samples. The percentages calculated from the weights are summarized in Table 6.3.

Table 6.3 weight factors obtained from the quantitative analysis of the F K and Li K edges

Edges	References	Weight factors	
		Lithiated	Delithiated
F K	LiP**F**$_6$ + Li**F**	65% LiP**F**$_6$ + 35%Li**F**	45% LiP**F**$_6$ + 55%Li**F**
Li K	**Li**$_2CO_3$ + **Li**PF_6 + **Li**F	74%**Li**$_2CO_3$+25%**Li**PF_6	60%**Li**$_2CO_3$+40%**Li**F

The quantitative analysis of the F K edge is more complicated than for the C K and O K edges. Note that it is not possible to describe the left part of the curve between 680 and 690 eV with the references that we have measured. In comparison, the right part of the curve between 690 and 705 eV is reasonably fitted for both lithiated and delithiated samples.

Comparing the lithiated and delithiated electrode percentages, we obtain a higher quantity of $LiPF_6$ (65%) during lithiation, decreasing to 45% during delithiation. However, the obtained percentages for LiF and $LiPF_6$ are not that different. Thus, the (de)lithiated samples may have equivalent $LiPF_6$ and LiF, suggesting that $LiPF_6$ is trapped in the SEI layer, and some LiF is formed.

Michan *et al.* have reported using ^{7}Li and ^{19}F solid-state NMR that the increase in LiF becomes appreciable with multiple cycles; they found a minor amount of LiF during the first cycles[8]. Besides, in c-Si Nps analyzed by soft and hard XPS, Philippe *et al.* reported the formation of $LiPF_6$ at the outermost SEI surface, whereas LiF is formed within the SEI layer[13]. Given that XRS is a technique that uses hard X-rays and provides averaged information of the SEI, the average observation by Philippe *et al.* would result in equivalent LiF and $LiPF_6$ formation, similarly to our results.

6.4.3.4 *Li K edge spectra*

Figure 6.5 g and h show the Li K spectra and the quantitative study for the lithiated and delithiated samples, respectively. The references used and the percentages calculated from the weights are summarized in Table 6.3.

This Li K spectrum is fitted differently in comparison with the earlier ones. The reason is that there is no linear combination of Li-containing references (Li_2CO_3, LiF, and $LiPF_6$) that allows accounting for the global shape of the electrode spectra satisfactorily. For instance, if we focus on adjusting the first sharp peak at ~ 58.5 eV by tuning the Li_2CO_3 weight factor (where this feature is very characteristic), we obtain too much intensity around the second local maximum (~ 60–62 eV) and also the third one (~ 67–68 eV). This situation could mean that 1) the lithium environment is richer and cannot be described based on three compounds only, and/or 2) some particular bonds in Li_2CO_3 are present in a certain amount, while others may exist in a different amount due to interactions with the surrounding medium or modifications of the carbonates.

If we neglect to account quantitatively for the first peak at ~ 58.5 eV, we can simulate the Li K spectra of the electrodes at higher energy losses (in the range [60–79 eV]. We find that the lithiated electrode can be adjusted using 0.75 Li_2CO_3+0.25 $LiPF_6$, while the delithiated electrode spectrum is best reproduced using 60% Li_2CO_3 + 40% LiF (Figure 6.6). Note, in this particular case, the shoulder peak at ~ 61 eV, which has appeared after delithiation and corresponds very well to the first peaked feature of LiF. Globally, we must say that the agreement between experimental and reference-decomposed spectra

is relatively poor compared to other edges, but this treatment indicates the main species present in the materials.

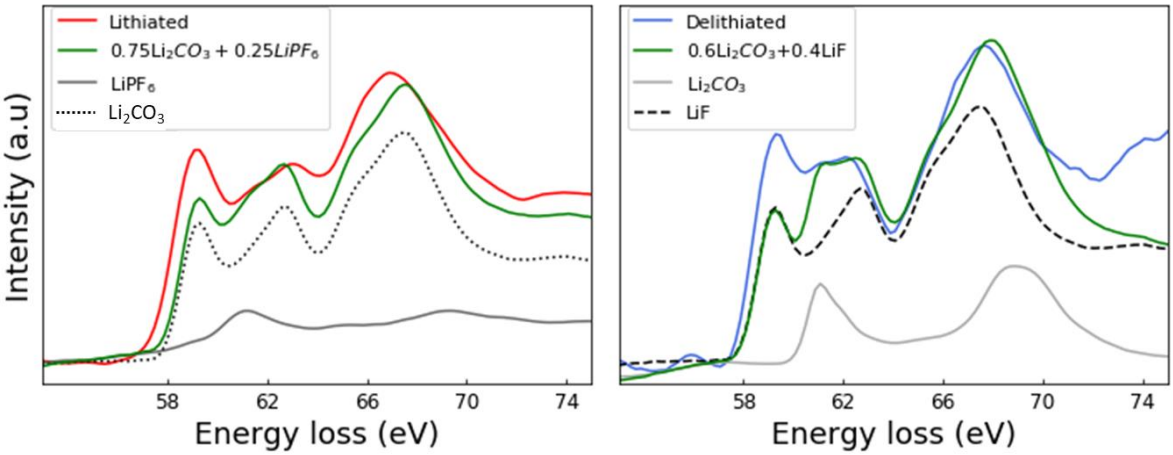

Figure 6.6 decomposition of the lithiated (red, left) and delithiated (blue, right) electrode spectra using a linear combination of Li_2CO_3 and LiPF6 (lithiated) or LiF (delithiated) spectra. The green line results from weight percentages of 75% carbonates and 25% salt for the lithiated material, 60% carbonates, and 40% LiF for the delithiated one.

A possible refinement of the analysis would consist of using different weight factors for the Li_2CO_3 contributions in distinct spectral regions, e.g., we can adequately account for the peak at 59.3 eV and the other higher energy features (as plotted in panels g–h of Figure 6.5) by using the following expressions:

$$I_{lithiated} = 1.1 \times Li_2CO_3[51.89 - 60.49\ eV] + 0.75 \times Li_2CO_3[60.68 - 79.69\ eV] + 0.25 \times LiPF_6[60.68 - 79.69\ eV]$$

$$I_{delithiated} = 1.1 \times Li_2CO_3[51.89 - 60.49\ eV] + 0.6 \times Li_2CO_3[60.68 - 79.69\ eV] + 0.4 \times LiF[60.68 - 79.69\ eV]$$

The above considerations do not yield a satisfying description of the Li edge spectra either. It seems unreasonable to adjust different spectra regions with different linear combinations, but we may underline that we are probably facing a limit of the technique. The 59.3 eV peak, for instance, is not documented in the literature, and the corresponding type of chemical bonds or environments. Further information is needed to account for Li-bonds types as references, instead of reference compounds that are usually composed of several atoms in a complex environment. There is, probably, a large margin to make progress in this direction.

Despite the limitations we mention, the Li K edge analysis indicates that a higher **Li**$_2CO_3$ percentage is obtained after lithiation, which corroborates the increased carbonates observed in C K and O K edges for the lithiated sample.

6.4.4 Conclusion of the XRS analysis in c-Si Nps

- The XRS spectra of electrodes at different states of charge have unique chemical signatures demonstrating the SEI formation and evolution.
- The chemical signatures can be differentiated when comparing qualitatively the high-resolution real electrode spectra acquired in the energy range of light elements (C, O, Li, F) with well-chosen representative reference compounds.
- The semi-quantitative analysis based on the linear decomposition of spectra can be satisfactorily used to follow the evolution of the chemical signatures. It allows extracting weight factors of relevant reference

compounds, revealing how they are formed or dissolved during (de)lithiation.

All results are gathered in Table 6.4. To recapitulate, we find a higher Li_2CO_3 percentage for the lithiated c-Si Nps and equivalent $LiPF_6$ and LiF formation, indicating that both are present in the SEI.

Table 6.4 summary of reference weight factors at measured edges.

Edges	Weight factors	
	Lithiated	Delithiated
C K	34% Li_2**C**O_3	28% Li_2**C**O_3
O K	74% Li_2C**O**$_3$	47% Li_2C**O**$_3$
F K	65% Li**F**$_6$ + 35%Li**F**	45% Li**F**$_6$ + 55%Li**F**
Li K	74%**Li**$_2CO_3$+25%**Li**PF_6	60%**Li**$_2CO_3$+40%**Li**F

Considering the increased quantity of Li_2CO_3 in the lithiated sample, we speculate that the SEI grows during lithiation due to the decomposition of organic electrolytes (EMC and FEC), additives (VC), and salt ($LiPF_6$). Then, after delithiation, the decrease in inorganic compounds may indicate that the SEI partially dissolves. The formation of more SEI compounds during lithiation agrees with studies using XPS. By evaluating the intensity of the C=C peak corresponding to carbon black and graphite in the electrode, Philippe *et al.* could assess the SEI thickness during the first cycle on c-Si Nps (using soft and hard XPS[1]). They reported a decreased intensity in the C=C peak during lithiation, indicating a thicker SEI[1], while on delithiation, the C=C peak was found to increase, suggesting a thinner SEI[1]. Our study confirms such dissolution of the SEI components during delithiation since we observed an evident decrease in the peak intensities associated with carbonates, which may be related to the capacity loss during the first cycle.

6.5 a-Si/c-$FeSi_2$/graphite composite electrodes: observation and evolution of the SEI

In this Section, we explore the effect of aging on the chemical environment of the composite a-Si/c-$FeSi_2$/graphite by XRS. Specifically, we focus on the differences in the XRS spectra of composite anodes cycled once and 300 times. To analyze the XRS spectra of the a-Si/c-$FeSi_2$/graphite electrodes, we use the same methodology as for the c-Si Nps, *e.g.,* we compare electrode spectra with the reference compounds spectra, as described in section 6.3.

6.5.1 Electrochemical lithiation of the a-Si/c-$FeSi_2$/graphite electrodes

Coin cells were assembled to perform the electrochemical lithiation using the a-Si/c-$FeSi_2$/graphite electrode as a working electrode with a volumetric capacity of 2.4 $mAh.cm^{-2}$ and lithium metal as the counter electrode. Details of the electrode fabrication were given in section 2.4. The once lithiated a-Si/c-$FeSi_2$/graphite electrode was cycled at C/20 between 1.0 and 0.005 V vs. Li/Li^+. For the 300 cycles electrode, different C-rates were used C/20, C/5, and C.

We study two a-Si/c-$FeSi_2$/graphite samples: once-cycled in the lithiated state and the 300^{th}-cycled electrode in the delithiated state. Figure 6.7 shows the potential vs. Li metal against the capacity for the first and 300^{th} cycle. The green points indicate the electrodes analyzed by XRS.

The a-Si/c-$FeSi_2$/graphite has a delithiation capacity during the first cycle of 2.2 mAh.cm^{-2} with an irreversible loss of 8%. After 300 cycles, the cell has a delithiation capacity of 1.4 mAh.cm^{-2}, yielding a significant capacity fading of ~37%.

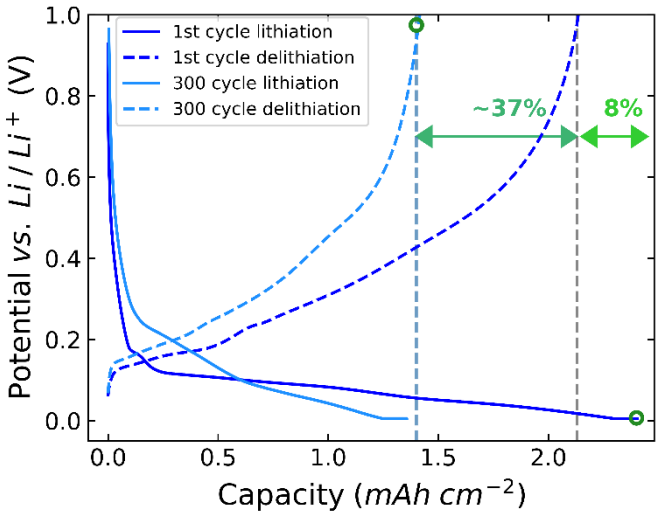

Figure 6.7 potential vs. Li/Li+ for the first electrochemical cycle in a coin-cell at C/20. The electrodes analyzed are indicated by green points.

6.5.2 Morphology of the composite electrode after one cycle and effects of aging after 300 cycles

To illustrate how the electrode morphology is affected by aging, our collaborators P-H Jouneau and P. Kumar at CEA-IRIG/Lemma obtained microscopy images after 300 cycles in the negative electrode and compared them with a one-cycle electrode. The results were published in Small 2020 and are summarized in this Section[35]. The a-Si/c-$FeSi_2$/graphite was cycled against Li metal at C/20 for preparing the one cycle sample, and sequences of C/20, C/5, and C between 1 and 0.005 V vs. Li/Li$^+$ for 300 times. Each charge was ended with a constant voltage of 60 min to reach maximum cell reversible capacity.

6.5.2.1 *Impact on the morphology after one cycle*

Figure 6.8 shows the FIB-SEM images of the negative electrode once-cycled in its lithiated state. At this stage, the morphology of the electrode has already changed. For instance, graphite particles present an increase of internal porosity, filled with a greyish phase. However, the morphology of the a-Si/c-$FeSi_2$ remains similar to the pristine electrode (see Figure 5.2). STEM-EDX investigations were performed on the lamella (acquired by FIB-SEM) to obtain additional chemical information.

Figure 6.8c shows the EDX chemical mapping in Figure 6.8b. To identity the a-Si/c-$FeSi_2$ alloy particles, graphite, and regions that could correspond to the SEI, a chemical mapping was performed to detect elements like Si, Fe, F O, and C. The light gray region corresponds to the a-Si/c-$FeSi_2$ alloy particle since it is composed of Fe and Si. Besides, a shell containing oxygen surrounding the a-Si/c-$FeSi_2$ alloy in the first layer next to the particle may correspond to the natural SiO_x. Dispersed patches and a fine layer on the right are observed with carbon and fluorine rich regions that could correspond to the SEI phase, e.g., to the main SEI components formed due to electrolyte decomposition, LiF and Li_2CO_3. The significant amounts of F could also be remaining electrolyte traces, even though all samples were dried before the characterization under vacuum.

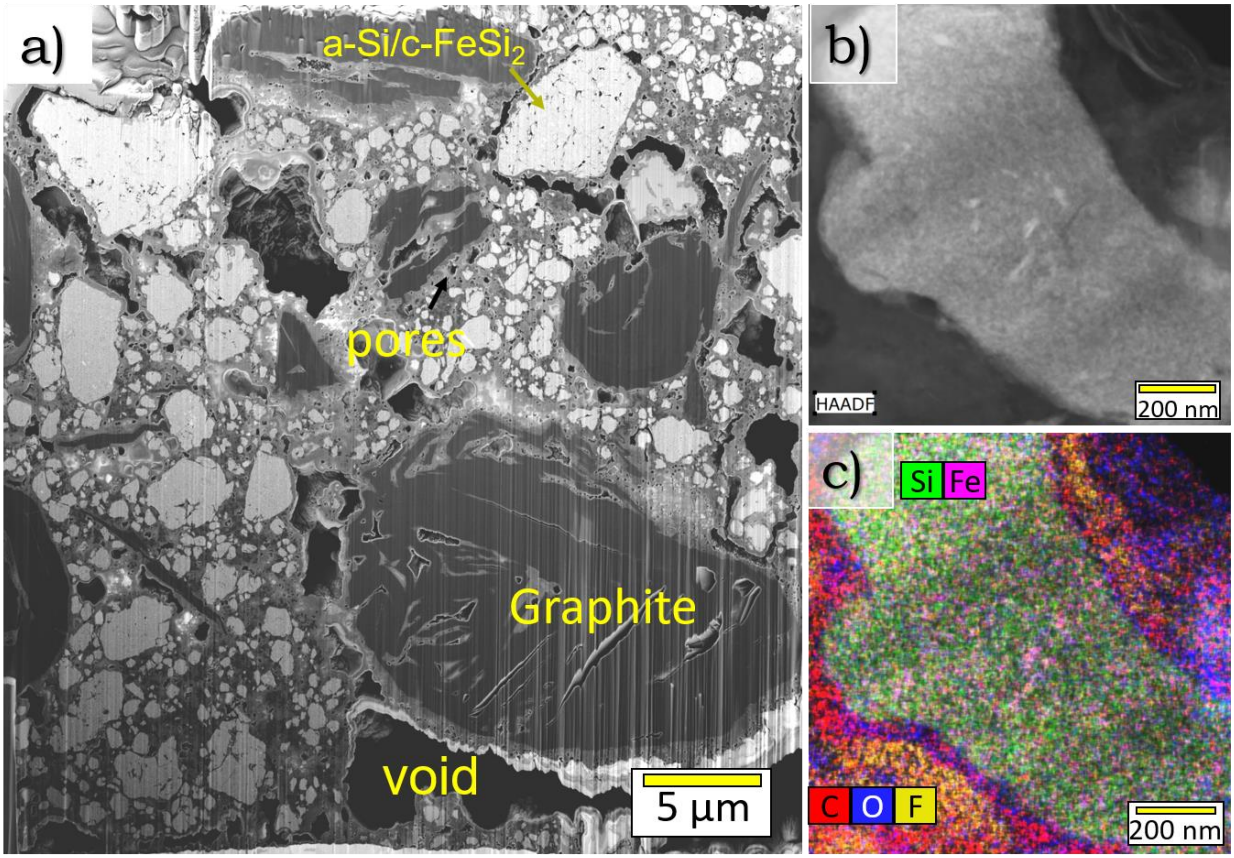

Figure 6.8 Morphological modifications and SEI evolution of the a-Si/c-$FeSi_2$/graphite electrode after one cycle at C/20 a) FIB-SEM slices. b) and c) HAADF image and corresponding EDX elemental mapping of Si, Fe, C, O, and F elements to identify the SEI components after the first lithiation.

In summary, the morphology has slightly changed during the first cycle compared to the pristine electrode. Internal porosity appears in the graphite, while the alloy particles are similar in morphology with the pristine negative electrode. The SEI starts to form around the a-Si/c-$FeSi_2$ particles with patches composed of C, O, and F that could correspond to LiF and Li_2CO_3.

6.5.2.2 *Aging effects on the morphology*

Figure 6.9a and b show the FIB-SEM images of the aged electrodes after 300 cycles. The most remarkable results from the aging are i) the formation of a core-shell tree-branch structure. The core of the tree-branch (light-greyish

areas) corresponds to a-Si/c-$FeSi_2$ particles. The dark-greyish areas around the alloy particles (the shell that envelops the branches) are related to the SEI.

ii) The appearance of opening/cracks as marked by red arrows.

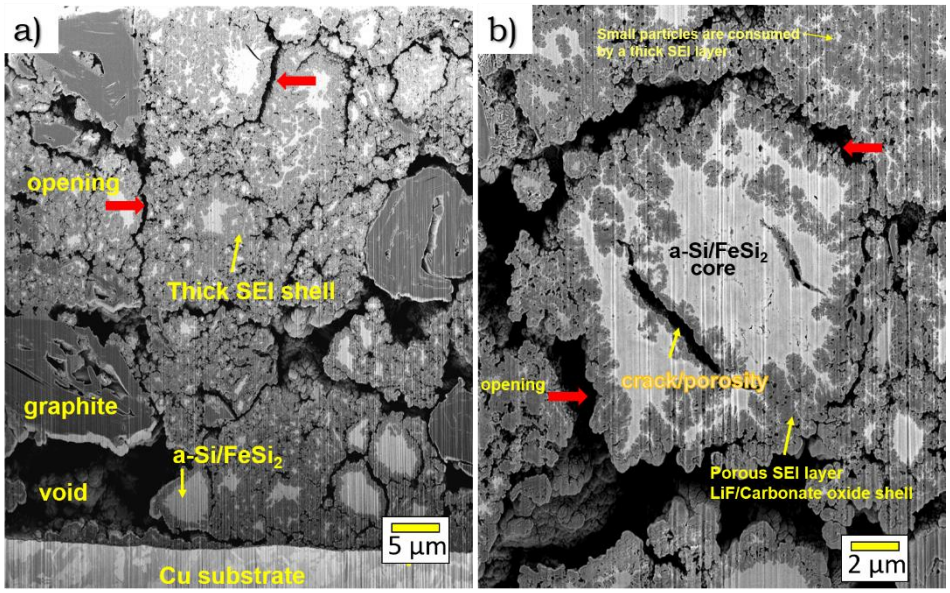

Figure 6.9 a) and b) High-resolution cross-sectional FIB-SEM slices for the a-Si/c-$FeSi_2$/graphite electrode after 300 cycles upon lithiation.

Figure 6.10d confirms that the light gray zone corresponds to the a-Si/c-$FeSi_2$ alloy since the chemical mapping shows Fe and Si, especially in the lighter gray core and branches. Figure 6.10b and e–h shows the elemental EDX mapping of Figure 6.10a and c, respectively. It is seen that O signals are much higher in the shell region than the core of the alloy particle. The shell bordering the a-Si/c-$FeSi_2$ particle also presents C, F, P, and O. This chemical mapping confirms that the shell is a complex SEI. The SEI is both thick and thin, depending on its localization. In comparison, the SEI layer next to the branches is relatively thin, while the SEI in the shell, where alloy-branches have been consumed, is thick.

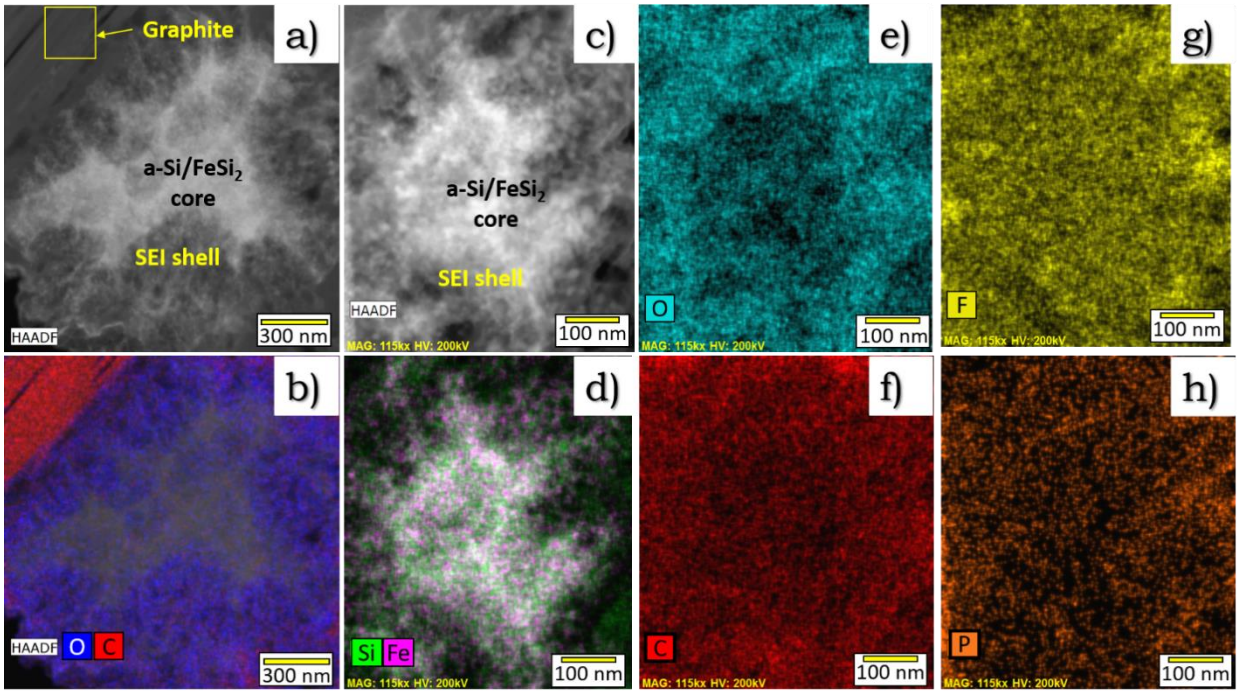

Figure 6.10 a) and c) HAADF image of the alloy particle and corresponding b) and d–h) chemical mapping of Si, Fe, F, O, C, and P elements for the 300 cycles a-Si/c-$FeSi_2$/graphite electrode.

The tree-branch shape of the aged particle may allow an alternative path to lithiate and delithiate the active material in the core, potentially reducing the diffusion length. Besides, the thick SEI that connects adjacent particles within the electrode may provoke sluggish Li-diffusion.

The aging mechanism of the a-Si/c-$FeSi_2$/graphite composite electrode points to the formation of intricate channels that possibly allow lithium-ions diffusion more effectively, thus avoiding significant losses of Coulombic efficiency during cycling. However, the thick SEI could impede the effective lithiation of the anode material compared with a fresh cell, contributing to a capacity loss of 28.7% after 300 cycles.

6.5.3 Qualitative analysis of the XRS spectra for the a-Si/c-$FeSi_2$/graphite electrode

We follow the evolution of the SEI environment for two a-Si/c-$FeSi_2$/graphite electrodes measured at the first cycle and the 300th cycles. Figure 6.11e–h shows the C, O, F, and Li K edge spectra for the electrodes compared to the references described in section 6.3.

Unfortunately, we could not measure the XRS spectra for the binder used in the electrode, which is Li-PAA, due to beam time constraints. Like Na-CMC, this binder also has C=O bonds that form covalent bonds or stronger hydrogen bonds with the active materials, as reported in Na-CMC[26,27]. Even though we could not measure the exact binder, we used as a reference the Na-CMC + Super P C K spectrum that probably reflects the typical interactions of the binder-particle surface bonds[38].

6.5.3.1 *C K and O K edge*

Figure 6.11e shows the C K edge spectra of the once-cycled electrode in the lithiated (red lines) and delithiated (blue lines) states, as well as the 300th-cycled sample in the delithiated state (yellow line). The once-cycled lithiated sample spectrum shows similar peaks to the reference Na-CMC + Super P and Li_2CO_3. Specifically, the C K edge spectrum for the one-cycle lithiated presents sharp and intense peaks at 285 (C=C) and 290 (C=O), characteristic of binder and carbonates, respectively, as well as a broader feature at 292 eV (C-C).

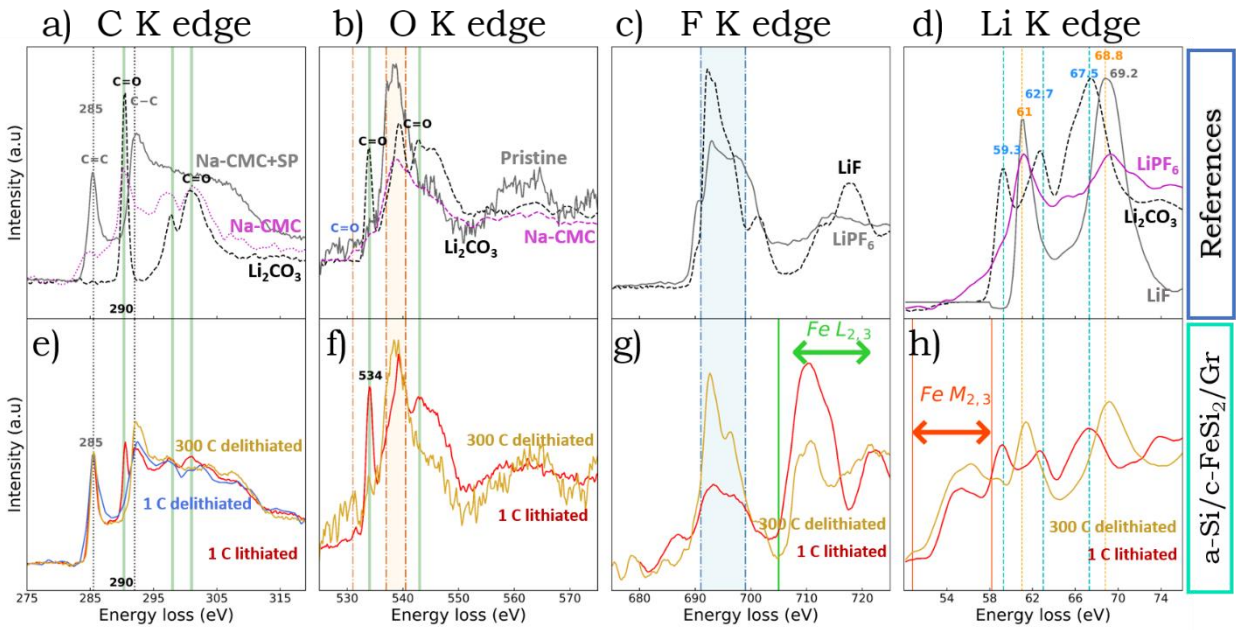

Figure 6.11. C K, O K, F K, and Li K edge spectra of a–d) the references measured to compare the electrodes, and e–h) a-Si/c-$FeSi_2$/graphite electrode during the first cycle at the lithiation and after 300 cycles at delithiation.

Remarkably, both the once-cycled delithiated and the 300th-cycled delithiated do not present the sharp, intense peak at 290 eV (C=O), therefore lacking a significant presence of carbonates. A subtle feature from the 300th-cycled sample is an increased intensity of the peak at 292 eV.

Due to beamtime limitations, we could not measure other edges for the once-cycled delithiated sample neither the pristine electrode for a-Si/c-$FeSi_2$/graphite. Consequently, we used the c-Si Nps pristine electrode to compare the O K edge spectra since it presents similar features from 535 to 540 eV as the composite electrodes. This similarity may come from the type of typical interaction of the binder-active material, as explained previously.

Figure 6.11f shows the O K edge spectra for the once-cycled lithiated and 300th-cycled delithiated electrode. Similarly to the C K spectra, the once-

cycled lithiated sample presents features from the Li_2CO_3 reference, such as the peaks at 534, 539, and 542 eV. The peak at 534 eV for the 300th-cycled sample has almost vanished, and the aged electrode spectrum shares mostly the features of the c-Si Nps pristine electrode.

The disappearance of the peak corresponding to CO_3^{2-} supports the SEI dissolution during delithiation, as already observed for the c-Si Nps electrodes, which presented less intense carbonyl peaks.

This observation is in agreement with previous studies on Si Nps[1,13] and graphite[39,40]. In fact, by using XPS, Hernandez *et al.* observed in this a-Si/c-$FeSi_2$/Gr electrode that the amount of carbon and oxygen species in the SEI are very low using similar electrolyte like us[15].

6.5.3.2 *F K and Li K edge*

The F K spectra for the once-cycled lithiated and 300th-cycled delithiated samples are shown in Figure 6.11g and exhibit neat differences. The once-cycled lithiated electrode presents a broad and low-intensity bump from 680 eV to 705 eV. In contrast, the F K spectrum of the 300th-cycled delithiated sample shows a step bump in the same region. Note that, in the F K edge spectra, the XRS profile also shows peaks corresponding to the Fe $L_{2,3}$ edge in between 705 eV and 720 eV, which come from the c-$FeSi_2$ in the composite.

The shape of the F edge spectra could indicate that $LiPF_6$ is probably the dominant compound in the once-cycled lithiated sample, and, after aging, it has evolved to LiF.

Finally, the Li K spectra for the a-Si/c-$FeSi_2$/Gr electrodes, once-cycled lithiated, and 300th-cycled delithiated, are shown in Figure 6.11h. The once-cycled lithiated electrode presents peaks at 59.3, 62.7, and 67.5 eV that resembles Li_2CO_3. On the other hand, the 300th-cycled delithiated electrode presents the peaks that may correspond to $LiPF_6$ or LiF.

Note that, in the Li K edge spectra, the XRS spectra show the Fe $M_{2,3}$ edge below 58 eV, coming from c-$FeSi_2$.

6.5.3.3 *Summary of qualitative analysis in composites*

In summary, we can conclude that the Li_2CO_3 is formed during lithiation, confirming the formation mainly of CO_3^{2-} in this state of charge, as observed in the Li K, C K, and O K spectra. In contrast, Li_2CO_3 is not observed in the 300th-cycled delithiated sample. After aging, we obtained mainly LiF in the Li K edge, corroborated by the F K edge spectrum.

6.5.4 A quantitative study of the a-Si/c-$FeSi_2$/graphite electrodes

Again, as for c-Si Nps electrodes, we attempt a more quantitative analysis of the data at this stage. Note that we could not perform the linear combination for the Li K edge spectrum since there is a significant contribution from the Fe $M_{2,3}$ signals.

6.5.4.1 C K edge spectra

The quantitative analysis results for the C K edge are shown in Figure 6.12a. The green line is the best linear combination obtained using references and must be compared to the original electrode data, 1c-lithiated electrode (in red), and 330c-delithiated electrode (in yellow). The obtained weight factors and references are summarized in Table 6.5.

The linear combination fairly simulates the C K XRS spectra. We find a higher Li_2CO_3 quantity for the lithiated electrode (13%) and a much lower value for the 300th cycled delithiated (3%).

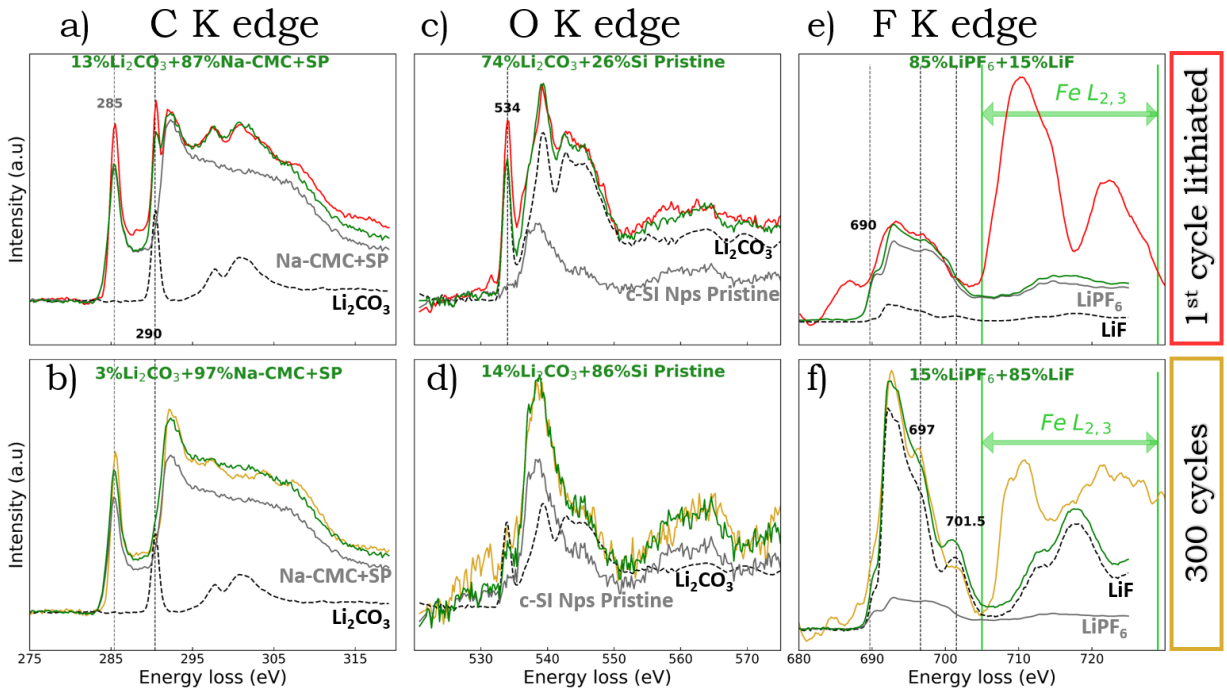

Figure 6.12 results of the quantitative analysis for the XRS spectra of a–b) C K edge, c–d) O K edge, and e–f) F K edge for the electrodes one-cycled lithiated and 300th-cycled delithiated a-Si/c-$FeSi_2$/graphite.

Table 6.5 Weight factors obtained from the quantitative analysis of the C K, O K, and Li K edges for the a-Si/c-$FeSi_2$/graphite electrodes

Edges	References	Weight factors	
		Lithiated	300th cycle Delithiated
C K	Li_2CO_3+Na-CMC+Super P	13% Li_2**C**O_3	3% Li_2**C**O_3
O K	Li_2CO_3+c-SiNps electrode	74% Li_2C**O**$_3$	14% Li_2C**O**$_3$
F K	Li**P**F_6 + Li**F**	85% Li**P**F_6 + 15%Li**F**	15% Li**P**F_6 + 85%Li**F**

Even though the a-Si/c-$FeSi_2$/graphite electrodes were prepared with lithium polyacrylate (Li-PAA) as a binder, the Na-CMC + Super P compound is a useful reference since it shares the same peaks as the XRS spectra found in the a-Si/c-$FeSi_2$/graphite electrodes. We speculate that the XRS spectrum obtained in the reference Na-CMC + Super P compound illustrates the type of hydrogen bonds (or covalent ester-like bonds) resulted from the interaction of the binder with the active material such as the Super P, graphite, or silicon since the binder contains carboxylates ($RCOO^-$)[26,27]. These organic groups react by a condensation reaction with the OH groups from the silicon surface[26,27].

We find 13% Li_2**C**O_3 for the once-cycled lithiated electrode, a value significantly lower than the one found in c-Si Nps (38%). This lower percentage may indicate a more stable SEI for the composite electrode than for the c-Si Nps electrode. This could be explained by the peculiar architecture of the silicon phase, where a-Si forms a continuous matrix embedding c-$FeSi_2$+graphite that confer mechanical stability. Therefore, fresher and newly exposed silicon particles while cycling are less, producing a more stable SEI.

6.5.4.2 O K edge spectra

Figure 6.12 c and d show the O K spectra and the quantitative analysis for the composite electrodes. The obtained weight factors are summarized in Table 6.5.

We use the c-Si Nps pristine reference to simulate the XRS spectra of the once-cycled and 300th-cycled electrodes since we could not measure the pristine composite electrode. Even though we did not measure the pristine composite electrode, the c-Si Nps pristine reference shows a typical chemical environment resulting from the mixture of active material, binder, and graphite.

The linear combination used for the O K once-cycle lithiated sample has acceptably simulated the range from 535 to 575 eV, except for the noisy bump at 530 eV.

Considering this, we obtained 74% and 14% of Li_2CO_3 for the once-cycled lithiated and 300th cycles delithiated, respectively. The weight factors found here are in line with the qualitative observations. Note that in the c-Si NPs electrodes, we found 74% and 47% of Li_2CO_3 based on the O K edge analysis. Therefore, it seems that a major difference regards the partial dissolution of the SEI organic compounds during the delithiation.

6.5.4.3 F K edge spectra

Figure 6.12 e and f show the F K spectra and the quantitative analysis for the composite electrodes. The obtained values of weight factors are summarized Table 6.5.

The quantitative analysis for the F K spectrum moderately reproduces the electrodes XRS spectra. Note that the pre-edge peak at ~ 690 eV and the small bumps at 697 eV and 701.5 eV are poorly described. In this quantitative analysis, we can describe only the range from 680 to 705 eV since the bumps at higher energies correspond to Fe $L_{2,3}$, obstructing the complete description of the XRS spectra.

We obtain 85% $LiPF_6$ for the once-lithiated electrode, agreeing with the qualitative analysis where the sample spectrum presents a broader bump similar to the reference compound $LiPF_6$. In contrast, we obtain mainly LiF (85%) in the 300th cycled delithiated electrode.

6.5.5 Summary of the XRS analysis of composites

Table 6.6 summarizes the weight factors extracted from the quantitative XRS analysis, providing insights into the SEI chemical composition in the two a-Si/c-$FeSi_2$/Gr electrodes, once-cycled lithiated, and 300th cycles delithiated.

Table 6.6 Summary of the weight factors found in c-Si Nps and a-Si/c-FeSi2/Gr electrodes.

Edges	Weight factors			
	c-Si Nps electrodes		a-Si/c-FeSi2/Gr electrodes	
	Lithiated	Delithiated	Lithiated	300th cycle Delithiated
C K	38% Li_2**C**O_3	28% Li_2**C**O_3	13% Li_2**C**O_3	3% Li_2**C**O_3
O K	74% Li_2C**O**$_3$	47% Li_2C**O**$_3$	74% Li_2C**O**$_3$	14% Li_2C**O**$_3$
F K	65% Li**F** + 35%Li**F**	45% Li**F** + 55%Li**F**	85% Li**F** + 15%Li**F**	15% Li**F** + 85%Li**F**

- We studied the SEI composition in the electrodes once-cycled and 300th-cycled.
- We observed differences in the XRS spectra, depending on the state of charge of the electrode.
- We evaluated the SEI evolution by analyzing the intensities related to LiF, Li_2CO_3, or $LiPF_6$.

Specifically, we demonstrated the key features of the composite material:

1) Short-term behavior: the chemical environment in the first cycle.

We found mainly Li_2CO_3 and $LiPF_6$ in the once-cycled lithiated electrode. Interestingly, the Li_2CO_3 percentage is lower for the composite electrodes than for the c-Si Nps electrodes. These results may indicate that in a-Si/$FeSi_2$/Gr composites, the solvent decomposition is lower. Additionally, the Li_2CO_3 compound is higher in the lithiated state than in the delithiated one, and the carbonyl composition decreases after delithiation, suggesting the SEI dissolution, as observed for c-Si Nps.

2) Long-term aging: the chemical environment after 300 cycles.

We suppose that the lower amounts of Li_2CO_3 found in the aged electrode imply that the carbonates have polymerized in an inhomogeneous environment like R-COO-R (ester) or R-CO-R (ketone). Our hypothesis is based on two facts. The first one lies in the EDX chemical mapping, showing C and O elements in the thick SEI. The second one is based on the broad peak present in the O K spectrum, analogous to the c-Si Nps pristine reference. This similarity reveals a chemical environment product of the condensation of groups COO^-, resulting in R-COO-R (ester) or R-CO-R (ketone) in a polymerized environment.

Indeed, after aging, polymers have been found in silicon anodes. Using ^{13}C and ^{29}Si solid NMR, Jin *et al.* demonstrated that the SEI of the crystalline Si electrodes is made of polyethylene oxide (PEO-type, expressed as $H-(O-CH_2-CH_2)_n-OH$). These polymers are bonded covalently to organosiloxanes (Si–O–C) from the Si particles[9].

Using XRS, it is quite tricky to corroborate the existence of these specifically Si-O-C bonds in the Si, O, or C edges since the signal-to-noise ratio spectra of these bonds may be low because of their specificity and small quantities.

As the EDX mapping shows a higher concentration of O nearby the $Si/FeSi_2$ alloys, we suppose the formation of Si–O bonds and, next to these bonds, the possible formation of polymerized carbonyls chains. In other words, the porous and thick SEI region could be formed of carbonyls (C=O) polymerized in an inhomogeneous chemical environment bonded to Si.

A high quantity of LiF was found in the 300-cycle material (85%), which is qualitatively corroborated by the Li K edge spectrum, similar to the LiF reference compound. We suppose that this high amount of LiF comes mainly from the FEC decomposition, as reported in the literature [1,41,5,42]. According to the reported studies, the differences in LiF concentration are more evident after aging when using FEC[1,2]. That may explain the equivalent $LiPF_6$-LiF formation for c-Si Nps electrodes during the first cycle and the higher $LiPF_6$ in the once-cycled a-Si/c-$FeSi_2$ electrode.

Globally, the comparative study of nanoparticles-based anodes and silicon/graphite composite allowed us to establish the following SEI mechanisms:

● SEI Partial dissolution. In c-Si Nps electrodes, we obtained a higher quantity of carbonyls (C=O) after lithiation, that probably dissolved during delithiation. These results validate previous observations in c-Si Nps, demonstrating that the SEI is a dynamic layer and possibly explains the irreversible capacity of 16% in the first cycle. A more effective dissolution of the SEI was found in the composite anodes, probably associated with a limited electrolyte degradation.

● SEI stability. Our findings suggest a lower carbonate formation for a-Si/c-$FeSi_2$/graphite composite compared to c-Si Nps. These results imply that probably the a-Si/c-$FeSi_2$/graphite composite undergoes fewer volume variations and, thus, favors the formation of a more stable SEI.

● SEI aging. In the nanoparticles-anodes, we could not differentiate a preferential compound formation regarding the F-contained compounds since

both LiF and $LiPF_6$ are obtained in equal proportions. However, the composite results corroborate the primary F-containing component after aging, which is LiF. Regarding the C and O containing components, we hypothesized the formation of polymerized carbonyls that are probably bonded to Si-O. After long-term cycling, we revealed the complex chemical environment of carbonates that may have polymerized, showing an inhomogeneous environment.

As a last remark, we may comment on the bumps corresponding to Fe $L_{2,3}$ in the F K edge, which could indicate the valence state of Fe in the $FeSi_2$ alloy[20,43,44]. Qualitatively, the Fe $L_{2,3}$ edge intensity of the 300-cycle delithiated sample is lower than the one-cycle lithiated intensity. These changes could indicate that the valence state of the $FeSi_2$ has changed after 300 cycles. However, the bump analysis is not straightforward, and we have not measured references for the Fe edges.

6.6 General conclusions on XRS

The present study attempted to explore the capabilities of X-ray Raman Scattering to study the bulk chemical environment in two types of silicon-based electrodes: c-Si Nps and a-Si/c-$FeSi_2$/graphite composite.

XRS is a technique that allows probing soft edges (with E<1000 eV) by using hard X-rays beams (~10 keV). Using hard X-rays, this technique can probe much deeper depths (~ 1 µm) as compared to XPS or XAS, thus avoiding surface contamination and self-absorption. As a consequence, XRS appears, in principle, as an interesting method to study the SEI in aged electrodes since

the SEI thickness is higher than 100 nm. However, unlike XPS, XRS is a scarcely used technique for studying the chemical environment in LiBs. This implies that there is a lack of knowledge on the experimental data acquisition, treatment, and analysis, applied to the materials used in batteries, requiring instrumental and analytical developments. To start filling this gap, we measured some reference compounds and demonstrated the value of a quantitative analysis of real materials spectra by using these references. This approach is clearly adapted from methodologies currently employed in many spectroscopies, where large bumpy signals need to be appropriately deconvoluted to isolate the various contributions. For instance, reference spectra have been used to deconvolute EELS spectra from electrode materials[18], and so is it for NMR or XPS. Tools as Principal Component Analysis also allow for a very powerful attribution of distinct lines/peaks to elementary components and were employed successfully by Fehse and co-workers[45]. Yet, PCA or equivalent methods, including more sophisticated machine-learning-based tools, require a certain number of data for statistics and may be better suited to analyze important batches of real-time characterizations. Worth mentioning at this point is the need for combining different spectroscopic experiments (e.g. XPS and XRS, NMR and XRS, XAS and XRS) as well as integrating simulations to analyze data. Theoretical calculations based on DFT are, in this regard, extremely valuable to simulate vibrational or inelastic spectra, as very often done to analyze EXAFS or XANES data, for instance.

Our work here has been a first trial towards developing more advanced methodologies, and we have identified many further steps that could be implemented in the XRS analysis for the battery materials and provide an effective tool to probe electrode/electrolyte interfaces:

- The reference spectra are critical. Many other basic compounds are left to be measured in order to start constituting a library usable by the community. For instance, Li_2O_2, LiOH, are missing. Obviously, lithiated states of silicon, Li_xSi alloys, would be very important, as well as Li_xSiO_y. Sample preparation might be an issue due to the extreme reactivity of some of these materials, metastability of lithiated phases, etc.
- Types of binders, conductive additives, salts could be damaged.
- The different constituents of a pristine electrode should be measured separately and selectively mixed to evaluate their interactions. We did this with the binder and binder + super P, but this should be generalized. Archetypal oligomers and polymers (PEO-types, but not only) could be measured to understand the transformations of organic compounds in the long term.
- We performed our study on a limited number of samples, which hardly allows generalizing the findings and capturing a full picture. It would be ideal to measure a larger number of electrodes in different states (not only at the end of lithiation or delithiation). Possibly, by focusing on one edge, in-situ measurements could be envisaged to bring knowledge on a particular chemical element and its environment. Besides, modeling

would be needed to help to rationalize small energy shifts and intensity variations.

- We extracted weight percentages from the linear decomposition on the reference basis, but these values cannot directly be transformed into the amount of reference compound present in the material (%wt). Normalization should be applied to exploit these numbers further.
- XRS in silicon-based electrodes is promising to correlate knowledge on the chemical environment to the electrochemical performance and morphological variations. Si-based electrodes have a dynamic SEI that may consume more Li-ion and electrolyte. This consumption is unfavorable in real systems such as full cells where the Li content is limited. Composites are promising materials since they use a matrix to mitigate volume expansion and allow a more stable SEI. Li et al. studied the SEI composition of Si/C composite electrodes by solid NMR, XPS, and X-PEEM techniques. The chemical composition of the SEI for this composite was reported to be dense, compact, uniform, and have a large amount of LiF from the decomposition of FEC, covering the Si particles and suppressing the volume changes during cycling[2]. Other studies on Si-Graphite electrodes have demonstrated thicker SEI on Si-rich areas compared to graphite-rich areas[46]. The morphology of the a-Si/c-$FeSi_2$ alloys after 300 cycles evolved into a branch-shaped-like a-Si/c-$FeSi_2$ with active channels within a thick porous SEI layer, containing elements such as O, C, F, and P (see Figure 6.9 and Figure 6.10). This morphology is totally consistent with other studies where the SEI mainly grows next to Si areas.

- Our study evidenced the capabilities of X-ray Raman scattering to discern the chemical composition at the bulk of electrodes, depending on the cycle number and state of charge, therefore opening paths to the investigation of new chemistries, including for post-lithium ion technologies.

6.7 Bibliography

1. Xu, C. *et al.* Improved Performance of the Silicon Anode for Li-Ion Batteries: Understanding the Surface Modification Mechanism of Fluoroethylene Carbonate as an Effective Electrolyte Additive. *Chem. Mater.* **27,** 2591–2599 (2015).
2. Li, Q. *et al.* Identification of the Solid Electrolyte Interface on the Si/C Composite Anode with FEC as the Additive. *ACS Appl. Mater. Interfaces* **11,** 14066–14075 (2019).
3. Gauthier, M. *et al.* Electrode–Electrolyte Interface in Li-Ion Batteries: Current Understanding and New Insights. *J. Phys. Chem. Lett.* **6,** 4653–4672 (2015).
4. Nie, M., Abraham, D. P., Chen, Y., Bose, A. & Lucht, B. L. Silicon Solid Electrolyte Interphase (SEI) of Lithium-Ion Battery Characterized by Microscopy and Spectroscopy. *J. Phys. Chem. C* **117,** 13403–13412 (2013).
5. Martínez de la Hoz, J. M. & Balbuena, P. B. Reduction Mechanisms of Additives on Si Anodes of Li-Ion Batteries. *Phys. Chem. Chem. Phys.* **16,** 17091–17098 (2014).
6. Schroder, K. *et al.* The Effect of Fluoroethylene Carbonate as an Additive on the Solid Electrolyte Interphase on Silicon Lithium-Ion Electrodes. *Chem. Mater.* **27,** 5531–5542 (2015).
7. Tasaki, K. *et al.* Solubility of Lithium Salts Formed on the Lithium-Ion Battery Negative Electrode Surface in Organic Solvents. *J. Electrochem. Soc.* **156,** A1019–A1026 (2009).
8. Michan, A. L. *et al.* Solid Electrolyte Interphase Growth and Capacity Loss in Silicon Electrodes. *J. Am. Chem. Soc.* **138,** 7918–7931 (2016).
9. Jin, Y. *et al.* Understanding Fluoroethylene Carbonate and Vinylene Carbonate Based Electrolytes for Si Anodes in Lithium-Ion Batteries with NMR

Spectroscopy. *J. Am. Chem. Soc.* **140,** 9854–9867 (2018).

10. Hu, B. *et al.* Understanding of Pre-Lithiation Of Poly(Acrylic Acid) Binder: Striking the Balances Between the Cycling Performance and Slurry Stability for Silicon-Graphite Composite Electrodes in Li-Ion Batteries. *J. Power Sources* **416,** 125–131 (2019).
11. Michan, A. L. *et al.* Fluoroethylene Carbonate And Vinylene Carbonate Reduction: Understanding Lithium-Ion Battery Electrolyte Additives and Solid Electrolyte Interphase Formation. *Chem. Mater.* **28,** 8149–8159 (2016).
12. Xu, C. *et al.* Interface Layer Formation in Solid Polymer Electrolyte Lithium Batteries: an XPS Study. *J. Mater. Chem. A* **2,** 7256–7264 (2014).
13. Philippe, B. *et al.* Nanosilicon Electrodes for Lithium-Ion Batteries: Interfacial Mechanisms Studied by Hard and Soft X-ray Photoelectron Spectroscopy. *Chem. Mater.* **24,** 1107–1115 (2012).
14. Philippe, B. *et al.* Role of the LiPF6 Salt for the Long-Term Stability of Silicon Electrodes in Li-Ion Batteries – A Photoelectron Spectroscopy Study. *Chem. Mater.* **25,** 394–404 (2013).
15. Hernández, G. *et al.* Elimination of Fluorination: The Influence of Fluorine-Free Electrolytes on the Performance of LiNi 1/3 Mn 1/3 Co 1/3 O 2 /Silicon–Graphite Li-Ion Battery Cells. *ACS Sustain. Chem. Eng.* **8,** 10041–10052 (2020).
16. Nanda, J. *et al.* Unraveling the Nanoscale Heterogeneity of Solid Electrolyte Interphase Using Tip-Enhanced Raman Spectroscopy. *Joule* **3,** 2001–2019 (2019).
17. Ruther, R. E. *et al.* Chemical Evolution in Silicon–Graphite Composite Anodes Investigated by Vibrational Spectroscopy. *ACS Appl. Mater. Interfaces* **10,** 18641–18649 (2018).
18. Boniface, M. *et al.* Nanoscale Chemical Evolution of Silicon Negative Electrodes Characterized by Low-Loss STEM-EELS. *Nano Lett.* **16,** 7381–7388 (2016).
19. Braun, A. *et al.* Hard X-Rays In-Soft X-Rays Out: An Operando Piggyback View Deep Into a Charging Lithium-Ion Battery With X-Ray Raman Spectroscopy. *J. Electron Spectros. Relat. Phenomena* **200,** 257–263 (2015).
20. Liu, X. *et al.* Phase Transformation and Lithiation Effect on Electronic Structure of Li x FePO 4 : An In-Depth Study by Soft X-ray and Simulations. *J. Am. Chem. Soc.* **134,** 13708–13715 (2012).
21. Stutz, G. E. *et al.* Intercalation Stage Dependence of Core Electronic Excitations in Li-Intercalated Graphite from Inelastic X-Ray Scattering. *Appl. Phys. Lett.* **110,** 253901(1-5) (2017).

22. Nonaka, T., Kawaura, H., Makimura, Y., Nishimura, Y. F. & Dohmae, K. In-Situ X-Ray Raman Scattering Spectroscopy of a Graphite Electrode for Lithium-Ion Batteries. *J. Power Sources* **419,** 203–207 (2019).
23. Boesenberg, U. *et al.* Electronic Structure Changes Upon Lithium Intercalation Into Graphite – Insights From Ex-Situ And Operando X-Ray Raman Spectroscopy. *Carbon N. Y.* **143,** 371–377 (2019).
24. de Boer, T. *et al.* Direct Evidence of Charge Transfer upon Anion Intercalation in Graphite Cathodes through New Electronic States: An Experimental and Theoretical Study of Hexafluorophosphate. *Chem. Mater.* **32,** 2036–2043 (2020).
25. Wang, J., Zhang, L. & Zhang, H. Effects of Electrolyte Additive on the Electrochemical Performance of Si/C Anode for Lithium-Ion Batteries. *Ionics (Kiel).* **24,** 3691–3698 (2018).
26. Hochgatterer, N. S. *et al.* Silicon/Graphite Composite Electrodes for High-Capacity Anodes: Influence of Binder Chemistry on Cycling Stability. *Electrochem. Solid-State Lett.* **11,** A76–A80 (2008).
27. Vogl, U. S. *et al.* Mechanism of Interactions between CMC Binder and Si Single Crystal Facets. *Langmuir* **30,** 10299–10307 (2014).
28. Frati, F., Hunault, M. O. J. Y. & de Groot, F. M. F. Oxygen K-edge X-ray Absorption Spectra. *Chem. Rev.* **120,** 4056–4110 (2020).
29. Urquhart, S. G. & Ade, H. Trends in the Carbonyl Core (C 1S, O 1S) → π* C=O Transition in the Near-Edge X-ray Absorption Fine Structure Spectra of Organic Molecules. *J. Phys. Chem. B* **106,** 8531–8538 (2002).
30. Joly, Y., Cavallari, C., Guda, S. A. & Sahle, C. J. Full-Potential Simulation of X-ray Raman Scattering Spectroscopy. *J. Chem. Theory Comput.* **13,** 2172–2177 (2017).
31. Obrovac, M. N. & Christensen, L. Structural Changes in Silicon Anodes during Lithium Insertion\Extraction. *Electrochem. Solid-State Lett.* **7,** A93–A96 (2004).
32. Obrovac, M. N. & Krause, L. J. Reversible Cycling of Crystalline Silicon Powder. *J. Electrochem. Soc.* **154,** A103 (2007).
33. Pinilla, S. *et al.* 0D-1D Hybrid Silicon Nanocomposite as Lithium-Ion Batteries Anodes. *Nanomaterials* **10,** 515(1-13) (2020).
34. Bridel, J.-S., Azaïs, T., Morcrette, M., Tarascon, J.-M. & Larcher, D. Key Parameters Governing the Reversibility of Si/Carbon/CMC Electrodes for Li-Ion Batteries. *Chem. Mater.* **22,** 1229–1241 (2010).
35. Kumar, P. *et al.* Nano-Architectured Composite Anode Enabling Long-Term

Cycling Stability for High-Capacity Lithium-Ion Batteries. *Small* **16,** 1906812(1-14) (2020).

36. Radvanyi, E. *et al.* Study and modeling of the Solid Electrolyte Interphase behavior on nano-silicon anodes by Electrochemical Impedance Spectroscopy. *Electrochim. Acta* **137,** 751–757 (2014).
37. Radvanyi, E., De Vito, E., Porcher, W. & Jouanneau Si Larbi, S. An XPS/AES Comparative Study of the Surface Behaviour of Nano-Silicon Anodes for Li-Ion Batteries. *J. Anal. At. Spectrom.* **29,** 1120–1131 (2014).
38. Porcher, W. *et al.* Understanding Polyacrylic Acid and Lithium Polyacrylate Binder Behavior in Silicon-Based Electrodes for Li-Ion Batteries. *J. Electrochem. Soc.* **164,** A3633–A3640 (2017).
39. Ciosek Högström, K. *et al.* The Influence of PMS-Additive on the Electrode/Electrolyte Interfaces in LiFePO4/Graphite Li-Ion Batteries. *J. Phys. Chem. C* **117,** 23476–23486 (2013).
40. Ciosek Högström, K. *et al.* The Buried Carbon/Solid Electrolyte Interphase in Li-ion Batteries Studied by Hard X-ray Photoelectron Spectroscopy. *Electrochim. Acta* **138,** 430–436 (2014).
41. Lin, Y.-M. *et al.* High Performance Silicon Nanoparticle Anode in Fluoroethylene Carbonate-Based Electrolyte for Li-Ion Batteries. *Chem. Commun.* **48,** 7268–7270 (2012).
42. Leung, K. *et al.* Modeling Electrochemical Decomposition of Fluoroethylene Carbonate on Silicon Anode Surfaces in Lithium-Ion Batteries. *J. Electrochem. Soc.* **161,** A213–A221 (2014).
43. Cosandey, F., Su, D., Sina, M., Pereira, N. & Amatucci, G. G. Fe Valence Determination and Li Elemental Distribution in Lithiated FeO0.7F1.3/C nanocomposite Battery Materials by Electron Energy Loss Spectroscopy (EELS). *Micron* **43,** 22–29 (2012).
44. Sina, M. *et al.* Structural Phase Transformation and Fe Valence Evolution in Feoxf2−X/C Nanocomposite Electrodes During Lithiation and De-Lithiation Processes. *J. Mater. Chem. A* **1,** 11629 (2013).
45. Fehse, M. *et al.* Applying Chemometrics to Study Battery Materials: Towards the Comprehensive Analysis of Complex Operando Datasets. *Energy Storage Mater.* **18,** 328–337 (2019).
46. An, S. J. *et al.* Electrolyte Volume Effects on Electrochemical Performance and Solid Electrolyte Interphase in Si-Graphite/NMC Lithium-Ion Pouch Cells. *ACS Appl. Mater. Interfaces* **9,** 18799–18808 (2017).

Conclusions and perspectives

Silicon has been intensively studied as a promising active anode material for Lithium-ion batteries due to its high specific capacity (3576 mAh/g, compared to 372 mAh/g for the commercial graphite). However, Si experiences significant volume expansion upon the alloying-dealloying reactions with lithium-ions, leading to subsequent pulverization and premature aging. One strategy developed to improve the cyclability and durability is using nanostructured composite materials in which silicon is mixed with other active or inactive components. An alternative is to look at other column IV elements such as Ge, which, beyond its theoretical capacity (1623 mAh/g), has appealing characteristics such as better electronic conductivity, Li diffusivity, and stability than Si.

In this thesis, we addressed both strategies. We aimed at investigating the (de)lithiation mechanisms in, on the one hand, silicon and germanium-based negative electrodes, focusing on two types of systems, Ge and SiGe-alloys nanoparticles, and on the other hand in a commercial-grade silicon-based composite. The structural evolution occurring upon (de)lithiation was probed mainly by *operando* X-ray scattering techniques and was correlated to the electrochemical behavior.

Chapter 3 was devoted to crystalline germanium nanoparticles. The cycling mechanism was analyzed using sequences of partial and complete lithiations and combining *operando* XRD and *post-mortem* ^{7}Li NMR to describe the structural changes of the system.

The investigation of a complete lithiation of Ge allowed correlating structural and electrochemical behaviors, identifying the voltage value of the first dQ/dV lithiation peak obtained from galvanostatic cycling as the one at which the c-Ge starts to be amorphized (0.3 V).

A detailed study of the c-Ge lattice evolution during partial lithiation cycles was performed, and the results compared to the behavior of c-Si Nps. The most striking difference concerns the very limited strain release in the first stage of the delithiation in the case of silicon, while the Ge lattice relaxation is complete. Consequently, the Ge strain evolution is very similar from one cycle to another, while Si lattice strain strongly increases upon cycling. This has a direct impact on the cyclability.

Finally, the complete lithiation performed after three partial cycles evidenced the formation of the c-$Li_{15}Ge_4$ phase, in contrast with Si, for which the corresponding $Li_{15}Si_4$ phase is metastable in the case of nanoparticles. We showed that this phase is thermodynamically stable. Experimental results on c-$Li_{15}Ge_4$ are scarce and mainly qualitative as the associated diffracted signal is frequently poor. Thanks to high-quality XRD data, we were able to precisely follow the evolution of the lattice parameter as well as phase amount, which we believe will be useful for supporting theoretical predictions.

Chapter 4 was devoted to a detailed study of the (de)lithiation mechanisms in $Si_{100-x}Ge_x$ alloys, which combine the high specific capacity of silicon with the mechanical resilience of germanium. We investigated three compounds synthesized by laser pyrolysis and differing by their germanium content.

The characterization of the pristine powders evidenced strong heterogeneities in composition and size. For instance, the Ge-rich alloy appeared to be mainly a mixture of four different $Si_{100-x}Ge_x$ phases, with x ranging between 67% and 100%.

We showed that upon cycling, the different phases in a given sample start lithiating sequentially depending on their Ge content. Despite the heterogeneous character of these alloys, the different $Si_{100-x}Ge_x$ component phases behave remarkably consistently, their characteristic lithiation voltage following a linear increase with Ge content.

Galvanostatic cycling performed with coin-cells evidenced different voltage signatures for the three alloys, with a monotonous evolution of the characteristic voltage values with Ge content. Surprisingly, the structural heterogeneities are not reflected in the electrochemistry curves. While the Si-rich alloy is reminiscent of pure Si, the two others behave qualitatively as pure Ge. In particular, they evidence a sharp peak in the delithiation stage, which we show to be directly correlated to the disappearance of the c-$Li_{15}(Si_{100-x}Ge_x)_4$ phase.

This crystalline $Li_{15}(Si_{100-x}Ge_x)_4$ phase forms with the Ge-rich and Si≈Ge alloys at the end of the lithiation and disappears in the delithiation stage at a voltage value increases with the Ge content. Its structural properties are very similar to those of $Li_{15}Ge_4$. Moreover, the $Li_{15}(Si_{100-x}Ge_x)_4$ peak shape can be accounted for considering a single peak that does not support the existence of composition heterogeneities. This leads us to propose that under the lithiation

conditions, which are those of our measurements, the lithiated crystalline phase $Li_{15}(Si_{100-x}Ge_x)_4$ is formed only in a very restricted range of composition, namely for x close to 1.

The studied $Si_{100-x}Ge_x$ *alloys*, characterized by a strong heterogeneity, consequently present an intrinsic variability of composition and, therefore, in the mechanical properties, which must reinforce their robustness. Indeed, they exhibit remarkable electrochemical properties and aging behavior.

Chapter 5 was devoted to investigating the electrochemical cycling behavior of a commercial a-Si/c-$FeSi_2$/graphite using *operando* and simultaneous small-angle and wide-angle X-ray scattering (SAXS/WAXS). The graphite and lithiated graphite evolution were followed using WAXS. Considering the evolution of the diffraction intensities combined with the full-cell capacity allows the estimation of the relative contribution of graphite and silicon. The mechanism of (de)lithiation was corroborated by SAXS, where the (de)increasing of silicon volume was followed thanks to the (de)increasing of the integrated SAXS intensity.

SEI was the motivation of Chapter 6. We explored synchrotron X-ray Raman scattering (XRS) capabilities for investigating *post-mortem* the SEI composition and evolution in two types of electrodes: crystalline silicon nanoparticles and the composite a-Si/c-$FeSi_2$/graphite at different states of charge. XRS is a non-resonant technique that allows probing soft edges (with E < 1000 eV) by using hard X-rays beams (~ 10 keV). Using hard X-rays allows probing deeper depths (~ 1 µm) compared to XPS or XAS, thus avoiding surface contamination and self-absorption. As a consequence, XRS appears, in principle, as an

interesting tool to study the SEI in aged electrodes since the SEI thickness is higher than 100 nm. We developed a qualitative and semi-quantitative analysis of XRS spectra based on the decomposition of real electrode spectra at selected edges (basically, Li K, Si $L_{2,3}$, C K, O K, and F K) using reference compounds spectra. This allowed us to determine the main species formed in the SEI and their evolution as a function of aging and state-of-charge. Having access to the chemical environment of light elements in bulk, like lithium, is potentially very important to help to quantify interfacial phenomena and their impact on the performances.

To summarize, this thesis presents detailed results on the behavior upon electrochemical cycling of promising negative electrodes for Li-ion batteries based on column IV elements. Our findings highlight the significant role of the mechanical properties, either in the case of Ge, which is softer and more resilient than Si or with the a-Si/c-$FeSi_2$/graphite composite in which the mainly inactive c-FeSi phase helps accommodating Si strain. Moreover, we have opened the way towards using the XRS technique for batteries studies, which appears as a highly promising technique to gain access to SEI composition and evolution.

Some perspectives

Our work opens several perspectives to use synchrotron techniques that were poorly, or not, applied in battery research, *e.g.,* the simultaneous SAXS/WAXS and the XRS techniques. Some ideas for future developments were already mentioned in the respective chapters, both underlying the needs and benefits to couple such kind of advanced characterization to modeling, and the

transferability of our methodologies to other types of active materials and/or battery technologies.

Additionally, an important part of the results presented in this thesis was obtained by in-lab techniques that complement, not only accessory to synchrotron experiments. The D8 diffractometer and the Le-Riche electrochemical cell used for the *operando* measurements were installed early in the second year of my thesis. The obtained data are very rich but necessitate advanced analysis to consider the positions of the different contributing phases and the different absorption corrections. This was done using Topas software. We believe that our results nicely show the potential of these studies. The self-supporting electrode preparation is a crucial step on which I spent lots of time, but, I finally succeeded in obtaining satisfactory electrochemical conditions, as shown by the correlation between the structural behavior determined from *operando* XRD and the electrochemical signature from the galvanostatic cycling in coin cells. However, better mastering the thickness and density of the electrode should allow more precise diffraction intensity corrections, improving the precision of the fitted structural parameters. Another perspective regards the in-depth understanding of model systems that we can tailor in the lab to bridge the behavior of pure silicon anodes to industrial composites. It would be indeed very interesting to perform the multi-scale multi-technique characterization of model composites, where critical parameters as silicon or germanium/graphite ratio, nature of the nanoparticles (amorphous vs. crystalline or polycrystalline, sizes in range 5 to

100 nm, coatings), electrode fabrication process (binders, additives), may be varied in a controlled manner.

Following this idea, we started some preliminary work on home-made silicon-graphite and germanium-graphite blends, as briefly presented below. We prepared two types of composites using commercial graphite and started investigating their structural changes during lithiation to understand the mechanism of cycling.

Crystalline silicon and graphite composite investigated by SAXS/WAXS

This composite was prepared using mild ball-milling to blend the graphite (65% wt) and crystalline silicon nanoparticles (25 %wt), using Super P and CMC as a binder (10%). We used a speed of 400 rpm for 10 min. The crystalline silicon nanoparticles are 70 nm in size, with a 30 nm crystalline core. This composite c-Si Nps/graphite was cycled partially vs. Li metal until 60 mV at C/10 in pouch-cell and characterized by *operando* SAXS/WAXS performed at the BM02 beamline at ESRF. Figure 7.1a shows the WAXS intensities during the first lithiation. The blue line corresponds to the material in a pristine state. Here, the resultant Bragg reflections for graphite are not visible. However, the bumps in the background are moving, depending on the state of charge. We supposed that graphite layers were oriented along with the X-rays, provoking the disappearance of the diffracted peaks and the lithiated graphite phases. Thus, only the diffracted peak of silicon (111) is clearly observed and continuously decreases in intensity with lithiation.

Figure 7.1b shows the simultaneously obtained SAXS intensities during the lithiation. Similarly, the blue line corresponds to the pristine electrode, and it has shifted to red at the end of the partial lithiation. The artifact at 8.7×10^{-3} Å corresponds to dead pixels. The SAXS profiles show a continuous change during lithiation (blue to red) over the whole Q-range. More specifically, in the high Q-range, Q = [10^{-2}; 10^{-1}] $Å^{-1}$ corresponding to mean characteristic distances of 6 to 60 nm, an excess intensity develops on lithiating silicon, while in the low-Q region [2×10^{-3}; 1×10^{-2}] $Å^{-1}$, corresponding to mean characteristic distances of > 60 nm, a global decrease in intensity is noticed. A kind of "isostatic" point marks the transition between these two ranges where the SAXS intensities vary oppositely. In the limited time we had to analyze these recent data, we could not rationalize this behavior, which is in contrast to the one observed in the industrial composite (where the silicon domains were smaller than here, and SAXS profiles were continuously increasing during lithiation, with an almost invariant low-Q Porod's behavior).

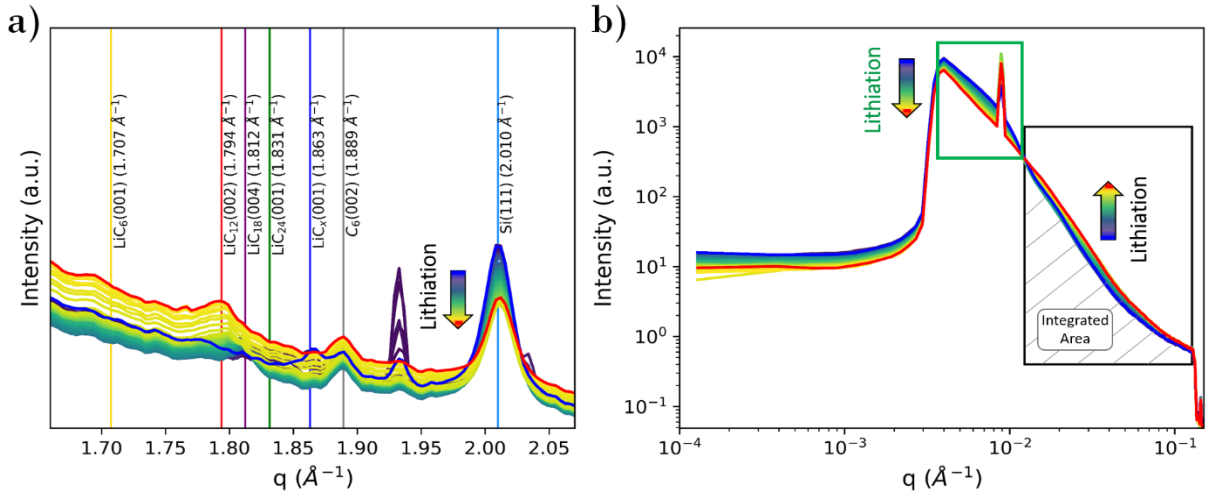

Figure 7.1 a) variations of the WAXS intensities of the Bragg reflection for the silicon during partial lithiation. b) SAXS intensity variations over partial lithiation from 1.0 to 0.06 V vs. Li metal.

The procedure to have more quantitative data consists of integrating the silicon Bragg reflection and the SAXS intensity (limiting ourselves in the zone Q = [10^{-2}; 10^{-1}] $Å^{-1}$) during partial lithiation. The results obtained from this analysis are presented in 7.2.

Figure 7.2a shows voltages vs. Li against time in hours for the partial lithiation until 60 mV. Figure 7.2b shows the normalized integrated intensity obtained by WAXS from the fit of the silicon (111) diffracted peak. The silicon phase begins to decrease at ~75 mV during the plateau of voltage. After this voltage, the silicon peak intensity continually decreases along time until approximately half of the initial WAXS intensity, denoting the gradual amorphization of the silicon. Note that the decrease seems to drop faster after 8 hours.

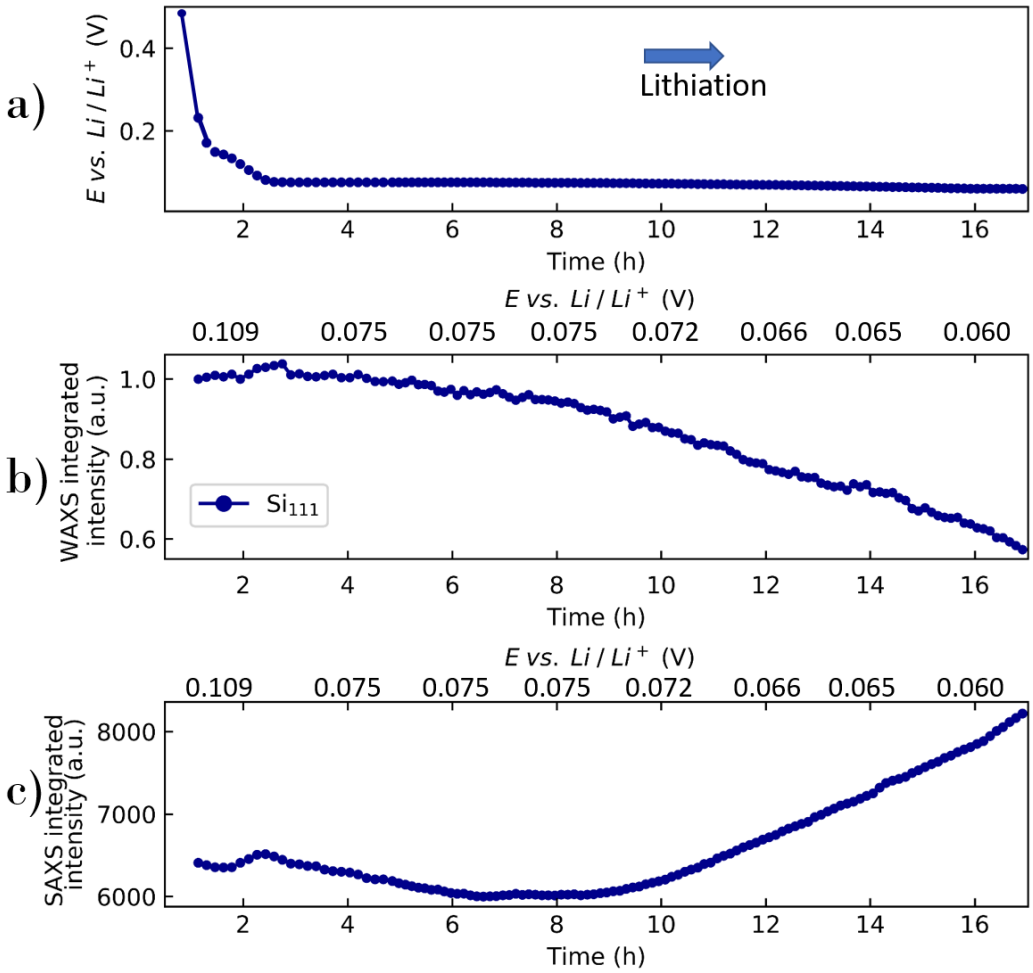

Figure 7.2 a) voltage vs.Li metal against time of the pouch-cell containing the composite c-Si Nps with graphite during lithiation at C/10 against lithium metal. b) Normalized silicon 111 peak area. c) SAXS integrated intensity variations in the zone Q = [10^{-2}; 10^{-1}] $Å^{-1}$.

In correspondence to the crystalline peak evolution, we have represented in Figure7.2c the SAXS integrated intensity in the Q-region 10^{-2} to 10^{-1} $Å^{-1}$ as a function of time. There are two distinct regions in the SAXS integrated intensity curve. The first one is a slight decrease in the integrated intensity until ~ 6-8 hours. The SAXS integrated intensity linearly increases with time until the cut-off voltage. This augmentation of the SAXS integrated intensity may correspond to the nanostructure changes related to silicon swelling due to lithium alloying, which is effective in this region of time/potential, as evidenced by the important reduction of the Si (111) peak. Further data collection is required to determine precisely the meaning of the two-regions

where SAXS profiles differently behave, which could be related to an inhomogeneous process of lithiation (may be related to the inhomogeneity in size and composition of the silicon particles) or arise from the sequential lithiation mechanism of graphite and silicon phases.

To recapitulate, simultaneous SAXS and WAXS show correlated changes in the atomic and nanoscale structure that confirm the potential of the technique to analyze synchronized structural changes at different scales with electrochemical cycling. It appears that phenomena more complex than those we documented on a-Si/c-$FeSi_2$/graphite electrodes may happen and revealed non-monotonous and Q-dependent SAXS features, which deserve further work to be analyzed.

Crystalline germanium and graphite composite investigated by operando in-lab X-ray diffraction

A self-supported electrode was prepared using 25% crystalline germanium nanoparticles used in Chapter 3, 65% graphite, 7% Na-CMC, and 3% Super P. Unfortunately, in this case, the delithiation stage could not be studied because of technical problems, either lack of pressure in the cell or side reactions due to the electrode thickness. This composite electrode was cycled at C/25 against Li metal.

Figure 7.3 shows on the *left* the evolution of the diffracted peaks for crystalline graphite and germanium during lithiation, and the *right* shows the electrochemical curve, voltage vs. Li/Li^+ against the time in hours, obtained from the lithiation. The diffracted profile variations around the graphite and

germanium show the different lithiation phases formed in graphite. Lithium is intercalated in the graphite layers resulting in different phases from the less to the highest lithiated LiC_{30}, LiC_{24}, LiC_{18}, and LiC_{12}, as explained in Chapter 5. Simultaneously, the Ge(111) diffraction intensity decreases due to the Li-alloying in the crystalline structure. At the end of lithiation, c-Ge has completely disappeared, while the diffraction peaks associated with the lithiated graphite correspond to LiC_{12}. In this case, LiC_6 is not obtained, probably due to voltage hysteresis owing to the side reactions in the self-supported electrode. The XRD data were fitted to get quantitative information.

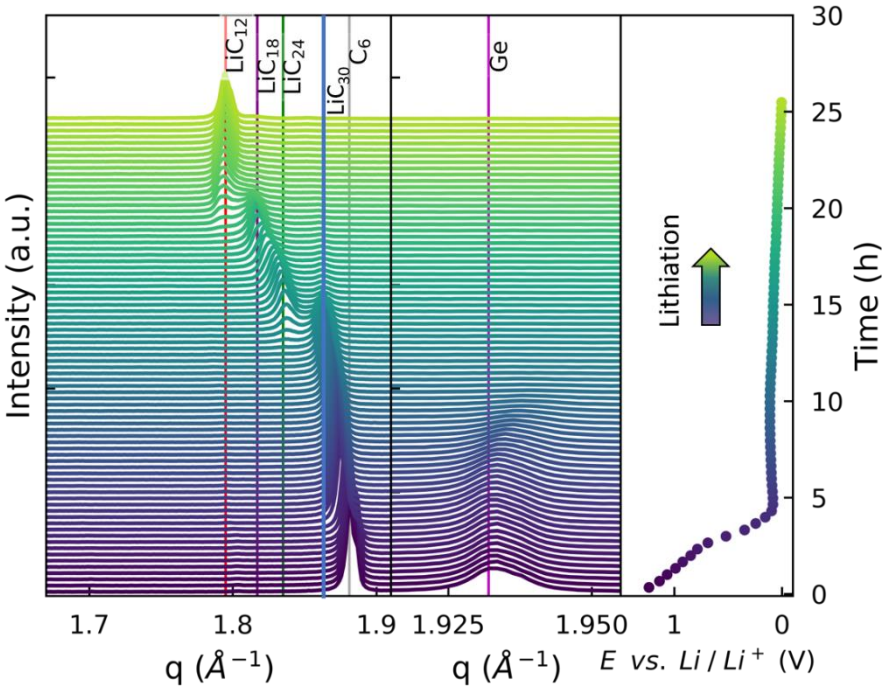

Figure 7.3 *left:* Operando XRD patterns corresponding to lithiation of graphite and germanium obtained from the electrochemical cycling. *Right:* voltage vs. Li metal against the time in hours during the complete lithiation of the composite crystalline germanium and graphite.

Figure 7.4b shows the integrated intensity variations of the Bragg peaks corresponding to graphite, its lithiated phases, and germanium against time, normalized with respect to the initial intensities measured at the pristine

state. We considered the Bragg reflections of graphite(002), LiC_{30}(006), LiC_{24}(001), LiC_{18}(004), LiC_{12}(002), and Ge(111).

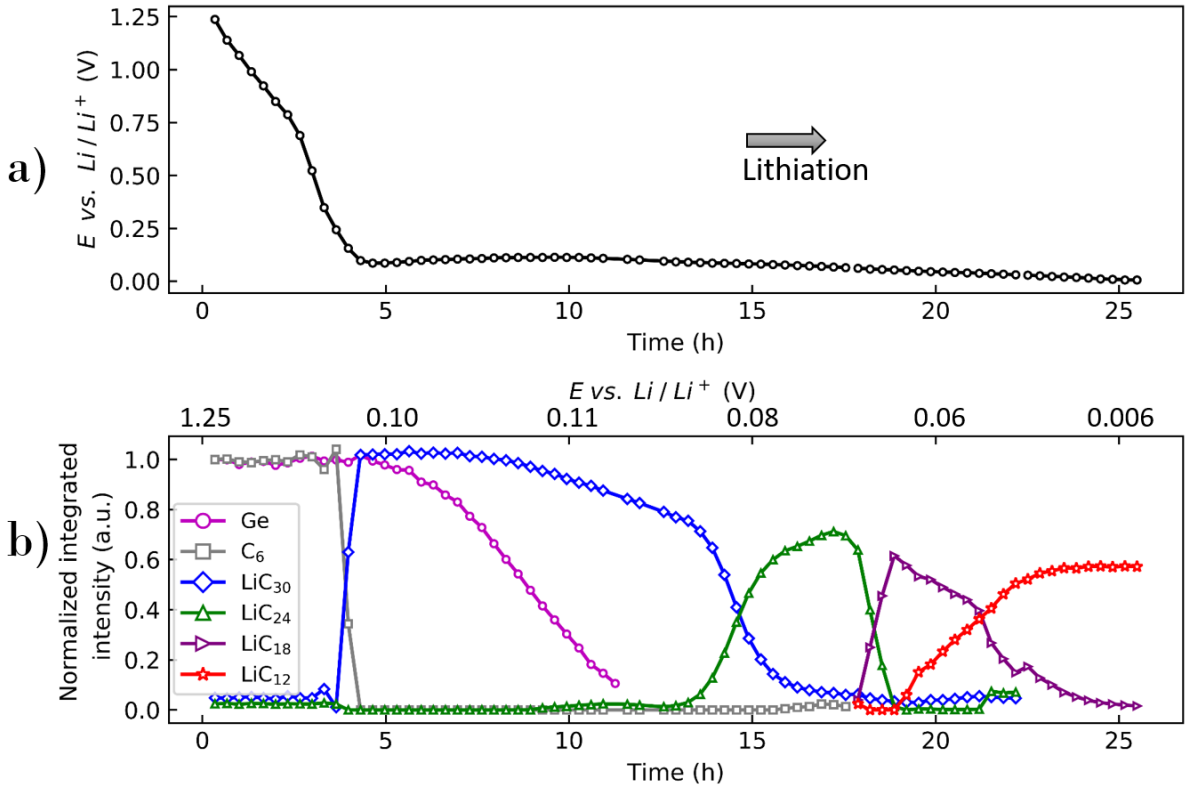

Figure 7.4 a) voltage vs. Li/Li^+ against time for the complete lithiation of the composite with crystalline germanium and graphite. b) Normalized integrated intensity obtained from the fit of Bragg reflections Ge(111), graphite(002), LiC_{30}(006), LiC_{24}(001), LiC_{18}(004), and LiC_{12}(002) during a complete lithiation. Note that time in the x-axis was added at the corresponding voltage.

Graphite lithiation and formation of LiC_{30} starts approximately after 4 hours of lithiation just before the voltage reaches 0.1 V vs. Li metal. LiC_{30} has been reported to be formed in pure graphite at 0.2 V vs. Li metal[1]. In comparison, germanium diffraction intensity starts decreasing after 0.1 V, a lower voltage value than the one determined for pure Ge in Chapter 3. Between 5 and 10 h (plateau at 0.1 V), both germanium and LiC_{30} phase decrease in intensity until and the appearance of LiC_{24} at ~0.08 V. Then, successively, LiC_{18} and LiC_{12} increase in intensity between 18 h (~0.06 V) and the end of lithiation. The late lithiation of graphite and germanium may provoke the absence of most

lithiated phase LiC_6, which is probably due to voltage hysteresis, as already mentioned.

To summarize, despite electrochemical conditions that need to be optimized by improving the preparation of the self-supporting electrode, this study shows the lithiation correlation of the distinct phases contained in the composite material. The most striking result is that germanium is firstly amorphized, and then lithiation continues with the intercalation of graphite shifted to the diluted phase LiC_{30}. This result has also been observed for composites made of graphite and SiO_x, where the different chemical potentials of graphite and SiO_x affect the structure evolution[2].

Consequently, the study of model composite materials should allow disentangling the contributions of the different active components during cycling. This information should be valuable for designing and optimizing performing composites for Li-ion batteries.

1. Missyul, A., Bolshakov, I. & Shpanchenko, R. XRD Study of Phase Transformations in Lithiated Graphite Anodes by Rietveld Method. *Powder Diffr.* **32,** S56–S62 (2017).

2. Park, J., Park, S. S. & Won, Y. S. In Situ XRD Study of the Structural Changes of Graphite Anodes Mixed with SiOx During Lithium Insertion and Extraction in Lithium Ion Batteries. *Electrochim. Acta* **107,** 467–472 (2013).

Appendices

8.1 Chapter 3: appendix

8.1.1 Coupling of sample height and lattice parameter

Both the lattice parameter value and the sample position have an impact on the diffraction peak position. Consequently, when performing Rietveld refinement, the coupling between these parameters must be considered. Figure 8.1 shows the evolution of the c-Ge phase lattice parameter and position and the Be phase position during cycling (the Be lattice parameters are kept constant). This latter varies monotonously, however, within 0.01 mm. This can be considered a sensitivity limit as modifying the position by this value results in a mainly unchanged Rwp value (for a definition of the different Rietveld error indices, see Toby[1]). The Ge position appears to vary by almost 0.2 mm, in correlation with the evolution of the lattice parameter. To evaluate the reliability of our results, we performed different tests, keeping constant independently one or the other of the parameters. They all proved the robustness of the results.

[1] Toby, B. H. R factors in Rietveld analysis: How good is good enough? *Powder Diffr.* **21**, 67–70 (2006).

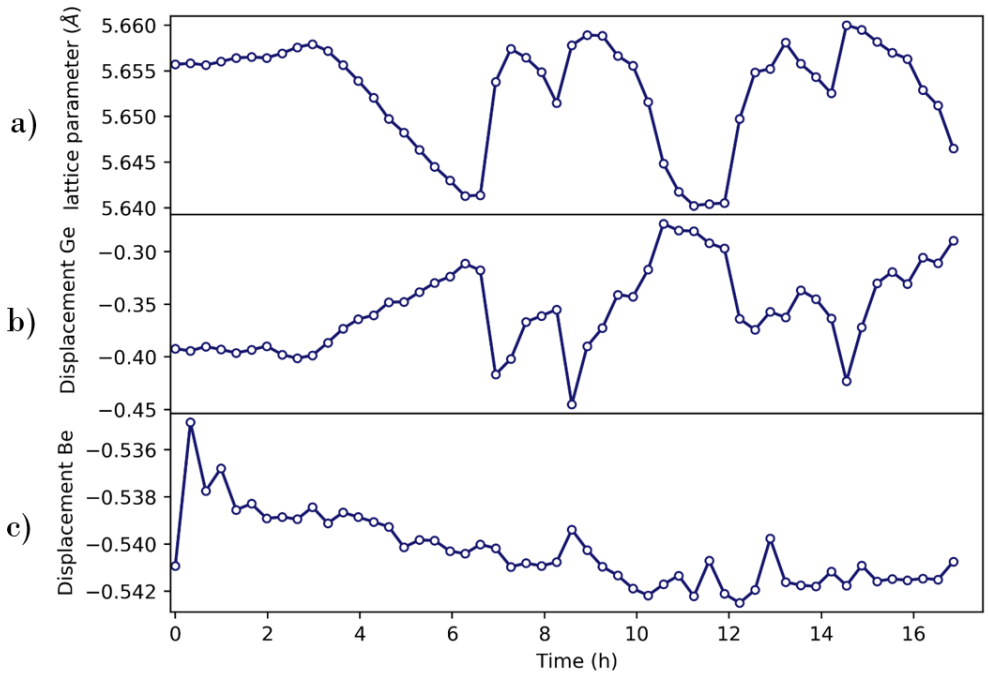

Figure 8.1 evolution of a) lattice parameter of Ge, b) displacement of Ge electrode, and c) displacement of Be with time for the *operando* study of c-Ge Nps partial lithiation. The displacement values are given in mm.

8.1.2 Partial lithiation of c-Si Nps

Figure 8.2 shows the time dependence of (a) the cell potential and the transferred specific capacity upon the two cycles, (b) the integrated X-ray diffraction intensity, and (c) the strain ε (= −Δq/q where q is the scattering vector) relative to the initial state.

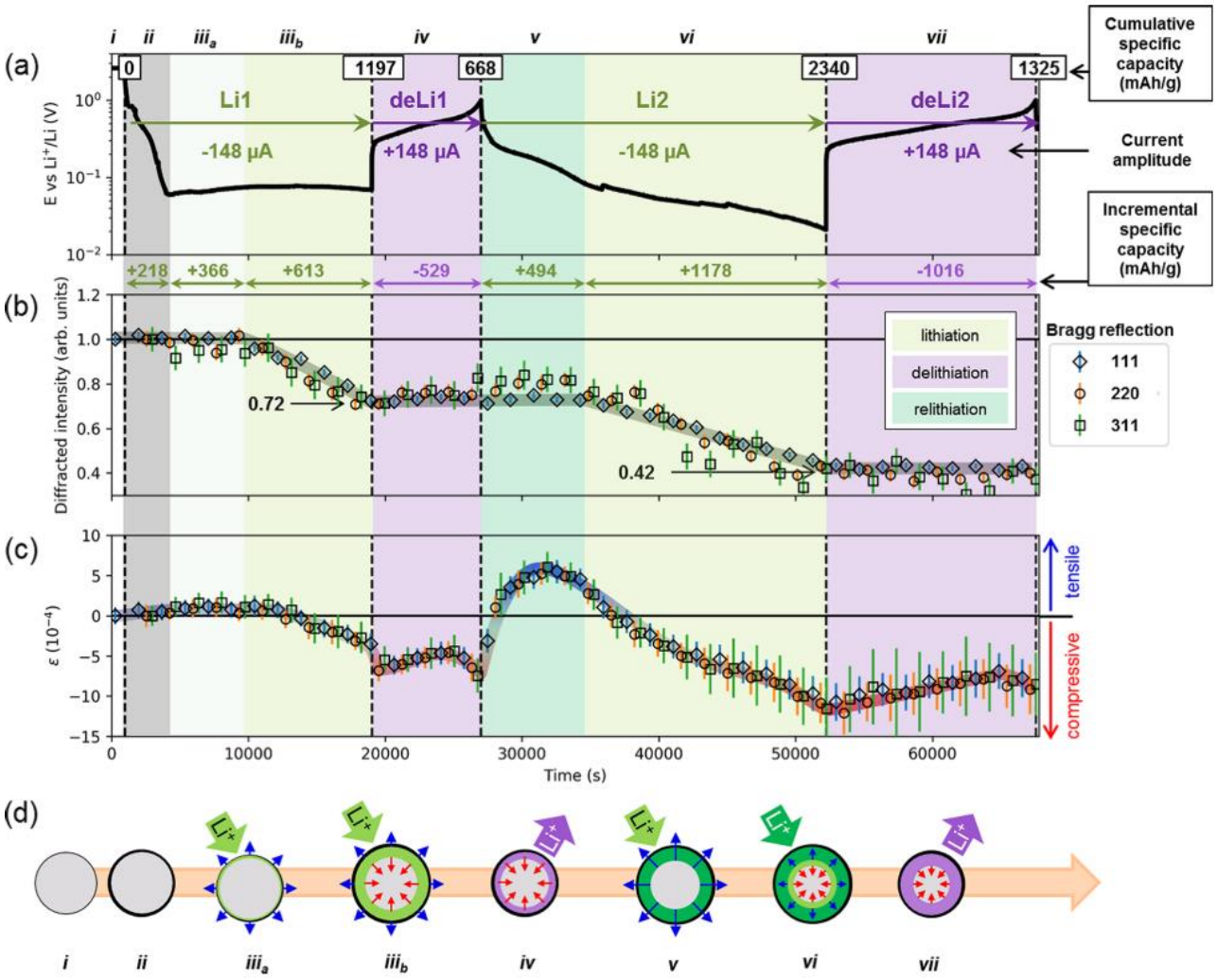

Figure 8.2 (a) Cell potential, (b) intensity of the SiNP Bragg reflection, and (c) strain in the SiNP over the first two partial lithiation/ delithiation cycles, as well as (d) a schematic view of the lithiation/delithiation process in the SiNP. Different steps corresponding to variations in the integrated intensity and/or the strain are identified (colored areas, green for lithiation, purple for delithiation). For each step (i to vii), values of the current amplitude and incremental and cumulative specific capacities are reported. In the cartoon representing the single-core–shell (first cycle) and double-core–shell (second cycle) mechanisms, compressive and tensile states are schematized using red and blue arrows, respectively. The crystalline core is colored in gray, and the outer amorphized shell in green on lithiation and purple on delithiation. [taken from Tardif *et al.*[2]]

[2] Tardif, S. *et al. ACS Nano* **11**, 11306–11316 (2017).

8.1.3 Examples of the diffracted patterns and Rietveld refinement results

Figure 8.3 shows the examples of the diffracted patterns and the Rietveld refinement results obtained on the short-scans on the *operando* lithiation of Ge when the $Li_{15}Ge_4$ phase is formed.

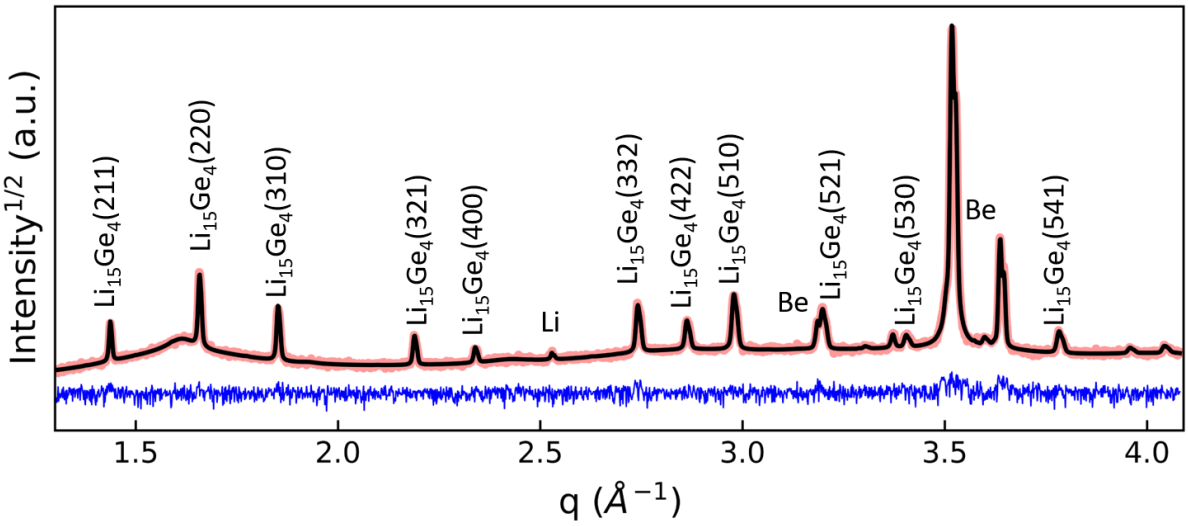

Figure 8.3 Example of the diffracted pattern and Rietveld refinements resulted from a) the long scans in-situ studies b) short-scans on the operando lithiation of Ge when $Li_{15}Ge_4$ phase is formed.

8.2 Chapter 4 Appendix

8.2.1 Morphological characterization of $Si_{100-x}Ge_x$ alloys

8.2.1.1 Complementary HRTEM and EDX mapping images of $Si_{100-x}Ge_x$ alloys

Figure 8.4a shows an additional HRTEM image on the Ge-rich alloy of particles, mostly spherical and faceted with sizes ranging between 105–180 nm. Figure 8.4b shows the EDX chemical mapping of Figure 8.4a, where the

Si-richer outer zone is no longer observed. Here Si and Ge are observed uniformly through the particle. Figure 8.4c shows the selected areas for quantitative mapping. Figure 8.4d shows the composition of Si and Ge for areas 1 and 2, showing in general Ge-richer alloys.

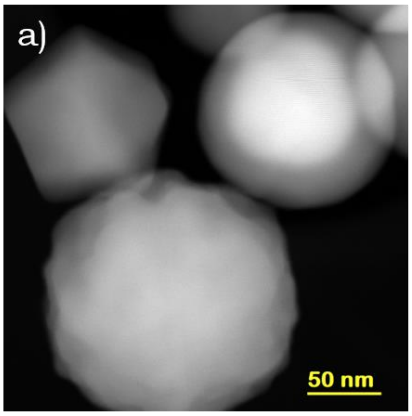

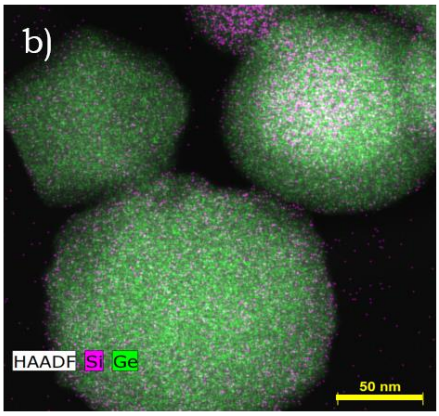

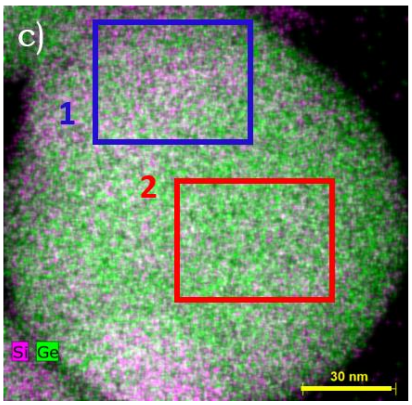

d)

Zone	Composition
Area 1	$Si_{30}Ge_{70}$
Area 2	$Si_{21}Ge_{79}$

Figure 8.4 a) STEM-HAADF image obtained in the $Si_{21}Ge_{79}$ powder. b) and c) EDX elemental mapping showing the distribution of Ge and Si on the powder. d) quantitative results from EDX mapping.

Figure 8.5a shows a bimodal distribution of nanoparticle sizes as small as 50 nm and larger sizes between 70–150 nm. Figure 8.5b shows the inner and outer zones with a sharp interface with differences in intensity. The intensity strongly depends on the atomic number of the elements and the thickness of the sample. Figure 8.5c shows that the crystallographic planes in the interior of the particles are closer to Ge with approximate values of 3.35 Å.

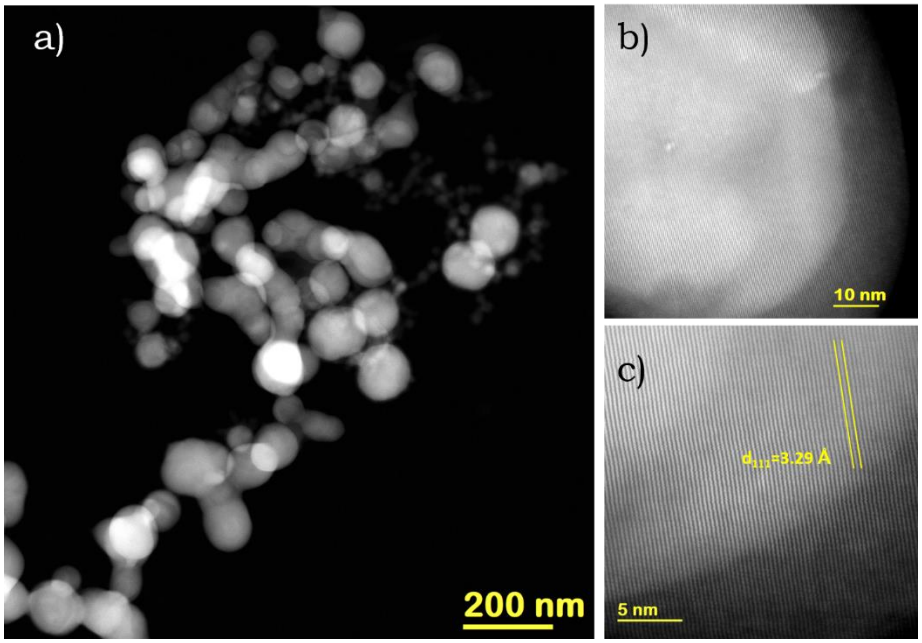

Figure 8.5 a–c STEM-HAADF image obtained in the $Si_{47}Ge_{53}$ powder.

8.2.1.2 Chemical composition across the line profile in the Si-rich alloy

Figure 8.6 shows the atomic percentage vs. distance in nm for the alloy with average composition $Si_{63}Ge_{37}$ for the line profiles in different particles. This Figure shows a heterogeneous atomic percentage across the three different zones. The particles, in general, show a richer Si atomic composition. Note that the edges of the particles are significantly Si-richer in composition than the middle of the particle.

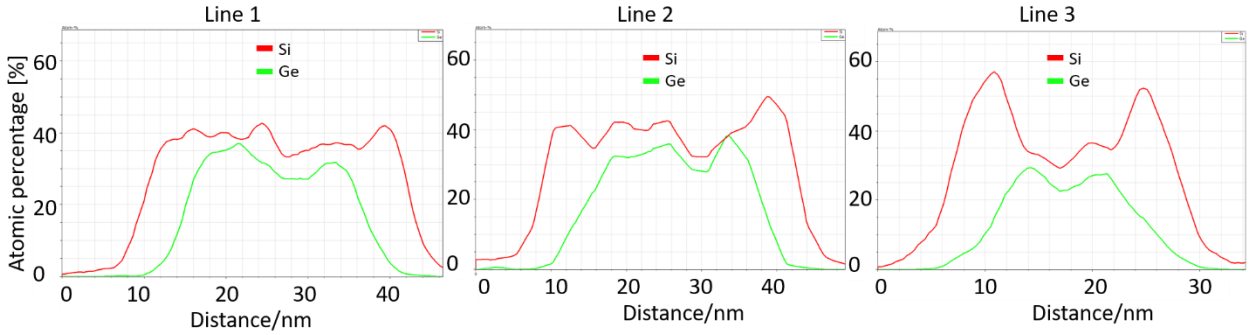

Figure 8.6 Silicon and Ge atomic composition across the line for the three particles. In each chemical mapping, the atomic percentage is plotted against the distance in nm.

8.2.2 *Operando* XRD studies on $Si_{100-x}Ge_x$ alloys

Figure 8.7a shows the first lithiation for the crystalline alloy Nps with an average composition: $Si_{47}Ge_{53}$ vs. Li metal down to 0.005 mV at C/20. Note that this Figure was plotted until 0.108 V. Beyond the intensity is too weak to be refined. Figure 8.7b shows the normalized integrated intensity against voltage that results from the fit of $Si_{47}Ge_{53}$(111) reflection during lithiation. An example of the different phases, which have to be considered to account for the peak. In this case, phases (x = 65 and x = 50) allow describing the broad peak of the alloy with an average composition $Si_{47}Ge_{53}$. As expected, the Ge-rich $Si_{35}Ge_{65}$ alloy decreases faster than the $Si_{50}Ge_{50}$ in the voltage range between 0.300 and 0.130 V.

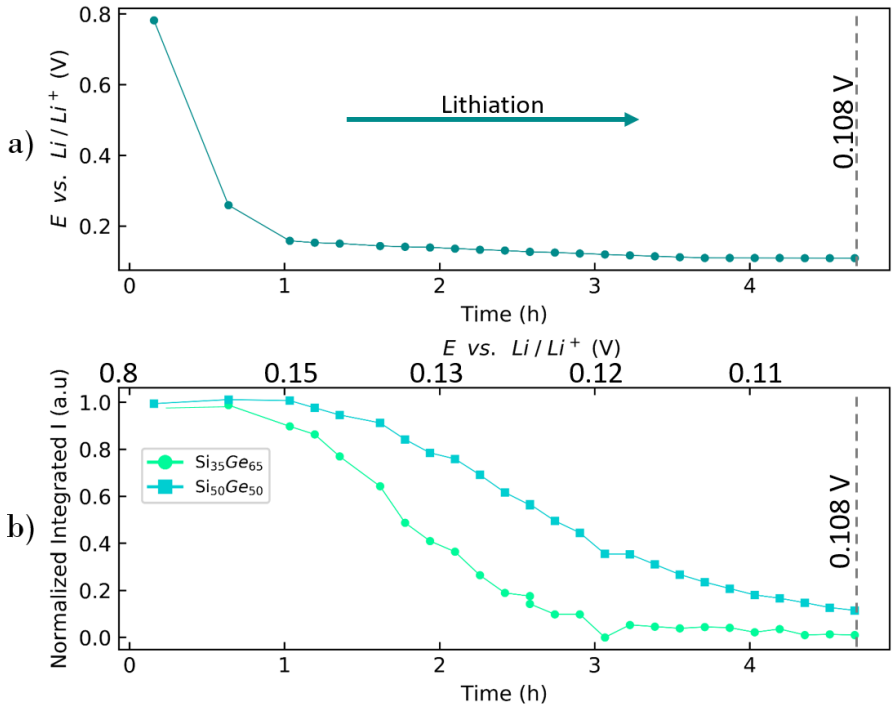

Figure 8.7 a) voltage vs. Li/Li^+ against time for the complete lithiation of the alloy with average composition $Si_{47}Ge_{53}$. b) Normalized integrated intensity obtained from the fit of the distinct phases in $Si_{47}Ge_{753}$ during a complete lithiation. Note that time in the x-axis was replaced for the corresponding voltage.

Figure 8.8a and b show the electrochemical lithiation and the normalized integrated intensity that results from the fit of the peak $Si_{63}Ge_{37}$(111). This compound appears to be less heterogeneous than the two others as one phase allows describing the broad peak of the alloy with an average composition $Si_{63}Ge_{37}$.

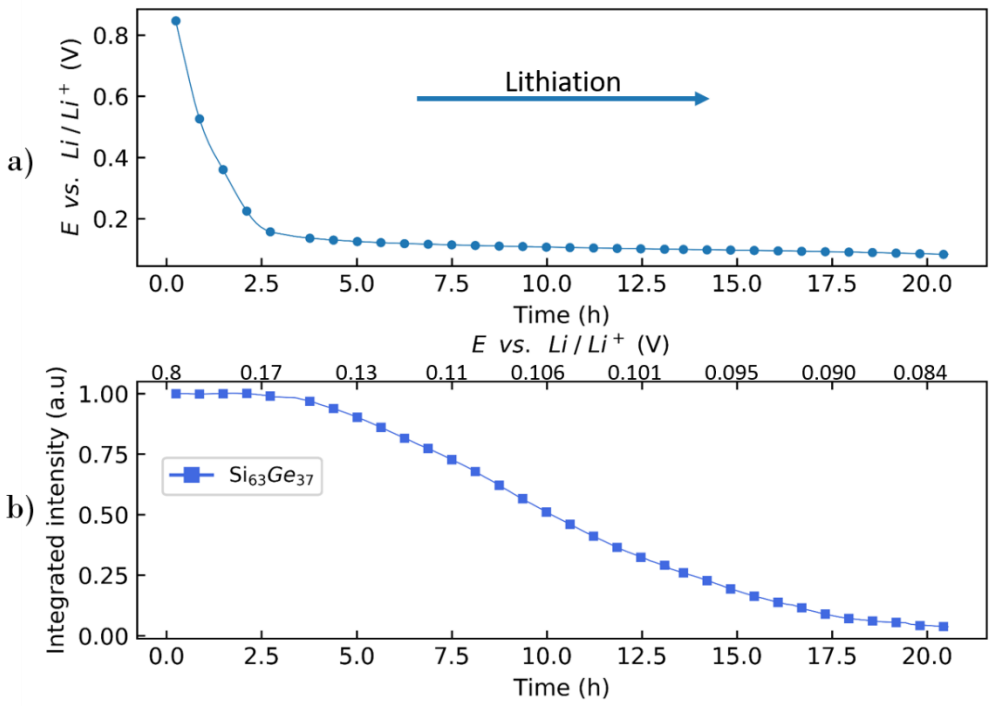

Figure 8.8 a) voltage vs. Li/Li⁺ against time for the complete lithiation of the alloy with average composition $Si_{63}Ge_{37}$. b) Normalized integrated intensity obtained from the fit of $Si_{63}Ge_{37}$ during a complete lithiation. Note that time in the x-axis was replaced for the corresponding voltage.

We also performed similar operando measurements with Si Nps self-supported electrode. Figure 8.9a and b show respectively the electrochemical lithiation and the normalized integrated intensity against time that results from the fit of Si(111) reflection during lithiation. Crystalline Si Nps are amorphized during lithiation between 0.041 and 0.055 V.

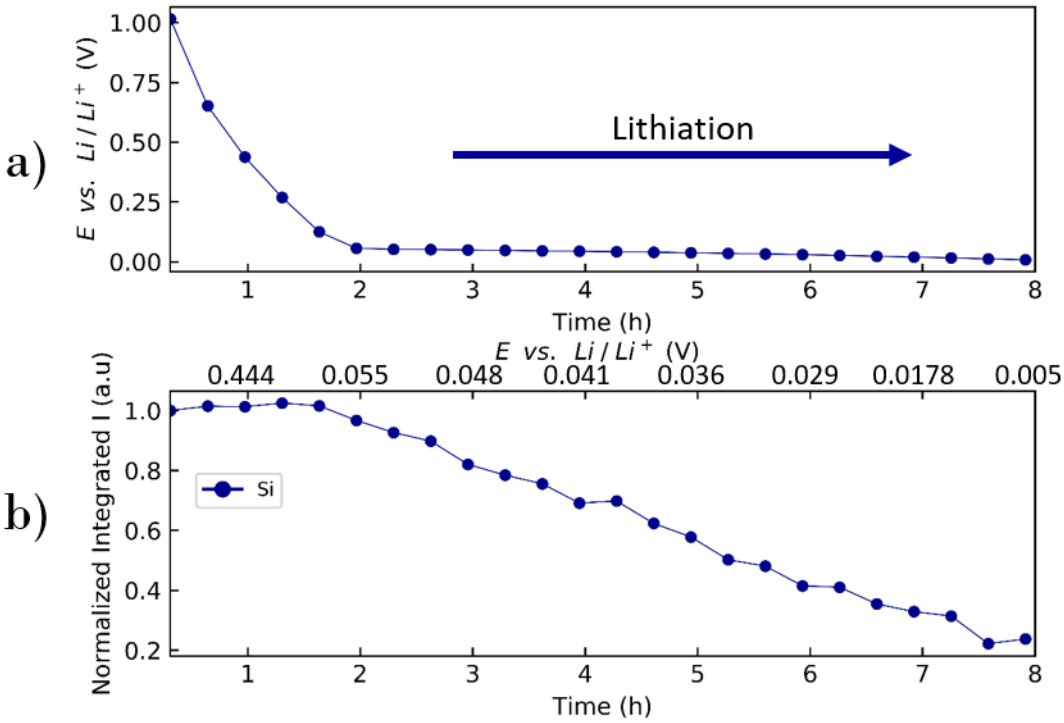

Figure 8.9 a) voltage vs. Li/Li^+ against time for the complete lithiation of crystalline Si Nps. b) Normalized integrated intensity obtained from the fit of Si Nps during a complete lithiation. Note that time in the x-axis was replaced for the corresponding voltage.

8.2.2.1 Formation of the phases $Li_{15}(Si_xGe_y)_4$

We follow whether the Si-rich alloy, $Si_{67}Ge_{37}$, forms crystalline $Li_{15}(Si_xGe_y)_4$. Figure 8.10 evidences the absence of diffraction peaks associated to $Li_{15}(Si_{100-x}Ge_x)_4$ in the XRD patterns recorded during lithiation and delithiation of the $Si_{63}Ge_{37}$ measured in-lab as a self-supported electrode at C/20. This result is coherent with the dQ/dV curve obtained from galvanostatic cycling, which is very similar to the case of Si Nps for which c-$Li_{15}Si_4$ does not form.

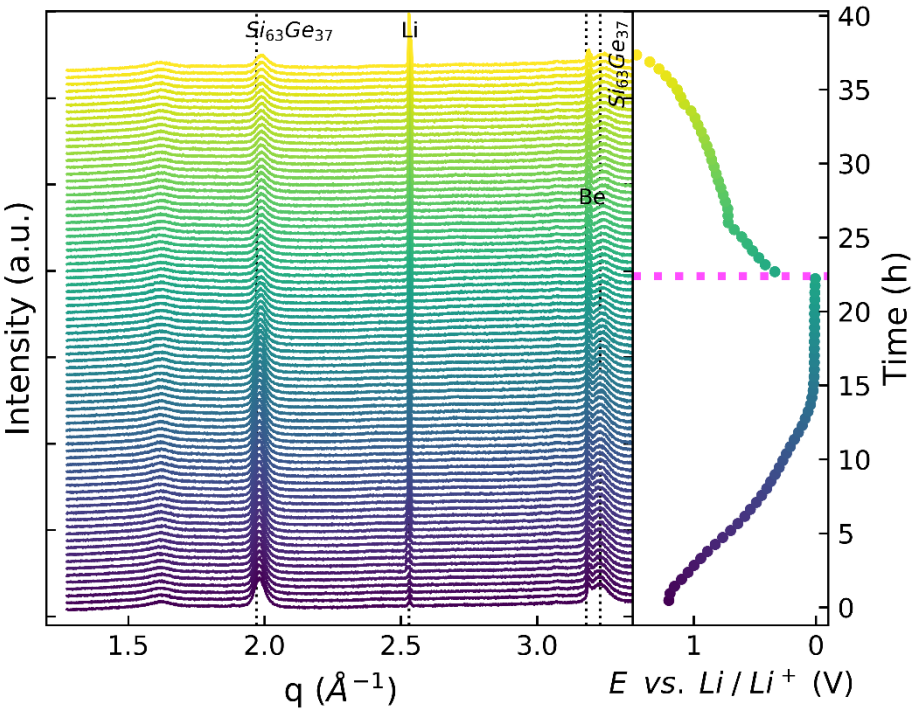

Figure 8.10 left: Operando XRD patterns, right: electrochemical cycling during the complete lithiation of $Si_{63}Ge_{37}$ at C/20.

Figure 8.11a–d shows the voltage vs. Li/Li⁺, normalized integrated intensity, full widths at half maximum (FWHM), lattice parameter against time for the $Si_{47}Ge_{53}$ compound. For clarity, the time (hours) was replaced by the corresponded voltage, and the dotted vertical line represents the end of lithiation.

During lithiation beyond 10 mV, the crystalline $Li_{15}(Si_{100-x}Ge_x)_4$ phase is formed. The associated diffraction intensity continues to grow until the end of lithiation at 0.005 mV vs. Li/Li+, while the full widths at half maximum (FWHM) for the different Bragg peaks are constant, the lattice parameter shows a slight increase. During delithiation, two different stages can be distinguished: the first part of delithiation until 0.455 V, and the second, from 0.455 V until 0.465 V. Through the first process, while the voltage is increasing considerably, the normalized integrated intensity and FWHM of the

$Li_{15}(Si_{100-x}Ge_x)_4$ reflections stay constant. In contrast, the lattice parameter gradually decreases. During the second stage, the voltage is almost constant. In this plateau, the diffraction intensity decreases. The increase in FWHMs, which is more marked for the peaks at larger scattering angles, is characteristic of an increasing distortion in the lattice. The lattice parameter evolution is similar to the one observed for the $Li_{15}Ge_4$ phase in chapter 3 and the $Li_{15}(Si_{100-x}Ge_x)_4$ for $Si_{21}Ge_{79}$.

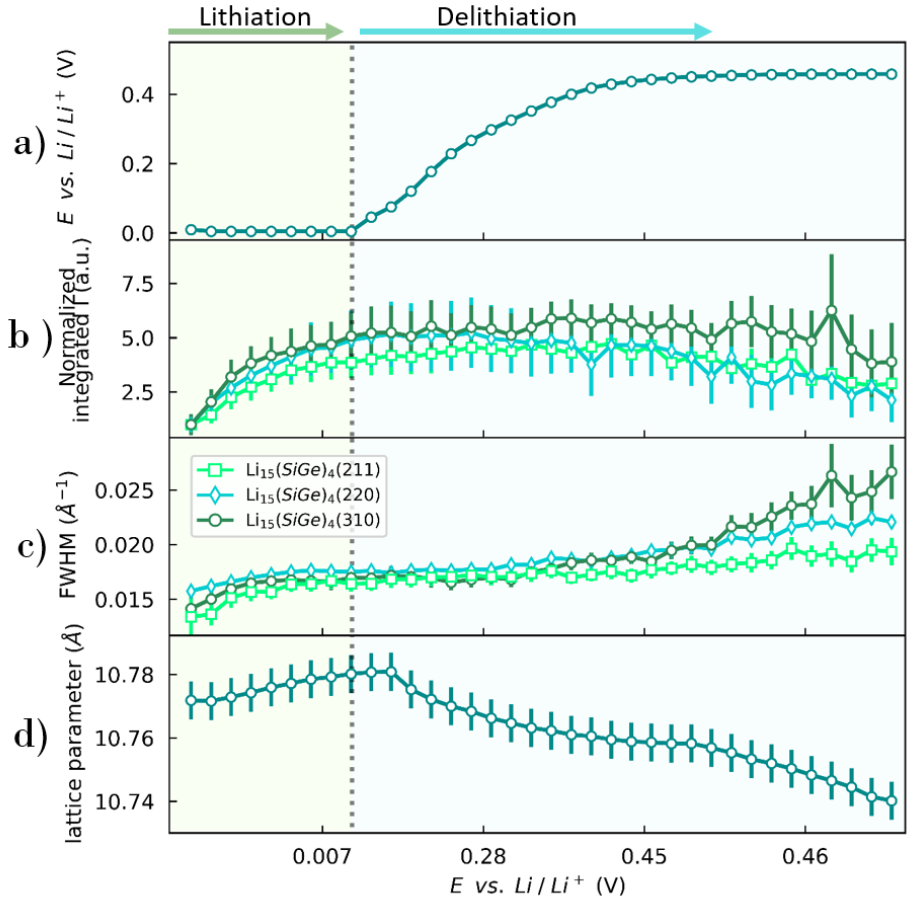

Figure 8.11 a) electrochemical cycling of the self-supported electrode with $Si_{47}Ge_{53}$ vs. Li metal during lithiation/delithiation. b) Intensity of the $Li_{15}(Si_xGe_y)_4$ Bragg reflections (211), (220), and (310). c) FWHM for the mentioned reflections, and d) Lattice parameter vs. time. Note that here, time was replaced by the corresponding voltage vs. Li/Li^+.